Experimental and numerical investigation of ductile damage mechanisms and edge fracture in advanced automotive steels

Mouhcine Kahziz

ParisTech
INSTITUT DES SCIENCES ET TECHNOLOGIES
PARIS INSTITUTE OF TECHNOLOGY

MINES ParisTech

École doctorale n°432: Sciences des Métiers de l'Ingénieur

Doctorat ParisTech

THÈSE

pour obtenir le grade de docteur délivré par

l'École Nationale Supérieure des Mines de Paris

Spécialité «Sciences et Génie des Matériaux»

Présentée et soutenue publiquement par

Mouhcine KAHZIZ

le 4 décembre 2015

Experimental and numerical investigation of ductile damage mechanisms and edge fracture in advanced automotive steels

---

Étude expérimentale et numérique des mécanismes d'endommagement ductile et rupture des bords découpés des aciers avancés pour l'automobile

Directeurs de thèse: **Éric MAIRE**
Thilo MORGENEYER
Co-encadrants de thèse: **Matthieu MAZIÈRE**
Astrid PERLADE

Jury

Mme Véronique FAVIER, Professeur, PIMM, Arts et Métiers ParisTech	Présidente
Mme Monique GASPÉRINI, Professeur, LSPM, Université Paris XIII	Rapporteur
M. Dirk MOHR, Professeur, DMPE, École Polytechnique Fédérale de Zurich	Rapporteur
M. Sébastien ALLAIN, Professeur, IJL, Ecole des Mines de Nancy	Examinateur
M. Éric MAIRE, Directeur de recherche CNRS, MATEIS, INSA-Lyon	Examinateur
M. Thilo MORGENEYER, Chargé de recherche HDR, CdM, Mines ParisTech	Examinateur
M. Matthieu MAZIÈRE, Maitre Assistant CNRS, CdM, Mines ParisTech	Examinateur
Mme Astrid PERLADE, Ingénieur de recherche, ArcelorMittal Global R&D	Examinateur

MINES ParisTech
Centre des Matériaux
10 rue Henri Desbruères, BP 87, 91003 Evry Cedex

Ce n'est qu'en essayant continuellement que l'on finit par réussir.
En d'autres termes, plus ça rate et plus on a de chances que ça marche.

Extrait de la BD "Les Shadoks"

Acknowledgements

Je tiens à remercier sincèrement tous ceux qui contribué de près ou de loin à l'aboutissement de ce projet. Je leur dis que leur amitié m'honore...

Dans un premier temps, je tiens à remercier Monique Gaspérini et Dirk Mohr d'avoir accepté d'être rapporteurs de ces travaux. Mes remerciements s'adressent également à Véronique Favier et Sébastien Allain d'avoir bien voulu faire partie de mon jury de thèse. Merci pour votre générosité et pour tous les commentaires que vous m'avez fait et qui m'ont apporté un point de vue extérieur sur mes travaux.

Cette thèse a été effectuée dans le cadre d'un contrat CIFRE accordé par l'Agence Nationale De la Recherche et de la Technologie (ANRT) et conclu en collaboration avec ArcelorMittal Global R&D et Centre des Matériaux - Mines ParisTech. A ce titre, je tiens à exprimer ma gratitude envers Astrid Perlade qui a encadré cette thèse côté ArcelorMittal et qui a apporté une nouvelle fraicheur et beaucoup de dynamisme à ce projet.

Dans un second temps, je présente ma profonde gratitude au duo du Centre des Matériaux qui m'a encadré et supporté pour mener à bien ce travail : Thilo Morgeneyer pour sa disponibilité, ses précieux conseils et son écoute et Matthieu Mazière pour ses idées, son aide et ses encouragements. Votre dynamisme et votre enthousiasme ont grandement contribué à l'aboutissement de ces travaux. Sans votre aide et votre soutien précieux, ce travail n'aurait pas abouti à ce qu'il est aujourd'hui.

Je souhaite exprimer ma reconnaissance également envers Eric Maire, qui a encadré cette thèse, pour son soutien au cours de ces quatre années, sa réactivité et les discussions très enrichissantes qu'on a eues et qui ont largement participé à entretenir ma motivation tout au long de ce projet.

Je souhaite remercier sincèrement Lukas Helfen de l'ESRF pour son aide très appréciable et ses précieux conseils dans la réalisation et la reconstruciton des essais de tomographie et laminographie à rayons X.

Je souhaite remercier les chercheurs et techniciens du CdM qui m'ont aidé au cours de cette thèse. Merci aux membres de l'équipe VAL, Farida, Kaiss, Djamel pour toutes les réponses aux problèmes que j'ai pu rencontrer sur ZéBuLon. Merci aux personnes de l'atelier pour l'usinage des éprouvettes. Merci également aux personnes du service administratif et informatique. Merci Anne et Maria pour votre aide dans la réalisation des observations MEB et des essais de traction in-situ sous MEB. Merci Abdennour pour ton aide sur Inventor. Je remercie également Odile de m'avoir aidé dans mes recherches bibliographiques.

J'associe à ces remerciements les personnes d'ArcelorMittal Global R&D qui m'ont aidé pendant mes séjours à Maizières, Abdellah, Laurent, Cédric, Coralie, Xavier, Anis, David, Ingrid et tous ceux que j'oublie maintement. Merci pour votre soutien et votre gentillesse.

Cette aventure scientifique et humaine aurait sans doute été moins agréable sans la présence de l'ensemble des thésards du CdM et autres personnes, jeunes et moins jeunes. Je tiens tout d'abord à remercier mes co-bureaux : les 2 geeks, Victor (Tom Cruz) et Aurélien, pour tous les renseignements sur Python, sur Linux ou encore sur ZéBuLon, Harry pour ta gentillesse et pour ton aide dans la reconstruction des données de l'ESRF, Justin et Hayat pour nos discussions sur des problèmes scientifiques ou autres. Merci à tous les thésards et post-doc que j'ai croisés au CdM : Franck, Geoffrey, Samuel, Raphaël, Rim, Adrien, Judith, Mickaël, Emmanuelle, Mona, Emma, Victor F., Victor B., Francesco, Jia, Nada, Hicham, Arina, Hiba, David, Guillaume, Mériem, Damien G., Christophe, Georges, Henri-Alexandre, Yin.

Merci également à tous mes amis d'Oujda, de Marrakech, de Nancy, de Paris ou d'ailleurs pour votre soutien et vos encouragements.

Mes dernières lignes iront à ma famille qui m'a toujours soutenu. Merci à ma mère, ma première fan, d'avoir toujours cru en moi et de m'avoir apporté un grand réconfort. Je remercie également mes frères et soeurs, mes neveux ainsi que mes cousins pour votre soutien tout au long de mon parcours. Je te remercie tendrement, Fadoua, pour ton amour et ton soutien sans pareil.

Une pensée émue pour mon père... qui aurait été fier !

Résumé

Étude expérimentale et numérique des mécanismes d'endommagement ductile et rupture des bords découpés des aciers avancés pour l'automobile

La performance mécanique des pièces de structures automobiles fabriquées à partir de tôles d'acier à très haute résistance (THR) est souvent réduite à cause des bords découpés. En effet, lors des étapes de mise en forme d'un acier DP, des déchirures s'initiant sur un bord cisaillé ont été détectées. L'objectif de cette étude est de mieux comprendre les mécanismes d'endommagement ductile et de rupture de bords d'un acier dual phase (DP) ayant une microstructure composite constituée d'une matrice ductile ferritique renforcée par des îlots de martensite, et d'un acier ferrite-bainite (FB). L'acier DP présente un gradient de dureté entre les phases (ferrite et martensite) et un écrouissage plus importants que ceux de l'acier FB.

Des essais de traction en MEB in situ, réalisés pour révéler le lien entre la microstructure et les mécanismes d'endommagement, ont montré que, pour l'acier FB l'endommagement a lieu sur les particules de la seconde phase. Pour l'acier DP, des cavités formées sur des particules ont été observées. La rugosité de la surface de l'éprouvette induite par la plasticité rend la visualisation de cavités qui pourraient être formées par décohésion des interfaces ferrite-martensite difficile. Les essais de tomogaphie in situ ont été réalisés afin de caractériser l'évolution de l'endommagement en trois dimensions à une échelle micrométrique dans le volume du matériaux où l'état de la triaxialité de contrainte et la déformation plastique sont plus élevées qu'à la surface. Pour l'acier DP, l'endommagement est allongé suivant la direction L (direction de laminage) quelle que soit la direction de chargement. Lors du chargement suivant la direction T, une cavité sous forme d'aiguille apparait dans la zone centrale de l'éprouvette qui correspondrait à une bande de ségrégation. Pour l'acier FB, lors du chargement suivant la direction L, la coalescence de cavités très allongées suivant la direction du chargement a lieu dans une zone perpendiculaire à la direction de traction. Dans le cas du chargement suivant la direction T, l'acier FB présente une forte tolérance à l'endommagement. La caractérisation MEB des sections de l'éprouvette de tomographie a montré, pour l'acier DP, que l'endommagement est essentiellement dû à la décohésion aux interfaces martensite-ferrite, par contre, pour l'acier FB des cavités de taille inférieure à 1 μm, qui ne sont pas détectables en microtomographie, ont été observées proche de la surface de l'éprouvette. Ces cavités s'amocent sur les carbures.

La quantification des données de tomographie a montré que l'acier DP contient deux fois plus de cavités initiales que l'acier FB et que la densité de cavités augmente clairement lors du chargement mécanique. La fonction de Chu et Needleman [Chu and Needleman, 1980] a été utilisée pour prédire la cinétique de germination de cavités pour les deux matériaux ayant un nombre maximal de sites de germination très différents. Pour la modélisation de la croissance de cavités le modèle de Huang [Huang, 1991] étant une modification du modèle de Rice et Tracey [Rice and Tracey, 1969] a été optimisé.

Les essais de laminographie ont permis de caractériser la rupture de bords découpés (bord poinçonné et bord usiné) en appliquant des conditions aux limites proches à celles de la mise en forme des aciers. La chute de ductilité mesurée par la réduction d'ouverture d'entaille est entre 30 et 40% pour l'acier DP et 5 et 10% pour l'acier FB. La caractérisation de l'état initial par laminographie a montré que les bords poinçonnés présentent une rugosité au niveau de la zone rompue et un micro-endommagement sous forme d'aiguille que s'initie sur la surface des bords poinçonnés. Pour l'acier DP, lors du chargement mécanique, ce micro-endommagement suit les lignes d'écoulement et coalesce avec la zone cisaillée. Aucune striction n'a été observée sur le bord poinçonné DP au moment de l'initiation de fissure. Par contre, pour le bord usiné, l'endommagement est plus important loin de la surface du bord ($\sim$800 μm) où le matériau subit une striction importante. Pour l'acier FB, une striction a été observée lors du chargement du bord poinçonné. La rupture de ce dernier s'initie sur

la surface sur bord, par contre, dans le cas du bord usiné la rupture s'est initiée loin du bord. Les données de laminographie ont montré que les deux matériaux présentent à l'état initial plus de cavités dans la zone affectée par la découpe que dans le volume. Pour les bords poinçonnés DP et FB, l'endommagement reste plus important proche de la surface des bord lors du chargement mécanique. En revanche, l'endommagement croit plus vite loin de la surface des bords ce qui est cohérent avec la striction observée dans cette zone.

Des calculs 3D par éléments finis couplés à la corrélation d'image ont été réalisés en utilisant les lois de comportement élasto-plastiques des matériaux étudiés. Ceux-ci ont montré que le profil de bord poinçonné ne permet pas de localiser la triaxialité de contrainte et la déformation plastique proche du bord. Ces paramètres mécaniques locaux ont été localisés loin de la surface des bords ce qui est cohérent avec le niveau d'endommagement important apparu dans cette région lors des essais de laminographie. Ces calculs ont servi pour valider les critères d'endommagement de germination et de croissance de cavités identifiés sur les matériaux de bases. Pour les deux matériaux étudiés, en introduisant le pré-écrouissage et le pré-endommagement induits par la découpe, la fraction volumique de cavités est maximale proche de la surface du bord poinçonné lors du chargement mécanique. Par contre, la fraction volumique de cavités est relativement plus importante, pour les deux matériaux, loin des bords usinés lors du chargement mécanique.

L'essai d'expansion de trou a été utilisé pour réaliser une étude paramétrique permettant de valider les critères de germination et de croissance de cavités développés en faisant varier l'épaisseur de la tôle et la pré-déformation. Pour les deux matériaux, une chute de ductilité, relative à la réduction de ratio d'expansion de trou, est observée pour les bords poinçonnés. Pour l'acier FB, les résultats expérimentaux et numériques ont montré que le ratio d'expansion de trou, pour les quatre épaisseurs étudiées, augmente quand l'épaisseur de la tôle augmente. Il a été expérimentalement et numériquement montré que la pré-déformation n'a aucune influence sur la formabilité du bord usiné FB. Par contre, les calculs éléments finis ont mis en évidence la sensibilité de la nuance DP à la pré-déformation et au pré-endommagement.

Abstract

Experimental and numerical investigation of ductile damage mechanisms and edge fracture in advanced automotive steels

The mechanical performance of automotive structures made of advanced high strength steels (AHSS) is often seen reduced by the presence of cut edges. Some cases of failure in DP steels, which initiate via ductile fracture mechanisms on blanked edges were detected during forming processes. Here is an attempt to gain insight into the ductile damage mechanisms and edge fracture of a dual phase (DP) steel consisting in a ferrite-martensite composite microstructure and a ferrite-bainite (FB) steel with an ultimate tensile strength of approximately 600 MPa for both materials and higher phase hardness gradient and higher work hardening for the DP steel.

Using in situ tensile testing in SEM to reveal damage mechanisms in link with the microstructure, it was found that damage mainly arises from second phase particles for the FB steel. For the DP steel, damage nucleated on particles has been observed and damage on ferrite-martensite interfaces may be present, however, it hard to observe it due to the increased surface roughness caused by plasticity. In situ X-ray synchrotron tomography experiments have been carried out to assess damage evolution at micrometer resolution in three dimensions in the bulk material, where stress triaxiality and plastic strain are known to be higher than at the surface. For DP steel, it was found that, during mechanical loading, damage is elongated in L direction (rolling direction) whatever the loading direction. However, for testing in T direction, a needle-shape void appeared at the specimen center which could be linked to a segregation band. For FB steel, during testing in L direction, final coalescence of highly elongated voids in loading direction occurs through narrow region oriented normal to the loading direction. During T testing, the FB steel exhibits a high damage tolerance. Indeed, a very long needle-shaped void nucleated at the specimen center normal to the loading direction grew substantially. SEM observations of cross-sections of tomography specimens showed that damage in the studied DP steel mainly occurs in ferrite-martensite interfaces. However, on the observed cross-section of FB steel, voids with sizes below 1 μm are found close to the fracture surface in link with carbide interfaces.

In terms of damage quantification, It is found that the DP steel contains twice more micrometer-size initial voids than the FB steel and that the density of cavities clearly increases with the applied deformation for DP and FB steels at L and T loading directions. A Chu and Needleman nucleation function [Chu and Needleman, 1980] is successfully fitted on both nucleation kinetics, with very different numbers for the maximum amount of possible nucleation sites. The growth of the largest voids has been investigated as a function of the applied strain and successfully fitted by a Rice and Tracey law [Rice and Tracey, 1969] with Huang's modification [Huang, 1991].

Using in situ X-ray synchrotron laminography that allows to observe regions of interest in thin sheet-like objects at micrometer resolution keeping the mechanical boundary conditions of engineering relevance close to metal forming conditions, edge fracture has been assessed using two edge conditions for both materials: punched edge and machined edge produced using Electrical Discharge Machining (EDM). It was found that the punched edge causes a reduction of ductility (measured by Crack Mouth Opening Displacement CMOD) of about 30% - 40% and about 5% - 10% for the studied DP and FB steels respectively. X-ray laminography observations at initial state show that the fracture zone of the punched edges is rough and some needle-shape voids which might be linked to segregation zones and to anisotropic void growth during the punching process are initiated at the fracture zone surface. For the DP punched edge, the needle voids following the ferrite-martensite flow lines grew during loading and coalesce with the sheared zone. The DP punched edge did not show localized necking before fracture. In contrast, during loading of DP machined edge, the damage starts ahead of the edge ($\sim$800 μm) where substantial necking has occurred. During mechanical loading of the

FB punched edge, needle voids grew and coalesce with the internal damage and necking has been observed close to the edge surface. In contrast, failure occurs via necking of a zone about 800 μm away from the FB machined edge surface and subsequent failure via classical ductile fracture mechanisms. 3D image analysis performed to quantify the initial damage and its evolution shows that in the initial state, there are twice more micrometer-size voids close to the fracture zone than ahead of the edge for both materials. For both materials also, void growth is increased close to edge surface for the punched edges. In contrast, for the machined edges void growth is maximal away from the edge which is consistent with the increased necking in this zone.

Combined surface digital image correlation and 3D finite element analysis were carried out using elasto-plastic constitutive laws of the investigated materials. It was found that meshing the edge profile geometry does not allow to localise in the edge region the stress triaxiality and plastic strain known to favor ductile damage growth and numerically accounting for the pre-straining introduced in the cutting-affected zone does not localize stress triaxiality in the edge region either. The stress triaxiality and the plastic strain are localized in the simulation far ahead of the edge which is consistent with the increased level of void growth in the machined edge observed during in situ laminography experiment. These 3D finite element analysis have been used to validate the void nucleation and growth criteria developed. It was found that for the punched edge, taking into account pre-damage and pre-strain of the punching-affected zone void volume fraction was maximal close to the edge surfaces. However, for the machined edges, void volume fraction was slightly increased in the bulk material.

Experiments and finite element simulation of hole expansion have been carried out using four sheet thickness in order to validate the identified criteria of void nucleation and growth. It was found that hole expansion ratios (HER) increase for increased sheet thicknesses. Up to ε=0.5, HER of machined edge is found to be independent on the pre-strain levels. However, the FE analysis shows that HER decreases for high pre-strain levels for the DP machined edge. For both materials, reduction of ductility (measured by HER) is observed due to the presence of punched edges.

Contents

Introduction

Contents

Résumé

Dans le contexte environnemental actuel, les aciers à très haute résistance (THR) sont largement utilisés dans l'industrie automobile pour une réduction de la consommation des véhicules ainsi qu'une diminution des émissions de CO_2. La performance mécanique des pièces de structures automobiles fabriquées à partir de tôles d'acier THR est souvent réduite à cause des bords découpés. En effet, lors des étapes de mise en forme d'un acier DP, des déchirures s'initiant sur un bord cisaillé ont été détectées. L'objectif principal de ce présent travail est de mieux comprendre les mécanismes d'endommagement ductile et de rupture de bords d'un acier dual phase (DP) ayant une microstructure composite constituée d'une matrice ductile ferritique renforcée par des îlots de martensite, et d'un acier ferrite-bainite (FB). Cet objectif peut être scindé en plusieurs points :

- Caractérisation des mécanismes d'endommagement des deux matériaux de base FB600 et DP600;
- Identification de modèles de germination, croissance et coalescence de cavités basés sur des paramètres physiques identifiés expérimentalement;
- Compréhension et quantification de l'endommagement d'un bord découpé à l'état initial et de son évolution lors d'un chargement mécanique;
- Étude de l'influence de l'endommagement et de l'écrouissage de la zone affectée par la découpe sur le comportement d'un bord découpé;
- Caractérisation de deux types de bord découpé : bord poinçonné et bord usiné par électro-érosion;
- Identification des mécanismes d'endommagement ductile conduisant à la rupture des bords découpés pour les deux matériaux étudiés en utilisant la laminographie à rayons X;
- Développement d'une approche numérique basée sur des paramètres physiques identifiés par les techniques tomographie/laminographie à rayons X permettant de comprendre l'effet de la plasticité et de l'endommagement initial d'un bord découpe.

La démarche de cette étude se base sur la compréhension des mécanismes d'endommagement ductile des deux matériaux de base et de l'effet de microstructure en utilisant les techniques de traction en MEB in-situ et de tomographie in-situ à rayon X. L'état initial d'un bord découpé a été caractérisé par microscopie optique, MEB et des mesures de microdureté pour quantifier l'effet du procédé de découpe. Les essais de traction in-situ en tomographie ont permis d'identifier des critères de germination et de croissance de cavités qui seront utilisés pour la simulation numérique. Le comportement des deux types de bord découpé pour les deux matériaux étudiés a été caractérisé par des essais d'ouverture d'entaille in-situ en laminographie à rayons X. La corrélation d'images a été utilisée afin d'identifier les champs de déplacements subis par la zone d'intérêt. A l'issue de ces essais, un critère d'endommagement micromécanique a été développé pour simuler les essais d'ouverture d'entaille et d'expansion de trou en utilisant le code éléments finis Z-Set.

Motivations

In the last decade, Advanced High Strength Steel (AHSS) grades offering high strength have been developed and proposed by steelmakers for automotive industry. For environmental and safety reasons, the use of AHSS expands increasingly in automotive industry in order to reduce the vehicle weight and therefore the fuel consumption and CO_2 emissions. Compared to conventional steel grades, these steels are known for their improved formability and crash worthiness. Among these AHSS grades, dual phase (DP) and ferrite-bainite (FB) steels with their composite microstructure consisting of ferritic ductile matrix containing respectively a hard martensitic or bainitic second phase in the form of islands present a good compromise between strength and resistance to damage. The use of automotive parts made of DP steels is often seen reduced due to the presence of cut-edges. Indeed in automotive industry, most used cutting processes are shearing and punching because of their speed, simplicity and low cost. Using these forming operations the mechanical performance of formed automotive parts can be affected. Cases of failure in DP steels which initiate via ductile fracture mechanisms on blanked edges were detected (fig. 0.1).

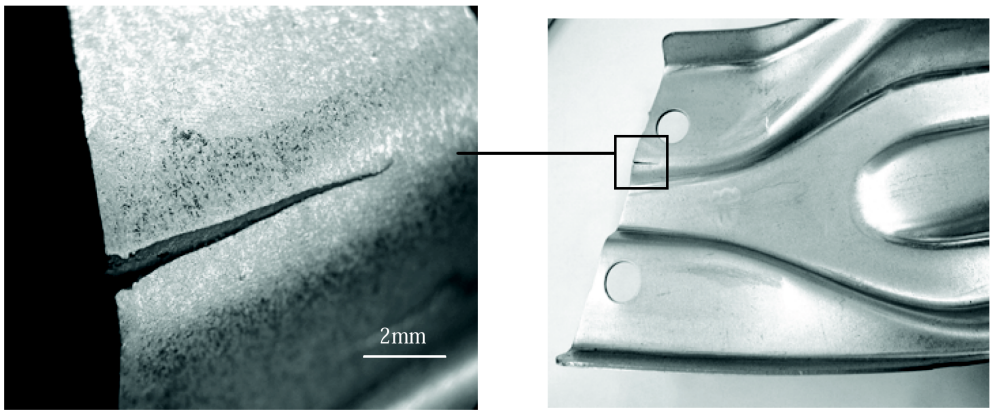

Figure 0.1 – Failure initiated on cut-edge in an automotive part made of DP steel (ArcelorMittal credit)

Objectives

The overall aim of the present work is to offer a better understanding of the effect of cut-edges on the ductility of AHSS steels. The objectives of this work are detailed in the following:

- investigate the damage mechanisms of base materials and identify physically based criteria for void nucleation and growth prediction;
- understand and quantify the damage at initial state caused by cutting process in the cutting-affected zone;
- study the effect of initial damage of the cutting-affected zone and work hardening induced by cutting process on the mechanical behavior of punched edge during subsequent forming;
- identify ductile damage mechanisms leading to edge fracture of the two investigated materials during mechanical loading;
- compare the damage mechanisms of two types of edges: punched edge and machined edge made by electrical discharge machining (EDM);
- understand the damage in link with steel microstructure and its effect on the mechanical behavior at edges;
- develop a physically based numerical model using experimental data provided by X-ray tomography/laminography to better understand the plasticity and damage mechanisms involved in edge fracture phenomenon.

Approach

The objective of this work is to clarify the effect of edge quality on the mechanical behavior of AHSS grades ductility in link with microstructure and damage mechanisms of the base materials. The approach proposed to complete this research project is detailed in the following:

- Two materials, DP (ferrite-martensite microstructure) and FB (ferrite-bainite microstructure), with an ultimate tensile strength of approximately 600 MPa and higher phase hardeness gradient and higher work hardening for the DP steel, are investigated.
- Characterization and quantification of damage in a punched edge at initial state using classical techniques: optical microscopy, scanning electron microscopy and micro-hardness measurement;
- In situ tensile testing in scanning electron microscope in order to better understand the phenomena involved in ductile fracture of base materials (DP and FB)
- In situ X-ray tomography tensile testing to quantify ductile damage mechanisms of base materials and identify nucleation and growth criterion to be used in numerical simulation;
- In situ X-ray laminography bending and tensile testing on specimen containing punched edge or machined edge to assess damage in 3-D at initial state and its evolution from the edge during mechanical loading;
- Characterization of two types of edges: punched edge and machined edge;
- Surface digital image correlation carried out simultaneously with in situ laminography testing to determine the displacements applied to the region of interest (ROI);
- Characterization of two microstructures: DP and FB steels in order to clarify the effect of microstructure on the damage mechanisms occurring during edge fracture;
- Development of a micromechanical damage criterion based on relevant microstructural parameters identified by X-ray laminography using Z-Set finite element software. Once established, the model is also used for a parametric study of the effect of the microstructure, including role of interfaces, the gradient in hardness between phases and initial damage induced by the cutting process.

Chapter 1

Literature review

Contents

1.1 Résumé

Dans ce chapitre, un état de l'art de la métallurgie des aciers Dual-Phase (DP) et Ferrite-Bainite (FB) est établi, leurs microstructures ainsi que leurs propriétés mécaniques sont présentées afin de mieux comprendre les paramètres clés permettant l'amélioration des propriétés mécaniques de ces deux matériaux étudiés. La caractérisation des trois étapes de l'endommagement ductile : la germination, la croissance et la coalescence de cavités, a fait l'objet de plusieurs travaux de recherches. L'endommagement des aciers DP est dû essentiellement à la décohésion aux interfaces ferrite-martensite et à la rupture de la seconde phase, i.e. la martensite, tandis que l'endommagement ductile des aciers FB est majoritairement gouverné par la décohésion aux interfaces des carbures et la germination sur les inclusions. Le développement des techniques de caratérisation micromécaniques 3D a permis une nette amélioration de la compréhension et la quantification des mécanismes d'endommagement ductile. Plusieurs approches numériques ont été proposées dans la littérature pour modéliser l'endommagement ductile des aciers DP et FB.
L'effet de la découpe sur la ductilité des aciers avancés est présenté en étudiant l'influence de la microstructure ainsi que des paramètres de procédés de découpe. Des techniques de caractérisation de comportement mécanique des bords découpés ainsi que des approches numériques permettant de modéliser la découpe de tôle d'acier sont discutées. Enfin, une étude numérique comparative des procédés de découpé, cisaillage et poinçonnage, réalisée en utilisant un modèle d'endommagement ductile de type GTN, à partir de données disponibles dans la littérature, a permis de valider l'équivalence de ces deux procédés de découpe en terme de courbe de découpe effort-pénétration.

In this part, a literature review of ferrite-martensite dual phase steels and ferrite-bainite steels is presented. Their microstructure formation and mechanical properties are reviewed in this chapter in order to provide a better knowledge of key parameters allowing to improve the mechanical properties of the investigated steels. The state of the art of ductile damage mechanisms (i.e. void nucleation, growth and coalescence), their characterization techniques as well as their modeling approaches are a major part of this chapter. Finally, steel cutting processes and the cut-edges mechanical tests found in the literature are also briefly discussed. The knowledge acquired from this part will further the understanding and the interpretation of experimental and numerical results found in this work.

1.2 Introduction

Because of their mechanical properties and low cost, steels are considered among the most important engineering materials. To reduce the weight of vehicles and thus energy consumption (i.e. CO_2 emissions) as much as possible, Advanced High Strength Steels (AHSS) were developed by steelmakers with specific microstructures to be used in automotive industry especially in the automotive body in white to improve safety and crash-worthiness property (figure (1.1)).

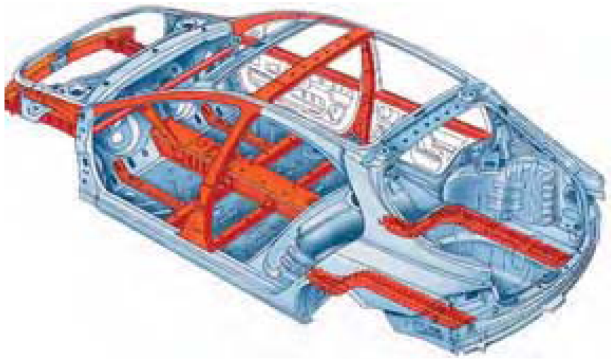

Figure 1.1 – Applications of AHSS in automotive industry for crash resistance - appearing in orange (Arcelor-Mittal credit)

Steelmakers taking into account the environmental concerns are designing new steel grades for automotive manufacturers to provide lighter vehicles. It is therefore advantageous to reduce the weight of automotive structural components by using engineering materials with excellent strength properties. Figure (1.2) shows the ultimate tensile strength - elongation diagram of the main grades of high strength steels. It can be noticed that an increase in mechanical strength is accompanied by a decrease of ductility (elongation at fracture). Dual phase (DP) and ferrite-bainite (FB) steels with their ferrite-martensite/bainite microstructures offer a good compromise between mechanical strength and resistance to damage. In order to design new AHSS grades providing an improved resistance to damage and a high mechanical strength, a better understanding of damage mechanisms of these grades, the mechanisms involved during sheet cutting processes and the mechanical behavior leading to edge fracture should be reached.

1.3 DP steels metallurgy

The figure (1.3) illustrates the different steps of DP steels industrial production via continuous casting process.

1.3.1 Microstructure formation

DP microstructure can be obtained by hot rolling or cold rolling. A schematic diagram of these heat treatments are given in figure (1.4)(b) and (c). The most common way to produce DP steel sheets for automotive components is by cold rolling because it permits to obtain lower sheet thicknesses which allows to produce

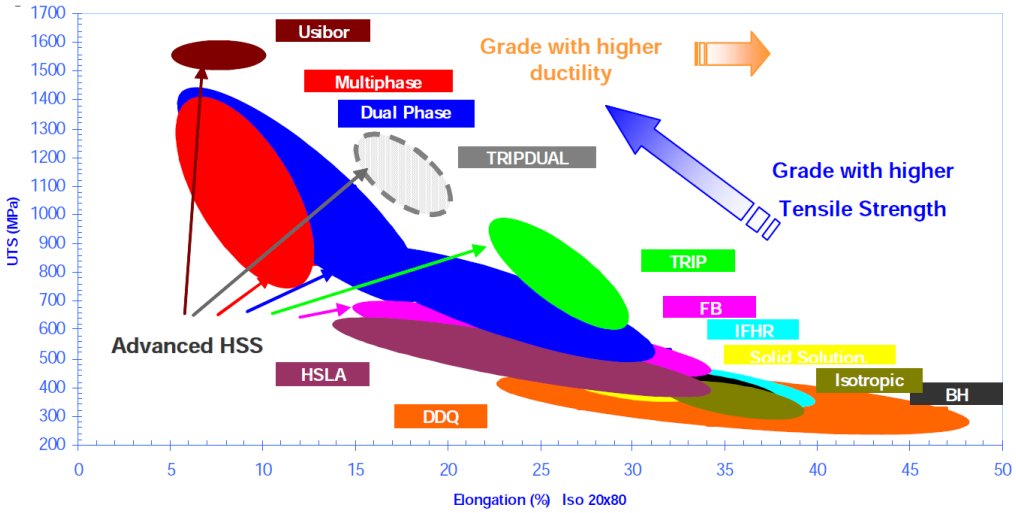

Figure 1.2 – Comparison of ultimate tensile strength - elongation diagram of high strength steels (ArcelorMittal credit)

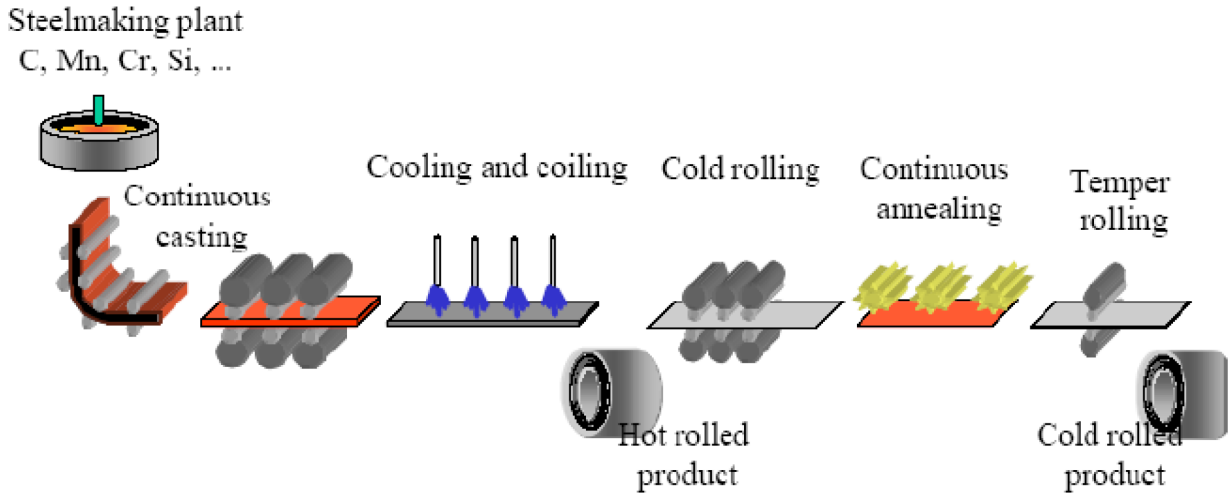

Figure 1.3 – Schematic picture of DP steels production layout (ArcelorMittal credit)

lighter parts followed by an intercritical annealing. The term «intercritical» refers to the two phases field of austenite (γ) and ferrite (α) shown in figure 1.4(a). The symbol α' refers to the martensite phase in figure (1.4). Here a brief discussion of mechanisms involved in ferrite-martensite DP steel formation is presented.

During intercritical annealing, the first step consists in austenite formation by decomposition of pearlite from ferrite-pearlite mixture [Speich et al., 1981]. This formation is controlled by carbon diffusion in the austenite along the austenite-pearlite interfaces. The second step consists in the growth of the high carbon content austenite into ferrite to reach equilibrium. The austenite growth kinetic during this step is controlled by carbon diffusion in austenite and manganese diffusion in the ferrite [Speich et al., 1981].

During cooling, at a temperature below the intercritical, the austenite-ferrite transformation can occur by pre-existing ferrite epitaxial (figure (1.5)) growth into austenite [Speich et al., 1981]. The martensite phase forms when the temperature is below Ms generating a plastic deformation and residual stresses in the surrounding ferrite. Transformation of austenite to bainite phase can occur when temperature decreases in austenite when cooling rate is decreased [Speich et al., 1981].

DP microstructure is heavily influenced by processing parameters particularly cooling rate. It can be controlled only by martensitic transformation if the cooling rate is very high. Indeed, epitaxial ferrite and bainite do not have enough time to occur. The other parameter influencing the DP microstructure is the hardenability of austenite which can be enhanced by high carbon content and manganese enrichment [Speich et al., 1981].

Transformation kinetics in DP steels are strongly dependant on the alloying elements content. The martensitic

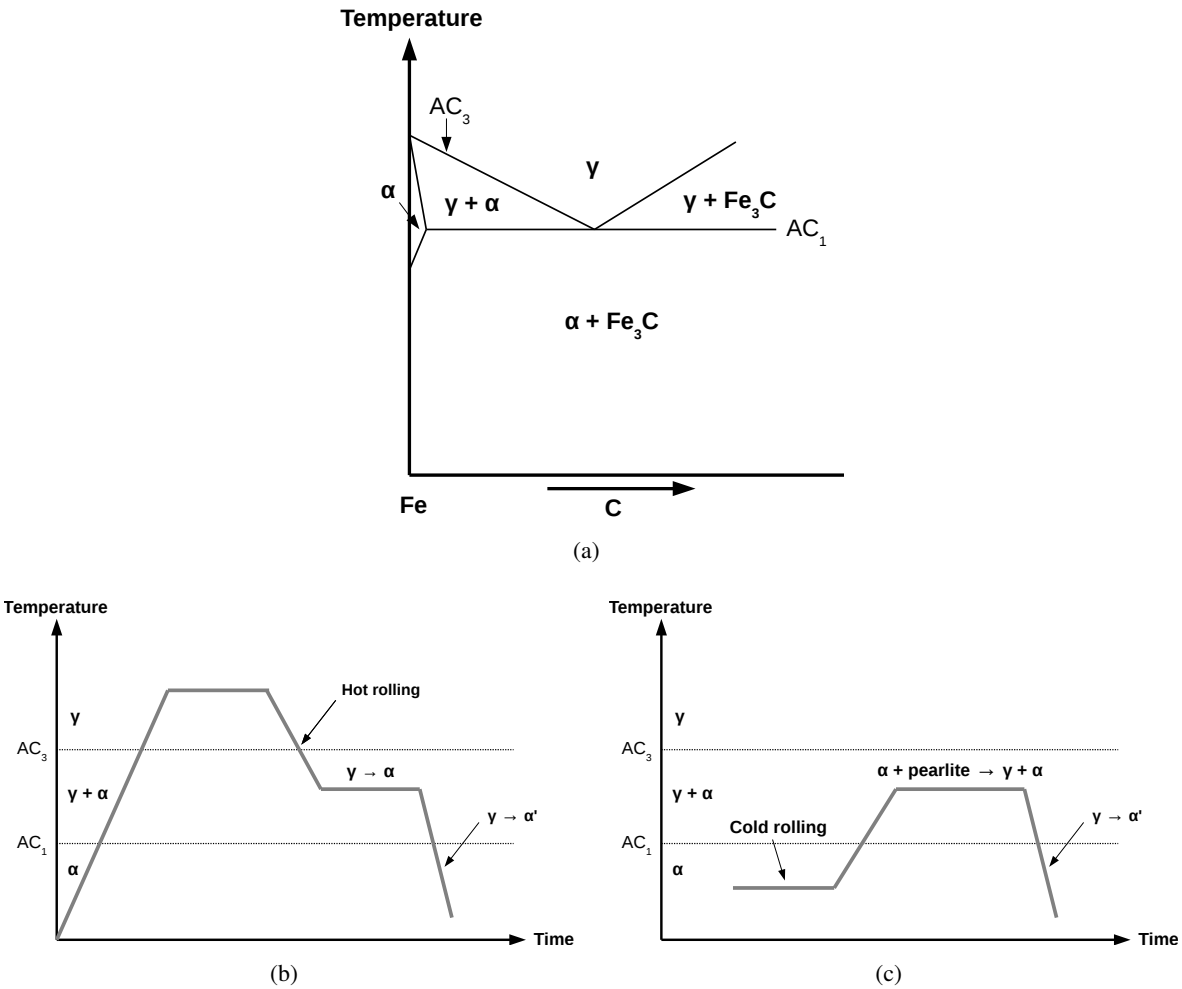

Figure 1.4 – (a) A schematic Fe-C diagram, Typical heat treatments to obtain DP microstructure: (b) hot rolling, (c) cold rolling

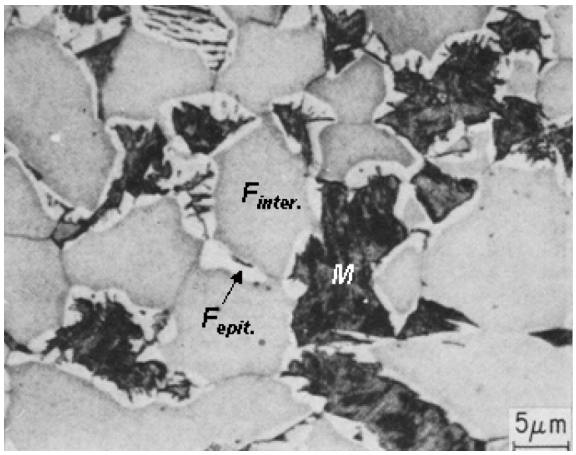

Figure 1.5 – Epitaxial (or new) ferrite formation in DP steels - ferrite appear in gray and martensite in black [Speich et al., 1981].

transformation start temperature Ms can be changed by alloying elements. The influence of alloying elements on Ms temperature can be investigated using Adrews formula [Lafrance, 1999]:

$$Ms = 539 - 423C - 30.4Mn - 12.1Cr - 17.7Ni - 7.5Mo - 11Si \tag{1.1}$$

An other commonly used empirical relationship to predict Ms as a function of the chemical composition was proposed in [Steven and Haynes, 1956]

$$Ms = 561 - 473C - 33Mn - 17Cr - 17Ni - 21Mo \tag{1.2}$$

Where Ms is in °C and concentrations in weight %.

Using the 3D X-ray holotomography technique based on phase contrast, in [Landron et al., 2012a], Landron and authors investigated qualitatively (figure (1.6)) and quantitatively the distribution of martensite on a DP steel. It was observed that the martensite phase forms a partial network around the ferritic grains.

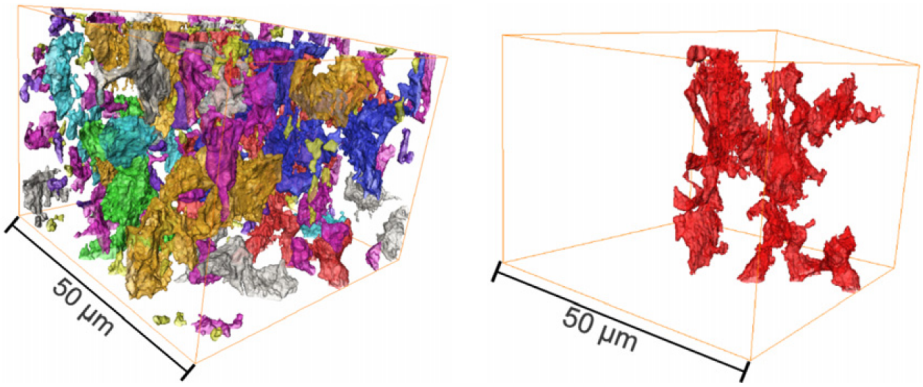

(a) (b)

Figure 1.6 – Holotomography reconstructed data showing the spatial distribution of martensite in a DP steel: (a) colors correspond to unconnected martensite islands, (b) the largest martensite island [Landron et al., 2012a].

1.3.2 Mechanical properties

To better understand the mechanical behavior of DP steels, the properties of its two constituents, i.e. ferrite and martensite phases should be separately studied.

Mechanical properties of ferrite (α)

Ferrite (α phase) has a body-centered cubic (BCC) crystal structure. Typical stress-strain curve of ferrite is given in figure (1.7) illustrating the yield point or sharp transition between elastic and plastic deformation in a fully ferritic steel. A uniform propagation of plastic deformation at a front along the specimen which is physically referred to as Luders band [Bhadeshia and Honeycombe, 2006] can be observed in typical tensile curve of fully ferritic steels (figure (1.7)[B-C]). There are many possible strengthening mechanisms for ferrite including substitutional solid solution, precipitation strengthening and grain size control [Bhadeshia and Honeycombe, 2006].

Mechanical properties of martensite (α')

The martensite is formed by a shear mechanisms which is a diffusionless transformation of austenite. This transformation occurs when austenite is quenched at room temperature (for instance water quench). Indeed, during rapid cooling, carbon atoms within austenite (FCC crystal structure) do not have time to diffuse out of austenite crystal structure. As a result, martensite highly strained supersaturated with carbon is formed by austenite crystal structure [Bhadeshia and Honeycombe, 2006].

The martensite microstructure and thus mechanical behavior are strongly dependant on the composition, particularly carbon content. The operating strengthening mechanisms in martensite which depend on the composition and testing conditions include grain size, dislocation strengthening and solid solution [Grange et al., 1977, Krauss, 1999, Allain et al., 2012, Arlazarov et al., 2013]. The decarburization of martensitic steels can be a way to improve their ductility without reducing the strength [Roumina et al., 2013].

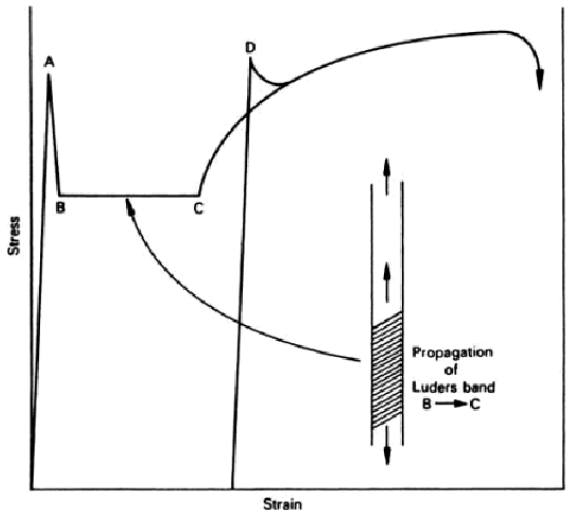

Figure 1.7 – Yield point or sharp transition between elastic and plastic deformation tensile test carried out on a ferritic steel [Bhadeshia and Honeycombe, 2006].

Compared to the ferrite properties the hardness of martensite is much higher unlike the ductility which is more important in ferritic steels. Steelmakers use tempering process for martensitic steels to adjust the compromise between strength and ductility.

Mechanical behavior of DP steels

It is indicated that for DP steels the strength and the ductility are functions of ferrite and martensite properties, volume fraction of the martensite and morphology and distribution of the martensite phase [Avramovic-Cingara et al., 2009b, Avramovic-Cingara et al., 2009a, Paul, 2013, Nakada et al., 2014].

The mechanical behavior of DP steels is influenced by the heat treatment used and many microstructural parameters including the martensite volume fraction and the carbon content of the martensite. Martensite can have a ductile behavior after the elastic strain regime [Krauss, 2001]. In DP steels, the strain distribution between martensite and ferrite has been observed to be heterogeneous during mechanical loading. During loading, the strain in DP steels is inhomogeneously distributed between the two components (ferrite and martensite) due to the high hardness gradient between these phases. This deformation incompatibility can be considered as a driving force for the generation of back stress which is always associated to the work hardening of the materials containing hard particles [Brown and Clarke, 1975].

Investigating different ferrite-martensite microstructures, it was found that the strength of DP steel is dependent on the ferrite grain size and the volume fraction of martensite [Davies, 1978]. It is reported that the 0.2% yield stress and the ultimate tensile strength are linear functions of volume fraction of martensite and are not dependent on the composition and strength of martensite while the martensite does not deform plastically [Davies, 1978]. Using averaging equations, the tensile curves of martensite and ferrite were plotted together with the macroscopic flow curve for a DP steel [Jacques et al., 2007]. The result is given in figure (1.8).

The influence of martensite volume fraction and carbon content of martensite on macroscopic mechanical properties (UTS and yield strength) and uniform elongation is given in figure 1.9(a) and (b) respectively.

In [Al-Abbasi and Nemes, 2003], a description of deformation stages of DP steels was proposed:

1. Elastic deformation of both component (ferrite and martensite)
2. Plastic deformation of ferrite while martensite continues to be deformed elastically
3. Plastic deformation of martensite

- **Continuous yielding behavior**

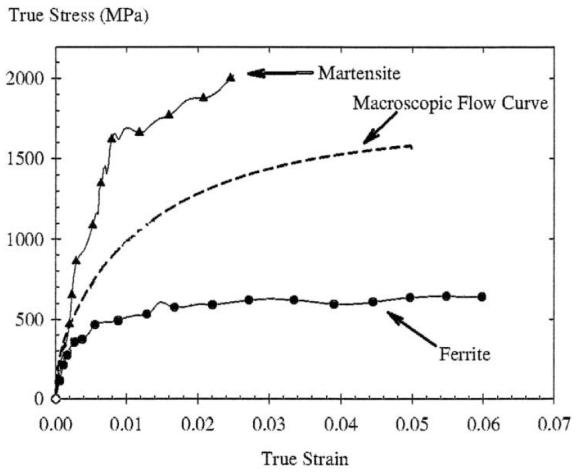

Figure 1.8 – Tensile curves of ferrite and martensite phases. Macroscopic stress-strain of a DP steel (50% martensite - 50% ferrite) [Jacques et al., 2007]

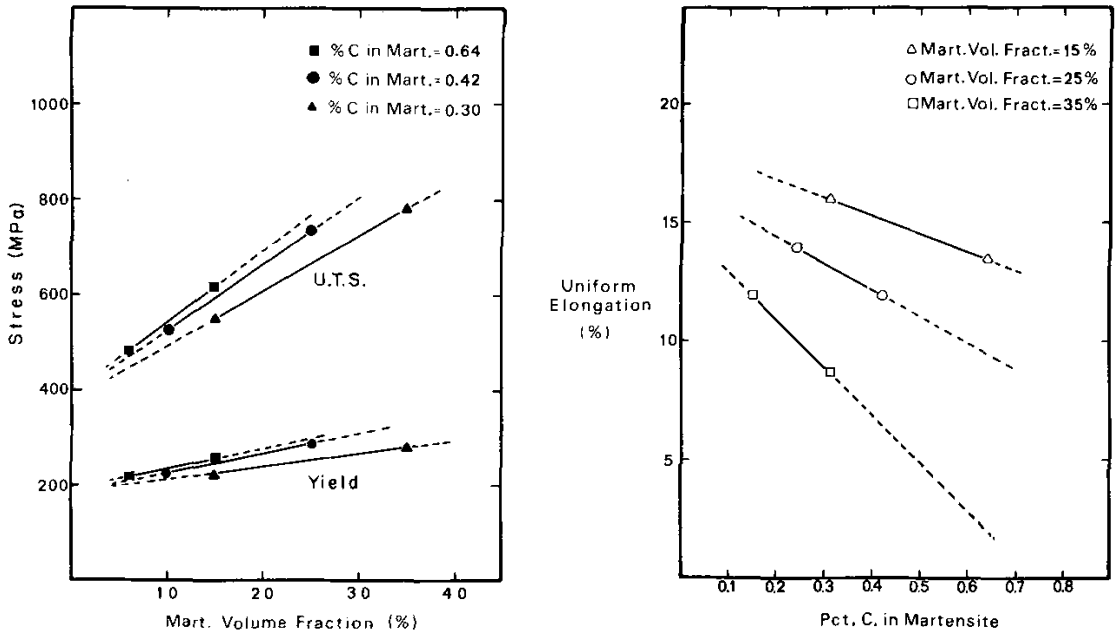

Figure 1.9 – (a) Ultimate tensile strength (UTS) and yield stress (US) as a function of martensite volume fraction in DP steels (b) Uniform elongation as a function of carbon content in martensite for DP steels with different values of martensite volume fraction [Ramos et al., 1979]

The residual stresses and the dislocations around the martensite islands induced by the diffusionless transformation of austenite to martensite which involves a volume expansion cause plastic deformation to occur at low plastic strain levels in DP steels. Indeed, DP steels generally present a low yield stress and a continuous yielding behavior.

In the work performed by Hansen and Pradhan [Hansen and Pradhan, 1981], the conditions for a DP steel to present the continuous yielding behavior have been listed:

- Density of mobile dislocations should exceed a critical value (about $10^{12} - 10^{14} m^{-2}$).
- At room temperature, the dislocations induced by the martensite transformation should remain mobile.

An explanation of the continuous yielding in DP steels was proposed in [Sakaki et al., 1983]. They have reported that the origin of this behavior is the residual stresses introduced by the austenite-martensite transformation in the ferrite grains surrounding the martensite islands. During loading, initial yielding begins

simultaneously from these zones under a low applied stress compared to the normal yield strength of the ferrite [Sakaki et al., 1983].

1.3.3 Damage mechanisms in DP steels

Generally the fracture of DP steels is governed by the three sequential ductile damage mechanisms, i.e. void nucleation, void growth and void coalescence.

1.3.3.1 Void nucleation

In materials science, void nucleation can be classified in two types:

- Homogeneous nucleation: void formation occurs inside the grain and is not associated to the presence of a second phase.
- Heterogeneous nucleation: void formation is associated to the presence of an heterogeneity (inclusion, second phase or grain boundary).

The most frequent void nucleation origins in DP steels are heterogeneous, namely the martensite fracture and the ferrite-martensite interface decohesion [Maire et al., 2008, Avramovic-Cingara et al., 2009b, Avramovic-Cingara et al., 2009a, Landron et al., 2010, Azuma et al., 2012, Ramazani et al., 2013]. The figure (1.10) illustrates these two cases of heterogeneous nucleation occurring in DP steels. The first one consists in the fracture of martensite (figure 1.10(a)) and the second presents the void formation at ferrite-martensite interfaces (figure 1.10(b)).

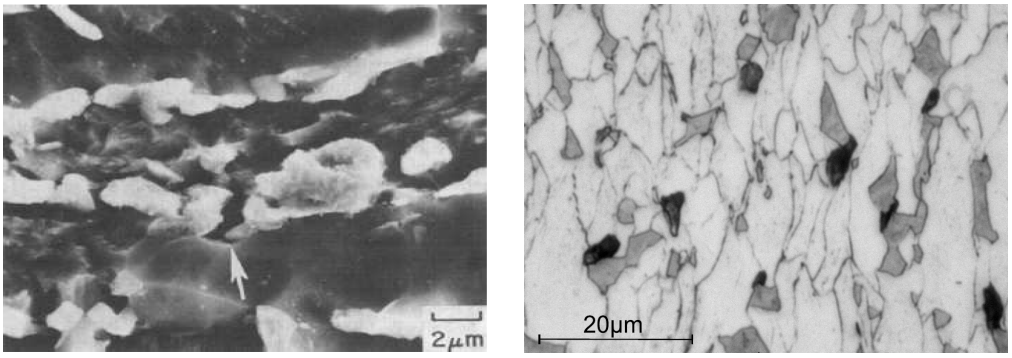

(a) (b)

Figure 1.10 – (a) SEM micrograph showing the fracture of martensite phase in a DP steel [Steinbrunner et al., 1988], (b) optical micrograph of a DP steel where void formation occurs by decohesion at ferrite-martensite interfaces (ferrite appears in dark gray, martensite in white gray and cavities in dark) [Landron et al., 2010]

Kadkhodapour and co-workers have suggested from their observations that void nucleation (figure (1.11)) in DP steels occurs because of the ferrite-ferrite grain boundaries decohesion [Kadkhodapour et al., 2011]. But we can notice that ferrite-ferrite interfaces decohesion occurs close to martensite islands.

Many studies of void nucleation in DP steels were performed in order to characterize in qualitative and quantitative ways this ductile damage stage using 2D techniques and X-ray tomography. Figure (1.12) exhibits the results of void nucleation measurements found in the studies of [Avramovic-Cingara et al., 2009a] and [Maire et al., 2008].

Nucleation along the interface between the two phases in DP steel has been numerically studied using a microstructure model with both phases deforming plastically according to a physics-based hardening law and a cohesive zone to model martensite-ferrite interface [Yerra et al., 2013]. The different of phase properties influence the local stress triaxiality evolution which significantly affects damage nucleation and interface decohesion.

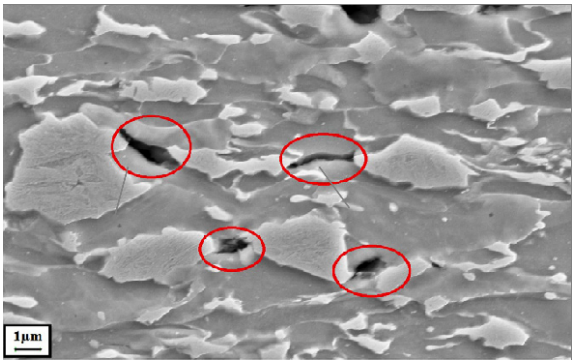

Figure 1.11 – SEM micrograph illustrating ferrite-ferrite interfaces decohesion [Kadkhodapour et al., 2011]

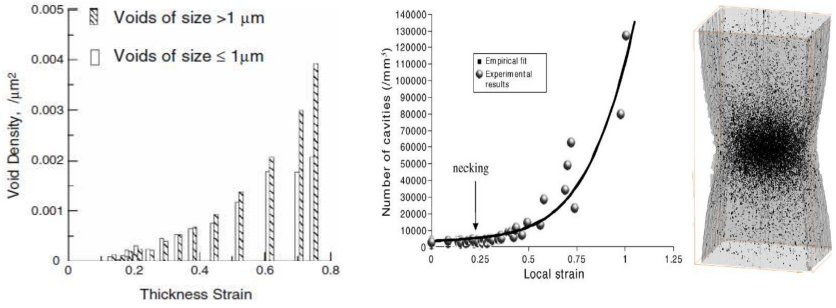

(a) (b)

Figure 1.12 – Void nucleation quantification in DP steels (a) from 2D measurements [Avramovic-Cingara et al., 2009a], (b) from X-ray tomography experimental data (3D volume of a deformed DP specimen) [Maire et al., 2008].

Saeidi and co-workers [Saeidi et al., 2014] investigated void nucleation mechanism in a DP steel using smooth and notched tensile specimens. By SEM microstructural analysis on fractured and sectioned specimens, they quantified the void area fraction evolution as a function of true strain. Figure (1.13) shows the measurement methods of void area fraction and thickness strain and results found for the investigated DP steel.

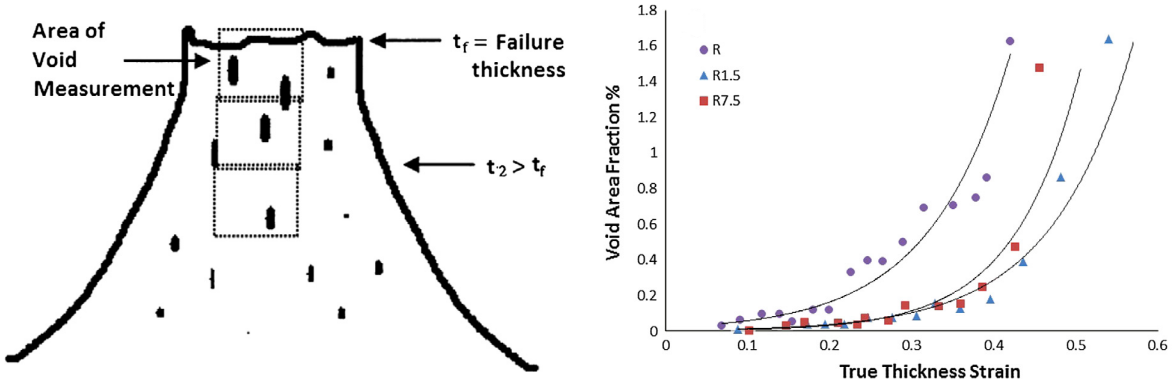

(a) (b)

Figure 1.13 – Quantification of void nucleation in a DP steel using smooth and notched specimens: (a) measurement methods of void area fraction and thickness strain, (b) evolution of void area fraction with strain [Saeidi et al., 2014].

In the case of X-ray tomography characterization of void nucleation, it is important to notice that the spatial resolution influences highly the damage measurement [Landron et al., 2012a]. The observation performed on a DP steel at a very high resolution (voxel of $0.1\mu m$) showed that a large part of damage is not detected at a low resolution (voxel of $1.6\mu m$). Figure (1.14) exhibits the results found in this study for an analyzed volume of $(100\ \mu m)^3$ located in the central area of the tensile specimen [Landron et al., 2012a].

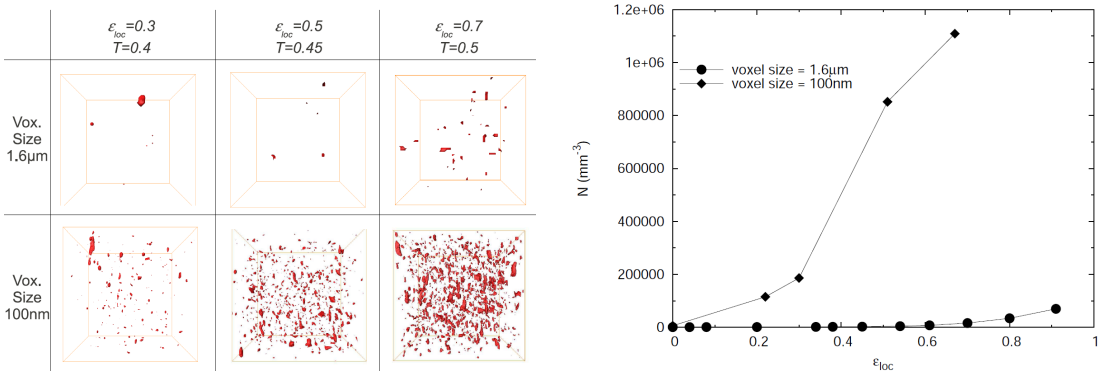

(a) (b)

Figure 1.14 – Resolution effect on the void nucleation a DP steel analyzing a volume of $(100\ \mu m)^3$: (a) 3D images of the analyzed volume for 2 spatial resolutions 1.6 μm and 0.1μm, (b) Void number evolution in the investigated volumes (same data as in (a)) with different resolution values [Landron et al., 2012a]

1.3.3.2 Void growth

The second stage of ductile damage process is the void growth. During plastic deformation, once the cavities have nucleated, they instantly start to grow mainly in the loading direction. The void growth is influenced by many mechanical parameters. The most important one is the stress triaxiality which was studied in several works in literature [McClintock, 1968,Pardoen and Delannay, 1998,Geni and Kikuchi, 1999]. The conclusion of all these works was that stress triaxiality favors ductile damage growth.

To experimentally characterize void growth in DP steels, 2D techniques have been used for polished and etched sections of tensile specimens [Szewczyk and Gurland, 1982, Han and Margolin, 1989, Kadkhodapour et al., 2011] (see figure (1.15)).

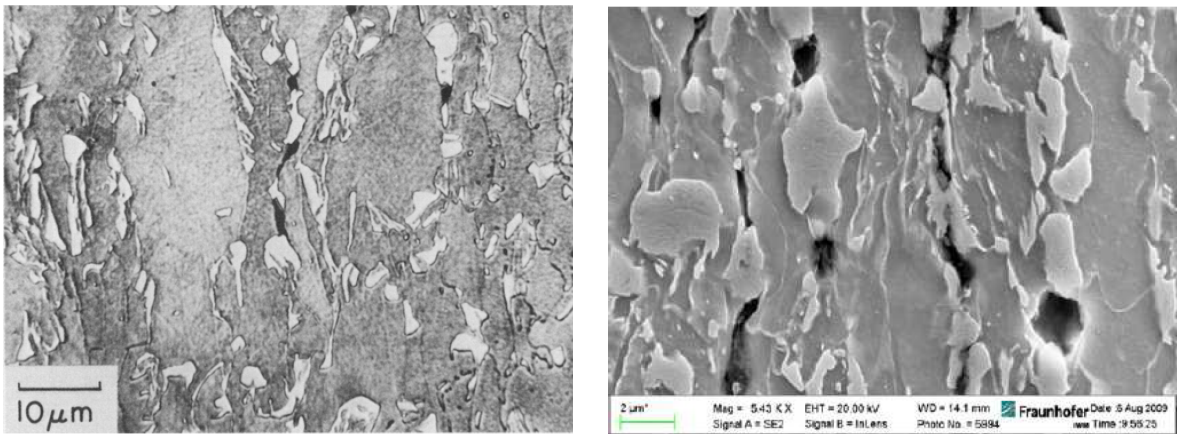

(a) (b)

Figure 1.15 – (a) A micrograph of a DP tensile specimen at ε=0.89 observed in optical microscope after polishing and etching (tensile direction is vertical) [Szewczyk and Gurland, 1982], (b) DP section after fracture observed using SEM [Kadkhodapour et al., 2011].

[Maire et al., 2008] and [Landron et al., 2011b] performed in-situ tensile testing on DP steel specimens using X-ray tomography acquisition. Considering only largest voids, they showed that its mean diameter increased during loading. However, the mean diameter of the entire void population remains constant. This can be explained by the nucleation of new small cavities while pre-existing ones are growing. Figure (1.16) gives the evolution of voids equivalent diameter as a function of local deformation for the investigated DP steels in [Maire et al., 2008, Landron et al., 2011b].

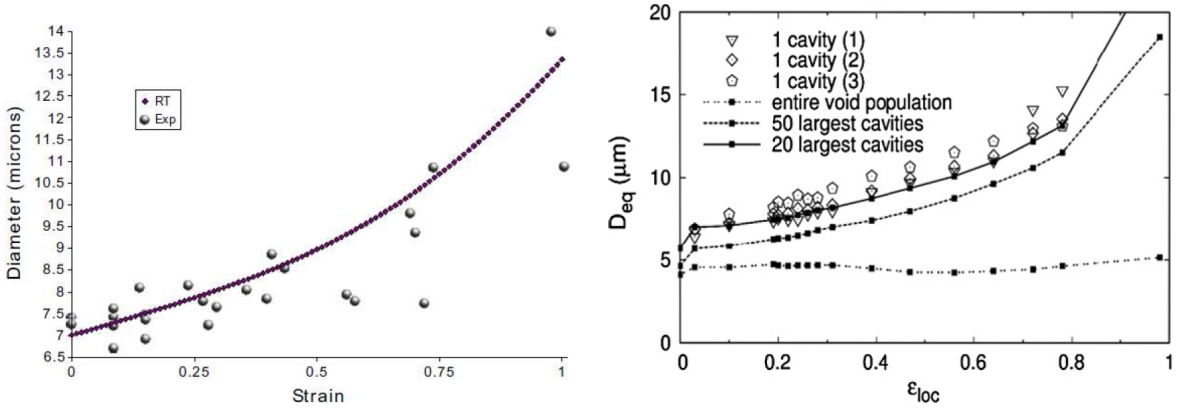

(a) (b)

Figure 1.16 – Void equivalent diameter evolution with the local strain in a DP steel observed via X-ray tomography: (a) [Maire et al., 2008], (b) [Landron et al., 2011b]

1.3.3.3 Void coalescence

The third and last step of ductile damage process which leads to the final fracture is void coalescence, it occurs when the ligaments between cavities are broken. According to the literature, there are three kinds of coalescence that have been experimentally observed [Pardoen and Pineau, 2007]. Thompson in his work [Thompson, 1987] has emphasized the internal necking mode where voids take a shape of a diamond when the applied strain increases. Using in-situ tensile tests performed on drilled plates by laser cutting process, Weck and Wilkinson [Weck and Wilkinson, 2008] have observed a shear localization when closest voids are located at 45° compared to the loading direction. The third mode of void coalescence called necklace was observed by Benzerga [Benzerga, 2000] in steels when voids are aligned along the loading direction.

There are only few experimental works on void coalescence in dual phase steels because of the short time between the beginning of the coalescence and the specimen final fracture. Figure 1.17 exhibits 2D sections taken inside the observed volume using X-ray tomography revealing a local event of coalescence and the macroscopic coalescence inside the DP investigated specimen.

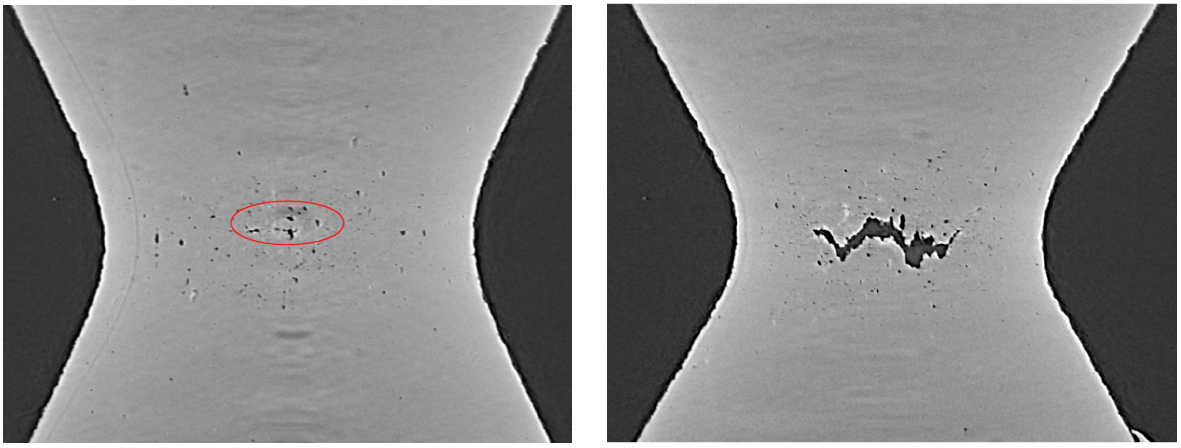

(a) (b)

Figure 1.17 – 2D sections inside an imaged volume of a DP steel using X-ray tomography (a) local event of coalescence at ε_{loc}=0.69, (b) macroscopic coalescence leading to the final fracture at ε_{loc}=0.83 [Landron et al., 2013].

1.4 FB steels metallurgy

Advanced High Strength Steels based on hot rolled ferrite-bainite microstructure were developed to respond to the current environmental concerns. They are advantageous to reduce the vehicle weight due the increased ductility of their ferrite matrix coupled with the high strength of hard bainite which offers a good compromise between strength and formability

Here a brief description of transformation leading to the bainite formation, mechanical properties characterizing the ferrite-bainite steels and the most commonly known damage mechanisms of bainitic steels is presented. Only few works are available on FB steels.

1.4.1 Microstructure

The time-temperature-transformation diagram given in figure (1.18) shows a range of intermediate temperatures wherein pearlite and martensite transformations can not take place. A cooling rate in this domain of intermediate temperatures allows the formation of thin aggregates called bainite composed from ferrite laths and cementite particles.

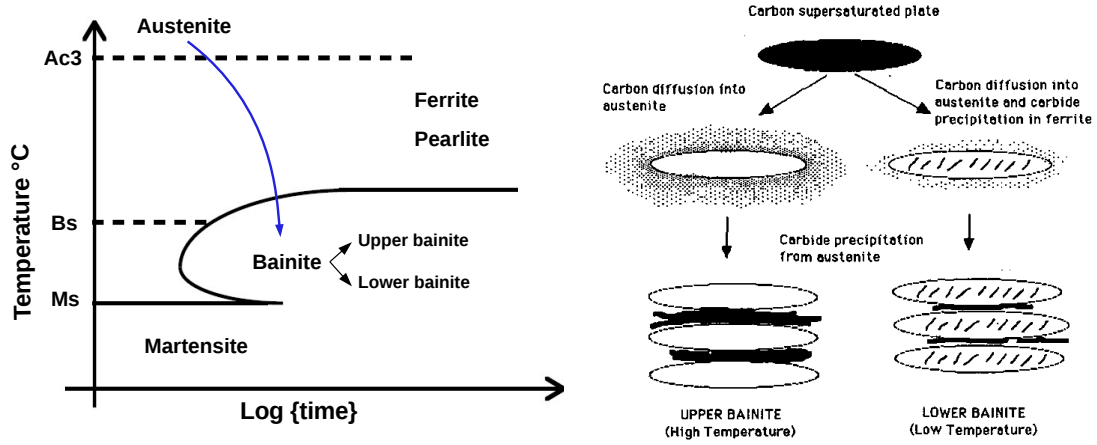

(a) (b)

Figure 1.18 – (a) Schematic time temperature transformation(TTT) diagram showing the domain of bainitic transformation [Bhadeshia and Honeycombe, 2006], (b) steps of the development of a bainitic microstructure [Bhadeshia and Honeycombe, 2006].

The bainite microstructure depends highly on the transformation temperature. Three types can be distinguished: upper bainite, lower bainite and granular bainite [Bhadeshia and Honeycombe, 2006].

- Upper bainite: it is a microstructure consisting of $0.2\mu m$ thick and $10\mu m$ long parallel thin laths of ferrite which have the same crystallographic orientation.
- Lower bainite: it has a microstructure and crystallographic characteristics quite similar to those of upper bainite. The main difference is that the cementite particles precipitate in the ferrite plates.
- Granular bainite: granular bainite is commonly used to describe the microstructure of bainite obtained by continuous cooling. It consists of blocks of bainite and retained austenite partially transformed to martensite.

FB steels, based on carbon-manganese concept, are hot rolled products. They are obtained by continuous cooling from the austenite region to an intermediate temperature in the ferritic region where 80-90% of the austenite transforms to ferrite. The last step consists in a rapid cooling in bainitic region in order to transform the retained austenite into bainite [Shaimi and Moulin, 2004]. Strengthening is obtained by both grain refinement and second phase hardening with bainite [AHSS Guidelines, 2009].

1.4.2 Mechanical properties

FB steels are often used in automotive industry because of their good edge stretchability properties. They allow to improve the mechanical behavior by avoiding cracks initiation at blanked edge [AHSS Guidelines, 2009]. Hot rolled FB steels can be used in structural automotive parts made of HSLA steels presenting a decreased stretch-flangeability capacity [Cho et al., 1999a]. Figure (1.19) illustrates the stretchability improvement in terms of a hole expansion that can be reached using ferrite-bainite microstructure.

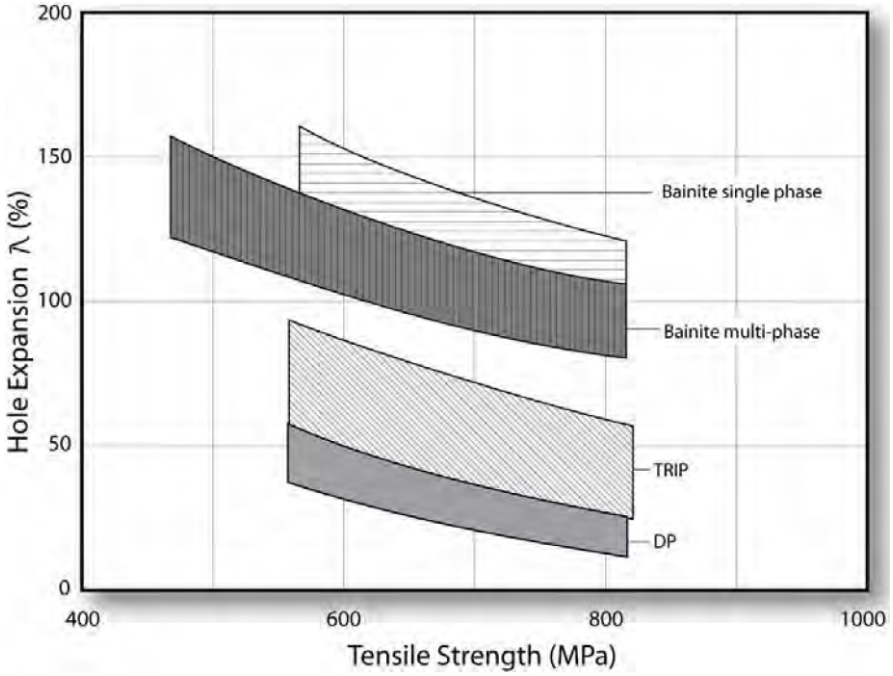

Figure 1.19 – Hole expansion performance of some steel microstructures [AHSS Guidelines, 2009]

1.4.3 Damage mechanisms

Ductile fracture is frequently observed in bainitic steels at room temperature. It starts usually by void nucleation on inclusions/particles and occurs by the growth and coalescence of cavities following ductile damage process. Carbides have a major influence on the ductility of bainitic steel with very low inclusion volume fraction. Indeed, a higher carbide density is associated with a higher void density which reduces the inter-cavity distance and leads to an earliest void coalescence [Hell, 2011].

In bainitic steel containing a small amount of martensite, it was shown that voids can nucleate either by martensite/matrix decohesion or fracture of the martensite phase. The martensite contained in bainitic steels is considered as preferred sites of damage [Lambert-Perlade, 2000].

The loss of ductility induced by high inclusion/carbides density in FB steels is illustrated in figure (1.20). The strain at fracture becomes more important for steels with low carbide density, i.e. high inter-carbide distance.

Choi and co-workers [Cho et al., 1999b] investigated experimentally the micromechanical behavior of FB steels using hole expansion test and SEM observation. They observed that the damage occurred during hole expansion was strongly related to three mechanisms: decohesion at ferrite-bainite interface (I), void formation at the ferritic phase (II) and fracture of the bainitic phase (III). Figure (1.21) exhibits microcracks formed during hole expansion of a FB steel in two locations [Cho et al., 1999b]. It has been observed that the first mechanism, i.e. decohesion at ferrite-bainite interface, influences strongly void initiation in the investigated FB steel during the hole-expansion test.

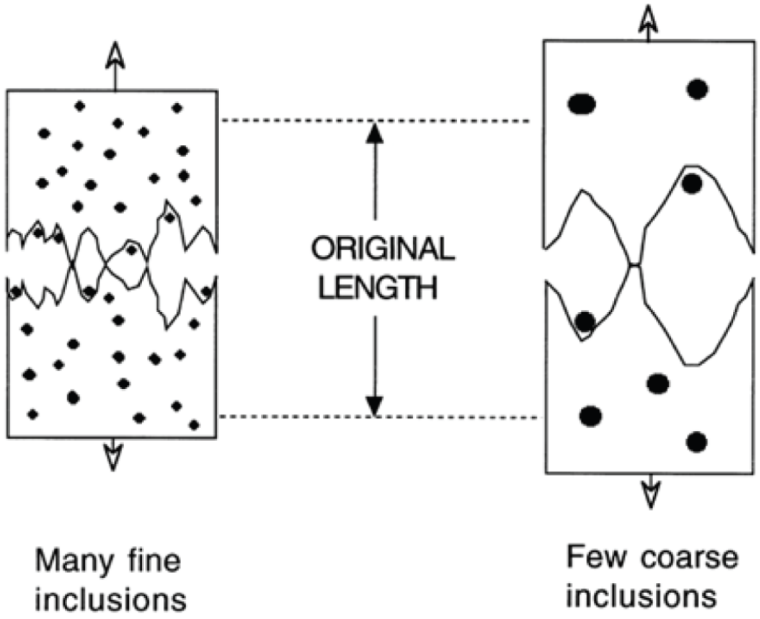

Figure 1.20 – Schematic illustration of ductility reduction induced by high carbide density [Bhadeshia and Honeycombe, 2006].

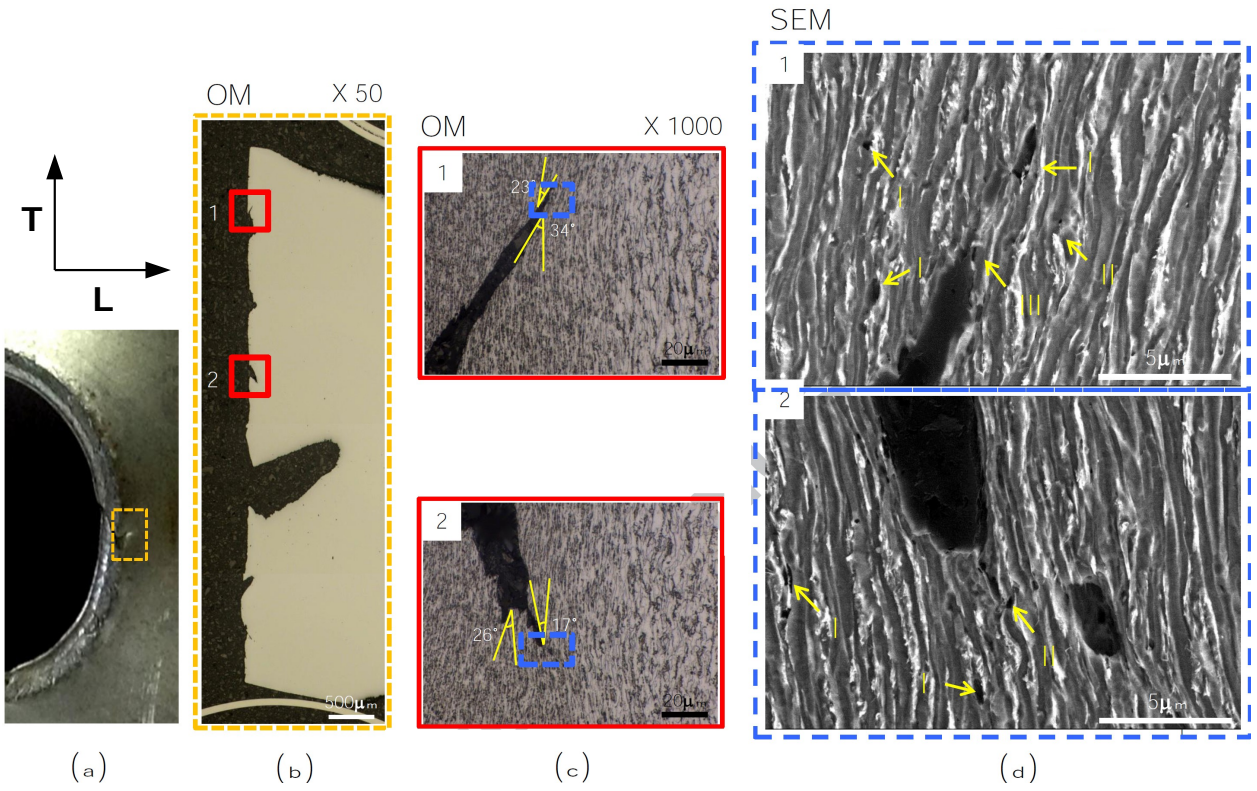

Figure 1.21 – Damage mechanisms in a FB steel: (a) cracked specimen after hole expansion test, (a) optical microscopy observations of a polished cross section of the tested specimen, (c) optical microscopy observations at high magnification (×1000) after polishing and etching of a cross section, (d) SEM pictures of damage produced in FB steel after hole expansion [Cho et al., 1999b].

1.5 Ductile damage modeling

Several models were developed to predict the different mechanisms involved in ductile fracture. In materials science field, modeling and numerical simulation are still considered to be a challenging issue due to the development of new techniques and computation hardware. Many numerical approaches were developed to predict ductile damage mechanisms, they can be classified as uncoupled models and coupled models.

- The uncoupled models family is based on models which take into account an external variable that predicts the failure when a critical value is reached. However, the plasticity of the material remain uncoupled with the calculated damage variable.
- The second family, i.e. coupled family gathers models allowing to take into account the loss of the mechanical properties of the material, essentially plasticity, due to the damage development.

In this part, a brief description of the most common physically based approaches used to predict the ductile damage process, i.e. the void nucleation, growth and coalescence is given. This is also called local approach to fracture.

1.5.1 The role of stress triaxiality

Before introducing the models allowing to predict the different steps leading to the ductile fracture, it seems essential to discuss the effect of the stress triaxiality on ductile damage. In fact, the stress triaxiality is known as a driving force for void nucleation and growth leading to ductile fracture.

Stress triaxiality is used to describe the state of stress generated during mechanical loading and is defined as follows:

$$T_r = \frac{\sigma_H}{\sigma_{eq}} \tag{1.3}$$

Where σ_H is the hydrostatic pressure and σ_{eq} is Von Mises equivalent stress.

Based on 350 tests at constant levels of hydrostatic pressure ranging from 0 to 2700 MPa on several steel grades using notched tensile specimens, Bridgman [P., 1964] concluded that for a sufficiently high hydrostatic pressure the fracture does not occur but the specimen necks until the radius of the minimal cross section is locally zero (figure (1.22)). This statement was confirmed later by French and Weinrich [French and Weinrich, 1975] who pointed out that the strain at fracture for a ductile copper at high pressures approached infinity.

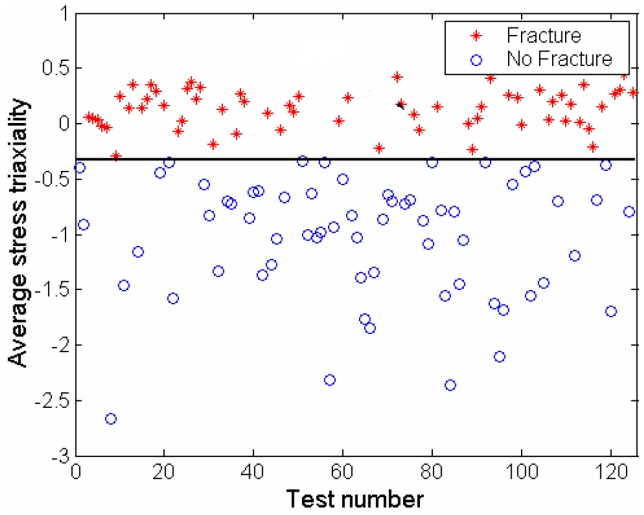

Figure 1.22 – Evolution of the magnitudes of average stress triaxiality of tensile tests with imposed hydrostatic pressure performed by Bridgman

In [Bao and Wierzbicki, 2004], Bao and Wierzbicki carried out experiments using specimens of different geometries to investigate the effect of stress triaxiality on the equivalent strain at the onset of fracture. They compared the numerical simulation results to those found by Bridgman and concluded that ductile fracture does not occur for any specimen under a stress triaxiality ratio less than -1/3. Figure (1.23) illustrates the results found by Bao and Wierzbicki for a 2024 aluminium alloy tested under different stress states.

In [Papasidero, 2014], the authors performed several tests with proportional and non-proportional loading using tension-torsion experiments in order to quantify the effect of stress triaxiality on ductile fracture of a 2024-T351 aluminium alloy and compared their results to those found by Bao and Wierzbicki [Bao and Wierzbicki,

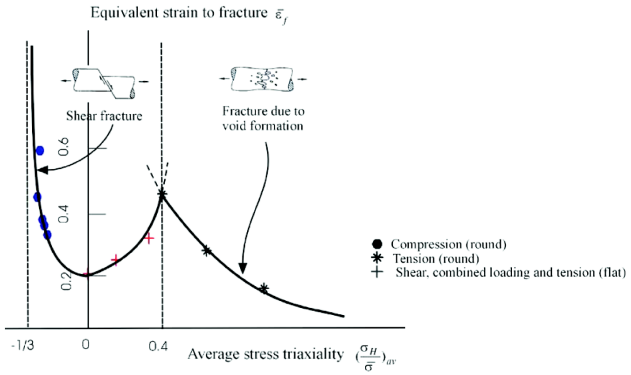

Figure 1.23 – Dependence of the strain at fracture on the stress triaxiality ratio for a 2024 aluminium alloy Bao and Wierzbicki [Bao and Wierzbicki, 2004].

2004]. The Von Mises equivalent strain as a function of stress triaxiality for each loading configuration was compared to Bao and Wierzbicki's results (see fig. 1.24). The quantitative comparison shows that the strains reported by Bao and Wierzbicki are often much higher (up to 0.46) as compared to the tension-torsion results provided by Papasidero et al. (up to 0.30). It was concluded that the differences in the microstructres of the tested 2024-T351 aluminium alloys and the non-adequate experimental techniques employed by Bao and Wierzbicki used for measuring the strain to fracture might be possibly in the origin of those ductility measurement differences [Papasidero, 2014].

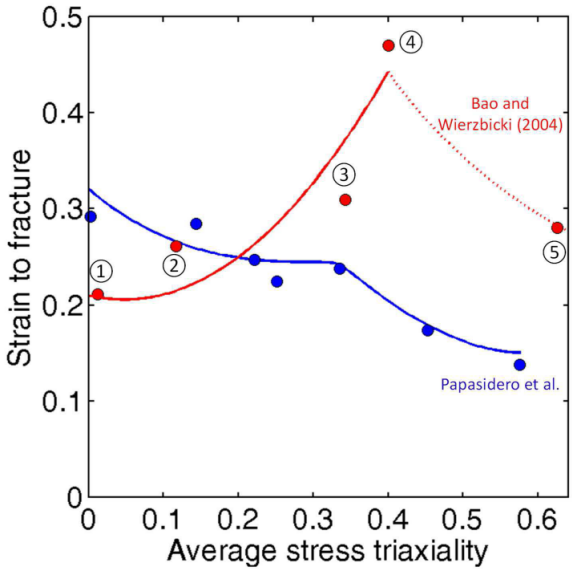

Figure 1.24 – Comparison of experimental (points) and numerical (lines) results found by Papasidero et al [Papasidero, 2014] and Bao and Wierzbicki [Bao and Wierzbicki, 2004] showing the dependence of strain at fracture with the stress triaxiality for a 2024 aluminium alloy.

- Stress triaxiality calculation using Bridgman analysis

A geometrical study of the stresses generated where necking occurs during tensile test was carried out by Bridgman. Using the geometrical parameters shown in figure 1.25(a), Bridgman has developed a relationship allowing one to approximate the local triaxiality generated by transversal stresses induced in a notch during tensile testing on an axisymmetric specimen.

$$T = T_0 + ln\left(\frac{r^2 + 2\,r\,R - a^2}{2\,r\,R}\right) \tag{1.4}$$

Where T_0 is the stress triaxiality corresponding to uniaxial tension (T_0=0.33), r and R are respectively the minimal cross section and the notch radii and a is the radial coordinate ($0 \leq a \leq r$).

This expression was revisited later by Bao and Wierzbicki [Wierzbicki and Bao, 2004] using finite element simulation to better estimate the maximal stress triaxiality at the center of the specimen ($a = 0$). Figure 1.25(b) shows the result of this analysis.

$$T = T_0 + \sqrt{2}\, ln \left(\frac{r^2 + 2\,r\,R - a^2}{2\,r\,R} \right) \tag{1.5}$$

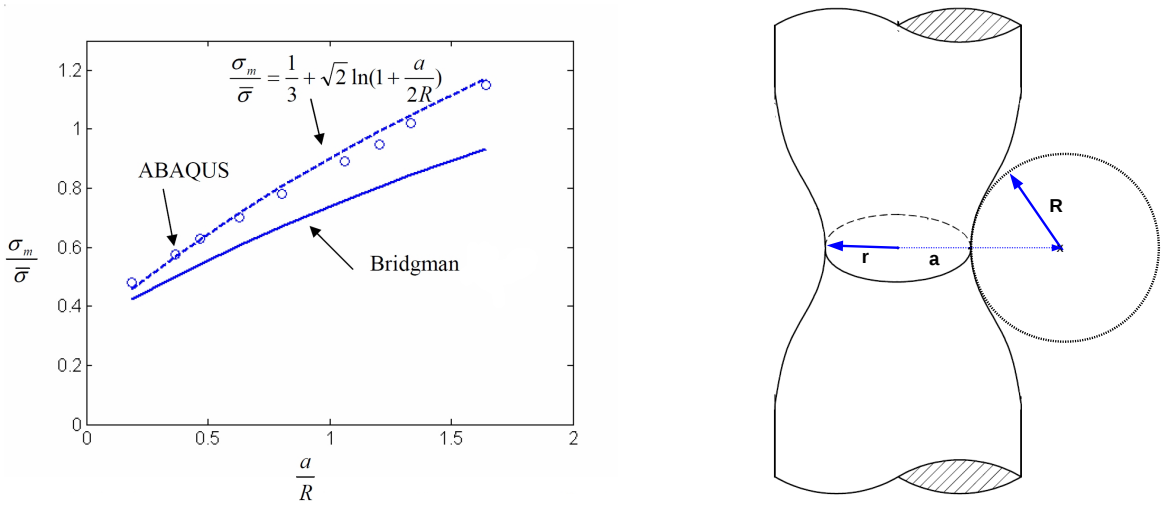

(a) (b)

Figure 1.25 – (a) Correction of Bridgman equation estimating the maximal stress triaxiality in a notch axisymmetric tensile specimen [Wierzbicki and Bao, 2004], (b) geometrical parameters involved in Bridgman analysis

1.5.2 Void nucleation

Argon model

Argon in [Argon et al., 1975] proposed a stress-based criterion for void nucleation by decohesion at the second phase-matrix interfaces. It takes into account the contribution of the Von Mises equivalent stress σ_{eq} and the hydrostatic stress $\sigma_H = \frac{1}{3}\,\mathrm{trace}(\sigma)$. The expression of the proposed criterion is given in

$$\sigma_C = \sigma_H + \sigma_{eq} \tag{1.6}$$

Where σ_C is the critical stress necessary to break the interface.

Beremin model

For a brittle inclusion inside a perfectly plastic matrix, Beremin et al. [Beremin, 1981] proposed a stress criterion based on Eshelby theory. It was supposed that voids nucleate either by inclusion fracture or interface decohesion.

$$\sigma_C = \sigma_I^{max} + k_s\,(\sigma_{eq} - \sigma_0) \tag{1.7}$$

Where σ_C is the critical stress for the interface decohesion or the inclusion fracture, σ_I^{max} is the maximal principal stress, k_s is the stress concentration factor that depends on the inclusion shape, σ_{eq} is the equivalent stress inside the material and σ_0 is the equivalent stress inside the matrix.

Chu and Needleman model

A strain based criterion was proposed by Chu and Needleman [Chu and Needleman, 1980] supposing that voids nucleate when a critical strain is reached inside the material. The proposed evolution of void number with the strain is given in equation (3.3)

$$\frac{\mathrm{d}N}{\mathrm{d}\varepsilon} = f\left(\varepsilon_p^{eq}\right) \tag{1.8}$$

with

$$f\left(\varepsilon_p^{eq}\right) = \frac{\psi}{\sqrt{2\pi}\, s_N} \exp\left(-\frac{1}{2}\left(\frac{\varepsilon_p^{eq} - \varepsilon_N}{s_N}\right)^2\right) \tag{1.9}$$

Supposedly the nucleation strain is distributed in a normal fashion (figure (1.26)). ε_p^{eq} is the equivalent plastic strain, ε_N is the critical strain for void nucleation and s_N is the standard deviation. ψ is determined so that the total void volume nucleated is consistent with nucleation sites density.

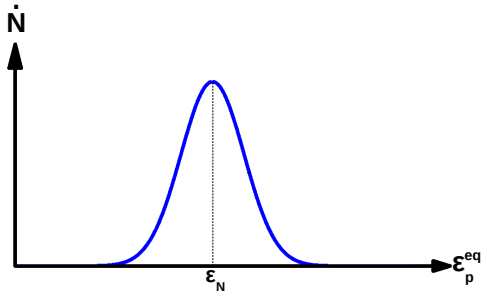

Figure 1.26 – Schematic curve of Chu and Needleman law for void nucleation [Chu and Needleman, 1980].

The integrated relationship is given in equation (3.5)

$$N\left(\varepsilon_p^{eq}\right) = N_0 + \frac{\psi}{2}\left(erf\left(\frac{\varepsilon_p^{eq} - \varepsilon_N}{\sqrt{2}s_N}\right) - erf\left(\frac{-\varepsilon_N}{\sqrt{2}s_N}\right)\right) \tag{1.10}$$

Where N_0 is the initial void volume fraction and erf is the error function defined as follows:

$$erf\left(x\right) = \frac{2}{\sqrt{\pi}} \int_0^x e^{-t^2}\, dt \tag{1.11}$$

Maximum void volume fraction N_{max} is thus deduced from the equation (3.5)

$$N_{max} = N_0 + \frac{\psi}{2}\left(1 - erf\left(\frac{-\varepsilon_N}{\sqrt{2}s_N}\right)\right) \tag{1.12}$$

In the literature, the more commonly used values of ε_N and s_N are 0.3 and 0.1 respectively. The expression of Chu and Needleman criterion can be defined as follows:

$$N_{max} = N_0 + \psi \tag{1.13}$$

1.5.3 Void growth

Mc Clintock model

To predict the growth of an isolated cylindrical void in a perfectly plastic infinite matrix, Mc Clintock [McClintock, 1968] had proposed an analytical model given in equation (1.14) as a function of the stress triaxiality ratio and the equivalent plastic strain.

$$\frac{\mathrm{d}R}{R} = 0.8 \exp\left(\sqrt{3}\,T\right) \mathrm{d}\varepsilon_p \tag{1.14}$$

Where R is the cylinder section radius.

Rice and Tracey model

Rice and Tracey model [Rice and Tracey, 1969] was proposed to predict the growth of an isolated spherical void in a rigid, infinite and perfectly plastic matrix that undergoes a uniform strain. The equation (1.15) gives the evolution of a spherical void growth with the stress triaxiality ratio and the equivalent plastic strain. The void growth is supposed to be fully isotropic.

$$\frac{\mathrm{d}R}{R} = 0.272 \exp\left(\frac{3}{2}\,T\right) \mathrm{d}\varepsilon_p \tag{1.15}$$

Where R is the spherical void radius.

A correction of Rice and Tracey model has been proposed by Bouaziz [Maire et al., 2008] in order to take into account the nucleation of new void population during growth step.

$$\frac{\mathrm{d}R}{\mathrm{d}\varepsilon} = 0.272 \exp\left(\frac{3}{2}\,T\right) R - \frac{1}{N}\frac{\mathrm{d}N}{\mathrm{d}\varepsilon}\,(R - R_0) \tag{1.16}$$

Where R_0 is the equivalent radius of the cavities just after nucleation which is supposed to be dependent on the strain at which the cavity has nucleated [Maire et al., 2008].

Huang model

Rice and Tracey model was revisited by Huang [Huang, 1991] in order to improve the void growth prediction for low stress triaxiality levels. The proposed modification of Rice and Tracey model is given in equation (3.9)

$$\begin{aligned} &\text{for } T \leq 1 && \tfrac{\mathrm{d}R}{R} = 0.427\, T^{1/4} \exp\left(\tfrac{3}{2}\,T\right) \mathrm{d}\varepsilon_p \\ &\text{for } T > 1 && \tfrac{\mathrm{d}R}{R} = 0.427 \exp\left(\tfrac{3}{2}\,T\right) \mathrm{d}\varepsilon_p \end{aligned} \tag{1.17}$$

It consists in predicting the evolution of the void growth of a spherical void with the stress triaxiality and the equivalent plastic strain by calculating the pre-exponential term which is dependant on the stress triaxiality T. This modification hase been successfully validated on void growth in DP steels in [Landron et al., 2011b].

Gurson model

Gurson model [Gurson, 1975] was the first micromechanical model that took into account the coupling between the damage and the elasto-plastic behavior. The model is based on the previous works of Rice and Tracey [Rice and Tracey, 1969] describing the evolution of an isolated spherical void inside an infinite isotropic perfectly plastic matrix. The presence of the damage (cavities) modifies the plastic yield surface of the material. The yield surface expression depends on the damage variable that is the volume fraction of porosity f proposed by Gurson is introduced in equation (1.18).

$$\Phi = \left(\frac{\sigma_{eq}}{\sigma_y}\right)^2 + 2\,f \cosh\left(\frac{1}{2}\frac{\sigma_{kk}}{\sigma_y}\right) - 1 - f^2 = 0 \tag{1.18}$$

Where σ_{eq} is the Von Mises equivalent stress, σ_y is the yield stress of the matrix and σ_{kk} is the trace of the stress tensor.

The void fraction rate is determined by using the mass conservation principle.

$$\dot{f}_{growth} = (1 - f)\,\mathrm{trace}\left(\underline{\dot{\varepsilon}_p}\right) \tag{1.19}$$

Where $\dot{\varepsilon}_p$ is the plastic strain rate tensor.

However, this model does not take into account the interactions between microcavities. Gurson model was modified in many studies in order to improve the ductile damage prediction taking into account some mechanical parameters influencing the ductile damage evolution, for example the plastic anisotropy [Benzerga et al., 2004] and the void shape effect [Pardoen and Hutchinson, 2000].

Gurson-Tvergaard-Needleman (GTN) model

To consider the interaction between microcavities, Tvergaard and Needleman [Tvergaard and Needleman, 1984] revisited Gurson model introducing three parameters. The proposed yield surface equation is given in equation 1.20.

$$\Phi = \left(\frac{\sigma_{eq}}{\sigma_y}\right)^2 + 2\,q_1\,f^*\cosh\left(\frac{q_2}{2}\frac{\sigma_{kk}}{\sigma_y}\right) - 1 - q_3\,f^{*2} = 0 \tag{1.20}$$

Where q_1, q_2 and q_3 are the constitutive parameters of the model. For steels, generally q_1=1.5, q_2=1 and q_3=$(q_1)^2$. f^* is a function of f (porosity volume fraction) introduced by Tvergaard and Needleman to take into consideration the void coalescence [Tvergaard and Needleman, 1984].

Ben Bettaieb and co-workers [Ben-Bettaieb et al., 2011] modified GTN model to take into account the plastic anisotropy and the mixed (isotropic + kinematic) hardening of the matrix. An extension of GTN model was proposed in [Fansi et al., 2013], integrating physically based void nucleation and growth laws identified on X-ray experimental measurements. The reader interested in GTN models and its extension should refer to [Besson2010].

1.5.4 Void coalescence

Void cell simulations are often used to understand the influence of some mechanical properties on void coalescence because of the difficulty to provide experimental data characterizing this third step of ductile fracture. Using void cell simulations, Koplik and Needleman [Koplik and Needleman, 1988] investigated, using the geometry given in figure (1.27), the effect of several parameters (initial porosity, stress triaxiality, initial void shape ratio, initial void spacing and strain hardening exponent) influencing void growth and void coalescence. In figure (1.27), only the shaded quadrant is analyzed numerically using cell simulations due to assumed symmetry. The cell geometry in numerical simulations is strongly dependent on initial porosity, void aspect ratio and cell aspect ratio. Benzerga developed a micro-mechanical framework for the whole coalescence regime to better understand the sensitivity of void coalescence stage to stress triaxiality and initial void spacing ratio [Benzerga, 2002]. Many approaches were proposed to model this ductile fracture step, the most commonly used criteria are briefly described hereafter.

Mc Clintock criterion

Mc Clintock [McClintock, 1968] proposed a fracture criterion for plastic materials containing an isolated cylindrical void. The fracture occurs by the growth and coalescence of voids. It was found that the fracture strain is highly dependent on the hydrostatic stress. This criterion does not take into account the localization phenomena and the interaction between voids.

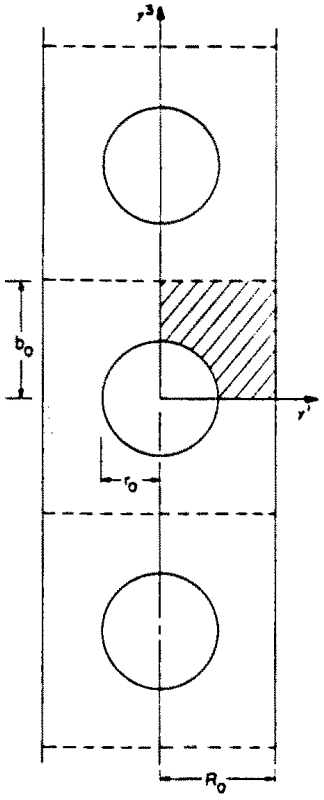

Figure 1.27 – Material geometry containing an array of spherical voids used in cell simulations [Koplik and Needleman, 1988].

Brown and Embury criterion

The criterion proposed by Brown and Embury [Brown and Embury, 1973] was based on the cavity length and intercavities distance. The fracture occurs by the internal necking of voids via the shear bands at 45°. For ellipsoidal cavities, the expression of the model is given in equation (1.21):

$$\chi \sqrt{1 + W^2} = 1 \tag{1.21}$$

Where χ is the relative intercavities distance and W is the cavity aspect ratio. For spherical voids, the criterion stipulates that the coalescence appears when the distance between the two void centers is equal to the diameter.

Thomason criterion

The criterion proposed by Thomason [Thomason, 1990] adapted to perfectly plastic materials is based on a plastic limit load condition for localized plastic failure of the inter-void matrix. The criterion expression is given in equation (1.22)

$$\frac{\sigma}{\sigma_0} = (1 - \chi) \left[0.1 \left(\frac{1 - \chi}{\chi W} \right) + 1.2 \frac{1}{\sqrt{\chi}} \right] \tag{1.22}$$

The criterion stipulates that coalescence appears when σ reaches a critical value, where σ_0 is the yield stress of the material, χ is the relative intercavities distance and W is the cavity aspect ration. The critical value of σ is strongly dependant on W and χ. This critical value increases when W (or χ) decreases.

The reader interested in coalescence models and their extensions and corrections should refer to [Weck, 20O7]. In his PhD work [Weck, 20O7], Weck summarized the most used criteria to model the void coalescence.

Author	Criteria	Limitations
McClintock (1968)	Hole impingement	Cylindrical holes No interaction between holes No localization
Brown and Embury (1973)	Void length equals intervoid spacing	For regular array of voids No Hydrostatic component No material properties
LeRoy (1981)	Brown and Embury with stress triaxiality	No interaction between holes Regular array of holes No material properties
Tvergaard and Needleman (1984)	Critical porosity and acceleration factor	Model rely on arbitrary parameters No hole geometry (average)
Thomason (1990)	Plastic limit load	No microshear localization possible Only for non-hardening materials
Pardoen and Hutchinson (2000)	Plastic limit load with strain hardening	No microshear localization possible
Benzerga (2002)	Plastic limit load adjusted for low triaxiality	No microshear localization possible
Gammage (2004)	Stress equals global work hardening rate	Local work hardening = Global work hardening rate

Figure 1.28 – Void coalescence models summarized by Weck [Weck, 20O7]

1.5.5 Summary

Ductile damage modeling has been the subject of many studies and is still a challenging topic in the materials science community.

- Void nucleation was investigated in a quantitative and qualitative way. In [Landron et al., 2010] and [Maire et al., 2008], this ductile damage stage in DP steels has been well assessed using X-ray tomography observation. In [Landron et al., 2010], the Argon and Beremin criteria for void nucleation were used and the effect of stress triaxiality was investigated.
- Growth, the second step of ductile damage was widely investigated. Void growth in DP steels was observed in 3D and quantified in [Landron et al., 2011b]. A model predicting the void size evolution with the local strain and the stress triaxiality was developed taking into account the nucleation of new void population.
- Because of the lack of experimental observation of coalescence, the validation of coalescence models has not been done in details. Landron and co-workers [Landron et al., 2013] characterized void coalescence occurring in a DP steel using X-ray tomography technique. The models of Brown and Embury and of Thomason were tested against the experimental data. It was found that because of the correlation between actual coalescing couples of cavities and local implementation, Thomason approach was the best criterion predicting the void coalescence in the investigated DP steels [Landron et al., 2013].

1.6 Steel cutting processes and cut-edges characteristics

The use of AHSS steels in automotive industry is often seen reduced by the presence of cut-edges that affect the mechanical performance of the automotive parts made of these grades. It is essential to understand the mechanisms involved in the sheet cutting processes and how these processes affect the quality of the cut-edges.

Cutting operation requires a detailed analysis. During this operation the behavior of the material shows a continuous degradation of the mechanical properties, leading to the sheet fracture and the obtention of the desired part.

There are several cutting methods used by steel manufacturers. In this work, descriptions of punching process and shearing process, which are the most used due to their speed, simplicity and low cost, are given.

1.6.1 Description of cutting processes

The most commonly industrial used processes for sheet cutting are shearing and punching. The shearing process, which is a cutting in a straight line over the entire width of the sheet by the action of a moving blade perpendicular to the plane of the sheet, is the most widely used and least expensive process for sheet cutting. The punching process produces edge profiles that are similar to the ones produced by shearing processes. In this work, the punching process is supposed to be in a given range equivalent to shearing process.

The edge profile is characterized by the existence of four zones: the rollover zone, the sheared zone (or burnish), the fracture zone, and burr zone. Figure 1.29(a) shows a schematic demonstration of the shearing process. The edge profile obtained by punching process presents exactly the same characteristic zones.

John and Slater [Johnson and Slater, 1967] provided a description of punching process which is illustrated in figure 1.29(b). They supposed that the punching process of a metallic material can be decomposed into four steps:

- [OA]: elastic deformation.
- [AB]: plastic deformation with hardening.
- [BC]: plastic deformation with necking.
- Crack initiation at [C] and propagation until the final fracture at [D].

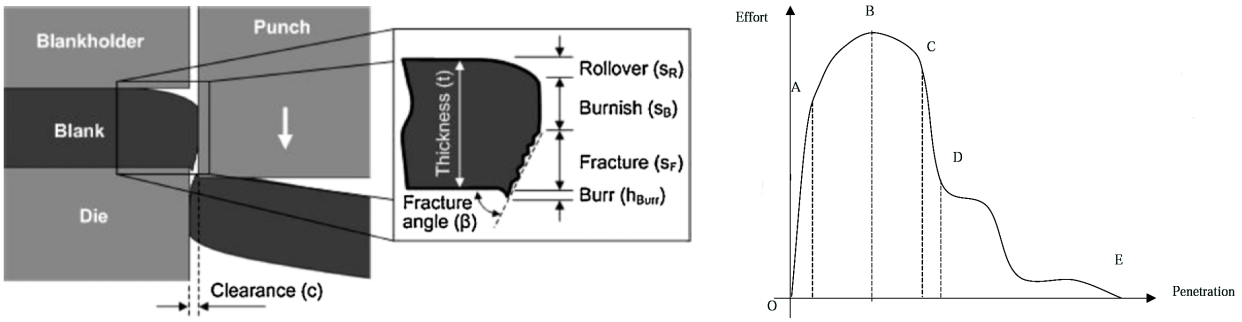

(a) (b)

Figure 1.29 – (a) Schematic description of the shearing process and the sheet cross section showing the edge profile [So et al., 2012], (b) Typical force-penetration curve acquired during cutting process [Johnson and Slater, 1967]

Many experimental investigations and numerical analysis were performed using ductile damage mechanisms in order to understand the mechanisms induced during sheet cutting [Maillard, 1991, Pyttel et al., 2000, Chen et al., 2004, Bacha, 2006, Dalloz, 2007].

1.6.2 Parameters influencing the cut-edge quality

Steel cutting operation influences the mechanical properties of the zones close to the edge surface. Indeed, this cutting-affected zone does not exhibit a similar behavior as the base material [Ismail, 20O7, Dalloz et al., 2009, Thomas, 2012, Lara et al., 2013]. This influence can be described as follows:

- Damage linked with the microstructure close to the edge surface (figure 1.30(a))
- Increased hardening in the cutting-affected zone assuming that the hardening is linked with the increase of the material hardness (figure 1.30(b))

The hardening was calculated using this expression:

$$Hardening = \frac{HV_l - HV_\infty}{HV_\infty} \times 100 \tag{1.23}$$

Where HV_∞ and HV_l are respectively the hardness of the base materials (away from the edge) and the hardness at a distance l from the edge surface.

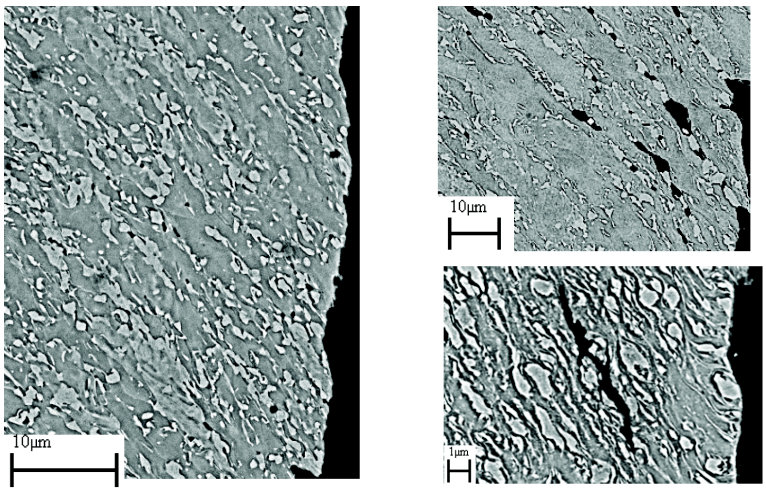

(a)

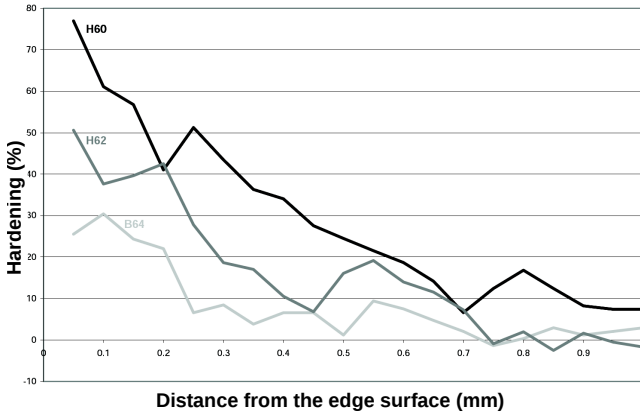

(b)

Figure 1.30 – (a) SEM picture of the damage induced by shearing process close to the edge surface in a DP steel, (b) increased hardening close to the edge surface in a DP steel [Dalloz, 2007]

The edge profile (or cut-edge quality) depends heavily on many parameters such as the material behavior, the clearance and the cutting speed. Many studies have pointed out this dependence [Lee et al., 1995, Hambli, 2001, Hambli, 2002, Hilditch and Hodgson, 2005, Mori et al., 2008, So et al., 2009, Sartkulvanich et al., 2010, So et al., 2012, Mori, 2012, Mori et al., 2013]. Some of these parameters are discussed hereafter.

The material ductile behavior

Many studies pointed out that the edge profile depends highly on the material behavior [Maillard, 1991, Pyttel et al., 2000, Chen et al., 2004, Bacha, 2006, Dalloz, 2007, Wu et al., 2012, So et al., 2012]. Figure 1.31(a) shows the fractography of a cut-edge produced by an aluminium sheet trimming [Bacha, 2006]. We can notice that the fracture during cutting occurred by shearing. However, in [Dalloz, 2007], it was shown that for a DP steel, the main mechanisms that occurred during blanking were the void nucleation and growth. Figure 1.31(b) gives a fractograph of a DP cut-edge showing the dimples on the edge surface.

Balendra and Tavis in [Balendra and Travis, 1970] performed punching tests varying the hardness of an HSLA steel using heat treatments. It was found, by comparing the load - punch displacement curves recorded during punching, that the maximum cutting force increases with the increase of the hardness, however, the penetration at fracture decreases. The cutting force is highly dependant on the grain size of the processed sheet [Goijaerts et al., 1999]. It increases with a decrease of grain size, this result has been explained by the effect of grain boundaries density. Indeed, when the sheet thickness decreases, the density of grain boundaries

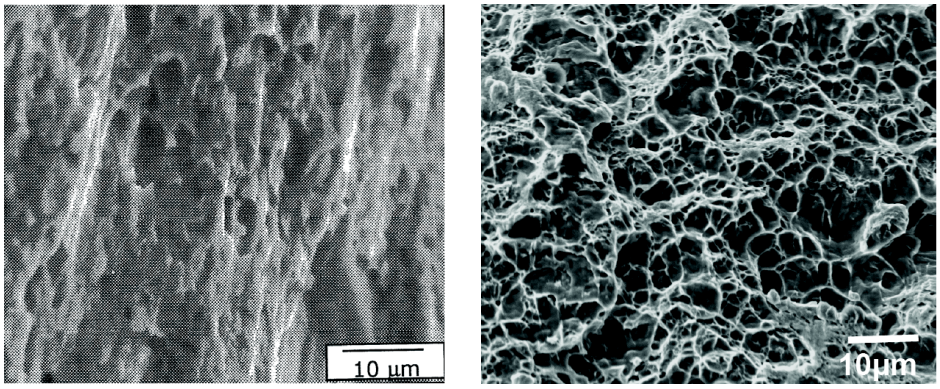

(a) (b)

Figure 1.31 – Fractograph showing fracture modes of cut-edges for: an aluminium alloy [Bacha, 2006], (b) a DP steel [Dalloz, 2007]

decreases. Thus these boundaries have fewer barriers to dislocations motion. In these conditions an increased deformation of the material during blanking can be observed [Goijaerts et al., 1999].

Many studies investigating the influence of materials microstructure on cut edge quality were performed. Levy and co-workers [Levy et al., 2013] investigated the failure during sheared edge stretching of DP Steels. It was found that the cutting process causes a highly strained region adjacent to the cut edge surface and that damage can be observed in this region after cutting process of a DP steel (figure 1.32(a)). Figure 1.32(b) shows experimental results found in the literature collected by Levy and co-workers [Levy and Van Tyne, 2011] showing the high dependency of fracture zone size on the clearance and the materials mechanical properties.

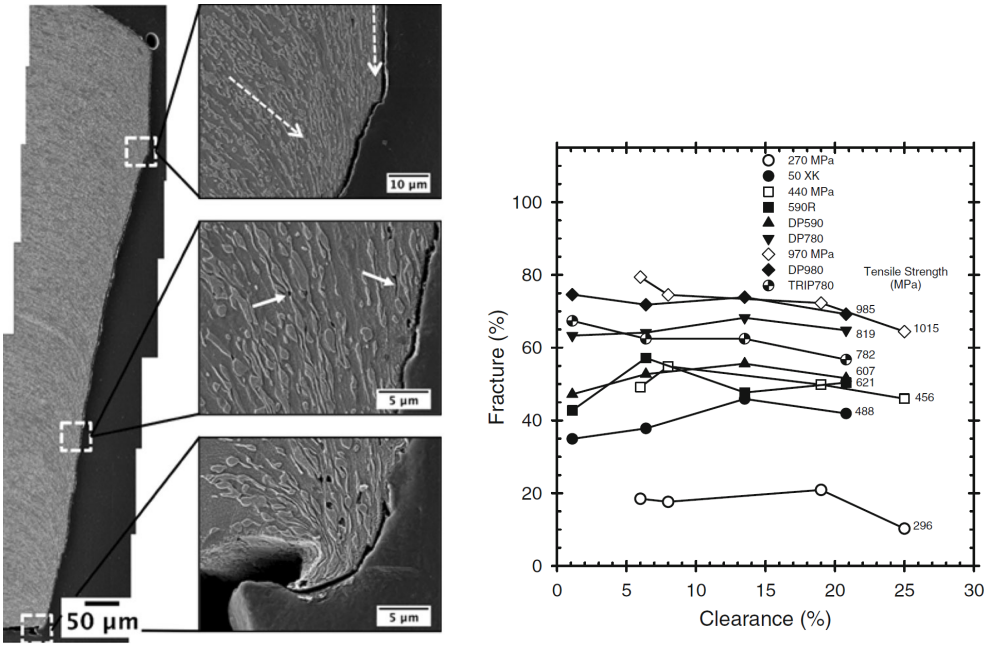

(a) (b)

Figure 1.32 – (a) Damage observed in the region close to the cut edge of a DP steel [Levy et al., 2013] (b) Effect of clearance and tensile strength on fracture zone percent for a range of steels [Levy and Van Tyne, 2011].

The effect of clearance

The clearance is a parameter characterizing the die-punch spacing defined in equation (1.24).

$$CL = \frac{D_d - D_p}{2\,t} \times 100 \tag{1.24}$$

Where D_d and D_p are the die and the punch diameters respectively and t is the initial sheet thickness.

Using experimental measurements and numerical simulations, it was pointed out in several works that the clearance has a major influence on the edge profile and thus its mechanical behavior. An increased burnish depth ratio was obtained for decreased clearance values [Taupin et al., 1996, Fang et al., 2002, Shim et al., 2004]. Figure (1.33) illustrates the dependence of the edge profile on the punch/die clearance. A clearance between 10 and 15% allows to improve the edge quality by increasing the depth ratio of roll-over and burr zones [Hilditch and Hodgson, 2005]. However, in [Mori et al., 2013], the depth ratio of the four characteristic zones of the cut-edge was measured for an ultra-high strength steel using different clearance values. They showed (figure 1.33(b)) that the sheared edge of high quality (maximal burnish zone) is limited to the very slight clearances (CL=8%) for an edge radius of punch of $0.13mm$. It was showed that too low clearance values increase the cutting energy [Fang et al., 2002]. DP cut-edges prepared using different clearance configurations was tested using the hole expansion test and that the HER increases for the clearance values between 5 and 20% [Sartkulvanich et al., 2010]. The results are shown in figure 1.33(c).

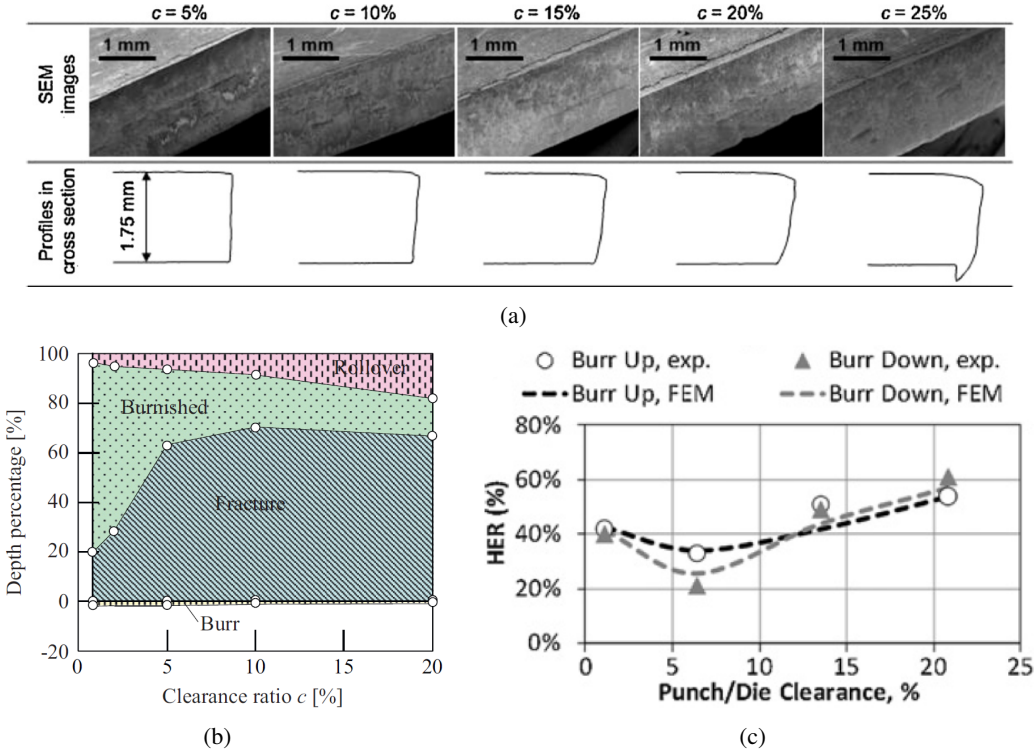

Figure 1.33 – (a) Sheared edge surface observed SEM for different clearance configurations [So et al., 2012], (b) Depth ratio of the characteristic zones of a cut-edge for an edge radius of punch of $0.13mm$ [Mori et al., 2013], (c) [Sartkulvanich et al., 2010].

The effect of temperature

The effect of the cutting temperature has been the subject of only few works. Johnson and Slater [Johnson and Slater, 1967], So et al. [So et al., 2012] and Mori et al. [Mori, 2012] pointed out the influence of temperature on the cutting process. It was concluded that the punch load decreases for increased temperature due to the decrease in flow stress. Figure (1.34) illustrated the works performed by So et al. [So et al., 2012]. The effect of the temperature was investigated for clearance values between 2.5 and 15% and the edge quality was improved in the case of a hot cutting.

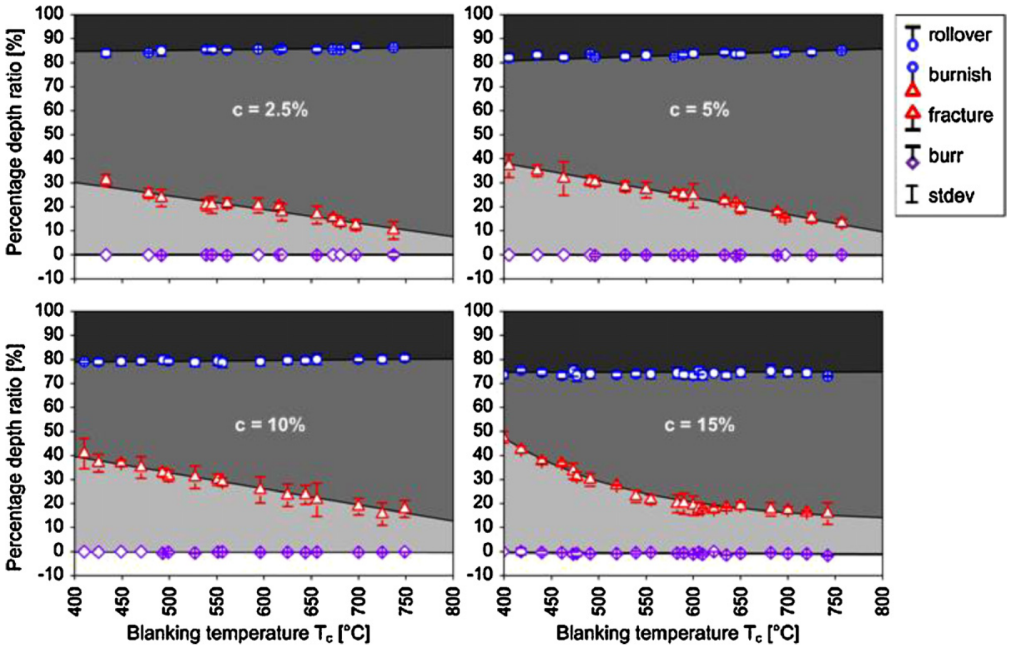

Figure 1.34 – Percentage depth ratios of the four cut-edge zones for different cutting temperatures [So et al., 2012].

1.6.3 Impact of cutting process on the cut-edge behavior

Cut-edges limit the use of AHSS in automotive industry because of their major influence on the formability of sheets made of these grades. The most commonly used mechanical tests to characterize the ductility of cut edge are the tensile test and the hole expansion test.

1.6.3.1 Tensile test

In [Dalloz et al., 2009] an experimental investigation was performed in order to quantify the impact of the cutting process on the mechanical behavior of DP cut-edges using tensile test. Vickers hardness ($10kg$) profile was measured from the edge surface in order to quantify the hardening of the shearing affected zone. The cutting affected zone was extended over about $800\mu m$ from the edge surface and the depth of the area where strain is larger than the uniform elongation was about $200\mu m$ [Dalloz et al., 2009] (figure 1.35(a)). Two types of tensile specimens were investigated: a tensile specimen containing sheared edges and a machined tensile sample (the shearing affected zone was eliminated by electrical discharge machining). They found that due to the presence of damage on the cut-edges the ductility reduction was higher than 50% (figure 1.35(b)). The fracture of the machined sample occured after necking and it initiated near the center of the neck. In contrast, the fracture of sheared specimen occured by the propagation of a microcrack initiated at one of the two cut-edges.

1.6.3.2 Hole expansion test

Hole expansion is a standard mechanical test (ISO/TS 16630) used by steel and car makers to evaluate the stretch-flangeability of metallic material sheets. It allows one to quantify the edge stretch limit. The principle of hole expansion is given in figure 1.36. It consists to :

1. Punching a hole in a thin sheet;
2. Expanding at room temperature the hole with a conical punch until a crack accrossing the sheet thickness appears;
3. Measuring along two perpendicular directions the diameter of hole after expansion and calculate the average value.

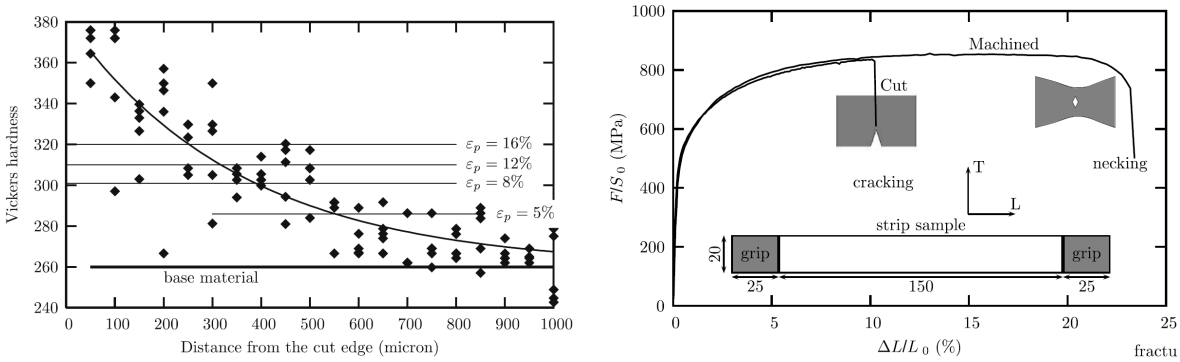

Figure 1.35 – Quantification of the impact of the cutting process on the mechanical behavior of DP cut-edges: (a) Vickers hardness measurements showing the hardening of the cutting affected zone, (b) tensile test curves illustrating the ductility reduction (more that 50%) due to the presence of cut-edges [Dalloz et al., 2009].

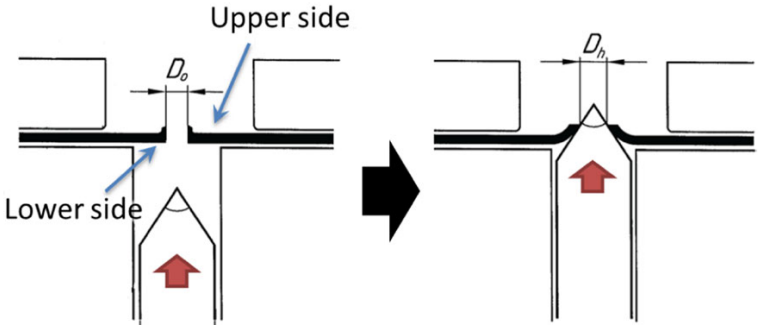

Figure 1.36 – Principle of hole expansion test [ISO/TS 16630]

The hole expansion ratio (HER) is calculated using the following formula:

$$\lambda = \frac{D_h - D_0}{D_0} \times 100 \tag{1.25}$$

Strain ε can be calculated from hole expansion test using the following formula:

$$\varepsilon_r = ln(\frac{D_h}{D_0}) = ln(1 + \frac{\lambda}{100}) \tag{1.26}$$

In the same way, ε_z can be estimated using:

$$\varepsilon_z = ln(\frac{e_h}{e_0}) \tag{1.27}$$

ε_θ can be deduced from ε_r and ε_z:

$$\varepsilon_\theta = -\varepsilon_z - \varepsilon_r = ln(\frac{D_0 e_0}{D_h e_h}) \tag{1.28}$$

Where D_0 and e_0 are respectively the initial hole diameter and sheet thickness. D_h and e_h are respectively the final diameter of the expanded hole and the final sheet thickness at the edge. Figure 1.37 shows a typical sample geometry after hole expansion test.

Several studies have been performed on the hole expansion test analyzing the dependency of the HER on some parameters. Paul et al. [Paul et al., 2014] found that the hole expansion performance (edge performance) of the six investigated steels is highly influenced by their microstructures. They developed a model allowing to predict the hole expansion ratio analytically from the true fracture strain. Figure 1.38 shows the results found for each steel grade investigated by Paul et al. [Paul et al., 2014]. The effect of steel microstructure was also studied by Misra et al. [Misra et al., 2001] and the results showed that edge mechanical performance

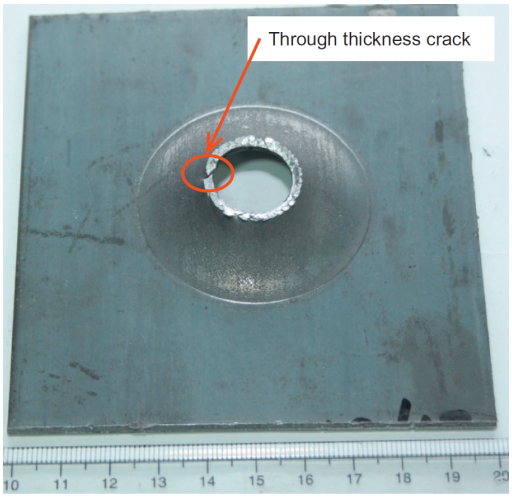

Figure 1.37 – A hole expansion sample after hole expanding [Paul et al., 2014].

decreases significantly when MnS inclusions are elongated. Fang et al. [Fang et al., 2003b, Fang et al., 2003a] have shown that for dual phase materials, hole expansion ratio depends strongly on the strength gradient between the hard and the soft phases. The higher the strength gradient, the smaller HER. The ferrite-bainite microstructure exhibits better formability properties compared to a TRIP (TRansformation Induced Plasticity) steel microstructure even if this latter microstructure is more ductile than the ferrite-bainite microstructure [Hyun et al., 2002]. Sudo et al. [Sudo and Iwai,] in their study on the understanding of dual phase steels characteristics pointed out that steels containing a volume fraction of bainite and a smaller amount of martensite in ferrite matrix exhibit a higher HER and their strength-ductility compromise is still similar to the dual phase (martensite-ferrite) one.

The influence of edge conditions on hole expansion performance were investigated in several studies using experimental measurements and numerical simulations [Levy and Van Tyne, 2012, Levy et al., 2013, Wang et al., 2014]. It was found that drilled edges (machined edges) exhibit a higher HER than the punched ones under the same testing conditions.

Several works have been carried out in order to correlate the hole expansion ratio to standard tensile testing results using regression analysis. For example, using hole expansion experimental results a correlation between the HER and total elongation and ultimate tensile strength was established in [Sudo and Iwai, , Adamczyk and Michal, 1986].

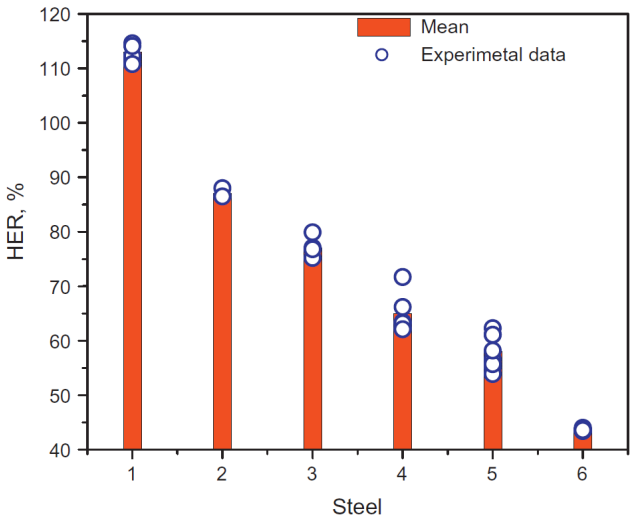

Figure 1.38 – HER experiment on six different steel grades [Paul et al., 2014]

Related to the position of the burr issued from hole punching, two configurations exist:

- Burr-up: the burr is on the side of the die (used in standard test).

- Burr-down: the burr is on the side of the punch.

Hole expansion test was used in this PhD work to validate the identified damage nucleation and growth criteria on X-ray tomography and laminography experimental data using different configurations of sheet thickness and hole diameter. The punching clearance used for samples preparation was chosen to be constant (12%).

In order to quantify the impact of cutting process on the formability of AHSS steel sheets, Wang et al. [Wang et al., 2014] performed an experimental and numerical analysis using the hole expansion test and the central hole tensile test. Three edge conditions were investigated using three cutting processes: punching, water jet cutting and machining (or milling). The hole expansion of the investigated DP sheet is around 14% for punched specimen and 38% and 35% for milled specimen and water jet cut specimen. Figure 1.39(a) shows the cracks distribution of the three edge conditions after hole expansion. The presence of punched edges reduces the HER and the strain at fracture for all the clearance investigated range.

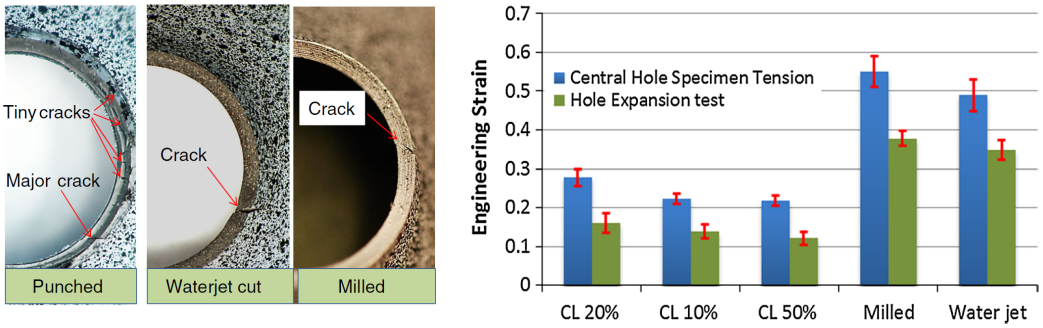

Figure 1.39 – Hole expansion and central hole tension tests used to quantify the influence of cutting process on the ductility of specimens with three edge conditions: (a) cracks distribution after holes expansion, (b) Strain at fracture of the investigated edge conditions [Wang et al., 2014].

The work performed by Hasegawa et al. [Hasegawa et al., 2004] investigates the effect of microstructure on stretch-flange-formability of high strength steel sheets using hole expansion test. The study was performed on Steels A and B in which the martensite volume fractions were 34% and 49%, respectively and a martensite single-phase steel grade named Steel C. In SEM images shown in fig.1.40(illustration 1) taken at the cross sections near the punched edge surfaces of steels A, B and C, we observe that flow-lines follow punching direction. Micro-voids were observed at martensite-ferrite interfaces in Steels A and B. The micro-voids were also observed in Steel C. In the imaged cross section of Steel A a micro-crack was observed beneath fracture zone surface. After hole expansion testing, the measured hole expansion ratios of machined edges were higher than ratios of punched edges for each steel. The martensite single phase steel exhibits the highest hole expansion ratio (see fig. 1.40(illustration 2)). It was also concluded that the volume fractions of phases also influence the formability [Hasegawa et al., 2004]. The punched edge surfaces at 30% and 50% of hole expansion are given in figure 1.40(illustration 3).

It is important to mention that the tensile test and the hole expansion test present some drawbacks: scattering in results observed and necking apparition before edge fracture which limit the use of these tests.

A very recent work [Wang et al., 2015] has been performed using finite element method to predict edge fracture in a DP780 steel with a good accuracy. They proposed a method to model edge fracture considering the pre-damage introduced in a punched edge by blanking process. Hole expansion simulation has been performed using different clearance values. Figure 1.41 gives the equivalent plastic strain and damage indicator distribution from punched edge surface obtained by sheet blanking simulation. These results have been used for hole expansion simulation with a mesh size of $0.1mm$. To model the ductile fracture of the DP steel investigated in this study, an uncoupled phenomenological approach was applied introducing a state variable of damage to the material that accumulates with the equivalent plastic strain.

Cracks distribution and orientation obtained using FE model considering pre-damage caused by blanking process are in good agreement with the experimental results [Wang et al., 2015] (see fig. 1.42). Is has been concluded that plastic deformation and pre-damage caused by the blanking process are the main factors that compromise ductility and cause edge fracture.

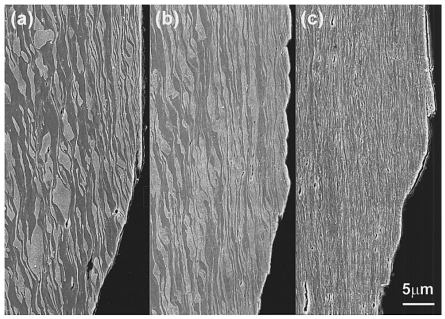

(a) Illustration 1

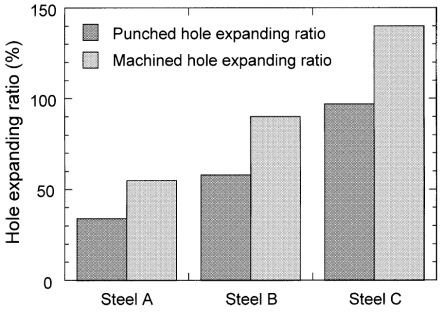

(b) Illustration 2

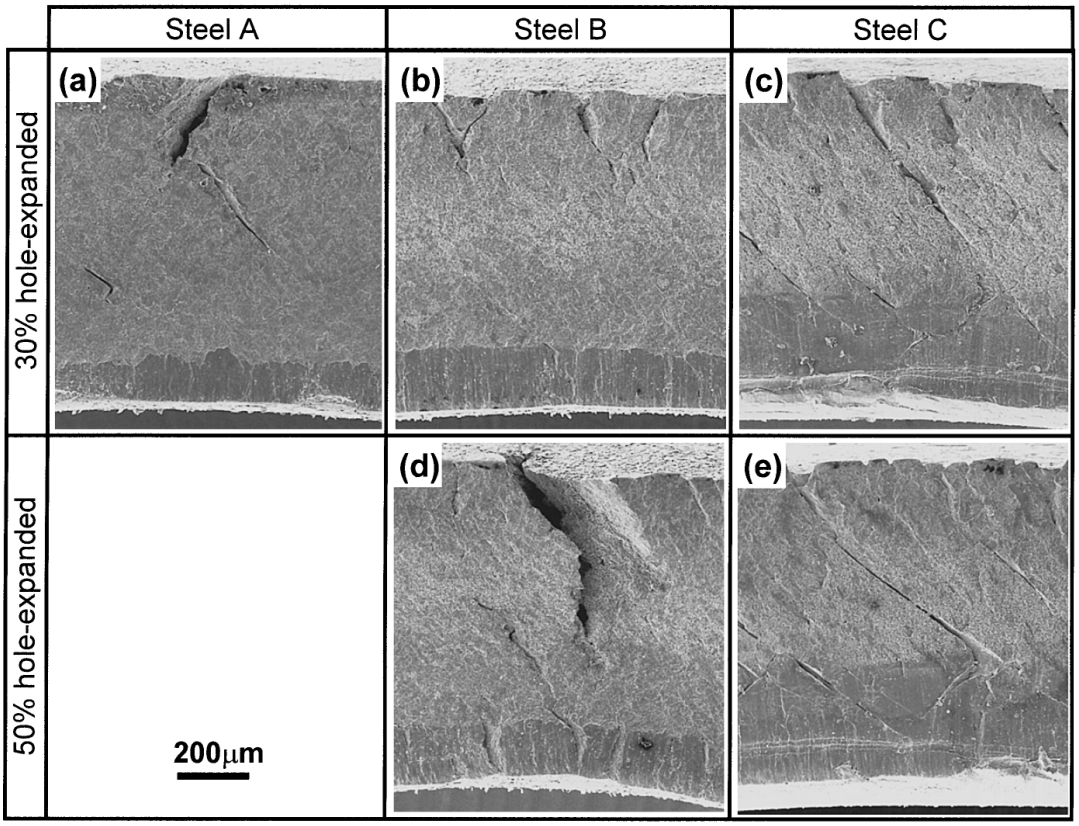

(c) Illustration 3

Figure 1.40 – Illustration 1: Microstructures of punched edge of (a) Steel A with 34% of martensite, (b) Steel B with 49% of martensite and (c) Steel C a fully martensitic steel. Illustration 2: Hole expansion ratios of punched and machined edges of the investigated steels. Illustration 3: Punched edge surfaces during hole expansion of the three studied steels [Hasegawa et al., 2004].

1.6.3.3 Double bending test

Bouaziz et al. [Bouaziz et al., 2010] developed a new technique called double bending test which can be used to characterize the sheared edges ductility. The principle of this test consists in a 90° flanging parallel to the sheared edge to be tested. The flange height should be less than 15mm in order to avoid sample buckling [Bouaziz et al., 2010]. This configuration permits to get the edge fracture with no necking and the measurement of the strain field can be directly done by digital image correlation. Figures 1.43(a) and (b) illustrate the principle of the double bending test.

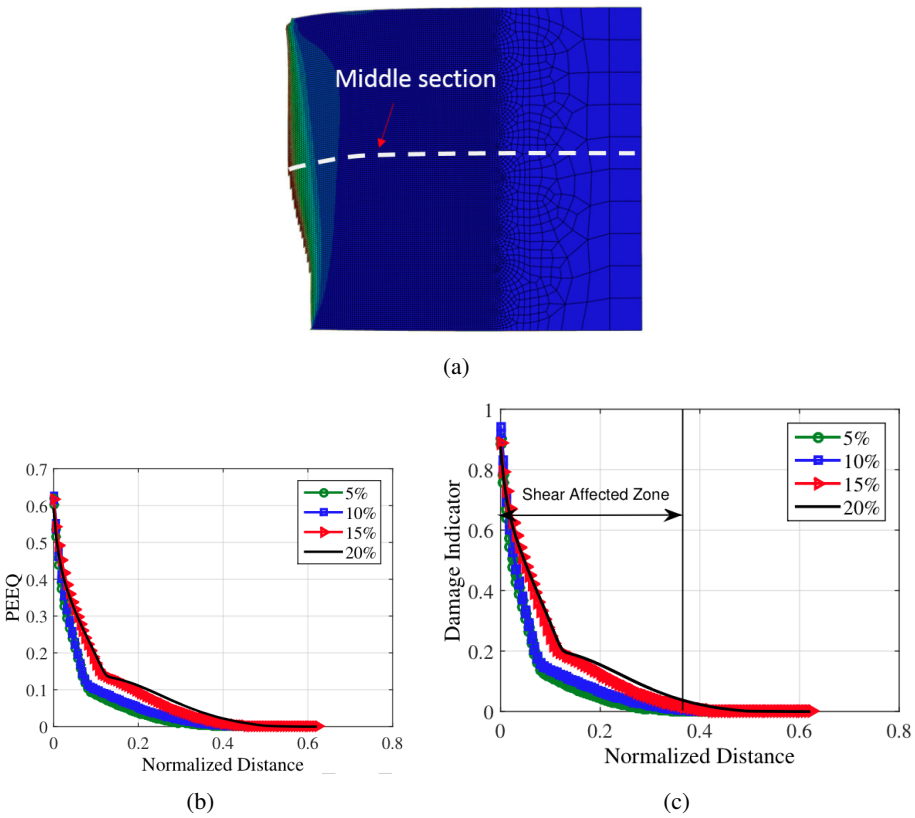

Figure 1.41 – Numerical simulation of hole expansion of a DP780 steel sheet. Damage and plastic strain distribution of blanked edge of four different die clearances. Distance to hole edge was normalized by sheet thickness: (a) The edge profile predicted by FE simulation, (b) The equivalent plastic strain, (c) Damage indicator [Wang et al., 2015].

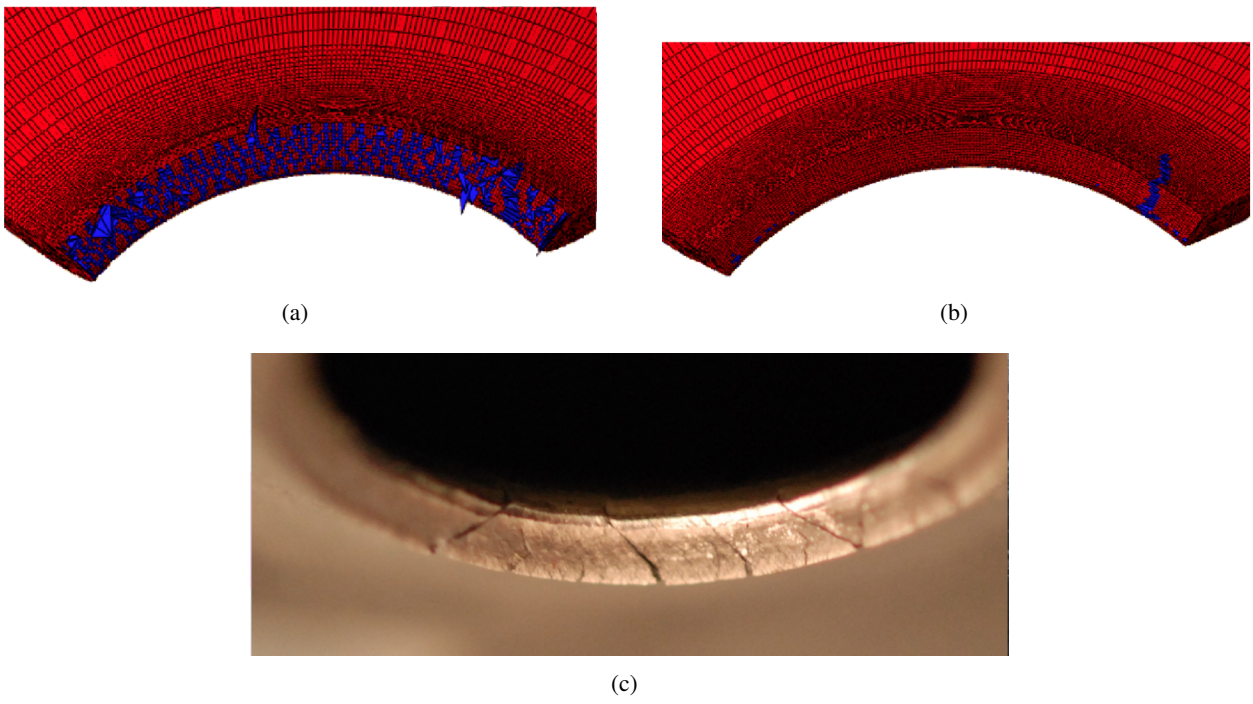

Figure 1.42 – Hole expansion of a DP780 steel sheet simulation : (a) with pre-damage, (b) no pre-damage. (c) Cracks orientation after a punched hole expansion test. Color code is element deletion flag and the blue code indicates the elements which are desactivated [Wang et al., 2015]

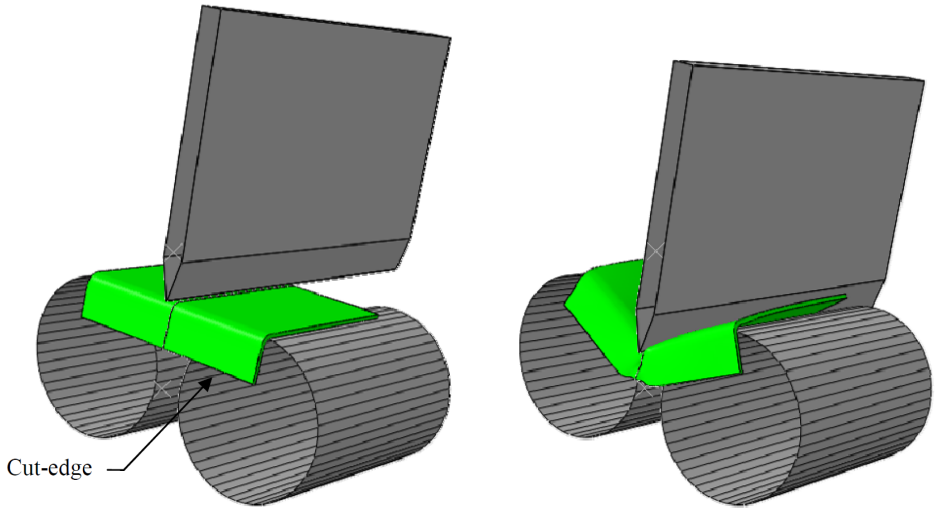

Figure 1.43 – Principle of double bending test: (a) sample to be tested containing a cut-edge, (b) the edge fracture after bending test [Bouaziz et al., 2010].

1.7 Comparison of sheet shear cutting and hole punching

In order to compare sheet shearing and hole punching, we have carried out a numerical simulation using the data provided in the literature by Dalloz and co-workers [Dalloz2009] related to the cutting modeling and simulation of a DP steel sheet. The reader interested in the investigated material and the used GTN model should refer to [Dalloz, 2007, Dalloz et al., 2009].

1.7.1 Material properties

Table 1.1 gives the mechanical properties of the studied DP steel. It is important to mention that the loss of ductility of this steel grade can reach 50% due to the presence of cut-edges.

Table 1.1 – Tensile properties of the DP780 investigated steel at room temperature

	YS (MPa)	UTS (MPa)	$A_{uniform}$ (%)	$A_{fracture}$ (%)	Lankford coefficient
L	525	858	14.3	21.8	0.87
T	481	853	14.1	19.5	0.78

1.7.2 Mesh for finite element simulation

The mesh used by [Dalloz et al., 2009] for numerical simulation of shearing and punching processes using Z-Set software are given in fig. 1.44. For shearing process simulation, we have performed a 2D FE plane-strain calculation. While axisymmetric elements have been used to simulate punching process. We notice that the studied punched hole diameter is $5mm$. In this part, we will not develop the constitutive equations used for this simulation, the reader can find all details in the paper cited hereinbefore.

1.7.3 Simulation results

The other mechanical parameter that allows one to compare those two cutting process is the effort applied for sheet cutting. The evolution of the mechanical linear effort as a function of the mobile blade displacement

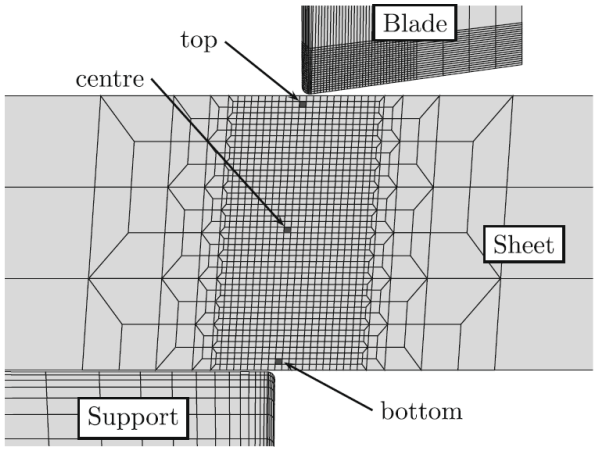

Figure 1.44 – 2D mesh used for finite element simulation of sheet shearing and $5mm$ hole punching

is given in fig. 1.45. We observe that the maximum force reached during $5mm$ hole punching is slightly increased (800 $N.mm^{-1}$) compared to the one obtained for the shearing process (700 $N.mm^{-1}$). In the present PhD work, the punching process is supposed to be in a given range equivalent to shearing process.

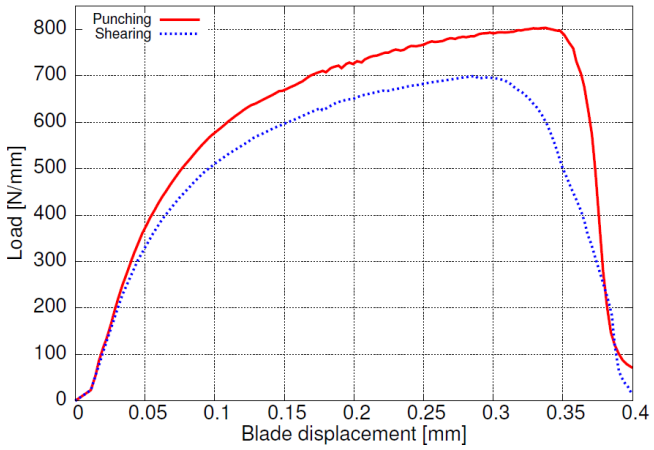

Figure 1.45 – Load - blade displacement curve obtained numerically for punching and shearing processes

Chapter 2

Materials and experimental methods

Contents

2.1 Résumé

La microstructure, la composition chimique ainsi que les propriétés mécaniques des deux matériaux étudiés sont présentées dans ce chapitre. Les micrographies MEB montrent que les deux nuances présentent un effet composite, une matrice ferritique ductile renforcée par des ilots de martensite pour l'acier DP et la bainite pour l'acier FB, ce qui leur confère un bon compromis entre formabilité et résistance mécanique. Une analyse inclusionnaire a permis de quantifier les différentes familles d'inclusions présentes dans les nuances étudiées, à savoir MnS, CaO et Al_2O_3. Les courbes de traction montrent que l'acier FB présente une anisotropie plastique entre le sens L et T.
Les différentes techniques expérimentales utilisées dans ce projet pour la caractérisation microstructurale et mécanique des matériaux de base et des bords découpés sont présentées dans ce chapitre. Le lien entre les mécanismes d'endommagement ductile des matériaux de base et la microstructure a été étudié via des essais de traction en MEB in-situ. La technique d'imagerie 3D de tomographie synchrotron à rayons X a permis d'étudier qualitativement et quantitativement les mécanismes d'endommagement ductile à une échelle micrométrique. Le comportement mécanique des bords découpés, quant à lui, a été étudié via la technique de laminographie synchrotron à rayons X par des essais d'ouverture d'entaille. Les champs de déplacement dans la zone d'intérêt, appliqués par le simple outil de chargement utilisé, ont été déterminés par corrélation d'images.

In this part is presented a brief description of base materials investigated in this work, their microstructures, mechanical properties and the nature of inclusions contained in these grades. The experimental methods used in this work to characterize qualitatively and quantitatively microstructures and damage in 2-D and in 3-D are presented. Two edge configurations were studied: punched edge and machined edge produced by electrical discharge machining. Finally, some mechanical tests used in this study to characterize the mechanical behavior of the investigated edges are described.

2.2 Materials

2.2.1 DP steel

2.2.1.1 Microstructure

DP steels have typically a composite microstructure as they consist of a soft ferrite matrix reinforced by a strong second phase of martensite. This composite microstructure offers to this steel grade a good compromise between strength and formability. The global composition of the investigated DP steel is given in table 2.1. The carbon concentration of the martensite phase is about 0.48% if we assume that all carbon present in the material is located inside the martensite. The surface fraction of martensite of this grade measured on binary scanning electron microscopy images is about $F_M = 15\%$. This value is slightly overestimated due to the presence of bainite, carbides and grain boundaries that are included in the calculated surface fraction of martensite.

Table 2.1 – Chemical composition of the investigated DP steel (weight %).

C	Mn	Si	Cr	Ni	Ti
0.095	1.89	0.24	0.2	0.012	0.0013

In this work the rolling direction will be referred to as L, the long transverse direction as T and the short transverse direction as S for all experiments presented. The micrographs in figure 2.1 show the alignment of martensite islands along the L-direction. The alignment of martensite islands is the origin of the banded microstructure that may DP steels exhibit. Ferrite and martensite respectively appear in dark and in light gray.

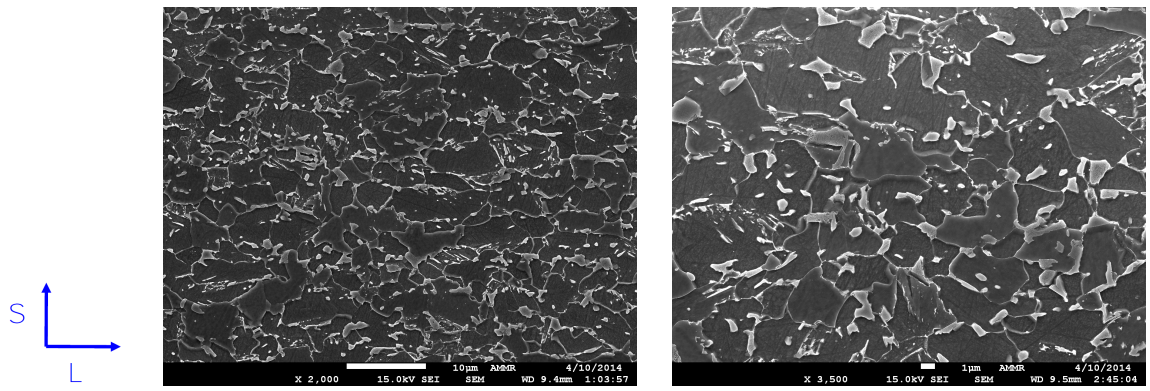

(b) (c)

Figure 2.1 – DP microstructure visualized at different magnifications by scanning electron microscope after polishing and 2% nital etching ((a) 2000× and (b) 3500×) (ferrite appears in dark and martensite in light gray).

2.2.1.2 Mechanical properties

The material was supplied as a $0.8mm$ thick cold rolled sheet. The figure 2.2 shows the stress-strain curve for this grade. The plastic strain of 0.2% is used to measure the offset yield strength which is approximately 420 MPa. The ultimate tensile strength is about 600 MPa at room temperature. The material exhibits an isotropic mechanical behavior and the three tested direction (L, T and 45○) present approximately the same total elongation (about 22%). These experiment have been performed by ArcelorMittal Maizières.

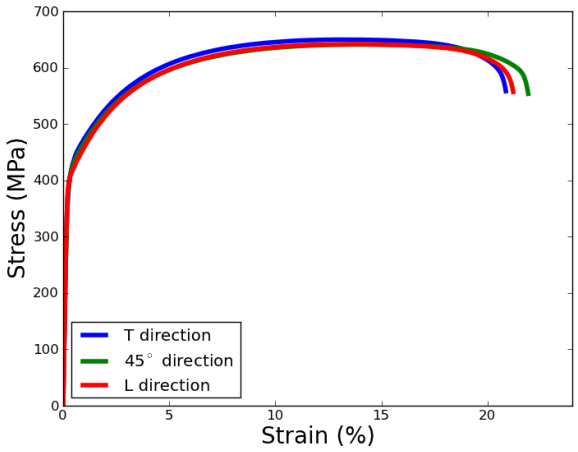

Figure 2.2 – Uniaxial engineering tensile stress–strain curves of investigated DP steel

Figure 2.3 shows the true tensile stress-strain and reverse shearing of the studied DP steel. These experiments have been performed by ArcelorMittal Global R&D. They allowed to identify the elasto-plastic constitutive equations and their optimized parameters which are discussed in chapter 5.

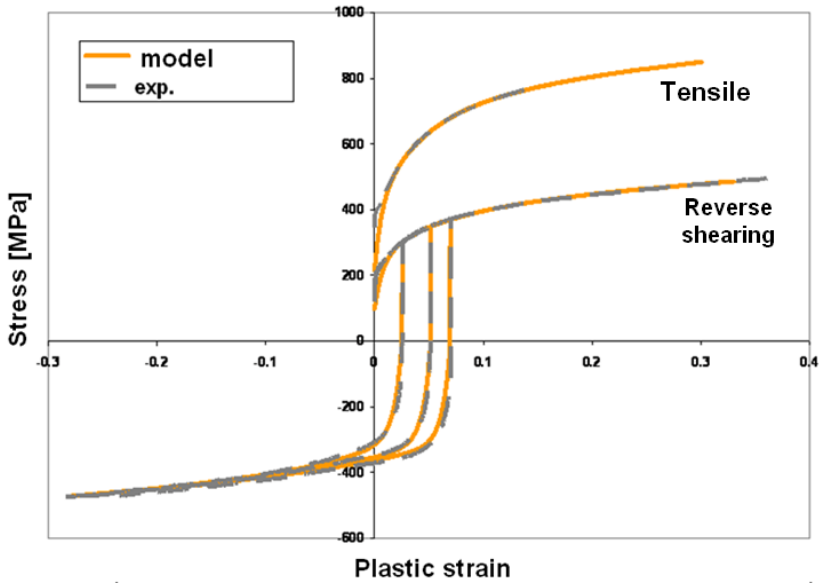

Figure 2.3 – True tensile stress-strain and reverse shearing of the investigated DP steel [ArcelorMittal credit]

2.2.1.3 Inclusions characterization

In order to characterize in qualitative and quantitative ways inclusions contained in the investigated DP steel, a surface of $3.99mm^2$ was analyzed at ArcelorMittal Maizières using energy-dispersive X-ray spectroscopy technique (EDS). We observe the presence of three types of particles: Al_20_3, CaO and MnS (figure 2.4(a)). The mean diameter of analyzed particles was about $3.77\mu m$. The density of particles and particle surface

fraction (PSF) measured in the analyzed area were respectively 34.07 $/mm^2$ and 0.07%. The histogram of particule size is given in figure 2.4, it shows that particule diameters are between 1.5 and 5 μm.

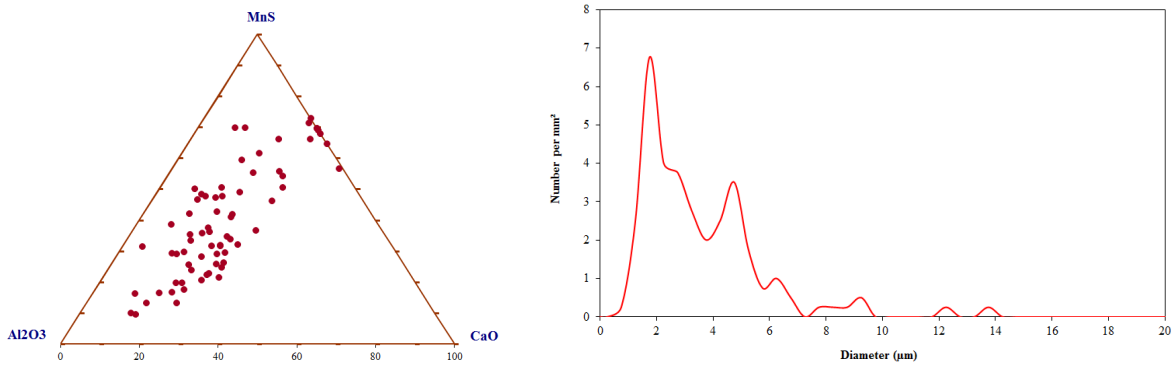

(a) (b)

Figure 2.4 – Inclusions characterization of the investigated DP steel using EDS technique: (a) ternary diagram showing the presence of MnS, Al_2O_3 and CaO particles, (b) inclusions equivalent diameter distribution (ArcelorMittal credit)

2.2.2 FB steel

2.2.2.1 Microstructure

FB steels with their ferrite-bainite microstructure based on carbon-manganese concept offer an excellent compromise between strength and ductility which leads to high energy absorbing performance. The global composition of the investigated FB steel is given in table 2.2. The investigated FB steel was supplied from a $3mm$ thick sheet. Micrographs in figure 2.5 show dispersion of bainitic grains within the soft ferrite matrix.

Table 2.2 – Chemical composition of the investigated FB steel (weight %).

C	Mn	Si	Cr	Ni	Ti
0.082	1.425	0.029	0.021	0.029	0.001

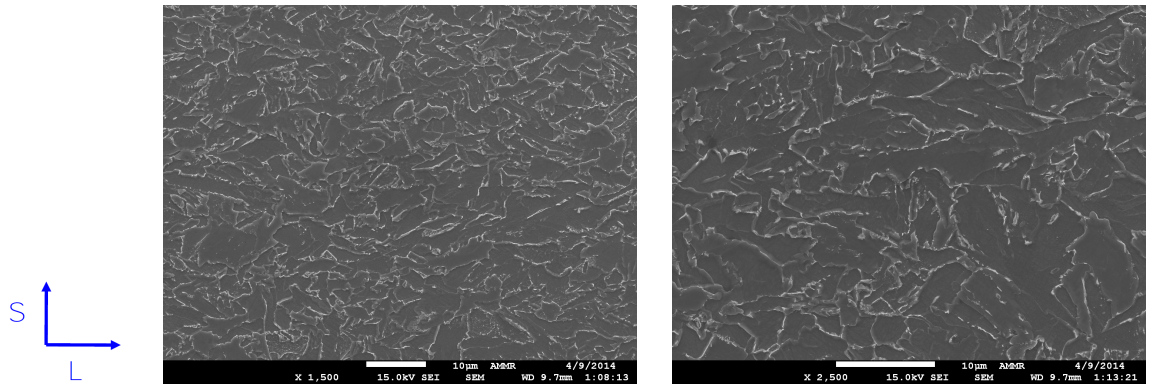

(b) (c)

Figure 2.5 – FB microstructure visualized at different magnifications by scanning electron microscope after polishing and 2% nital etching ((a) 1500× and (b) 2500×) (ferrite appears in grey).

2.2.2.2 Mechanical properties

The FB mechanical behavior during tensile test in L and T directions at room temperature is given in figure 2.6. These experiments have been performed at ArcelorMittal Maizieres. The investigated FB steel is characterized by a high yield strength which is approximately 500 MPa and an ultimate tensile strength about 600 MPa. This grade exhibits a high total elongation in L direction (approximately 17%) compared to the T and 45° where the total elongation is equal to 13% and 16% respectively.

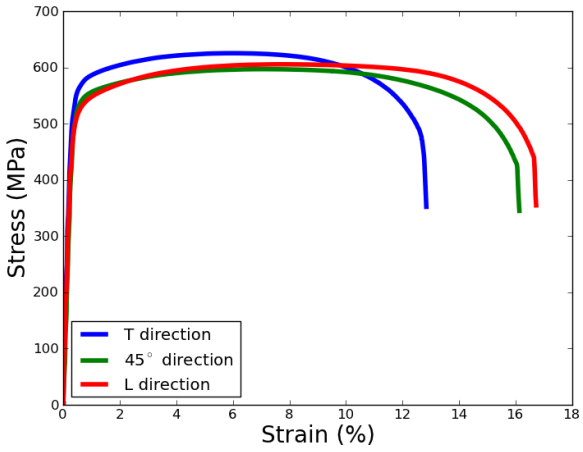

Figure 2.6 – Uniaxial engineering tensile stress–strain curves of investigated FB steel

The true tensile stress-strain and reverse shearing of the studied FB steel are given in figure 2.7. These experiments have been performed by ArcelorMittal Global R&D. They allowed to identify the elasto-plastic constitutive equations and their optimized parameters which are discussed in chapter 5.

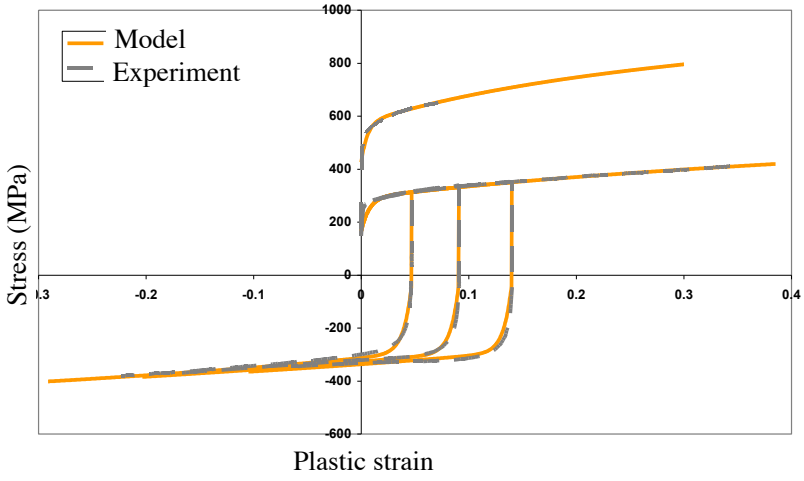

Figure 2.7 – True tensile stress-strain and reverse shearing of the investigated DP steel [ArcelorMittal credit]

2.2.2.3 Inclusions characterization

A surface of $2.9mm^2$ was analyzed using energy-dispersive X-ray spectroscopy technique to reveal nature and quantity of inclusions formed within the investigated FB steel. This analysis confirmed the presence of three types of particles Al_20_3, CaO and MnS (figure 2.8(a)). The mean diameter of particles was about $4.1\mu m$. The density of particles and particle surface fraction (PSF) measured in the analyzed area were

respectively 20.32 $/mm^2$ and 0.03%. Figure 2.8(b) shows the distribution of particule size in the FB steel. The majority of particle diameter is between 2 and 6μm.

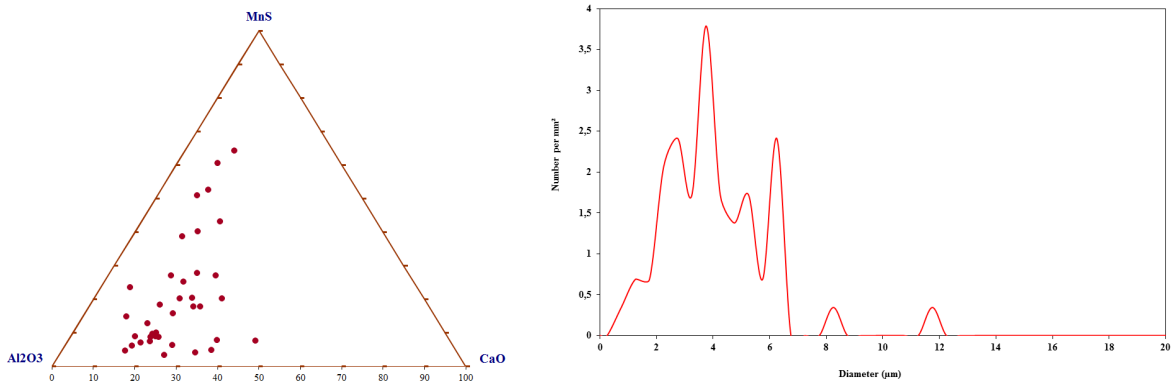

(a) (b)

Figure 2.8 – Inclusions characterization of the investigated FB steel using EDS technique: (a) ternary diagram showing the presence of MnS, Al_2O_3 and CaO particles, (b) inclusions equivalent diameter distribution (ArcelorMittal credit)

2.3 Experimental methods

2.3.1 In situ tensile testing in SEM

In situ tensile testing on micro-scale specimen (figure 2.9) in scanning electron microscope was performed in two directions L and T to identify damage mechanisms leading to ductile fracture of the investigated steel grades. Specimens were polished using SiC grinding paper, diamond paste (3μm to 0.25μm) and active oxide polishing suspension (OPS) for the last step. After polishing specimens were cleaned using ultrasound for approximately 30 min. To reveal DP and FB microstructures, specimens were etched using Nital 2%. The displacement speed was choosen to be 3$\mu m/s$ for the four tested specimens. This experiment allowed us to follow the damage evolution on specimen surface at microscale resolution during tensile test.

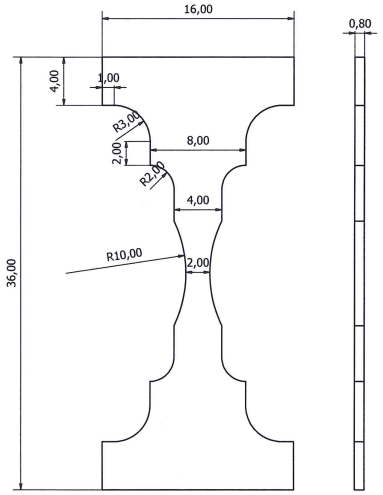

Figure 2.9 – Specimen geometry used in in situ tensile testing in SEM (dimensions in mm)

2.3.2 X-ray tomography

Materials damage mechanisms have been better understood due to the development of many new experimental techniques. 3D imaging methods are considered the best techniques providing, with a resolution up to the

micrometer, the internal damage evolution in the observed region of interest.

X-ray tomography principle

X-ray tomography is a nondestructive imaging technique that allows one to visualize in three dimension internal features within their geometries and properties compact or one-dimensionally elongated objects. The principle of X-ray tomography is given in figure 2.10.

Reconstruction of series of 2D X-ray absorption images recorded during rotation of the object is based on mathematical principles of tomography. The result of reconstruction is a 3D digital image made of many sub-volumes called voxels (volume element, the extension of pixel in 3D).

X-ray attenuation is a logarithmic function of the absorptivity of characterized materials which depends on the number and the type of atoms bombed by the X-ray beam. Chemical elements with lower Z absorb less than those with higher Z for a fixed X-ray energy. Figure 2.11 shows typical values of X-ray mass attenuation coefficients for iron and carbon [Henke et al., 1993].

$$I_x = I_0 e^{-\mu\rho x} \tag{2.1}$$

Where I_0 is the incident X-ray intensity, μ is the linear attenuation coefficient, ρ is the material density and x is the material thickness.

Important enhancements can be reached by using synchrotron radiation as an X-ray source. Synchrotron radiation can be produced from the bending of high-energy electron beam using a magnetic field. Magnification of emitted beam is many orders higher than that emitted by laboratory X-ray sources which improves the quality of acquired digital images and simplifies tomographic reconstruction.

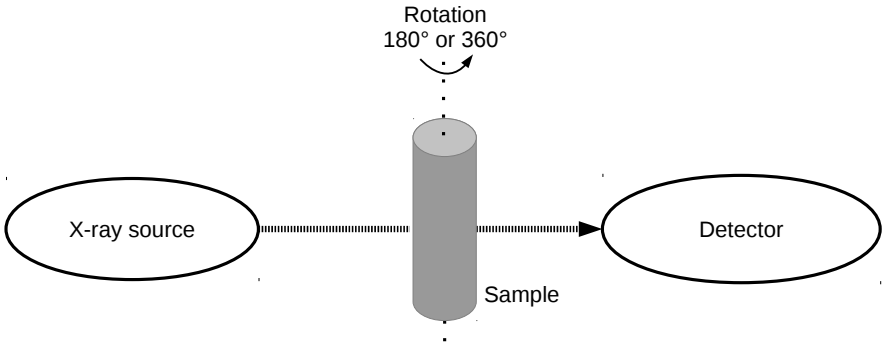

Figure 2.10 – X-ray tomography principle.

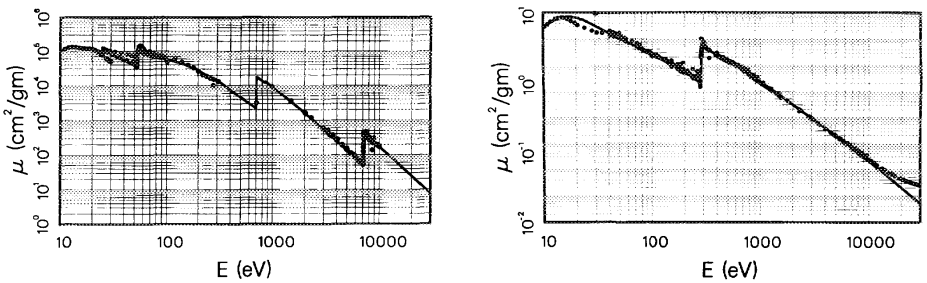

(a) Iron (b) Carbon

Figure 2.11 – Typical attenuation coefficients (μm) of Fe and C [Henke et al., 1993].

In situ experiment

It is important to mention that X-ray tomography does not allow to distinguish the ferritic phase from the martensitic and the bainitic ones because the attenuation coefficients of the three phases are very close.

In situ tensile tests were carried out at ID15 beam line at ESRF on flat square smooth specimens designed with adapted dimensions (figure 2.12(b)) using a dedicated tensile machine developed at MATEIS laboratory (INSA Lyon) described in [Buffiere et al., 2010]. For DP observations the specimens were polished after machining to make the section oval. Applied displacement speed was $5\mu m.s^{-1}$. The X-ray beam used was centered around $50keV$ for DP grade and $60keV$ for FB grade. The voxel size was $1.1\mu m$ for FB observations and $1.4\mu m$ for DP observations. The exposure time was between 0.04 and $0.15s$ and number of 2D projections recorded was 2000 over 180°.

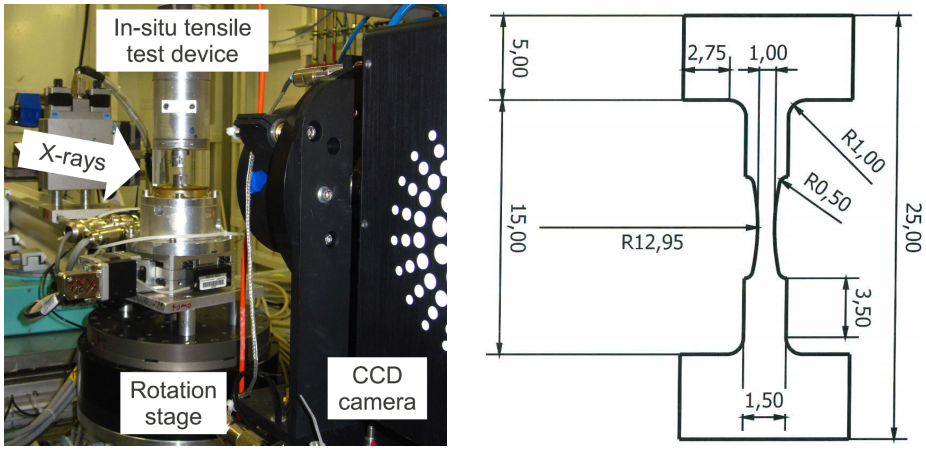

(a) (b)

Figure 2.12 – In situ experimental device used for x-ray tomography observation: (a) tensile test device at ID15 [Landron, 2011], (b) sample geometry

2.3.3 X-ray laminography

Principle of X-ray laminography

The principle of X-ray laminography is given in figure 2.13. X-ray laminography is a new non destructive technique that permits to observe regions of interest in thin sheet-like objects at micrometer three-dimensional spatial resolution. It allows one to avoid geometry restrictions of X-ray tomography. This technique provided us a unique way to qualitatively and quantitatively assess initial damage and its evolution during edge fracture of the investigated DP and FB specimens.

X-ray synchrotron laminography raw data was reconstructed using a filtered back projection (FBP) algorithm adapted to the computed laminography acquisition described in [Myagotin et al., 2013]. The reader interested in X-ray laminography theory and its application in materials science should refer to [Helfen et al., 2005, Helfen et al., 2007, Helfen et al., 2012, Xu et al., 2010, Bull et al., 2013].

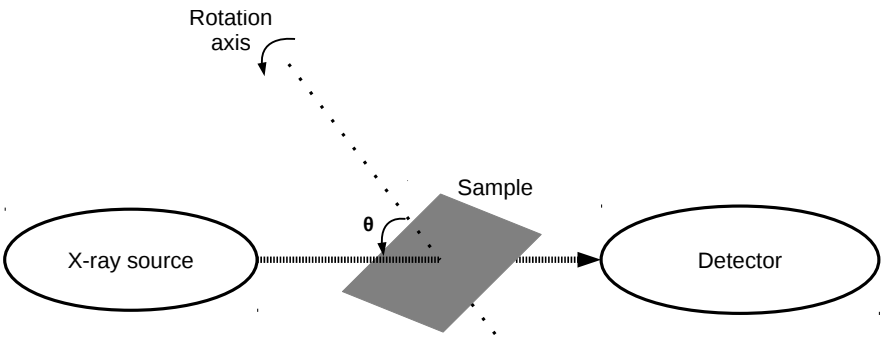

Figure 2.13 – X-ray laminography principle

In situ experiment

Experiments were performed at ID19 beam line at ESRF with a peak energy centered around 60 keV using a high-dose detector system [Douissard et al., 2012] with an isotropic voxel size of 0.778μm. The rotation axis inclination angle was chosen around 30°. About 2000 projections were acquired with an exposure time of 40ms.

Two edge configurations (punched edge and machined edge) were tested for each steel grade. The sample geometry shown in figure 2.14(b) was used. For DP steel, the first edge configurations was a hole with a radius of 5mm punched out from a 0.8 mm thick sheet and an elongated notch was machined up to one edge. The second edge configuration was a machined hole of 6mm produced by electrical discharge machining (EDM). The machined edge was slightly polished in order to eliminate the EDM wire affected zone. For FB steel, the tested punched and machined edges were of 5mm. The loading was applied perpendicular to the notch, via a two-screw displacement-controlled wedging device that allows us to incrementally open the notch and control the specimen crack mouth opening displacement (CMOD) similar to the one used in [Morgeneyer et al., 2011, Morgeneyer et al., 2013, Shen et al., 2013, Ueda et al., 2014]. Specimens were placed in an anti-buckling device to avoid sample buckling and out-of-plane motion (figure 2.14(a)). The entire rig was mounted in a dedicated plate that was removed from the laminography rotation stage between loading steps. After each loading step, a scan of the ROI containing the crack tip was carried out and a 2D surface picture was taken for digital image correlation.

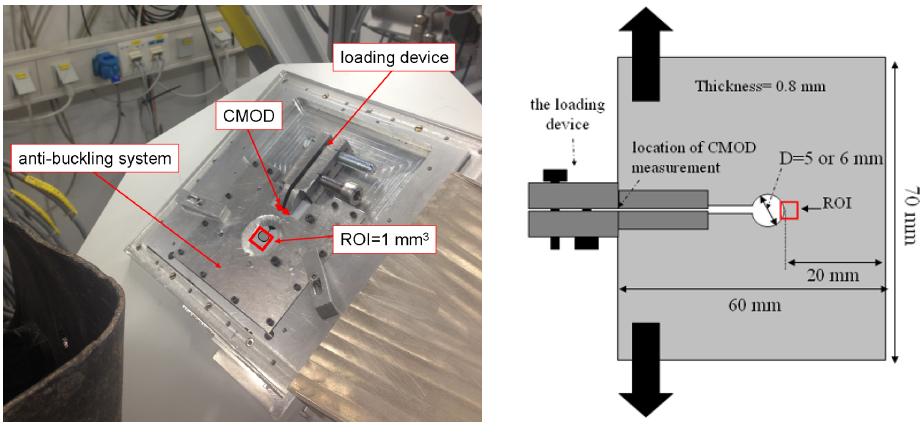

(a) (b)

Figure 2.14 – In situ experimental device used for x-ray laminography observation: (a) photograph of the loading device at ID19, (b) sample geometry

The table given in figure 2.15 shows the successful in situ X-ray tomography and laminography experiments performed at the ESRF that are presented in this work. It also gives some in formations about the experiment such as the beamline name, the voxel size and the project name.

2.3.4 Processing of tomography and laminography data

Filtering and segmentation

A filtering using a 3D median filter with a radius of two voxels was applied on raw volumes acquired at ESRF in order to reduce noise induced by the experimental methods. Figure 2.16 shows different processing steps necessary to visualize and quantify damage in tomography and laminography data. Raw section and two voxels median filtered section of DP machined edge are shown respectively in figure 2.16(a) and (b). A simple threshold determined from the histogram of gray levels applied on filtered volumes is used to create binary volumes. The outer shape and porosity of specimens was detected using a plug-in implemented on ImageJ based on Sobel edge detector that consists in highlighting sharp changes in intensity in 3D binary volumes. A result of this finding-edge process is presented in figure 2.16(d).

Material	Specimen	Loading direction	Voxel size (µm)	Beamline	Project N°	Test	Comments
DP600	Punched edge	T	0.778	ID19	IN771	In situ laminography	Artefacts
	Machined edge	T	0.778	ID19	MI1149	In situ laminography	
	Tensile specimen	L	1.34	ID15A	-	In situ tomography	Performed by Eric Maire
	Tensile specimen	T	1.34	ID15A	-	In situ tomography	Performed by Eric Maire
FB600	Punched edge	L	0.778	ID19	MI1149	In situ laminography	
	Machined edge	T	0.778	ID19	MA1149	In situ laminography	
	Tensile specimen	T	1.095	ID15	MA1932	In situ tomography	
	Tensile specimen	L	1.095	ID15	MA1932	In situ tomography	

Figure 2.15 – Successful in situ tomography and laminography experiments presented in this work.

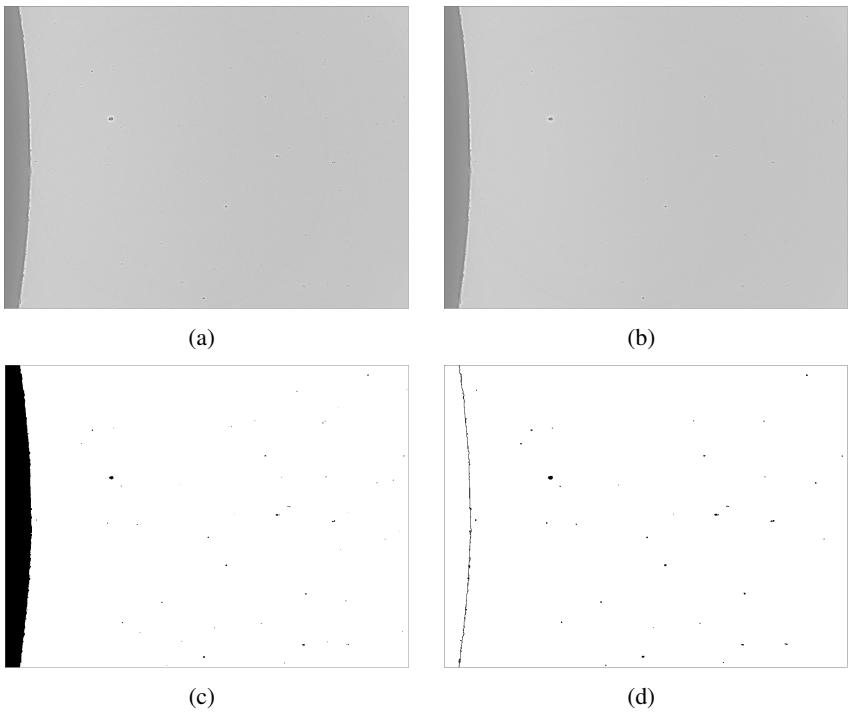

Figure 2.16 – Processing of laminography volume of DP machined edge. (a) raw volume acquired at ESRF ID19, (b) 3D median filtering with radius of 2 voxels, (c) result of the applied threshold on the filtered section, (d) binary section showing edge surface and porosity using ImageJ find-edges process

3D visualization

In this work, 3D visualization of damage in specimens was carried out using ImageJ 3D viewer for laminography data and Avizo software for tomography data. Porosity inside samples appears in red or blue and material in transparent. Figure 2.17 shows 3D visualization of damaged FB sample and DP machined edge at initial state obtained respectively by tomography and laminography. In figure 2.17(a), tomography volume of FB steel sample shows cavities in red and sample border in gray transparent. Initial porosity and machined edge surface appear in blue in figure 2.17(b) in laminography volume of DP steel sample.

Damage quantification

For tomography volumes, only a cubic central area of ($(300\ \mu m)^3$ for DP steel and $(240\ \mu m)^3$ for FB steel) where damage is localized was cropped for damage quantification. This chosen area (figure 2.18(a)) is the

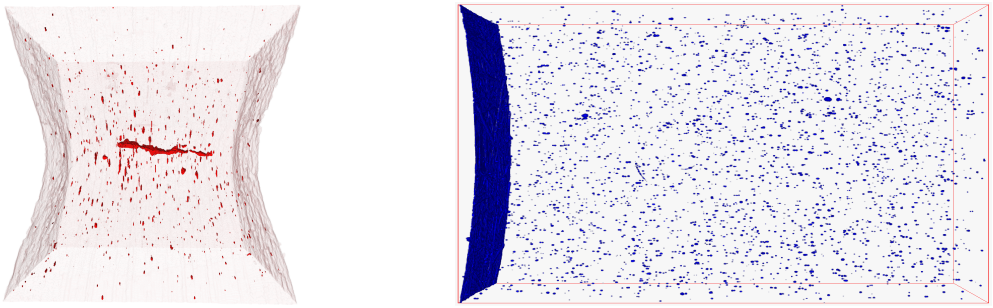

(a) (b)

Figure 2.17 – (a) 3D visualization of damaged FB steel samples (outer shape of specimen appears in gray transparent and cavities in red), (b) 3D visualisation of DP machined edge at initial state (porosity and edge surface appear in blue).

sub-region that undergoes the highest level of stress triaxiality and strain during tensile test [Maire et al., 2008, Landron et al., 2012b]. The stress triaxiality and strain are supposed to be spatially constant inside the central area. Using a plug-in implemented in ImageJ software developed at MATEIS that detects and labels each pore which must be a cluster of at least three connected voxels to be considered. The criterion of 3 connected voxels was used to eliminate noise induced by the experimental technique as porosity. For laminography data, a central area containing the edge surface was chosen to quantify damage evolution during mechanical testing. This sub-region (figure 2.18(b)) was $1200\times300\times300$ μm^3 for FB punched edge, FB and DP machined edges. For DP punched edge the sub-region was $600\times300\times300$ μm^3 due to the presence of laminography artefacts in the center of the volume. Damage evolution during laminography in situ tests was quantified using a Python in-house code consisting in discretization of the studied sub-volumes into boxes of $(50\ \mu m)^3$, in each box the void volume fraction (VVF) is calculated.

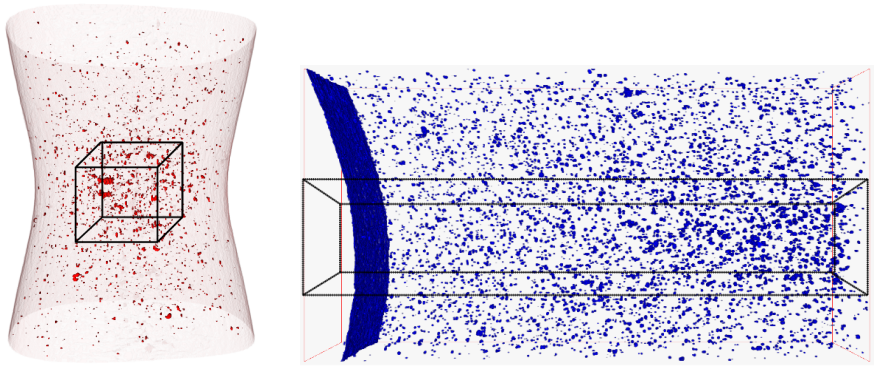

(a) (b)

Figure 2.18 – 3D visualization of chosen volume to quantify damage (a) tomography, (b) laminography

2.3.5 Digital image correlation

The in situ X-ray laminography test was performed with a simple loading device consisting of 2 screws. It does not allow to determine the displacement applied during notch opening. Surface digital image correlation (DIC) was carried out on 2D speckle images taken for each loading step using the software called Correli^{Q4} implemented in Matlab^{TM} in order to measure the displacement and strain fields in the region of interest.

The principle of digital image correlation is the measurement of the displacement field between an image of reference $f(x)$ and a deformed one $g(x)$ considering that each image is a scalar function of the spatial coordinate that is equal to the gray level at each pixel at position x. Knowing $f(x)$ and $g(x)$, the objective is to estimate the displacement field $u(x)$ using some dedicated mathematical algorithms. The reader interested in DIC theory and its extension should refer to [Hild, 2002].

In this correlation code a global approach is used in which the ROI is discretized in four-noded elements rather than in sub-sets as in the local approaches. In the global approach the continuity of the displacement fields is assumed. We used a Basler Pilot (piA2400-17gm) camera in a single shot mode for each load step with an exposure time of 50 ms. The pixel size was 2.59 μm. Between loading steps, images were taken in the region of interest where a spray paint speckle was applied onto the specimen surface. The DIC was performed by updating the reference image and using a mesh with cubic elements of $180\times180\mu m^2$ and a ROI of $2\times4mm^2$ (figure 2.19(a)). An example of typical result obtained from DIC for the DP punched edge at CMOD=2 mm. The DIC results were in good agreement with the displacement extracted from a plane-stress finite element analysis performed using Z-set software on the whole specimen geometry.

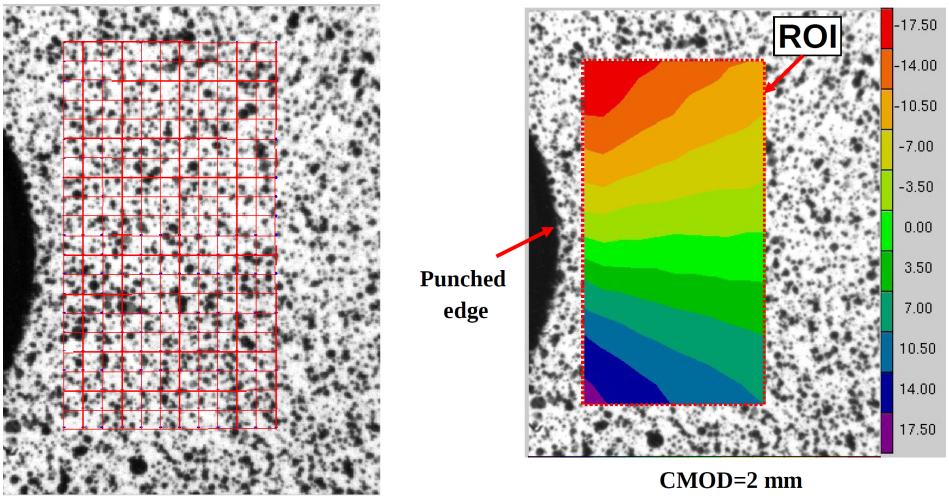

(a) (b)

Figure 2.19 – Digital image correlation using Correli^{Q4} software: (a) initial mesh, (b) example of result obtained for DP punched edge at CMOD= $2mm$

Chapter 3

Ductile damage mechanisms of DP and FB base materials: in situ SEM and X-ray tomography characterization and analytical modeling

Contents

3.1 Résumé

Des essais de traction en MEB in situ, réalisés pour révéler le lien entre la microstructure et les mécanismes d'endommagement, ont montré que, pour l'acier FB l'endommagement a lieu sur les particules de la seconde phase. Pour l'acier DP, des cavités formées sur des particules ont été observées. La rugosité de la surface de l'éprouvette induite par la plasticité rend la visualisation de cavités qui pourraient être formées par décohésion des interfaces ferrite-martensite difficile. Les essais de tomogaphie in situ ont été réalisés afin de caractériser l'évolution de l'endommagement en trois dimensions à une échelle micrométrique dans le volume du matériaux où l'état de la triaxialité de contrainte et la déformation plastique sont plus élevées qu'à la surface. Pour l'acier DP, l'endommagement est allongé suivant la direction L (direction de laminage) quelle que soit la direction de chargement. Lors du chargement suivant la direction T, une cavité sous forme d'aiguille apparait dans la zone centrale de l'éprouvette qui correspondrait à une bande de ségrégation. Pour l'acier FB, lors du chargement suivant la direction L, la coalescence de cavités très allongées suivant la direction du chargement a lieu dans une zone perpendiculaire à la direction de traction. Dans le cas du chargement suivant la direction T, l'acier FB présente une forte tolérance à l'endommagement. La caractérisation MEB des sections de l'éprouvette de tomographie a montré, pour l'acier DP, que l'endommagement est essentiellement dû à la décohésion aux interfaces martensite-ferrite, par contre, pour l'acier FB des cavités de taille inférieure à 1 μm, qui ne sont pas détectables en microtomographie, ont été observées proche de la surface de l'éprouvette. Ces cavités s'amocent sur les carbures.
La quantification des données de tomographie a montré que l'acier DP contient deux fois plus de cavités initiales que l'acier FB et que la densité de cavités augmente clairement lors du chargement mécanique. La fonction de Chu et Needleman [Chu and Needleman, 1980] a été utilisée pour prédire la cinétique de germination de cavités pour les deux matériaux ayant un nombre maximal de sites de germination très différents. Pour la modélisation de la croissance de cavités le modèle de Huang [Huang, 1991] étant une modification du modèle de Rice et Tracey [Rice and Tracey, 1969] a été optimisé. Après avoir identifié des critères de germination et de croissance, la simulation numérique 2D en contraintes planes et les résultats expérimentaux des essais de traction en MEB in-situ ont permis d'identifier une fraction volumique de cavités à coalescence f_c qui est de l'ordre de 0.2% pour les aciers étudiés. Cette fraction critique sera ensuite utilisé pour prédire la coalescence en bords de tôles.

In this chapter the ductile damage mechanisms of the base materials, i.e. dual phase and ferrite-bainite steels are characterized using in situ tensile tests in a scanning electron microscope (SEM) and X-ray synchrotron tomography. This has been carried out in order to characterize the damage behavior and the void nucleation and growth kinetics of these base materials before assessing edge fracture that is even more complex due to the edge predamage and prestrain induced by the punching process. Nucleation and growth mechanisms, in link with the two investigated microstructures, are investigated in quantitative and qualitative ways from the microstructural observations provided by SEM and the 3D data acquired by X-ray tomography during tensile testing. A modeling approach of void nucleation as well as void growth allowing to predict the ductile damage evolution in the investigated steels are discussed hereafter. Void volume fraction at coalescence was determined using X-ray tomography observations for the investigated materials.

3.2 Introduction

The aim of this part is to identify and quantify ductile damage mechanisms of the studied base materials using in situ tensile test in SEM and during X-ray tomography observation. *In situ* tensile tests in SEM, after polishing and 2% nital etching, have been performed in order to understand the link between the damage mechanisms of the studied materials and their microstructures. Specimens geometry and experimental conditions have been described in chapter 2. This SEM technique allows one to visualize the evolution of damage only on specimen surface during mechanical loading with a high resolution which has a different stress state than in the material bulk. Indeed, the specimen surface exhibits a plane stress state. In contrast, due to the necking, the stress triaxiality is increased in the material bulk than on the surface. Synchrotron *in situ* X-ray tomography was used to complete the 2D experimental results provided using *in situ* tensile testing in SEM. 3D volumes of the center of specimens, where the stress state and plastic strain are completely different from those in the specimen surface, were acquired during *in situ* tensile testing using this 3D imaging technique. This has allowed us to assess the evolution of ductile damage in a qualitative and quantitative way during mechanical loading. A polished and 0.2% nital etched cross section of the tested specimens in *in situ* X-ray tomography was observed using SEM in order to characterize damage with a high resolution. These observations allowed us to make a link between damage nucleation and microstructures of the studied materials. Fractography analysis using SEM with different magnifications was performed to observe the fracture surfaces of the two base materials.

3.3 Void nucleation

3.3.1 Qualitative observations

The inclusions characterization of the investigated materials discussed in chapter 2 showed the presence of some inclusions on the observed surface. The particle surface fraction measured for DP and FB steels was 0.07% and 0.03%, respectively. Void nucleation in DP and FB steels is investigated in this section using in situ tensile loading of polished and 0.2% Nital etched sample in a scanning electron microscope. This has allowed us to establish a link between damage evolution in the studied base materials and their microstructures. In order to better understand and quantify damage nucleation in three dimensions in the investigated steels, in situ X-ray tomography observations were performed during tensile testing using sample geometry presented in chapter 2.

In situ tensile test in SEM

in situ tests in the SEM have been carried out to complete the X-ray tomography observations which do not allow to distinguish between the three phases in the studied steels, ferrite/martensite in DP steel and ferrite/bainite in FB steel.

Figure 3.1 shows stress-strain curves for DP and FB steels tested in L and T directions obtained using the recorded load and displacement. To calculate stress and strain plotted in figure 3.1, S_0 is the initial minimal

section (1×0.65 mm^2). In figure 3.1, stars refer to the loading steps of observations during tensile testing. The obtained experimental curves are in acceptable agreement with the 2D plane-stress finite element simulation using elasto-plastic constitutive equations of DP and FB steels that are discussed in chapter 5.

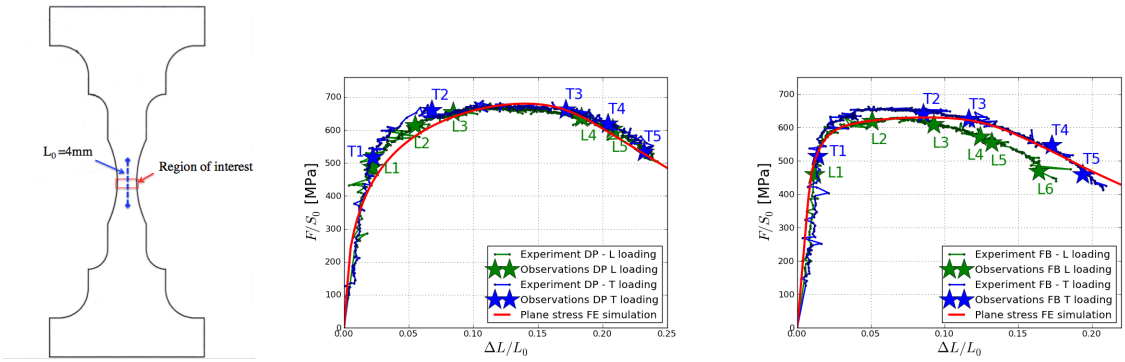

(a) (b) (c)

Figure 3.1 – Stress-strain curves of in-situ tensile tests in a scanning electron microscope: (a) sample geometry showing the location of the region of interest, (b) DP steel, (c) FB steel

- **DP steel**

During tensile loading in scanning electron microscope, observations were performed in the center of specimens. Figure 3.2 shows a region observed on the surface of DP steel specimen loaded in L direction at different loading steps. We observe the dual phase microstructure, i.e. martensite islands in ferritic ductile matrix. Figure 3.2 (L0) which presents the initial state, shows the existence of inclusions on the observed region. During mechanical loading, damage nucleates on these inclusions and grows along the loading direction (figure 3.2 (L3), (L4) and (L5)).

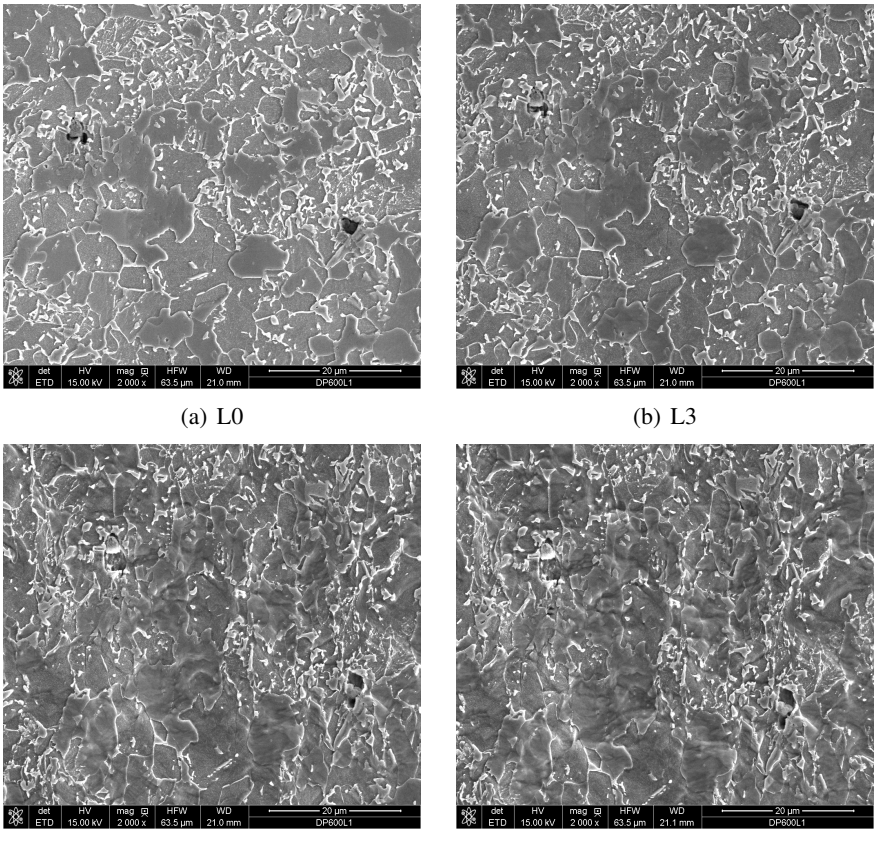

(a) L0 (b) L3

(c) L4 (d) L5

Figure 3.2 – DP steel L loading - SEM micrographs taken during in situ tensile test of DP steel after nital etching loaded in L direction (region 1) - loading direction is vertical

A second region was observed at different loading steps during tensile testing. Figure 3.3 (L1), which is obtained at the end of the elastic regime, presents an initial damage that grows with the applied load along martensite-ferrite interfaces (figure 3.3 (L4) and (L5)).

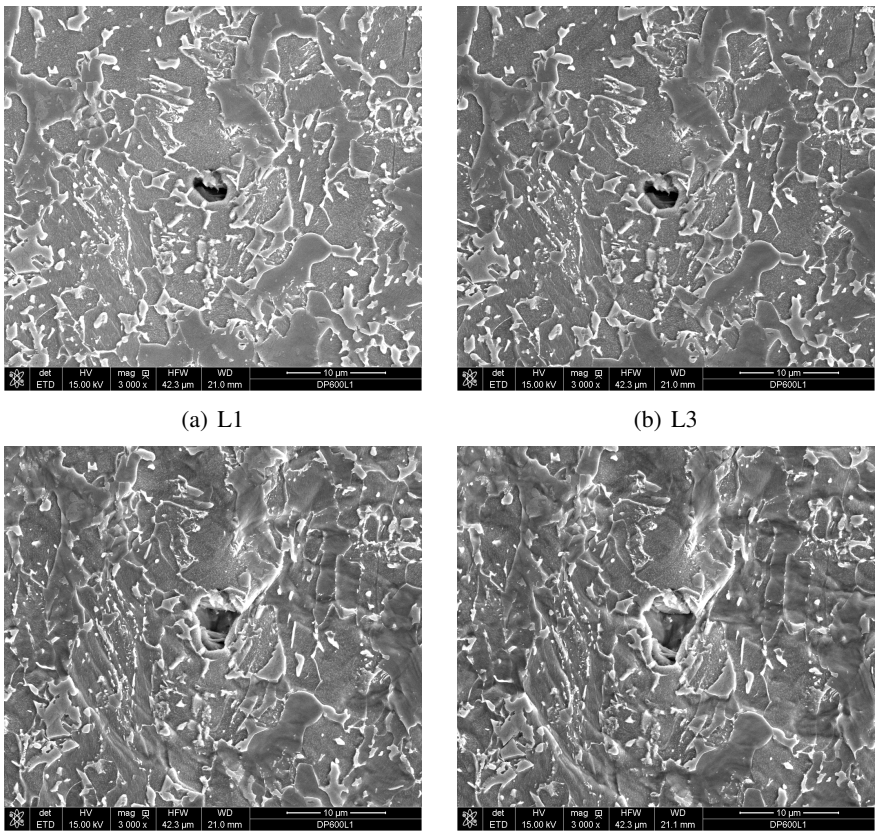

(a) L1 (b) L3

(c) L4 (d) L5

Figure 3.3 – DP steel L loading - SEM micrographs taken during in situ tensile test of DP steel after nital etching loaded in L direction (region 2) - The loading direction is vertical

Two cavities were observed in the region of interest located in the center of the specimen during tensile loading. Figure 3.4(cavity 2) shows that void nucleation occurs on a martensite-ferrite interface due to the presence of an inclusion. The growth of the nucleated void follows the alignment of martensite islands (figure 3.4(T4)).

Due to the surface roughness caused by plasticity it is hard to judge if the nucleation has been in martensite-ferrite interfaces.

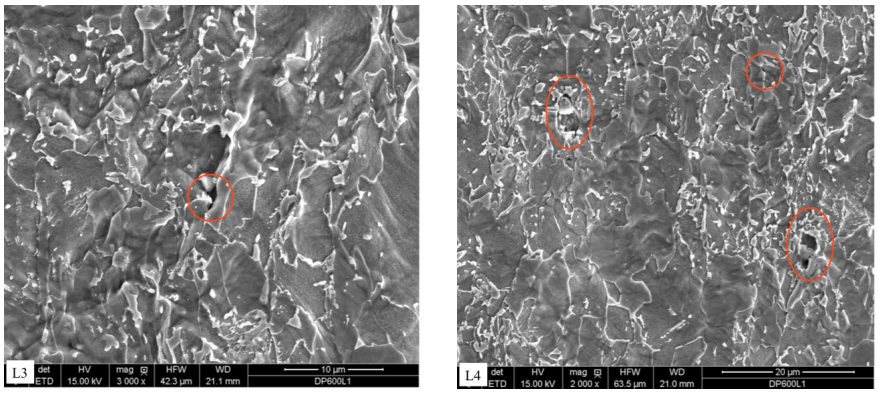

(a) (b)

Figure 3.5 – SEM micrographs taken during in situ tensile test of DP steel after 0.2% Nital etching at two different loading steps (L3) and (L4). The loading direction is vertical

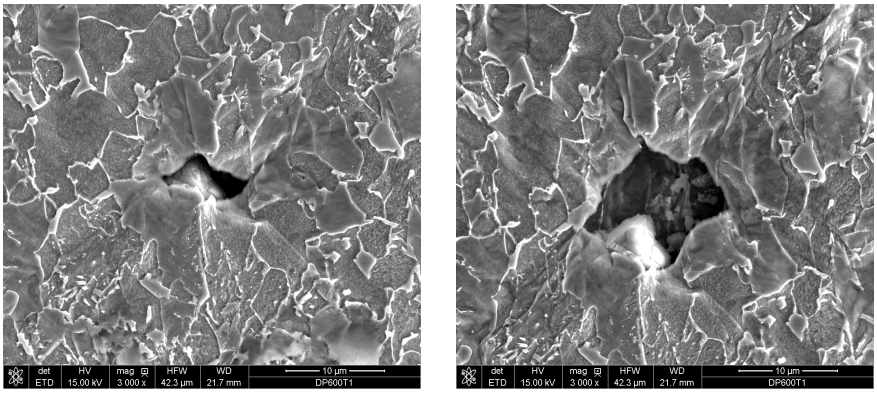

(a) Cavity 1, T3 (b) Cavity 1, T5

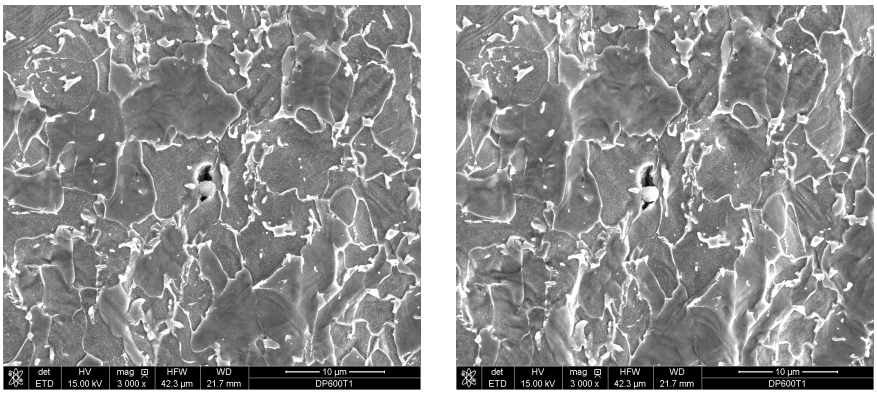

(c) Cavity 2, T2 (d) Cavity 2, T4

Figure 3.4 – DP steel T loading - SEM micrographs taken during in situ tensile test of DP steel after nital etching loaded in T direction - The loading direction is vertical

- **FB steel**

The observations performed on polished and etched surfaces of FB steel specimens for L and T loading directions are given in figures 3.6, 3.7 and 3.8. It is seen that void nucleation in the investigated FB steel is mainly initiated around particles present in this steel grade. For all observed regions of L and T loading directions, we observed the presence of particles at initial state that favor void nucleation. The nucleated voids grow along the loading direction. The third ductile damage stage, i.e. void coalescence was difficult to capture experimentally on the observed specimens.

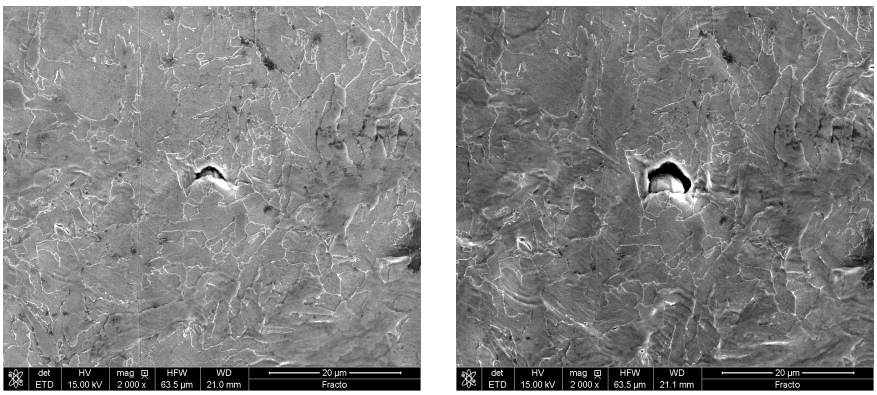

(a) L2 (b) L4

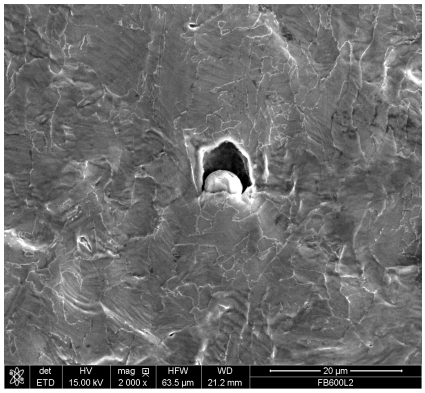

(c) L5

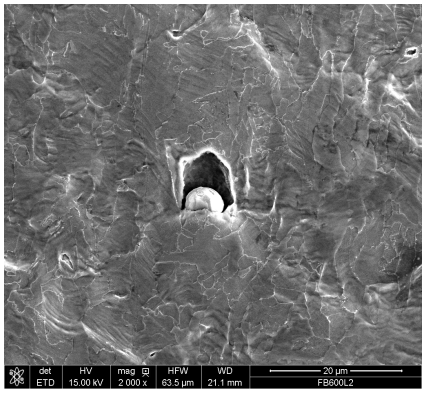

(d) L6

Figure 3.6 – FB steel L loading (cavity 1) - SEM micrographs taken during in situ tensile test of FB steel after nital etching loaded in L direction (cavity 1) - The loading direction is vertical

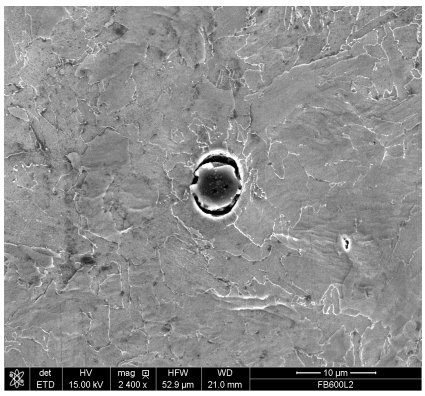

(a) L2

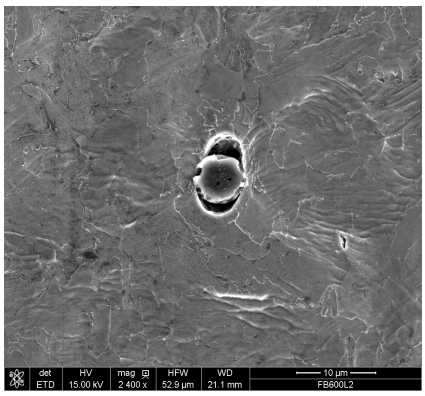

(b) L3

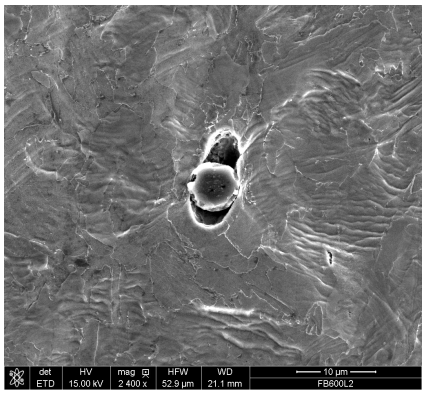

(c) L4

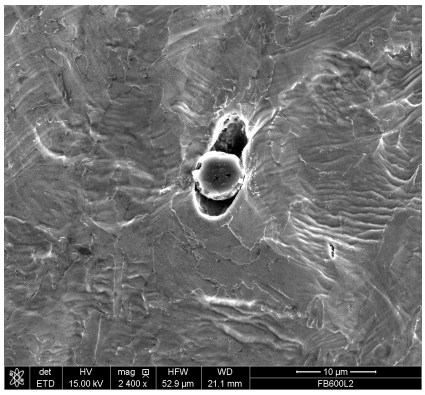

(d) L5

Figure 3.7 – FB steel L loading (cavity 2) - SEM micrographs taken during in situ tensile test of FB steel after nital etching loaded in L direction (cavity 2) - The loading direction is vertical

In situ tensile test during X-ray tomography observations

Figure 3.9 shows stress-strain curves for DP and FB steels loaded at L and T directions. To calculate applied stresses, S_0 and S_{min} are the initial minimal section of the observed specimen and the minimal section in the tomography image for each loading step respectively. The strain was calculated using X-ray tomography data using the following relationship:

$$\varepsilon_{loc} = log\left(\frac{S_0}{S_{min}}\right) \tag{3.1}$$

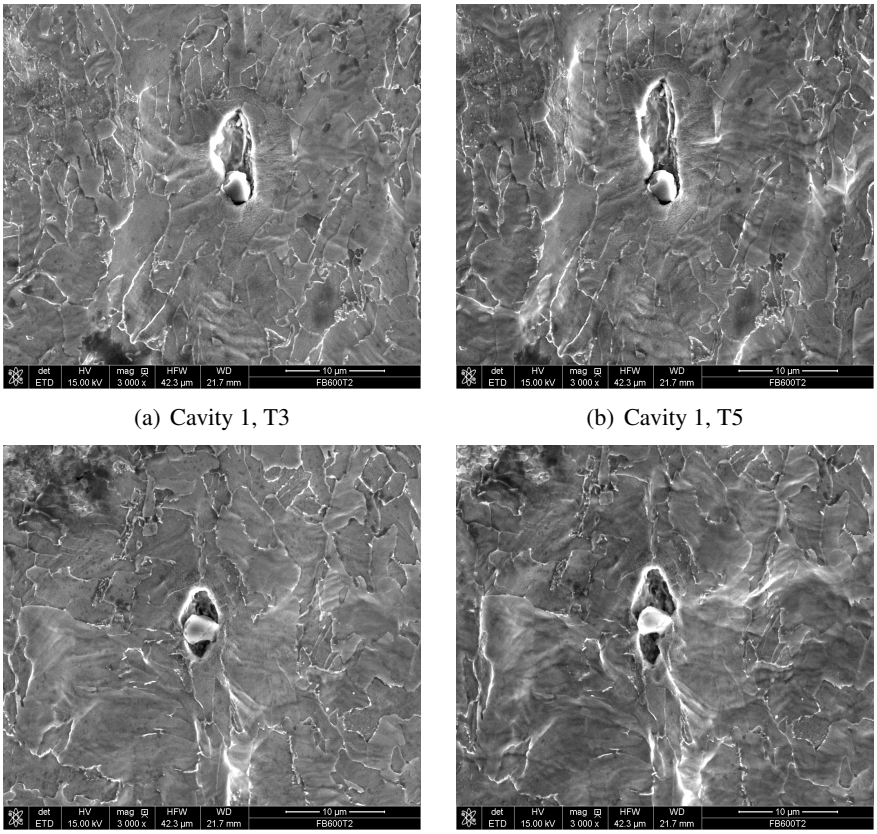

(a) Cavity 1, T3 (b) Cavity 1, T5

(c) Cavity 2, T2 (d) Cavity 2, T4

Figure 3.8 – FB steel T loading - SEM micrographs taken during in situ tensile test of FB steel after nital etching loaded in T direction - The loading direction is vertical

Based on experimental curves plotted in figure 3.9(a) and (b), we observed that the two investigated steels do not present any anisotropy along L and T directions.

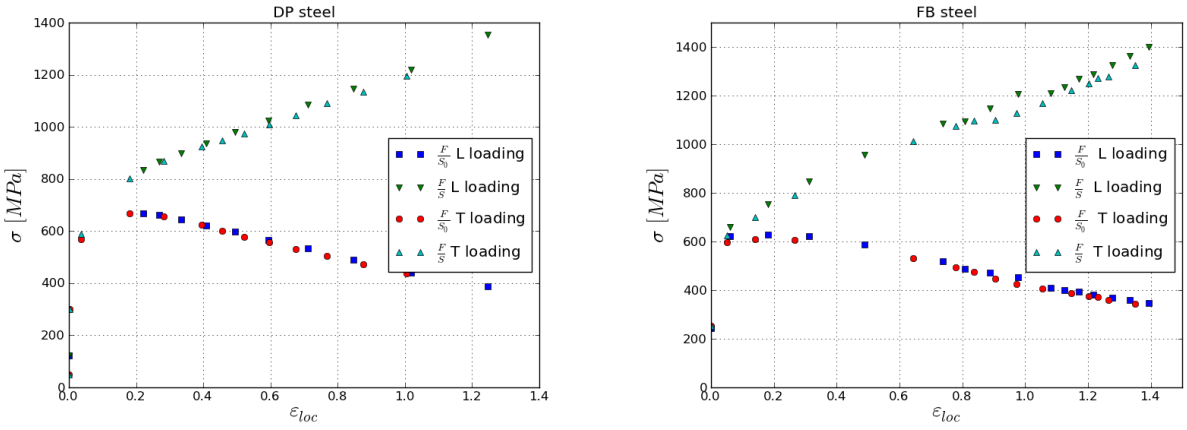

(a) (b)

Figure 3.9 – Stress-strain curves of in-situ tensile testing during X-ray tomography observations of (a) DP steel, (b) FB steel

X-ray synchrotron tomography technique was used in the present work to assess ductile damage mechanisms of DP and FB steels. The reconstructed volumes of the investigated materials acquired during in situ tensile loading are shown in this section. The void nucleation appears higher in the central region where the applied tensile strain and stress triaxiality are increased. These 3D volumes, compared to 2D sections observed on the sample surface during in situ tensile loading in SEM discussed before, show the advantage of X-ray

tomography technique. Indeed, only a few cavities can be seen on the sample surface during tensile loading. This is due to the decreased level of the stress triaxiality and the plastic strain that are known to favor ductile damage.

It is important to notice that the *in situ* tensile tests during X-ray tomography observations were performed using two different voxel size values. The resolution, as discussed in chapter 2, was $(1.34\mu m)^3$ and $(1.095\mu m)^3$ for DP and FB steels, respectively.

3.3.1.1 DP steel

The 3D data acquired during X-ray tomography observations of DP steel tested in the L and T loading directions are given in figures 3.10, 3.11, 3.12 and 3.13. We observe clearly that the number of voids increases with the applied deformation mainly in the region located in the center of specimens.

Comparing data acquired during L and T loading (figure 3.10 and 3.12), we observe that this steel grade presents a damage anisotropy. During L direction loading, the damage growth direction was parallel to the loading direction. In contrast, the damage growth direction was perpendicular to the loading direction during T loading. Indeed, for both loading directions the damage follows the rolling direction, i.e. the alignment of martensite islands, and that the fracture occurs by coalescence of formed void clusters. Voids are elongated normal to the loading direction, in L direction. In the center of the specimen, needle-shape voids with length of several hundreds of micrometers are observed. These are probably linked the central segregation zone. A segregation band was observed in the specimen loaded in the T direction (figure 3.13), it leads to early void coalescence in this band. This coalescence line observed in the DP steel during T direction loading is consistent with the needle-shape voids observed in the studied DP punched edge which is discussed in chapter 4.

DP steel - L loading

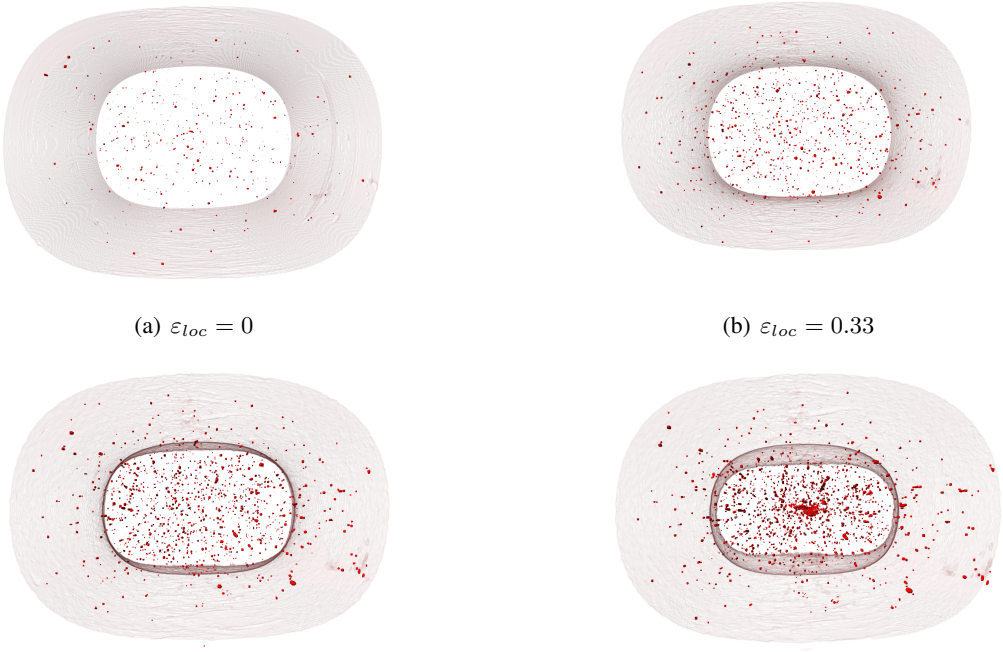

(a) $\varepsilon_{loc} = 0$ (b) $\varepsilon_{loc} = 0.33$

(c) $\varepsilon_{loc} = 0.85$ (d) $\varepsilon_{loc} = 1.25$

Figure 3.11 – X-ray tomography observations of DP steel loaded at L direction. The loading direction is perpendicular to projection views. Rendered voids are shown in red. The sample surface is made half-transparent.

DP steel - L loading

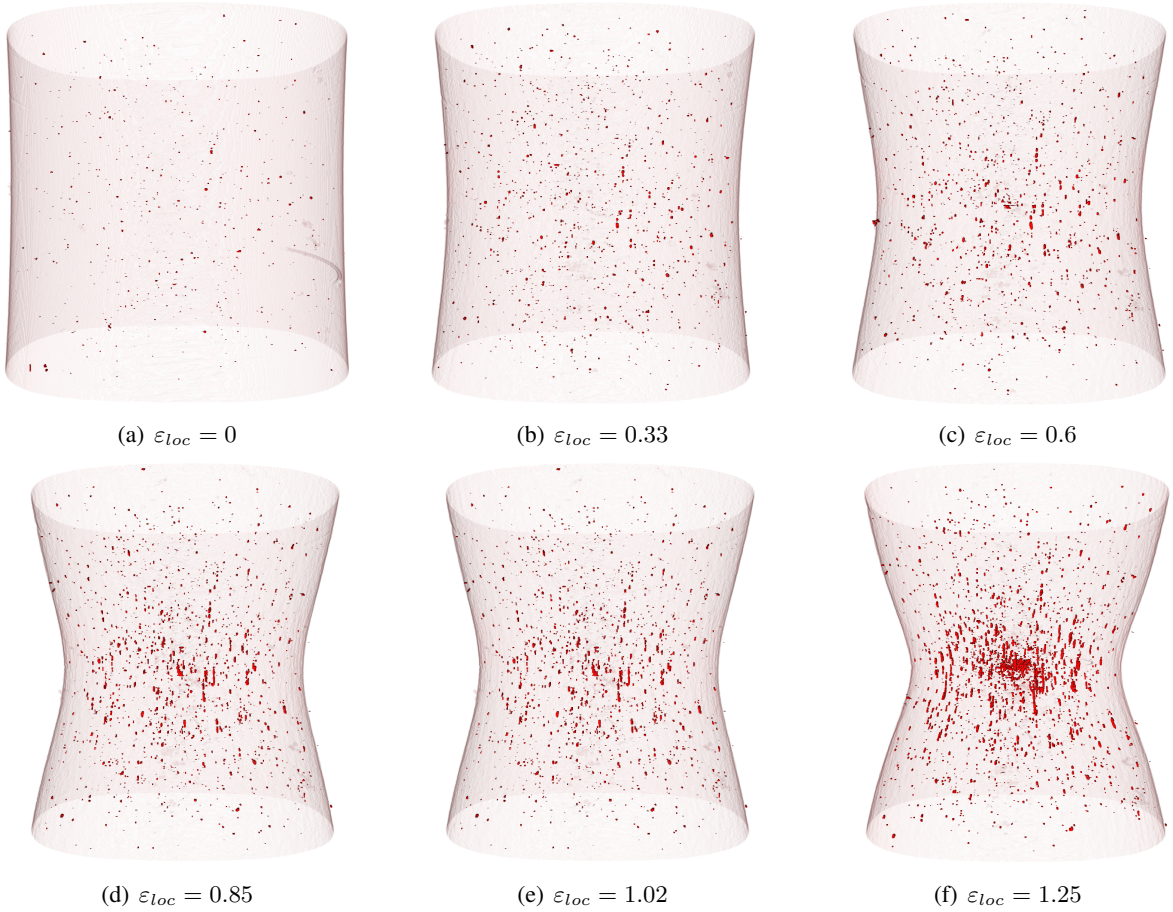

(a) $\varepsilon_{loc} = 0$ (b) $\varepsilon_{loc} = 0.33$ (c) $\varepsilon_{loc} = 0.6$

(d) $\varepsilon_{loc} = 0.85$ (e) $\varepsilon_{loc} = 1.02$ (f) $\varepsilon_{loc} = 1.25$

Figure 3.10 – X-ray tomography observations of DP steel in the L loading direction. The loading direction is vertical and the height of the observed sub-volume is 1 mm. Rendered voids are shown in red. The sample surface is made half-transparent.

DP steel - T loading

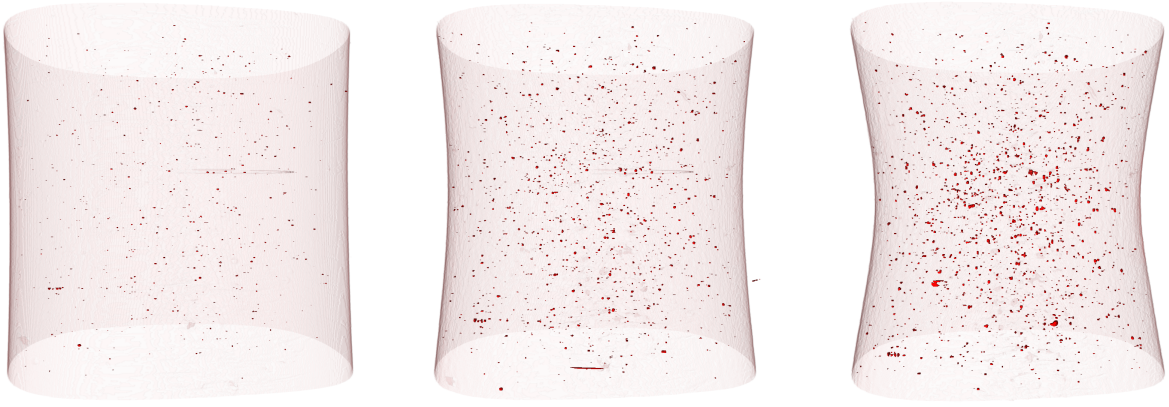

(a) $\varepsilon_{loc} = 0$ (b) $\varepsilon_{loc} = 0.28$ (c) $\varepsilon_{loc} = 0.52$

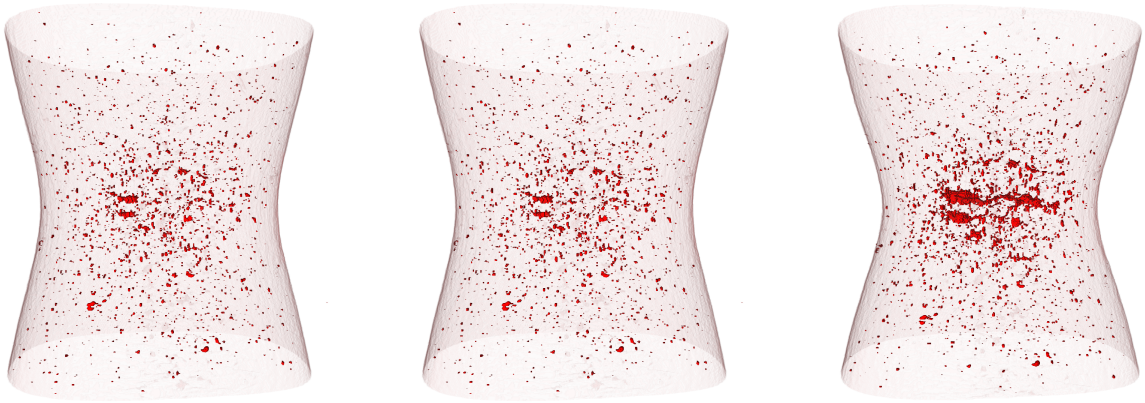

(d) $\varepsilon_{loc} = 0.77$ (e) $\varepsilon_{loc} = 0.85$ (f) $\varepsilon_{loc} = 1.00$

Figure 3.12 – X-ray tomography observations of DP steel in the T loading direction. The loading direction is vertical and the height of the observed sub-volume is 1 mm. Rendered voids are shown in red. The sample surface is made half-transparent.

DP steel - T loading

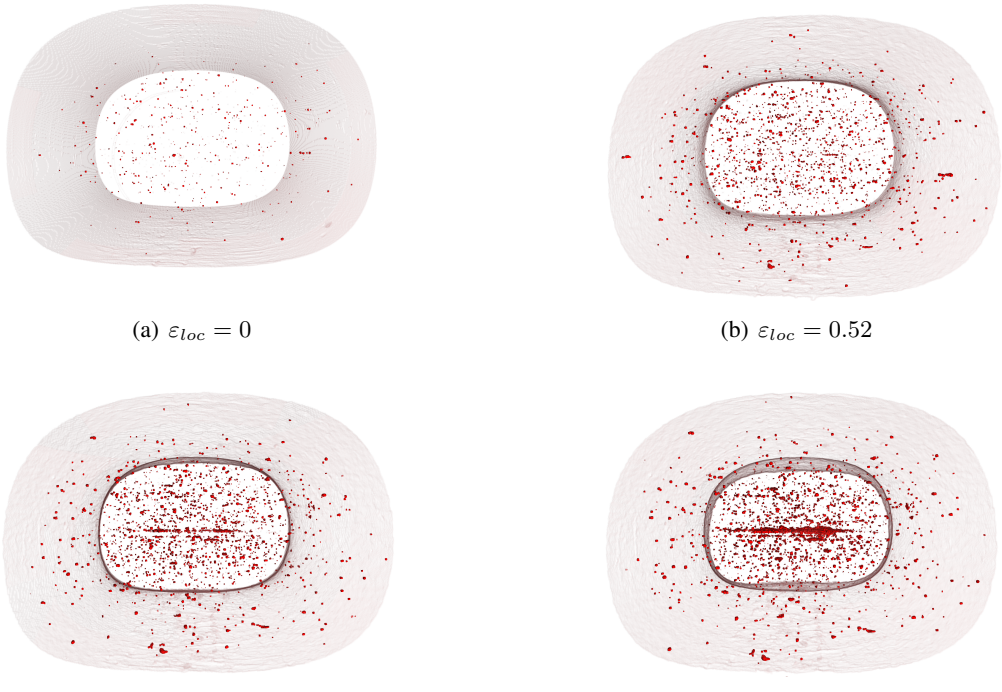

(a) $\varepsilon_{loc} = 0$ (b) $\varepsilon_{loc} = 0.52$

(c) $\varepsilon_{loc} = 0.77$ (d) $\varepsilon_{loc} = 1.00$

Figure 3.13 – X-ray tomography observations of DP steel loaded in the T direction. The loading direction is perpendicular to the figure plane. Rendered voids are shown in red. The sample surface is made half-transparent.

SEM observations have been carried out in order to better understand the link between damage nucleation and the DP microstructure. These observations allowed us to characterize the material bulk that undergoes an increased plastic strain and stress triaxiality compared to the sample surface. Figure 3.14 shows SEM micrographs at different magnifications taken at a cross section of the fractured DP steel specimen observed using X-ray tomography after polishing and 0.2% nital etching. Using SEM observations with such high resolution, we were able to visualize damage which is not detectable via X-ray tomography technique which allows in our case to visualize only damage with an equivalent diameter of at least $2.68\mu m$. The damage observed is essentially due to the decohesion at martensite-ferrite interfaces. Some fractured martensite islands have been observed (see 3.14(d) and (e)). This is consistent with the findings that have already been

widely discussed in the literature (see [Landron et al., 2010, Azuma et al., 2012, Avramovic-Cingara et al., 2009a] and others).

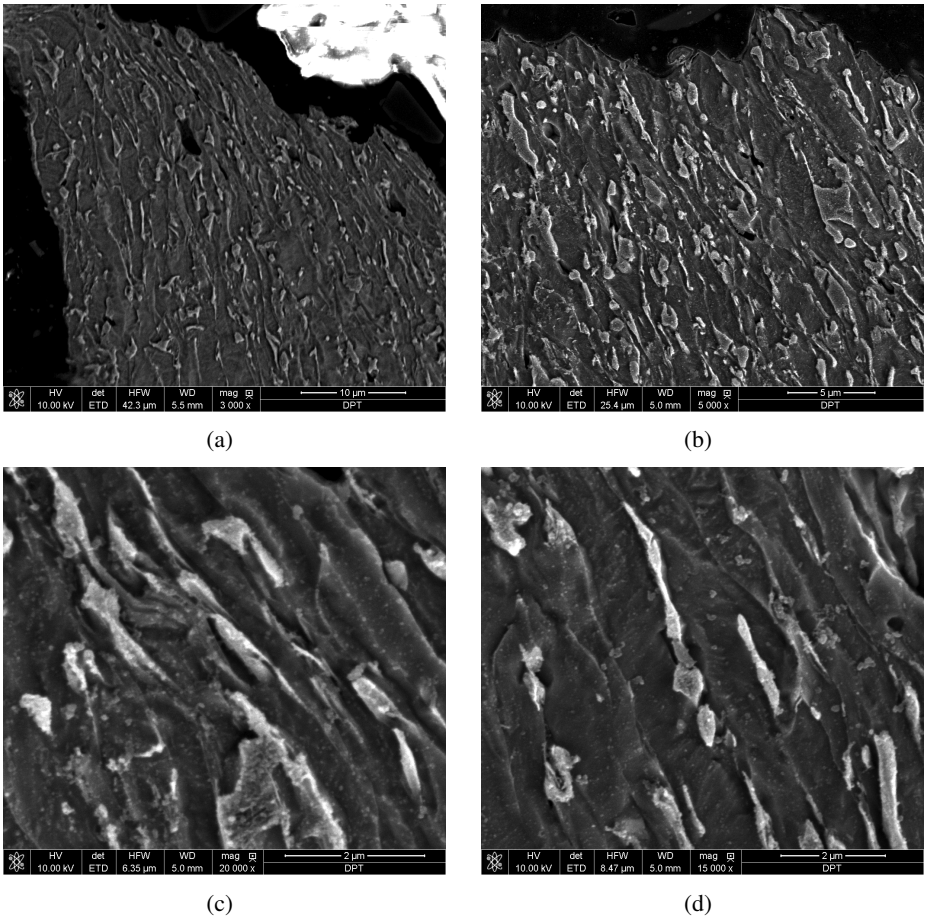

(a) (b)

(c) (d)

Figure 3.14 – SEM micrographs taken at cross section of the observed DP steel using X-ray tomography after 0.2% Nital etching loading. The loading direction is vertical.

3.3.1.2 FB steel

X-ray tomography data acquired during tensile loading of FB steel in the L and T loading directions are shown in figures 3.15 and 3.17. The used specimens for L and T loading directions present initially a rectangular section. The sub-volume shown in figures 3.15 and 3.17 is taken from the center of the imaged specimens. For L and T loading directions, we observe clearly that the number of voids increases with the applied deformation.

The data acquired during L and T loading show that the studied FB steel exhibits a damage anisotropy. For the L loading , we observe that the damage follows the loading direction. However, during T loading the damage coalescence direction is perpendicular to the loading direction. Indeed, the damage follows the rolling direction, i.e. the alignment of bainitic grains.

In figure 3.15 we observe a void elongation in the loading direction during mechanical loading. The void coalescence during loading is normal to the loading direction in regions without micrometre particles.

The 3D volumes presented in 3.16 are the same as those given in figure 3.15 but seen from the side of the loading direction. These 3D volumes show that the damage is higher in the central region of the specimen which may be a segregation line. We also observe in these volumes the increased necking that undergoes the specimen without failure.

During T loading (see figure 3.17), void elongation in the loading direction can be observed at increased local deformation values. A needle-shape void normal to the loading direction can be seen at $\varepsilon_{loc} = 1.07$. The growth direction of this needle-shape void is normal to the loading direction. A very long void nucleated

normal to the loading direction along the L direction (about 400 μm) that is probably linked to a central segregation zone. The 3D volumes given in figure 3.16 show the high damage tolerance that exhibit the studied FB steel. Indeed, the FB steel is tolerant to this kind of large damage feature as the specimen did not fail even when large fractions of the minimal section are covered by the large void.

Using X-ray tomography technique, we are not able to judge if the observed void nucleated on carbides or on inclusions.

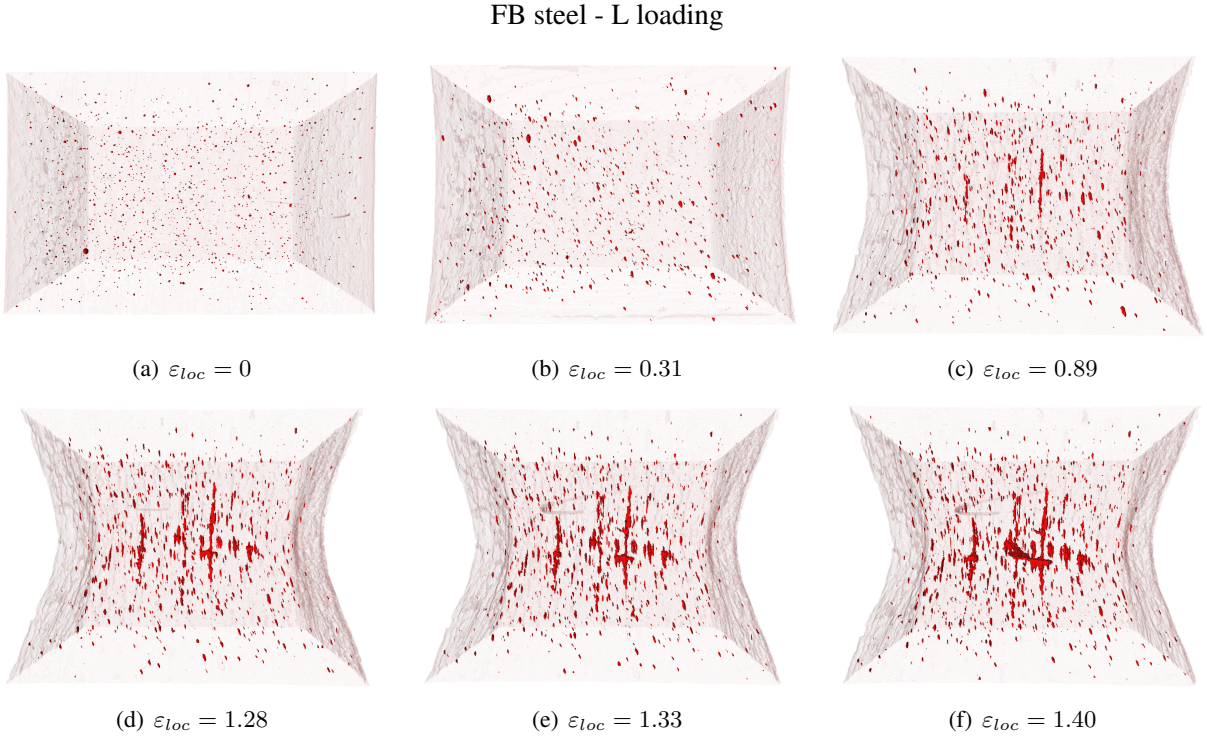

(a) $\varepsilon_{loc} = 0$ (b) $\varepsilon_{loc} = 0.31$ (c) $\varepsilon_{loc} = 0.89$

(d) $\varepsilon_{loc} = 1.28$ (e) $\varepsilon_{loc} = 1.33$ (f) $\varepsilon_{loc} = 1.40$

Figure 3.15 – X-ray tomography observations of FB steel in the L loading direction. The loading direction is vertical and the height of the observed sub-volume is 660 μm

SEM observations at cross sections of tomography specimens after polishing and 0.2% etching have been carried out in order to identify damage nucleation sites in the investigated materials. These observations allowed us to characterize the material bulk that undergoes an inceased plastic strain and stress triaxiality compared to the sample surface. The SEM micrographs taken at the polished and etched cross section of the tested FB steel specimen at L direction are given in fig. 3.19. In this imaged section using small magnifications (400× in fig. 3.19(b)), we observe the increased growth following the loading direction that occurs for voids nucleated on particles. However, at higher magnifications (2000×, 5000× and 10000× in 3.19(c), (d) and (e), respectively), fracture of carbides and decohesion of carbides-particles/ferrite interfaces have been observed. The observed damage in this imaged cross section is aligned following the loading direction (i.e. the rolling direction). X-ray tomography technique used for this study with a spatial resolution of 1.095μm, is not able to detect these small voids nucleated due to the carbides fracture and at carbides-ferrite interfaces. These results are consistent with those found on SEM micrographs of a FB600 steel during hole expansion test by Choi and co-workers [Cho et al., 1999b].

3.3.2 Quantification of void nucleation

For each loading step, a sub-volume was cropped in the central region of the sample to quantify the void nucleation. Using the quantification criterion described in chapter 2 supposing that a cavity must be a cluster of at least three connected voxels to be taken in consideration, the number of cavities was counted in the studied sub-volume for each loading step and the void density was counted as follows:

$$\frac{N_i}{N_0} = \frac{number\ of\ cavities\ at\ the\ state\ i}{number\ of\ cavities\ at\ the\ initial\ state} \tag{3.2}$$

FB steel - L loading

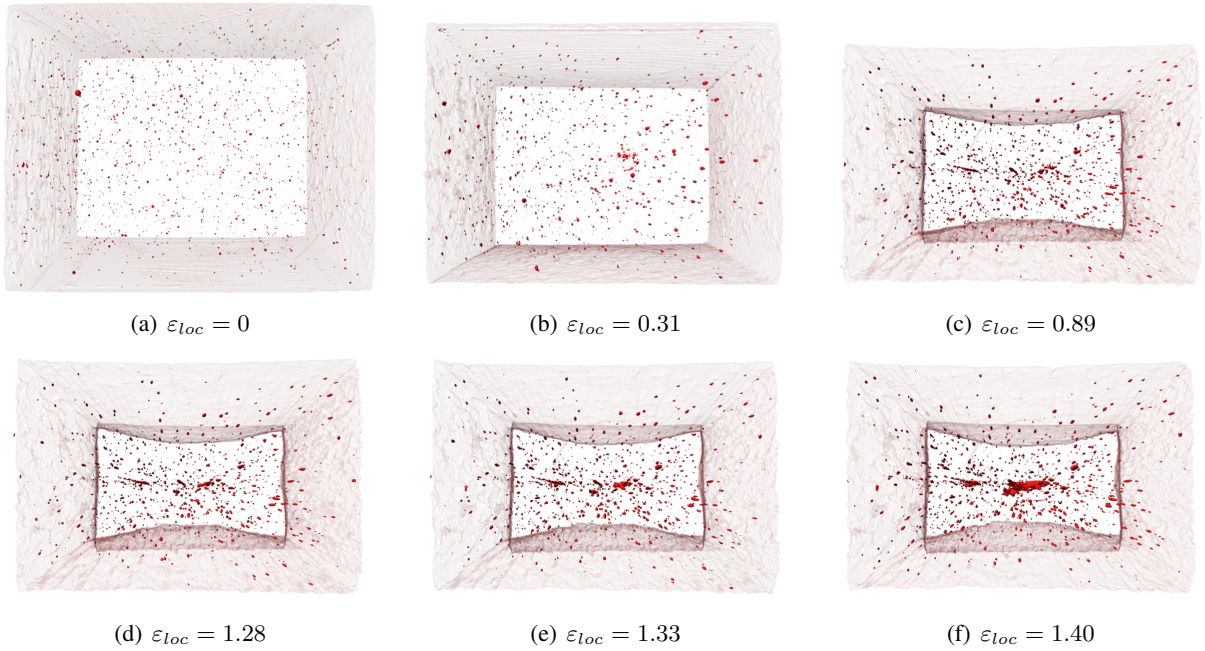

(a) $\varepsilon_{loc} = 0$ (b) $\varepsilon_{loc} = 0.31$ (c) $\varepsilon_{loc} = 0.89$

(d) $\varepsilon_{loc} = 1.28$ (e) $\varepsilon_{loc} = 1.33$ (f) $\varepsilon_{loc} = 1.40$

Figure 3.16 – X-ray tomography observations of FB steel loaded in the L direction. The loading direction is perpendicular to the figures plane. Rendered voids are shown in red. The sample surface is made half-transparent.

FB steel - T loading

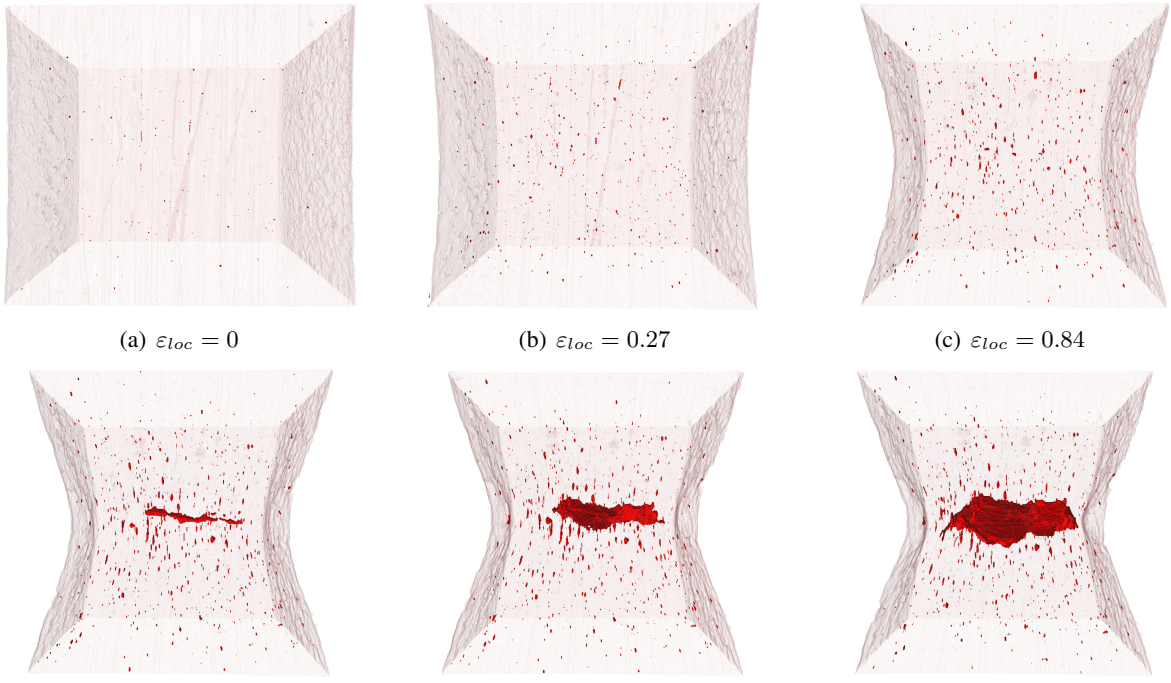

(a) $\varepsilon_{loc} = 0$ (b) $\varepsilon_{loc} = 0.27$ (c) $\varepsilon_{loc} = 0.84$

(d) $\varepsilon_{loc} = 1.07$ (e) $\varepsilon_{loc} = 1.27$ (f) $\varepsilon_{loc} = 1.35$

Figure 3.17 – X-ray tomography observations of FB steel in the T loading. The loading direction is vertical and the height of the observed sub-volume is 880 μm

The evolution of void density as function of the applied tensile strain is shown in figure 3.20 for the investigated steels loaded in L and T directions. From these quantitative data, some remarks on void nucleation mechanism in the investigated materials can be made:

- Void nucleation kinetic depends highly on the microstructure.

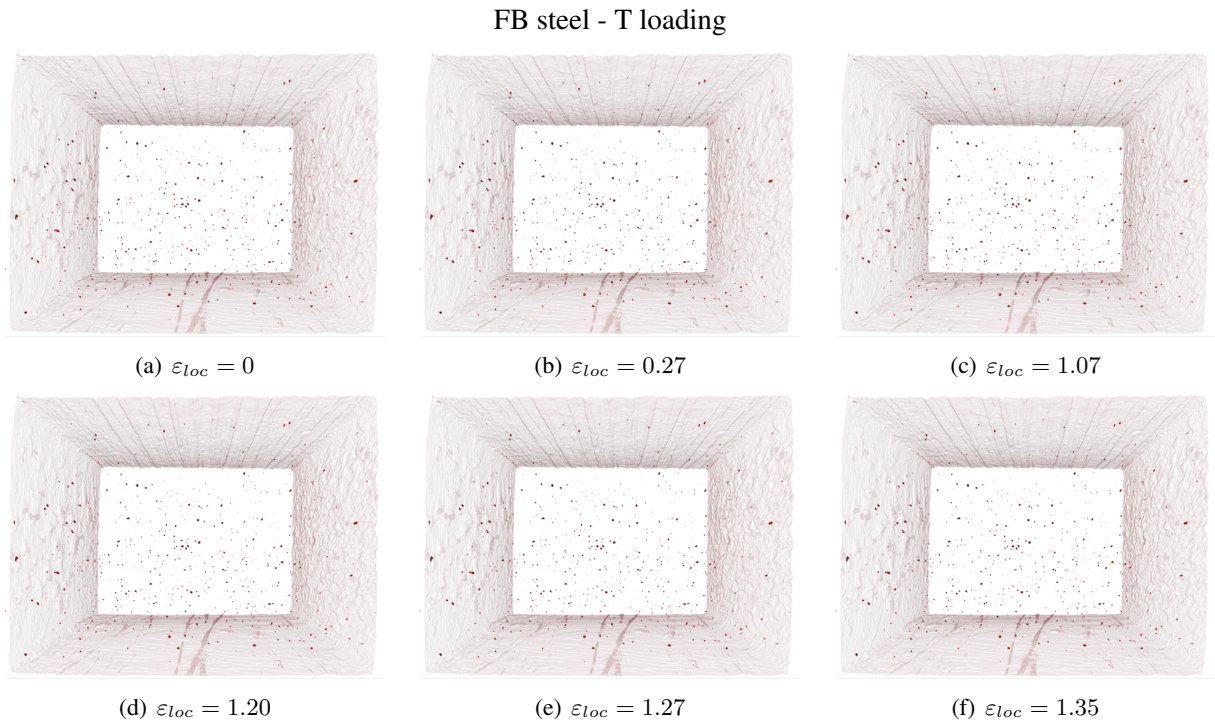

(a) $\varepsilon_{loc} = 0$ (b) $\varepsilon_{loc} = 0.27$ (c) $\varepsilon_{loc} = 1.07$

(d) $\varepsilon_{loc} = 1.20$ (e) $\varepsilon_{loc} = 1.27$ (f) $\varepsilon_{loc} = 1.35$

Figure 3.18 – X-ray tomography observations of DP steel loaded at T direction. The loading direction is perpendicular to projection views. Rendered voids are shown in red. The sample surface is made half-transparent.

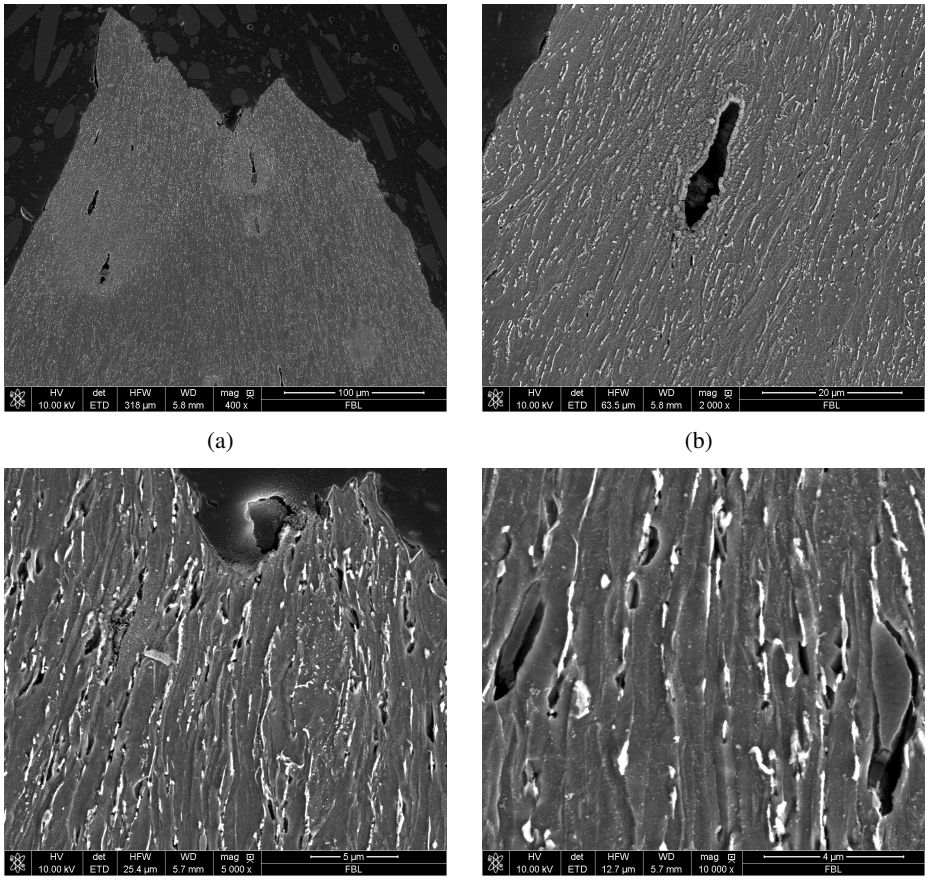

(a) (b)

(c) (d)

Figure 3.19 – SEM micrographs taken at cross section of the observed FB steel using X-ray tomography after 0.2% Nital etching loading. The loading direction is vertical.

- The void density during tensile test seems to be similar for the studied DP and FB steels.

The density of cavities clearly increases with the applied deformation for DP and FB steels at L and T loading directions. It is consistent with the results previously found in [Maire et al., 2008,Landron et al., 2010]. There are may be more voids that are not detectable in our experiments. It has been experimentally proved using X-ray tomography that the spatial resolution has a significant influence on damage quantification [Landron et al., 2011a].

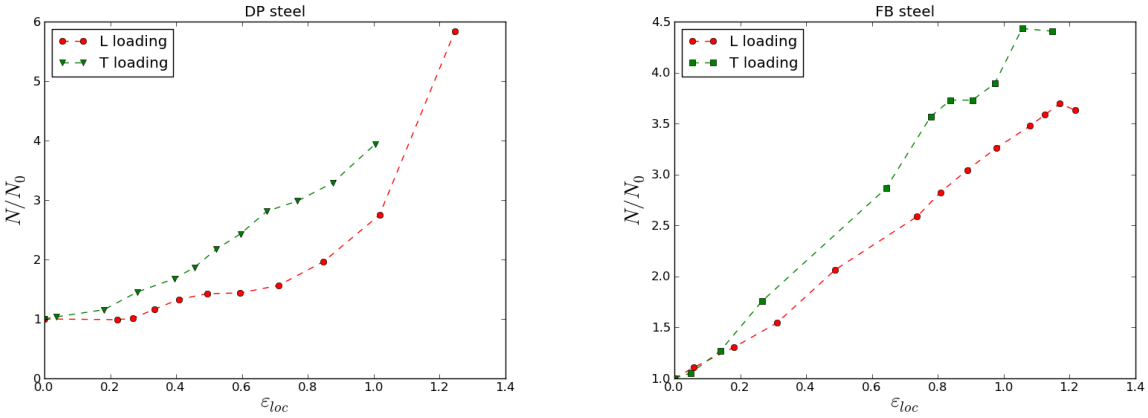

(a) (b)

Figure 3.20 – Evolution of void density with the applied tensile strain for DP and FB steels

3.3.3 Modeling of void nucleation

To model void nucleation in DP and FB steels, Chu and Needleman criterion was selected [Chu1980]. The identification of Chu and Needleman parameters was performed using the X-ray tomography data of DP an FB steels at L loading direction. Chu and Needleman criterion is given in equation 3.3

$$\frac{\mathrm{d}N}{\mathrm{d}\varepsilon} = f\left(\varepsilon_p^{eq}\right) \tag{3.3}$$

with

$$f\left(\varepsilon_p^{eq}\right) = \frac{\psi}{\sqrt{2\pi}\, s_N} \exp\left(-\frac{1}{2}\left(\frac{\varepsilon_p^{eq} - \varepsilon_N}{s_N}\right)^2\right) \tag{3.4}$$

Supposedly the nucleation strain is distributed in a normal fashion. ε_p^{eq} is the equivalent plastic strain, ε_N is the critical strain for void nucleation and s_N is the standard deviation. ψ is determined so that the total void volume nucleated is consistent with nucleation sites density.

The integrated relationship is given in equation (3.5)

$$N\left(\varepsilon_p^{eq}\right) = N_0 + \frac{\psi}{2}\left(erf\left(\frac{\varepsilon_p^{eq} - \varepsilon_N}{\sqrt{2}s_N}\right) - erf\left(\frac{-\varepsilon_N}{\sqrt{2}s_N}\right)\right) \tag{3.5}$$

Where N_0 is the initial void volume fraction and erf is the error function defined as follows:

$$erf\,(x) = \frac{2}{\sqrt{\pi}} \int_0^x e^{-t^2}\, dt \tag{3.6}$$

Maximum void volume fraction N_{max} is thus deduced from the equation (3.5)

$$N_{max} = N_0 + \frac{\psi}{2}\left(1 - erf\left(\frac{-\varepsilon_N}{\sqrt{2}s_N}\right)\right) \tag{3.7}$$

The density of cavities plotted in figure 3.21 can be calculated using the following relationship:

$$\frac{N\left(\varepsilon_p^{eq}\right)}{N_0} = 1 + \frac{\psi}{2\,N_0}\left(erf\left(\frac{\varepsilon_p^{eq} - \varepsilon_N}{\sqrt{2}s_N}\right) - erf\left(\frac{-\varepsilon_N}{\sqrt{2}s_N}\right)\right) \tag{3.8}$$

For DP steel, ψ was identified so that the total void density nucleated is consistent with martensite islands density which is about $10^6\ \mu m^{-3}$ assuming that the volume is compact. For FB steel, ψ was identified so that the normalized maximal density of cavities is consistent with the saturation level observed on experimental data. We notice that the initial void density N_0 has been measured on tomography data using the analyzed sub-volumes at the initial state.

Table 3.1 – Identified parameters of Chu and Needleman model for DP and FB steels.

Steel	$N_0\ [mm^{-3}]$	$\psi\ [mm^{-3}]$	ε_N	s_N
DP	6500	1.2 10^6	2.57	0.62
FB	3000	10^4	0.64	0.47

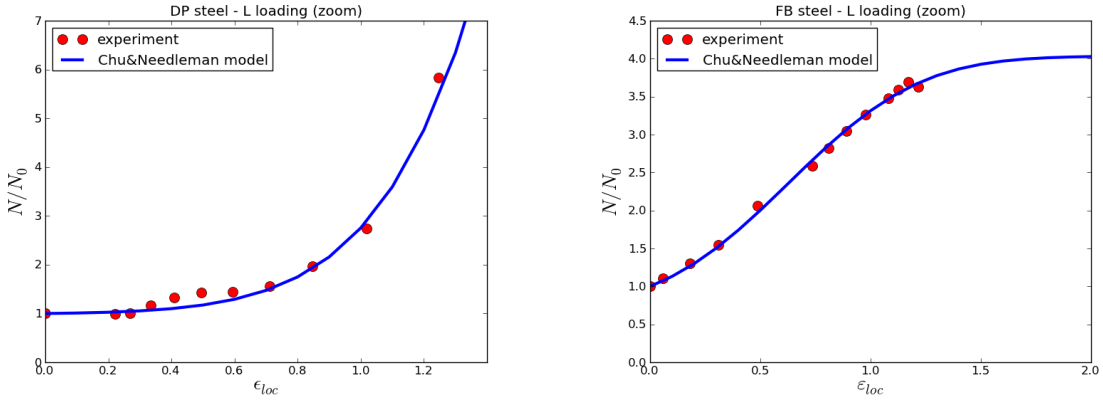

(a) (b)

Figure 3.21 – Comparison of the prediction of the nucleation model using Chu and Needleman criterion and experimental data acquired during in situ tensile test of a DP and FB steels at L loading direction

3.4 Void growth

The second stage of ductile damage process is the void growth. During mechanical loading, after nucleation, cavities instantly start to grow mainly in the loading direction. The quantification of void growth in DP and FB steels is carried out in this section using 3D data provided by X-ray tomography technique. The Huang model [Huang, 1991] was selected to predict void growth mechanism in the investigated DP and FB steels.

3.4.1 Quantification of void growth

Assuming that voids that are assumed here as clusters of at least 3 connected voxels, have a spherical shape, the equivalent diameter of each void was calculated. Tracking cavities from one loading step to the next can be achieved automatically when the number of cavities is constant. This technique has been used in [Toda et al., 2011] to quantify damage growth with the applied deformation. In this study, we used the same strategy described in [Landron et al., 2011b, Maire et al., 2008] which consist in the measurement of the size of the N largest cavities of a population assuming that the N largest cavities remain the same at each loading step,

to quantify the void growth. A quantification of void growth for the largest cavities and their evolutions were compared to the evolution of entire void population.

Using this quantification strategy the evolution of the equivalent diameter of N largest cavities (N=5; 10 and 20) is compared to the equivalent diameter of the entire population. Using the evolution of the normalized equivalent diameter of voids (figure 3.22) with the applied strain, void nucleation, void growth and void coalescence mechanisms can be detected. Void nucleation starts when the equivalent diameter of N largest cavities becomes bigger than the one of the entire population. Void growth regime can be observed after void nucleation regime when the equivalent diameter of the 20, 10 and 5 largest cavities increases with the same rate. The rate becomes higher close to the end of the tensile test. Void coalescence leading to the fracture of the sample starts when void growth per strain increment becomes higher for 5 largest cavities than for 10 and 20 largest cavities.

Figure 3.23 shows the results obtained for DP and FB steels for the two tested directions. It is important to notice that void growth is strongly dependent on the stress triaxiality. Indeed, increased level of stress triaxiality is known to be an accelerator of void growth. During mechanical loading, the stress triaxiality increases when the necking becomes higher.

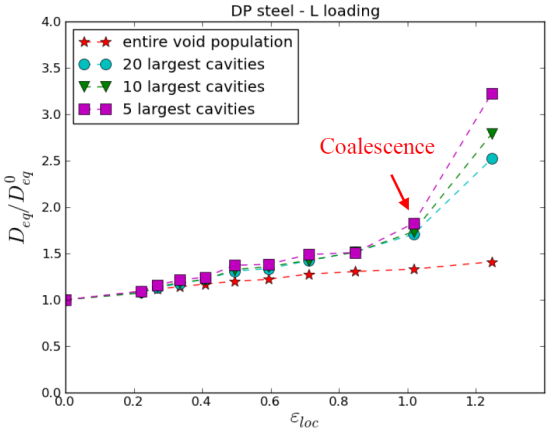

Figure 3.22 – Comparison of evolution of 5, 10 and 20 largest cavities with the entire void population of DP steel in the L loading direction

Comparing the evolutions of the measured average void equivalent diameter of the entire void population for the studied materials, we observe that for the DP steel it remains relatively constant. In contrast, for the FB steel it increases with the applied strain. This means that there was less void nucleation in the FB steel. At increased local strain values, the difference between the evolution of largest cavities and the entire void population equivalent diameter is more increased for the DP steel at both loading directions compared to the FB steel.

The table 3.2 gives the initial void radii of the studied materials. These values were measured using X-ray tomography data of the base material before any mechanical loading.

Table 3.2 – Measured average void size R_0 using X-ray tomography data at initial state for the investigated materials

Steel	DP	FB
R_0 [μm]	2.4	2.5

Figures 3.24(a) and (b) give the distributions of void size of the studied materials at the initial state and after deformation. For the investigated DP steel, we observe that small cavities (diameter about 5 μm) are the majority at the deformed state for the two tested directions. This is consistent with the quantitative X-ray results for a DP steel grade found by Landron and co-workers (Landron2011). These results confirm that, during mechanical loading, voids in the studied DP steel nucleate until macro coalescence. However, the void

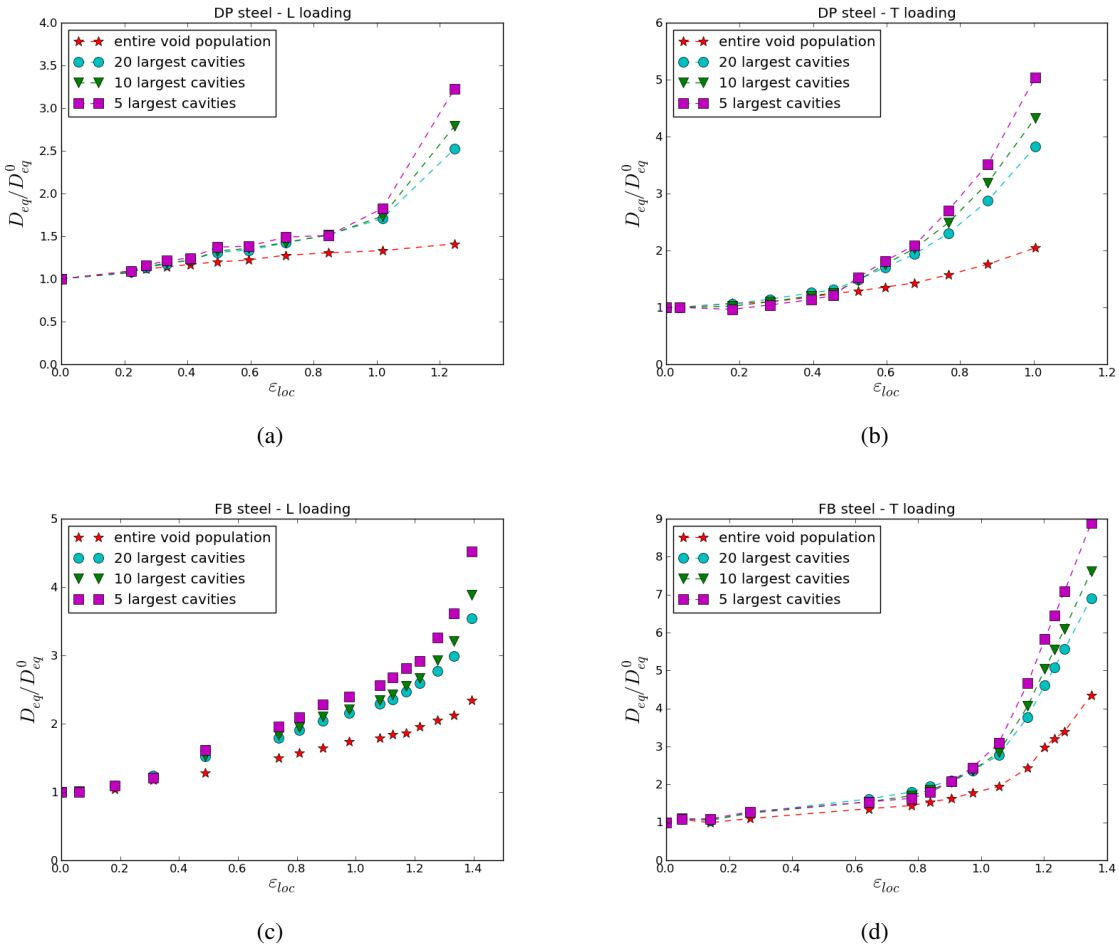

Figure 3.23 – Evolution of the normalized equivalent diameter of the entire void population, 50 largest cavities, 20 largest cavities and 10 largest cavities measured for DP steel using the experimental data provided by using X-ray tomography: (a) DP L loading, (b) DP T loading, (c) FB L loading, (d) FB T loading

size distributions of the analyzed sub-volumes (initial state and $\varepsilon_{loc} = 1.$) of FB steel given in fig. 3.24(c) and (d) show that only few small cavities are detected at the deformed state ($\varepsilon_{loc} = 1.$). At this state, void size is distributed in a normal fashion around $D_{eq} = 7\mu m$.

These quantitative analysis are highly dependent of the spatial resolution used (1.095 and 1.34 for FB and DP steel, respectively).

3.4.2 Modeling of void growth

To predict void growth mechanism for the investigated DP and FB steels, the model of Huang was selected [Huang, 1991]. Huang's prediction is an extension of Rice and Tracey model that allows to improve the void growth prediction for low stress triaxiality levels. The proposed modification of Rice and Tracey model is given in equation (3.9)

$$\text{for } T \leq 1 \qquad \frac{\mathrm{d}R}{R} = 0.427\, T^{1/4} \exp\left(\frac{3}{2} T\right) \mathrm{d}\varepsilon_p \tag{3.9}$$

It consists in predicting the evolution of the void growth of a spherical void with the stress triaxiality and the equivalent plastic strain by calculating the pre-exponential term which is dependant on the stress triaxiality T.

$$\frac{\mathrm{d}R}{R} = \alpha_H\, T^{1/4} \exp\left(\frac{3}{2} T\right) \mathrm{d}\varepsilon_p \tag{3.10}$$

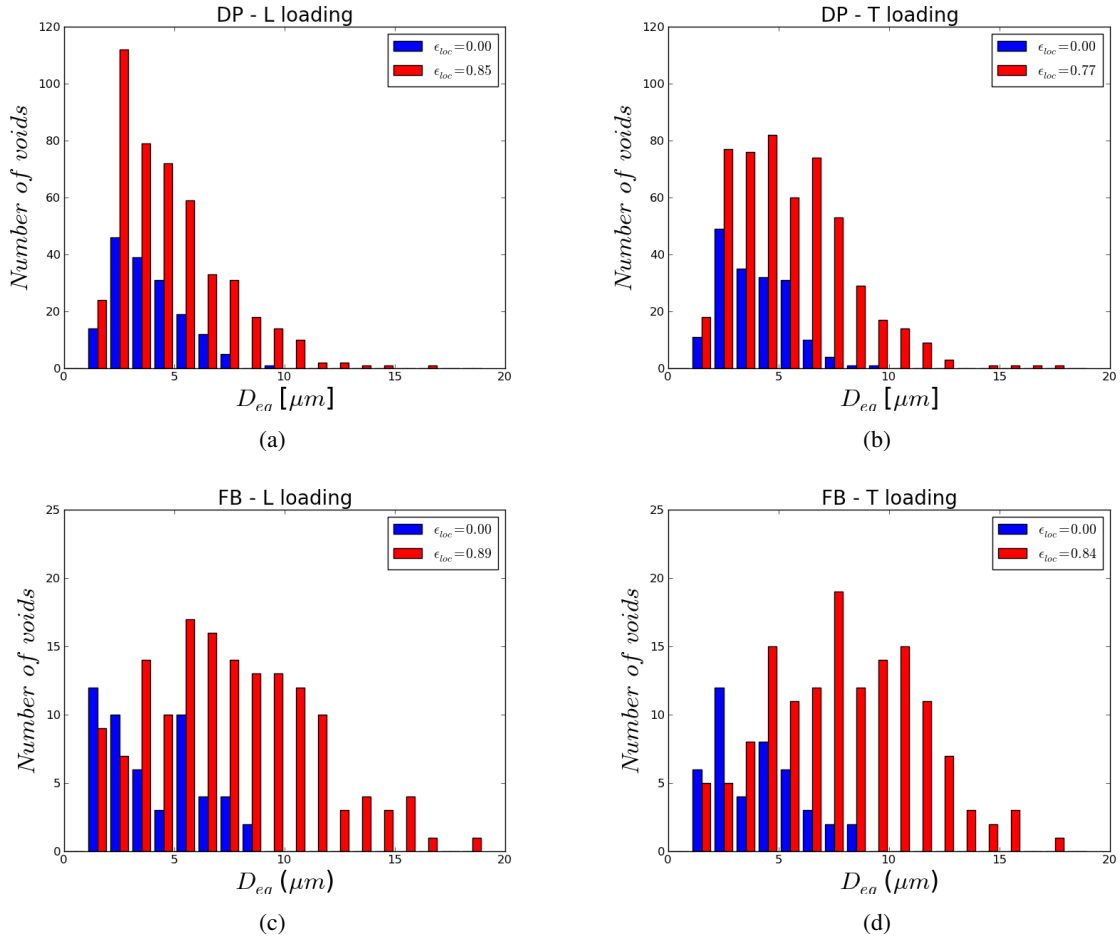

Figure 3.24 – Distribution of the equivalent diameter of the cavities measured for L and T loading directions in the investigated materials: (a) DP steel - L loading, (b) DP steel - T loading, (c) FB steel - L loading, (d) FB steel - T loading

The expression of Huang's prediction was used to model void growth of the investigated DP and FB steels. The pre-exponential term of the Huang's prediction (equation 3.10) was used as a fitting parameter to predict the evolution of the equivalent diameter of the 20 largest cavities for DP and FB steels. Figure 3.25 shows the values of the obtained fitting parameter (α_H) for DP and FB steels. The prediction of void growth using Huang model for the investigated DP and FB steels is compared to the experimental evolutions provided using in-situ X-ray tomography observations in figure 3.26.

The values of the pre-exponential term found for the investigated materials are quite different from those proposed by Rice and Tracey [Rice and Tracey, 1969] and by Huang [Huang, 1991]. These differences are due to the assumptions of Rice and Tracey model and Huang model predicting an isotropic growth of a spherical void in a infinite and perfectly plastic matrix.

Figure 3.25 – Identified Huang parameter α_H for the studied DP and FB steels for the evolution of the equivalent diameter of the 20 largest cavities

Steel	DP	FB
α_H	0.28	0.35

Figure 3.26 shows the equivalent experimental measurements for the N largest cavities in the studied materials (N=5; 10 and 20) in comparison with Huang's predictions. For DP and FB steels, an acceleration of void growth can be observed close to the end of the tensile test. This is due to the increased plastic strain and the substantial necking that undergoes the center of the imaged sample which generates an increased level of

stress triaxiality. Void coalescence is another reason for the observed void growth acceleration at the end of the tensile test.

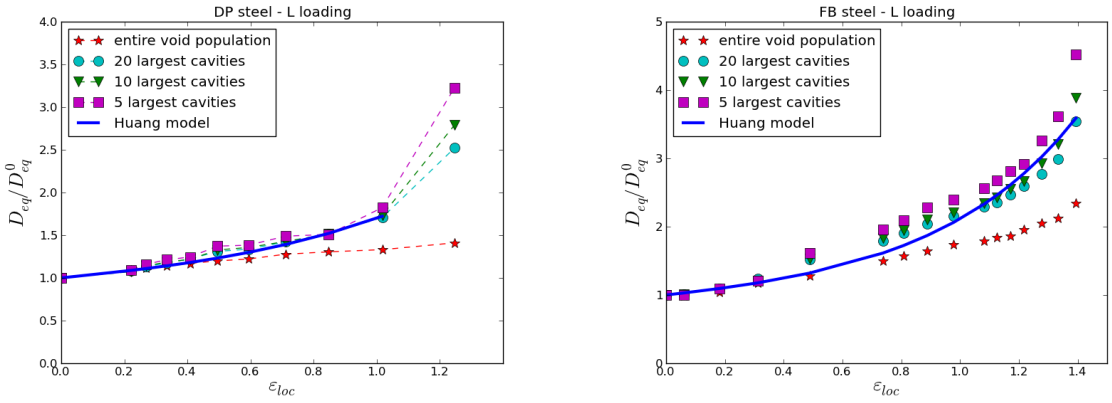

(a) (b)

Figure 3.26 – Comparison of the prediction of the growth model using Huang's approach and experimental data acquired during in situ tensile tests of the investigated DP and FB steels in the L loading direction

3.5 Void coalescence

The third and last stage of ductile damage process which leads to the final fracture is void coalescence, it occurs when the ligaments between cavities are broken. There are only few works in the literature investigating experimentally void coalescence mechanisms. It is due to the stochastic nature of the events of void coalescence and the difficulty to capture experimentally this last ductile damage process leading to 'fast' final fracture of specimen.

3.5.1 Qualitative observations

Thanks to in-situ X-ray tomography, the step of void coalescence was observed in 3D in the imaged samples when the acquisition of tomography volumes was performed at the right instant during the tensile test. Figures 3.27(a) and (c) give 2D sections of the investigated DP and FB steels loaded at L direction inside the acquired volumes showing the phenomenon of void coalescence. 3D volumes of void coalescence captured just before the final fracture of the imaged DP and FB steel specimens are given in figures 3.27(b) and (d) respectively. For the studied FB steel, we observe the presence of a void growth and coalescence in columns which may correspond a segregation line and that the final coalescence is normal to the loading direction (see figure 3.27(c) and (d)).

It is important to mention that, in addition to the plastic strain, the stress triaxiality influences on void growth events. An increased stress triaxiality level leads to a higher void growth [Maire2008, Landron2011].

3.5.2 Quantification of void coalescence

As described in the literature review presented in chapter 1, void coalescence is highly controlled by the distance between closest cavities. Assuming that cavities are homogeneously distributed in the sub-volumes used for damage quantification, an average value of the distance between closest cavities (λ_{mean}) in the studied sub-volumes using the void number N and the equivalent diameter of cavities can be calculated via the following relationship:

$$\lambda_{mean} = \frac{1}{N^{1/3}} - D_{eq} \tag{3.11}$$

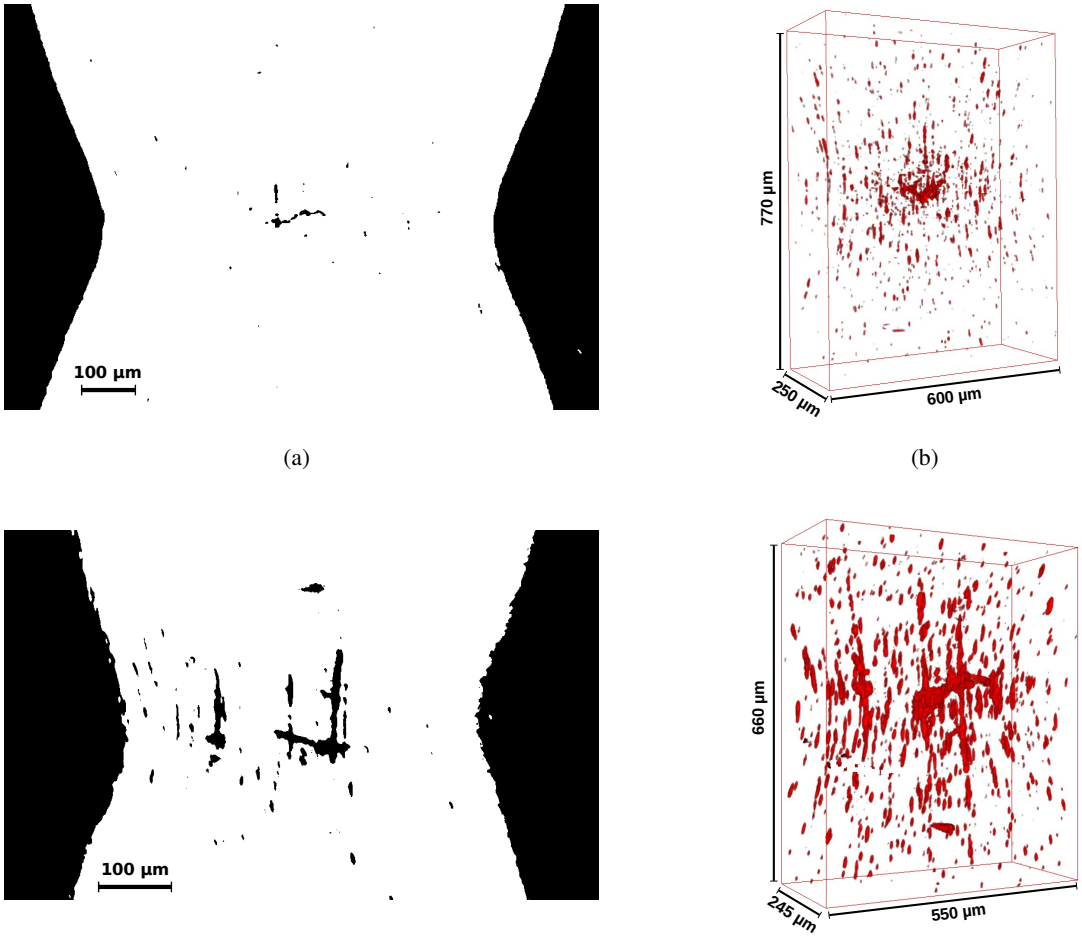

Figure 3.27 – Void coalescence observed in the imaged steels loaded in L direction using in-situ X-ray tomography: (a) 2D section DP steel, (b) 3D volume DP steel, (c) 2D section FB steel, (d) 3D volume FB steel

Figure 3.29 gives the evolution of the average value of the distance between cavities λ_{mean} as a function of local strain for the studied steels. At initial state λ_{mean} for FB steel is slightly higher than DP steel. However, during loading the distance between cavities decreases in the same way for the two studied grades. The final value of λ_{mean} calculated at the step before specimen fracture is about 20 and 35 μm for the studied DP and FB steels respectively. This is consistent with the results found for a DP steel by Landron and co-workers [Landron et al., 2013].

The evolution of the void volume fraction (VVF) calculated using the void density and the void equivalent radius (see equation 3.12) with the local strain for the investigated materials is given in fig. 3.30. We observe that VVF which is approximately 0.00015 and 0.0002 for the studied FB and DP steels respectively, increases during mechanical loading faster for the FB steel compared to the DP steel. Using X-ray tomography observations the identified void volume fraction at coalescence f_c are 0.0021 for the DP steel and 0.003 for the FB steel (see fig. 3.30). These values have been measured using the evolutions of the equivalent diameter discussed hereinbefore.

$$f = N \times \frac{4\pi}{3} R_{eq}^3 \tag{3.12}$$

To simplify, we used a void volume fraction at coalescence f_c=0.002 for the two studied materials as an on-set coalescence condition in numerical simulation presented in chapter 5. This value (f_c=0.002) has been validated using the *in situ* tensile test in SEM. Indeed, a numerical simulation of this test has been carried out using the identified criteria for void nucleation and void growth in order to calculate the f_c corresponding to

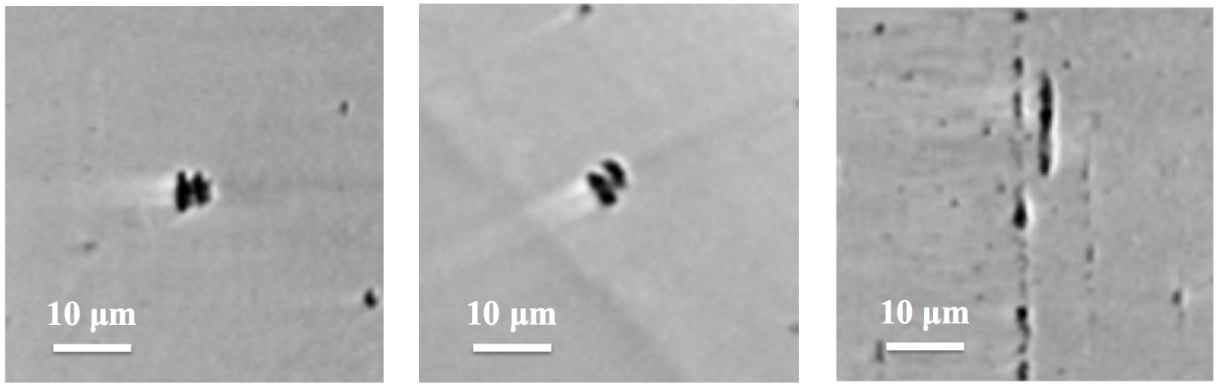

(a) DP steel (b) DP steel (c) DP steel

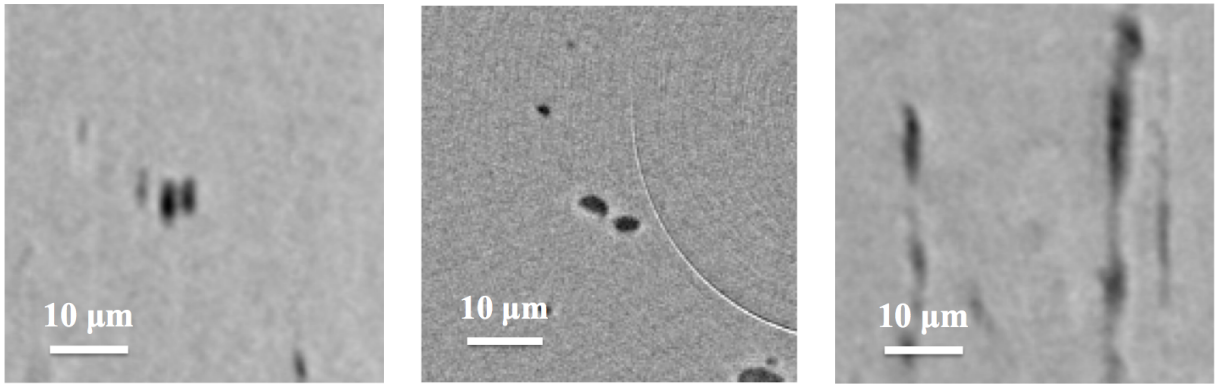

(d) FB steel (e) FB steel (f) FB steel

Figure 3.28 – Void coalescence modes observed in the investigated DP and FB steels: (a) and (d) coalescence by internal necking, (b) and (e) coalescence by shear localization, (c) and (f) necklace coalescence

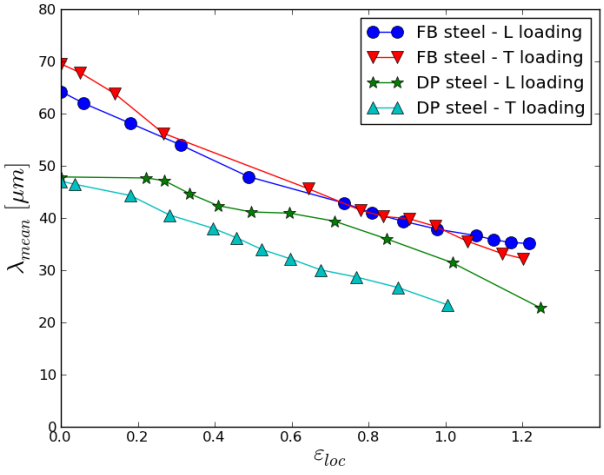

Figure 3.29 – Evolution of the average value of the distance between closest cavities λ_{mean} with the local strain for the investigated steels loaded in L direction

the strain calculated at the last loading step and to compare it to the one experimentally measured. Figure 3.31 shows the evolution of void volume fraction with deformation using elasto-plastic constitutive laws of the studied materials. For f_c=0.002, the measured values of strain at fracture for the FB and DP steels are 0.17 and 0.23 respectively. These values obtained from numerical simulations are consistent with those found experimentally during in situ tensile test in SEM (approximately 0.16 for the FB steel and 0.22 for the DP steel).

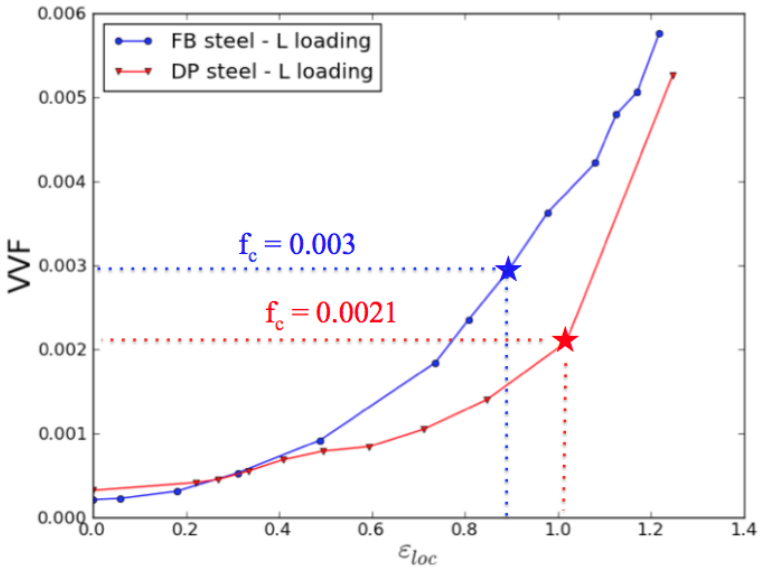

Figure 3.30 – Evolution of void volume fraction with the local strain for the investigated DP and FB steels using in situ tensile testing during X-ray tomography observation at L direction

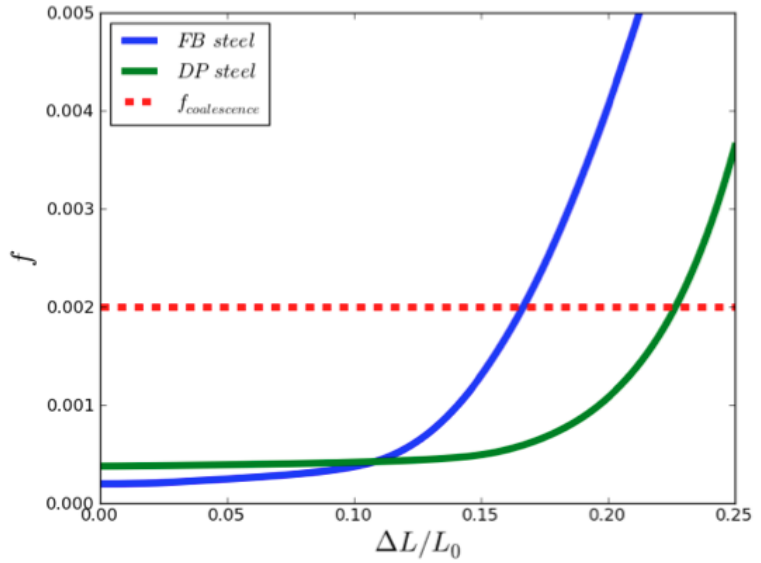

Figure 3.31 – Evolution of void volume fraction with deformation during in situ tensile test in SEM for the studied materials calculated using numerical simulations. Void volume fraction is calculated via the identified void nucleation and growth models using plane-stress finite element analysis.

3.6 Fractography of the studied materials

SEM micrographs of fracture surfaces of DP and FB steel tested using in situ X-ray tomography are given in figures 3.32 and 3.33. microvoids and dimples, characteristic of ductile fracture, are present on the imaged fracture surfaces. For the studied DP steel, the dimple size, approximately $2\mu m$, is fairly homogeneous in the observed fracture surfaces (see fig. 3.32). However, the fracture surfaces of the investigated FB steel shown in fig. 3.33 presents an heterogeneous dimple size. Larger dimples with a diameter more than $2\mu m$ can be observed. The presence of these larger dimples means that more void growth before coalescence occurs. This has been observed on the SEM fractographs of the tested FB specimens using in situ tensile testing in SEM. These dimples correspond to voids nucleated around particles. A high density of small dimples (size less than 1 μm) is observed on the fracture surfaces of the FB steel given in 3.33.

Figure 3.34 shows a fractograph of a tensile specimen tested in a scanning electron microscope observed at different magnifications. We observe in these SEM micrographs an increased elongation in the loading direction of the void nucleated on the shown particle (see 3.34(c)).

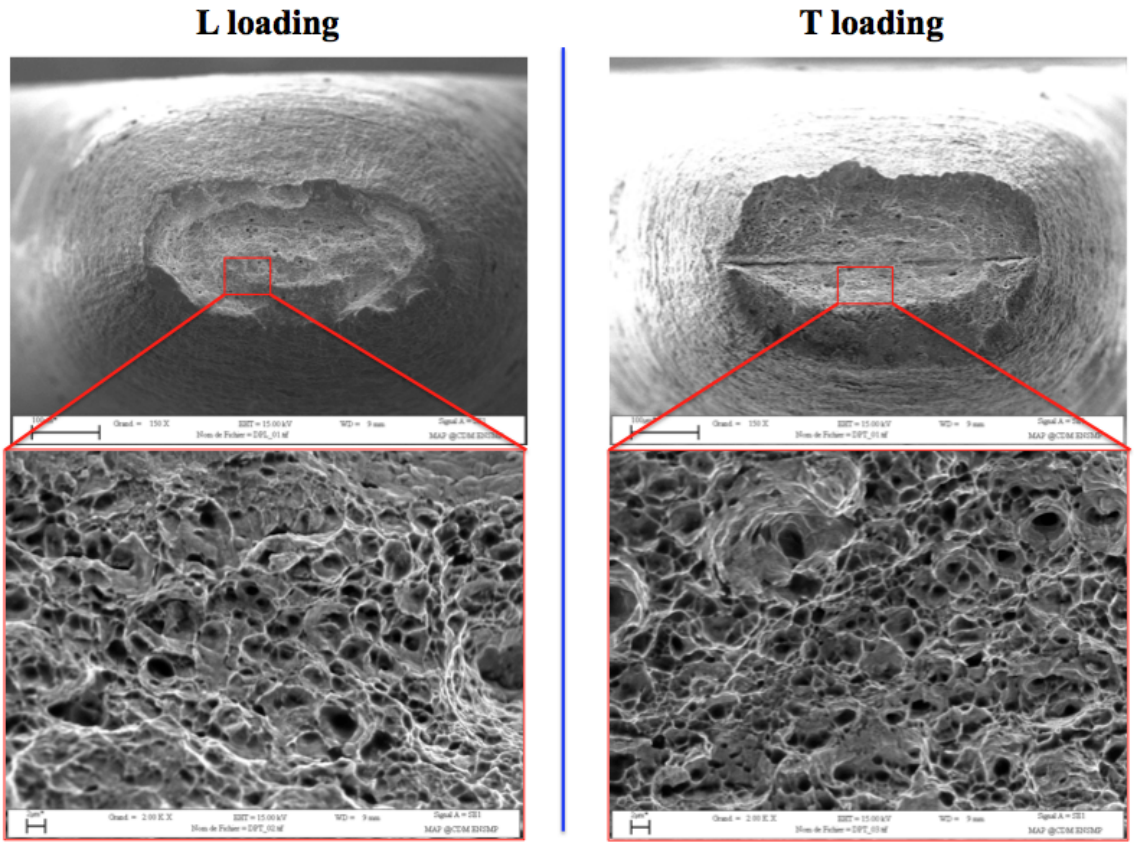

Figure 3.32 – Fractographs of the investigated DP steel using X-ray tomography at different magnifications ($\times$150 and $\times$2000)

3.7 Conclusions

Before assessing the edge fracture of the studied materials which seems to be complex due to the punched edge pre-damage and pre-strain induced by the punching process, damage mechanisms were investigated for the two studied base materials (DP and FB steel). Because of the limitations of X-ray tomography technique to reveal the microstructural components of the studied steels, i.e. ferrite, bainite and martensite, in-situ tensile tests were performed in a scanning electron microscope in order to establish a link between the microstructures and the mechanisms of void nucleation. It is found that for the DP steel damage appeared mostly linked to coarse particles. Some damage on ferrite martensite interface may be present, however, due to the increased surface roughness, caused by plasticity, it is hard to judge if this would have led to voids in the material bulk. For the FB steel, damage mainly arises from second phase particles. A three dimensional analysis of damage evolution in the materials bulk using qualitative and quantitative data provided by synchrotron X-ray tomography has been carried out in order to better understand and quantify the damage mechanisms of the materials bulk at micrometer resolution, where stress triaxiality level is known to be higher than at the surface. In situ tensile testing of both base materials using nearly smooth specimens in T and L directions leaded to the following results:

DP steel

- During loading in L direction, void elongation in the loading direction was observed
- Voids are elongated normal to the loading direction, in L direction. In the center of the specimen, needle-shape voids with length of several hundreds of micrometers are observed. These are probably linked with the central segregation zone.
- The increase in number of voids is consistent with void nucleation at ferrite martensite interfaces.

FB steel

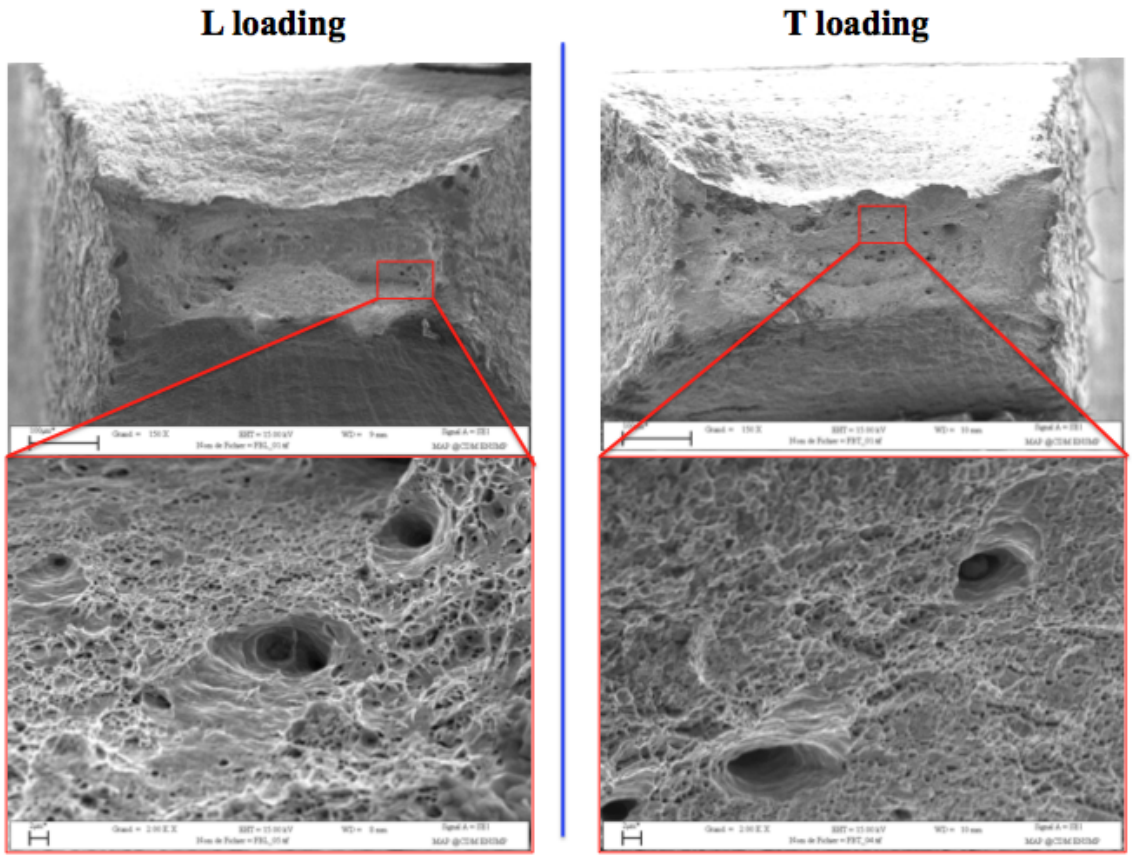

Figure 3.33 – Fractographs of the investigated FB steel using X-ray tomography at different magnifications ($\times$150 and $\times$2000)

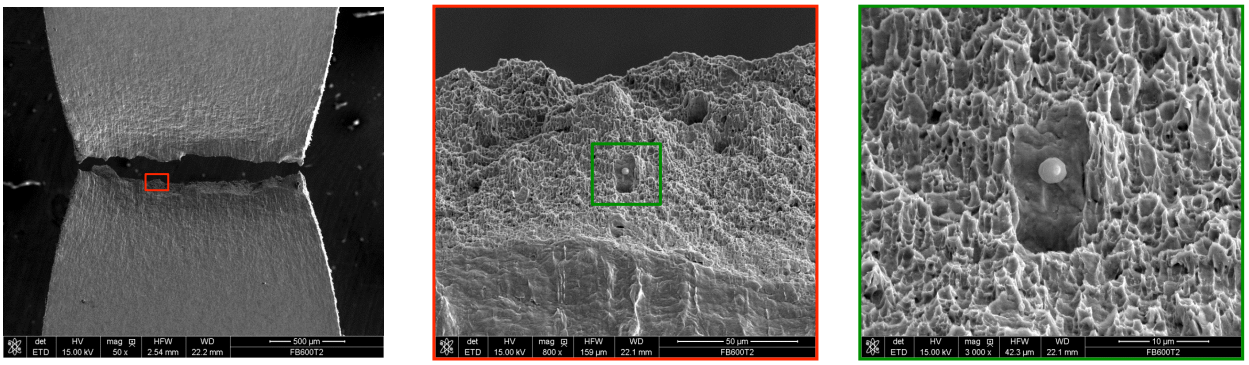

(a) (b) (c)

Figure 3.34 – Fractographs of a fractured FB steel specimen in scanning electron microscope taken at different magnifications

- During L loading, highly elongated voids in the loading direction are seen. The final coalescence of these voids occurs through narrow regions that are oriented normal to the loading direction.
- For T loading, a very long void nucleated normal to the loading direction along the L direction (about 400 μm) that is probably linked to a central segregation zone. The material is tolerant to this kind of large damage feature as the specimen did not fail even when large fractions of the minimal section are covered by the large void.

We observe that for the studied DP steel, comparing the void size distribution at initial state and at a step at the end of the tensile test, voids nucleate until the fracture of sample (see figure 3.24). However, during

tensile tests void nucleation in the studied FB steel seems to be less faster than in the DP steel. At a step close to the end of the tensile test, we observe that there are more grown cavities than nucleating ones.

The SEM micrographs taken at the cross section of the observed specimen via X-ray tomography after polishing and 0.2% etching to reveal steel microstructures show fracture of martensite and decohesion at martensite-ferrite interfaces for the studied DP steel. Some observed voids are smaller than the resolution limit in micro-tomography. However, for the investigated FB steel, the imaged cross section shows very small voids (less than 1 μm) which was not detectable on X-ray tomography data that are close to the fracture surface in link with carbide interfaces.

The fracture surface of DP steel during L loading is mainly covered by small dimples with a typical diameter of 2 μm. For the T loading of DP steel, the central segregation zone is clearly seen on the fracture surface. For the L loading of FB steel, the fracture surface exhibits two dimple populations. one population of large voids that originated from micrometric size particles. These are the voids also seen in tomography that elongated in the loading direction. The second population of small voids has diameters in the order of 1 μm, i.e. below tomography resolution limit. These small voids led to coalescence of the large voids of anisotropic shape.

Damage has been quantified via 3D image analysis in terms of evolution of the void density, the equivalent void diameter and the evolution of the largest cavities. It is found that the DP material contains twice more micrometric-size initial voids than the FB material. It is hard to distinguish inclusions from voids so that for the FB material most of the voids found may actually be inclusions. While the number of voids in the DP steel increases constantly, which is consistent with the high number of possible nucleation sites at ferrite and martensite interfaces, the number of nucleating voids in the FB steels decreases after some deformation indicating reduced nucleation compared to DP steel. A Chu and Needleman nucleation function is successfully fitted on both nucleation kinetics, with very different numbers for the maximum amount of possible nucleation sites.

Void growth was quantitatively studied for the two base materials (DP and FB steel) using X-ray tomography data. The investigation of void growth of entire void population and the largest cavities was carried out in sub-volumes taken at the center of the tested samples. Using a correction of the void growth model of Rice and Tracey taking into account the stress triaxiality in the pre-exponential term proposed by Huang where the stress triaxiality is calculated via Bridgman approach, the growth of the largest cavities was successfully fitted.

Figure 3.35 shows a schematic illustration of the different steps leading to the ductile fracture in the investigated materials. For the DP steel, the damage mechanisms observed during in situ tensile tests in SEM consist in nucleation on particles and martensite-ferrite interfaces decohesion. This is illustrated in figure 3.35(a), (b), (c) and (d) (red points refer to martensite and grey points to particles). For the studied FB steel, we observe the increased growth level of voids that nucleate on particles. The fracture occurs by coalescence of these larger voids and the very small damage that has been only observed on the cross section using SEM with high resolution.

Table 3.3 gives the optimized parameters of void nucleation and growth criteria identified using X-ray tomography quantitative data that will be used in post-processing calculations in chapter 5. We notice that void volume fraction, f, is deduced from the void density N and the void equivalent radius R_{eq}.

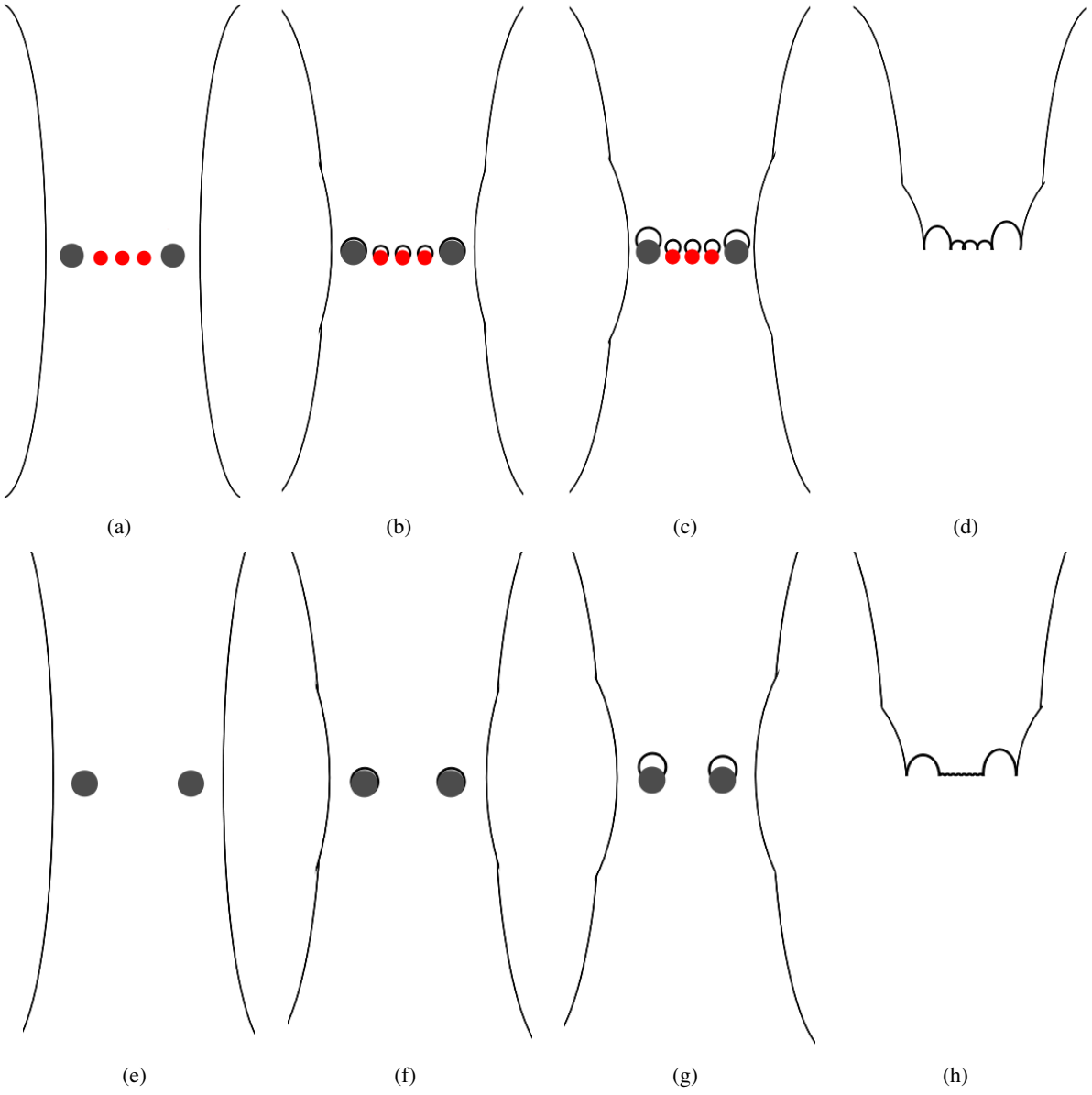

Figure 3.35 – Schematic illustration of ductile damage mechanisms observed during in situ tensile tests in SEM of the studied materials: DP steel: (a), (b), (c) and (d). FB steel: (e), (f), (g) and (h) ()

Table 3.3

Void nucleation		
DP steel		FB steel
6500	N_0 [mm^{-3}]	3000
1.2 10^6	ψ [mm^{-3}]	10^4
2.57	ε_n	0.64
0.62	s_N	0.47
Void growth		
DP steel		FB steel
2.4	R_0 [μm]	2.5
0.28	α_H	0.35
Void coalescence		
0.002	f_c	0.002

Chapter 4

Experimental investigation of edge fracture in DP and FB steels using in-situ synchrotron X-ray laminography

Contents

4.1 Résumé

Les essais de laminographie ont permis de caractériser la rupture de bords découpés (bord poinçonné et bord usiné) en appliquant des conditions aux limites proches à celles de la mise en forme des aciers. La chute de ductilité mesurée par la réduction d'ouverture d'entaille est entre 30 et 40% pour l'acier DP et 5 et 10% pour l'acier FB. La caractérisation de l'état initial par laminographie a montré que les bords poinçonnés présentent une rugosité au niveau de la zone rompue et un micro-endommagement sous forme d'aiguille que s'initie sur la surface des bords poinçonnés. Pour l'acier DP, lors du chargement mécanique, ce micro-endommagement suit les lignes d'écoulement et coalesce avec la zone cisaillée. Aucune striction n'a été observée sur le bord poinçonné DP au moment de l'initiation de fissure. Par contre, pour le bord usiné, l'endommagement est plus important loin de la surface du bord ($\sim$800 μm) où le matériau subit une striction importante. Pour l'acier FB, une striction a été observée lors du chargement du bord poinçonné. La rupture de ce dernier s'initie sur la surface sur bord, par contre, dans le cas du bord usiné la rupture s'est initiée loin du bord. Les données de laminographie ont montré que les deux matériaux présentent à l'état initial plus de cavités dans la zone affectée par la découpe que dans le volume. Pour les bords poinçonnés DP et FB, l'endommagement reste plus important proche de la surface des bord lors du chargement mécanique. En revanche, l'endommagement croit plus vite loin de la surface des bords ce qui est cohérent avec la striction observée dans cette zone.

In this part, the mechanisms involved in edge fracture in DP and FB steels have been characterized using X-ray synchrotron laminography. This work has been performed on two steel grades in order to understand the link between damage mechanisms leading to edge fracture and the studied microstructures. Two edge configurations have been investigated, i.e. punched edge and machined edge, to study the impact of cutting process on the mechanical behavior at the cut-edges. The first part of this work has been published in [Kahziz et al., 2015] so possible repetitions of material description and experimental methods can be observed.

Part 1: Edge fracture assessment in DP steels using X-ray synchrotron laminography (Part of the article [Kahziz et al., 2015])

4.2 Introduction

Advanced High Strength Steels (AHSS) grades are, beside other steel grades (as e.g. HSLA, bake hardenable...), widely used and developed materials in the automotive industry for environmental and safety reasons. Among these AHSS grades, dual phase (DP) steels with their ferrite-martensite composite microstructure present a good compromise between strength and formability. However, forming processes can affect the mechanical behavior of these grades. In automotive industry, the operations based on shearing and punching are the most used cutting processes due to their speed, simplicity and low cost. Cases of failure in DP steels, which initiate via ductile fracture mechanisms on blanked edges were detected [Dalloz et al., 2009]. This may lead to a drop in the mechanical performance of automotive parts and therefore of the vehicle safety [Dalloz et al., 2009]. It was shown that the cutting step can alter the mechanical properties of this grade [Dalloz et al., 2009, Thomas, 2012, Lara et al., 2013]. These studies have shown that the cutting process of DP sheets affects the adjacent material that extends into the bulk region of the sheet. While ductile fracture mechanisms of this steel and its base materials (i.e. ferrite and martensite separately) were discussed in the past (see [Landron et al., 2010, Landron et al., 2011b, Landron et al., 2011a, Landron et al., 2013] and others), the mechanisms of edge fracture in DP steels are not well known.

It is found for DP steels that the failure is governed by ductile damage mechanisms, e.g. void nucleation, growth and coalescence phenomena. Damage nucleation in dual phase steels was investigated in several studies [Mazinani and Poole, 2007, Maire et al., 2008, Landron et al., 2010, Avramovic-Cingara et al., 2009b, Kadkhodapour et al., 2011, Azuma et al., 2012, Ramazani et al., 2013]. Void formation in DP steels is mainly due to the ferrite/martensite interface decohesion, or to the fracture of the martensite particles. The growth of cavities in steels is evidenced in the literature using different microstructural characterization techniques like metallographic observation [Park and Thompson, 1988, Avramovic-Cingara et al., 2009b, Avramovic-Cingara et al., 2009a]. There are only few experimental works on void coalescence in dual phase steels due to the difficulty to observe this ductile damage stage. Using X-ray tomography, Landron and co-workers [Landron et al., 2013] have qualitatively assessed the void coalescence stage in a DP steel during *in situ* tensile test. The models of Brown and Embury [Brown and Embury, 1973] and of Thomason [Thomason, 1990] were identified in order to predict the void coalescence in the studied DP steel.

Several models were developed to model the initiation and the evolution of ductile damage in DP steels. The most used approach to model the void nucleation were proposed by Argon [Argon et al., 1975], by Beremin [Beremin, 1981] and by Chu and Needleman [Chu and Needleman, 1980]. These models do, however, not explicitly account for ferrite-martensite decohesion. Rice and Tracey's model [Rice and Tracey, 1969] and Huang's model [Huang, 1991] allow one to model the void growth taking into account the stress triaxiality and the plastic strain effect. Gurson [Gurson, 1975] has proposed an equation of the yield surface

depending on volume fraction of the porosity dedicated to the porous media to model the growth of a spherical cavity in an infinite matrix assuming that the matrix is isotropic, rigid and perfectly plastic. Ben-Bettaieb *et al.* [Ben-Bettaieb et al., 2011] and Fansi *et al.* [Fansi et al., 2013] have developed a modified GTN (Gurson–Tvergaard–Needleman) model which integrates physically based void nucleation and growth laws. The reader interested in GTN model and its extension should refer to [Besson, 2010].

Many experimental works were performed to understand the influence of cutting processes conditions on the formed edges (see [Pyttel et al., 2000, Chen et al., 2004, Wu et al., 2012, So et al., 2012] and others). The edge profile depends heavily on many parameters such as the material behavior, the clearance, the cutting speed [Lee et al., 1995, Hambli, 2001, Hambli, 2002, Hilditch and Hodgson, 2005, Mori et al., 2008, So et al., 2009, Sartkulvanich et al., 2010, So et al., 2012, Mori, 2012, Mori et al., 2013]. In the last decades several works linking experimental approaches and numerical methods were carried out on that topic (e.g. [Taupin et al., 1996, Breitling et al., 1997, Goijaerts et al., 2000, Goijaerts et al., 2001, Hambli, 2002, So et al., 2012]).

Tensile tests on samples containing sheared edges were used to investigate the sheared edges ductility [[Dalloz et al., 2009]]. However, during this test, necking occurred before the sheared edge fracture which makes the deformation analysis more complicated. The hole expansion test which is controlled by visual inspection was performed in many studies in order to investigate the local formability of punched edges [Kim et al., 2010, Jha et al., 2012, Taylor et al., 2014]. In [Wang et al., 2014], a study of three different edge conditions (milled edge, water jet cut edge and punched edge) was performed using hole expansion test. It was found that the punched edge exhibits the lowest hole expansion ratio (HER) compared to the two others investigated edges. However, this test is sensitive to the sample geometry and microstructure [Taylor et al., 2014]. Indeed, the important scattering in results observed for this test limits its use. In [Hasegawa et al., 2004],it has been observed that during hole expansion, cracks were mainly initiated at the fracture surface and the cracks became longer and deeper from the punched surface with the increase of hole expansion ratio. A new test was developed by Bouaziz and co-workers [Bouaziz et al., 2010] called double bending to investigate the sheared edges ductility which allows one to separate necking and damage behaviors by localizing the strain on the sheared edge. Using this test the sheared edge fracture is achieved without any necking and the strain field can be continuously determined by an image correlation system.

Few studies are available in the literature on the cut edges mechanical behavior and the mechanisms of edge fracture. Thomas *et al.* [Thomas, 2012] and Lara *et al.* [Lara et al., 2013] have investigated the influence of shearing and laser cut edge characteristics on the fatigue life performance of high strength automotive steels. In their recent study focused on failure during sheared edge stretching of DP steels, Levy *et al.* [Levy et al., 2013] observed that increased strength of martensite retards crack initiation from a sheared edge. Crack growth was found to be made easier with increasing surface fraction of martensite/ferrite interfaces. Additionally, increased strain hardening was found to lead to void formation at low macro strain. In the studies performed by Levy and co-workers [Levy and Van Tyne, 2011, Levy and Van Tyne, 2012], it was concluded that local deformation in the shear-affected zone in DP steels is the main factor controlling the failure during sheared-edge stretching.

Recent in situ X-ray synchrotron non-destructive techniques were developed to assess the ductile damage evolution. Synchrotron tomography, especially adapted to compact or one-dimensionally elongated objects which stay in the field of view of the detector system under rotation, was used in several studies to observe in 3D and in situ the ductile damage initiation and evolution in DP steels [Gammage et al., 2005, Maire et al., 2005, Maire et al., 2011, Landron et al., 2010, Landron et al., 2011b, Landron et al., 2013]. Synchrotron laminography was developed for 3D imaging [Helfen et al., 2005, Helfen et al., 2007, Helfen et al., 2011] of regions of interest (ROI) in plate-like specimens that are extended in two dimensions which provides a unique way to qualitatively and quantitatively assess damage and its evolution in sheet materials [Xu et al., 2010, Bull et al., 2013]. This technique was used in several studies to observe in 3D the ductile damage evolution in Aluminium alloys [Morgeneyer et al., 2011,Shen et al., 2013,Ueda et al., 2014]. Morgeneyer and co-workers [Morgeneyer et al., 2013] have combined in situ synchrotron laminography with digital volume correlation in order to measure in 3D the displacement and strain fields during the tensile test of a notched sample.

The present study aims at providing quantitative information about the microstructural initial state of a punched edge and a machined edge in terms off damage and its evolution. In situ synchrotron laminography was used during simultaneous bending and tensile mechanical loading of samples containing a punched

hole and an EDM (electrical discharge machining) machined hole. Here, three-dimensional laminography has been used for the first time to assess the damage evolution in steel sheets. The use of large specimens (several tens of mm in width and height) is an advantage over tomography at micrometre resolution: relevant large plastic zones can develop during the mechanical test using laminography as it is the case in forming processes. These techniques could also be applied to weldments [Tong et al., 2005] and valuable information could be gained if micrometre sized defects play a role [Le Jolu et al., 2014]. Quantitative image analysis of laminography data was performed in order to understand the ductile damage evolution during edge fracture. Surface digital image correlation (DIC) was carried out using the software Correli^{Q4} in order to measure the displacement fields in the region of interest. These are used for comparison and as input data for FE simulations. A 3D finite element analysis was performed using an elasto-plastic constitutive law of the investigated DP steel to interpret the behavior of the punched and machined edges in terms of mechanical fields.

4.3 Experimental methods

4.3.1 Material

The material investigated in this study is a laboratory dual phase steel (fig. 4.1) with an ultimate tensile strength of approximately 600 MPa and a fracture elongation around 20% in the as-received condition. The martensite surface fraction measured on scanning electron microscopy images was about 14%. This value is slightly overestimated due to the presence of some carbides and grain boundaries that are included in this surface fraction. The material was supplied as a 0.8 mm thick cold rolled sheet. The main alloying elements are: C (0.095), Mn (1.89) and Si (0.24) in weight%. The micrograph in fig. 4.1 shows that martensite islands appear to be aligned along the rolling direction. In the following the rolling direction will be referred to as L, the long transverse direction as T and the short transverse direction as S for all experiments presented in this work. The loading configuration was T-L, the first letter corresponds to the loading direction and the second to the crack propagation direction.

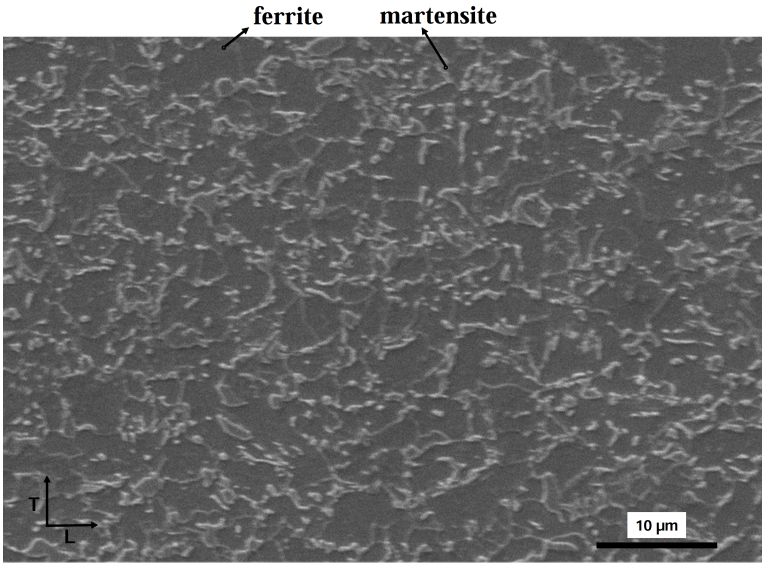

Figure 4.1 – DP microstructure visualized by scanning electron microscopy (after polishing and 2% nital etching)

4.3.2 The punched edge profile

The shearing process, which is a cutting in a straight line over the entire width of the sheet by the action of a moving blade perpendicular to the plane of the sheet, is the most widely used and least expensive process for sheet cutting. The punching process produces edge profiles that are similar to the ones produced by shearing

processes. In this paper, a punched edge, which was produced with a clearance of 15%, is investigated. This ratio is defined as the distance between the blades divided by the sheet thickness. The value used here is a typical value in automotive industry. Fig. 4.2(a) shows an optical micrograph of the polished surface of a punched edge after the cutting process. Flow lines shown in Fig. 4.2(a) induced by the cutting process are defined by grain (martensite) orientation. The edge profile is characterized by the existence of four zones: rollover zone, sheared zone, fracture zone, and burr zone (fig. 4.2(a)). The punched edge hardening profile shown in Fig. 4.2(b) has been measued by the Vickers microindentation method using a load of $50g$. The hardening was then calculated using the following formula:

$$Hardening[\%] = \frac{HV_l - HV_\infty}{HV_\infty} \times 100 \tag{4.1}$$

Where HV_l is the microhardness measured at the distance l from the edge surface and HV_∞ is the base material microhardness. An increased hardness in the cutting-affected zone can be seen. This profile will be taken into account in further numerical analysis in order to study the pre-straining effect.

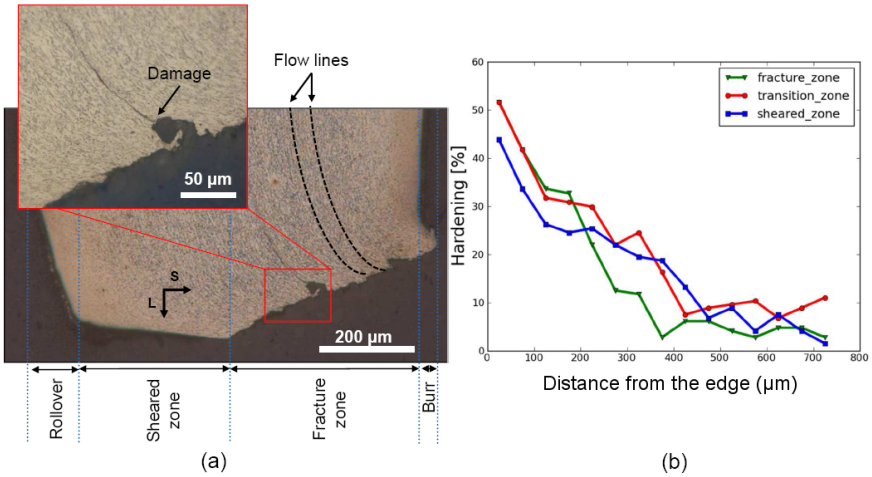

Figure 4.2 – (a) Optical Microscopy of a punched edge profile using a clearance ratio of 15%, etched in 2%-Nital showing the orientation of flow lines and a microcrack in the fracture zone. (b) hardening profile along L direction on the investigated punched edge measured by Vickers microhardeness technique in the fracture zone, sheared zone in the transition zone between both.

The fracture zone displays the highest damage and presents a high roughness in agreement with the findings in [Hilditch and Hodgson, 2005]. Some zones of decohesion at the ferrite-martensite interfaces can be observed in the fracture zone and are aligned along the flow lines. This had been already observed in [Dalloz et al., 2009].

4.3.3 In situ laminography and mechanical testing

The laminography experiments were performed at the ID19 beam line of the European Synchrotron Radiation Facility (ESRF) in Grenoble, France. The acquisition of projection images was performed employing a filtered white beam (centered around a $60keV$ X-ray energy) and using a high-dose detector system [Douissard et al., 2012] with an isotropic voxel size of $(0.778\mu m)^3$. The rotation axis inclination angle on the laminography device was chosen to around 30° (= θ - 90°). A simultaneous diffraction experiment was not carried out as this would require a lot more X-ray beam-time and a more complex experimental setup.

The sample geometry shown in fig. 4.3(a-b) was used. A hole with a radius of $5mm$ was punched out from a sheet of DP steel and an elongated notch was machined up to one edge. For the case of the machined edge the hole radius was $6mm$. The EDM (electrical discharge machining) machined edge surface was polished in order to eliminate the EDM wire cutting affected zone. The loading was applied perpendicular to the notch, via a two-screw displacement-controlled wedging device that allows us to incrementally open the notch and

control the specimen crack mouth opening displacement (CMOD) similar to the one used in [Morgeneyer et al., 2011] and [Shen et al., 2013]. To avoid the sample buckling and out-of-plane motion, an anti-buckling device was used. The entire rig was mounted in a dedicated plate that was removed from the laminography rotation stage between loading steps (see fig. 4.3(c)). After each loading step, a scan of the region of interest (ROI) containing the crack tip was carried out and a 2D surface picture was taken for digital image correlation (DIC) that can be used as optical extensometer to know the displacement field around the ROI.

A filtering operation was performed using a 3D median filter with a radius of 2 voxels in order to reduce the noise of the reconstructed images. An automatic threshold (Auto-thresholding) calculated from the histogram of the gray levels was used on the median-filtered volumes to create the binary images. The edge surface was detected using a plug-in implemented in ImageJ freeware ([Abramoff et al., 2004]) based on Sobel edge detector that consists in highlighting sharp changes in intensity in 3D binarized volumes. The 3D visualization was done using ImageJ 3D volume viewer. In this work, voids and edge surface always appear in blue and the material bulk in white. A scanning electron microscopy with X-ray micro-analysis (SEM/EDS) was carried out on a 4 mm^2 L-S section. It has shown that the investigated material contains three types of inclusions (MnS, CaO and Al_20_3) which are not all detectable using X-ray laminography. The image contrast is mainly due to absorption contrast, i.e. a density difference of the objects is needed to obtain a gray level difference in the 3D image. If particles and matrix have a similar density, the phases may not be distinguished. In addition if the particles are smaller than the voxel size (0.778 μm) they cannot be detected. The inclusion surface fraction measured in the observed surface was 0.08%.

It is important to mention that X-ray laminography does not allow to distinguish the ferritic phase from the martensitic one because the attenuation coefficients of the two phases are very close.

The in situ X-ray synchrotron laminography of the machined edge has offered low noise observations with a better signal/noise ratio than the punched edge observation experiment. The two observations were carried out using the same X-ray energy and the same resolution (isotropic voxel of $(0.778\mu m)^3$).

The experimental conditions had a higher signal/noise ratio for the punched edge scans than the observation of the machined edge performed during a later experiment. This has induced noise (artefacts) in the reconstructed data.

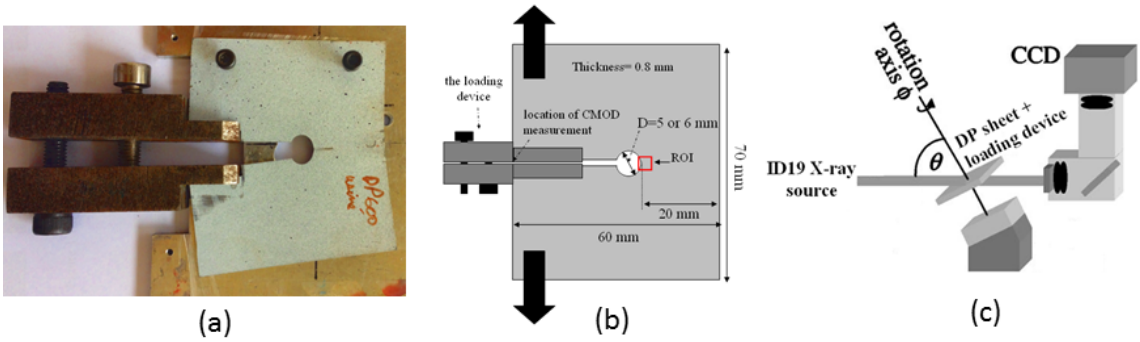

Figure 4.3 – In situ mechanical testing: (a) photograph of the loading device and specimen mounted on one of the two anti buckling plates (b) schematic drawing of the specimen geometry, the loading and crack growth directions and the region of interest (ROI). (c) schematic drawing of X-ray KIT synchrotron laminography installed at ID19 beam-line at the ESRF Grenoble [Helfen et al., 2005]

4.3.4 Method and tools for the post processing

4.3.4.1 Reconstruction and visualization

Synchrotron laminography scans were reconstructed using a filtered back-projection (FBP) algorithm adapted to the computed laminography acquisition geometry [Myagotin et al., 2013]. The reconstructed data is processed here in order to analyze qualitatively and quantitatively the mechanisms of edge fracture. All the processing operations are carried out using ImageJ dedicated to image processing [Abramoff et al., 2004].

4.3.4.2 Quantification of the initial state of punched and machined edge

Two sub-volumes $(310\mu m)^3$ were extracted from the reconstructed data of the machined edge and the punched edge at the initial state to calculate the mean value of void volume fraction and the distribution of voids using a home made plug-in implemented in ImageJ that detects and labels each pore which must be a cluster of at least three connected voxels to be considered. These sub-volumes were extracted away from the edge in order to avoid the cutting affected zone for the punched and machined edges. The average values of combined detectable particle volume fraction (PVF) and void volume fraction (VVF) found for the $(300\mu m)^3$ analyzed sub-volumes were 0.021% and 0.045% for the punched edge and machined edge respectively. As mentioned in [Landron et al., 2011a] the resolution has an important influence on the damage measurement. The observation performed on a DP steel at very high resolution (voxel of $(0.1\mu m)^3$) showed that a large part of damage is not detected at low resolution (voxel of $(1.6\mu m)^3$). Some small sub-micrometre features may not be detected here as they are smaller than the achieved resolution (voxel of $(0.778\mu m)^3$).

Fig. 4.4(a) shows the histogram of void size for the two sub-volumes (punched and machined edge) analyzed via in situ laminography in the as-delivered state.

Fig. 4.4(b) shows the profile of VVF (see next section for exact definition) as a function of the distance from the edge surface for the investigated edges in the as-received state. We observed that there are two times less cavities in the punched edge far from the edge than for the machined edge. This is due to the less good signal-to-noise ratio during the experiment for the punched edge. In order to improve the quantification of the initial state of punched edge and to better quantify the damage at the initial state, a second punched edge was observed via the laminography set-up located at ID15 beam-line at ESRF Grenoble. The observation was performed using a resolution of $1.1\mu m$. The average VVF value measured in a ($310\times310\times310$ μm^3) volume extracted far from the cutting-affected zone was 0.051%. The evolution of VVF in this punched edge is given in fig. 4.4(b) (punched edge 2). It shows that the damage (voids) is higher near the edge surface and it shows the same level as the machined edge away from it.

4.3.4.3 Quantification of void evolution by discretisation of the volume

To analyze quantitatively the 3D reconstructed laminography data, an in-house code based on Python [Morgeneyer et al., 2009] was used on median-filtered and binarized sub-volumes of ($1200\times300\times300\mu m^3$) in order to calculate the distribution of void volume fraction in the machined edge. For the case of the punched edge the analyzed sub-volumes were of ($600\times300\times300\mu m^3$) including the edge surface in order to avoid the artefacts in the center of the image. This code discretizes the studied sub-volumes into boxes of (50 $\mu m)^3$, in each box the void volume fraction (VVF) is calculated. For each elements column in the T direction, the maximum VVF value was calculated, named $max_T(VVF)$, assuming that the highest level of damage will be the most detrimental to structural integrity. Fig. 4.4(c) shows the maximum measured VVF in loading direction (T), $max_T(VVF)$, in discretized boxes ahead of the machined edge. The spatially heterogeneous distribution of $max_T(VVF)$, can be observed in this unloaded state. The average value of $max_T(VVF)$ was determined along the short transverse direction S (green lines in fig. 4.4(c)) resulting in $< max_T(VVF) >_S$.

4.3.4.4 2D digital image correlation

The in situ test was performed at the synchrotron facility with the already described simple loading device that does not allow to determine the displacement applied during notch opening. Surface digital image correlation (DIC) was carried out using the software called Correli^{Q4} implemented in Matlab^{TM} in order to measure the displacement and strain fields in the region of interest ([Hild, 2002]). In this correlation code a global approach is used in which the ROI is discretized in four-noded elements rather than in sub-sets as in the local approaches. In the global approach the continuity of the displacement fields is assumed. We used a Basler Pilot (piA2400-17gm) camera in a single shot mode for each load step with an exposure time of 50 ms. The pixel size was 2.59 μm. Between loading steps, images were taken in the region of interest where a spray paint speckle was applied on the specimen surface. The DIC was performed by updating the reference image and using an element size of $180\times180\mu m^2$ and a ROI of $2\times4mm^2$.

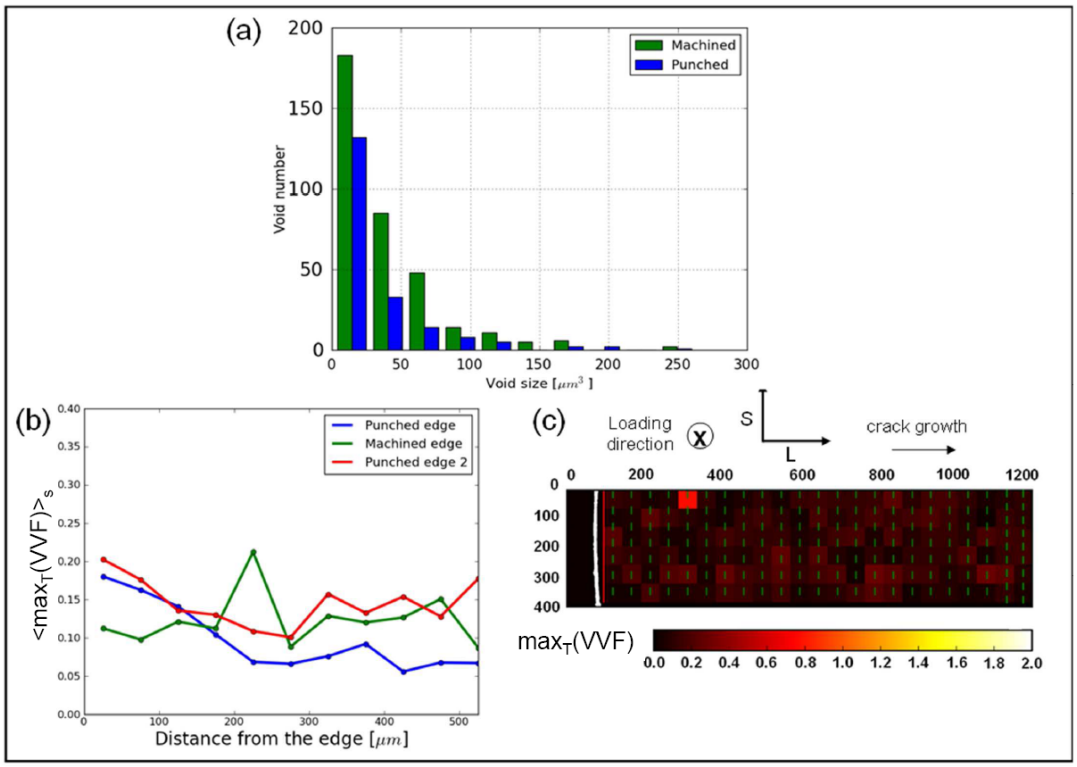

Figure 4.4 – (a) Void size distribution in a 3D sub-volume of $310\times310\times310\mu m^3$ for punched edge and machined edge; (b) $< max_T(VVF) >_S$ distribution at the initial state in punched and machined edges and the VVF mean values found for sub-volumes of $310\times310\times310\mu m^3$; (c) cartography of void distribution in the machined edge at the initial state using the in-house Python code (dimensions are in μm).

4.4 Experimental results

4.4.1 The punched edge

Fig. 4.5 shows the 2D sections taken at $320\mu m$ from the edge of reconstructed laminography raw data (before filtering and binarization) at different loading steps in the fracture zone of the specimen. The ferrite and martensite are shown in gray and the initial internal voids can be seen in black in the matrix. Ring artefacts that are not present for scans of the machined edge can be seen in the 2D sections of reconstructed data in fig. 4.5. Fig.4.5(a) shows a sketch illustrating the geometry of the observed specimen, the ROI for laminography which was about 1 mm^3 and the loading and crack growth directions. In the initial state, i.e. after punching and before mechanical testing of the hole, the roughness of the fracture zone and a geometrical defect caused by the punching process can be seen along the punched edge in fig. 4.5(b). The defect consists in a geometrical step with a height in the order of $30\mu m$. A cavity is formed at $50\mu m$ ahead of the crack tip. Laminography artifacts that appear in fig. 4.5(b) do not influence strongly the segmentation of the voids. The 2D section in fig. 4.5(d) taken at CMOD=4 mm shows that a microcrack initiates on the edge surface. A second crack that appears close to a geometrical defect can be seen in 4.5(d). In the 2D section given in fig. 4.5(e) corresponding to CMOD=4.5 mm, we can see the growth of the cavity formed in front of the crack. The 2D section given in 4.5(f) shows the coalescence of the crack and the void formed ahead of it via narrow void sheet and that the crack located close to the geometrical defect grows faster. This is consistent with the increased level of stress triaxiality caused by the geometrical defect. The void coalescence sheets are inclined at about 45° compared to the loading direction (see fig. 4.5(e)).

Thanks to X-ray laminography it is possible to visualize the damage evolution in three dimensions. Fig. 4.6 shows regions of $1240\times930\times310\mu m^3$ taken at different CMODs. The voids and the edge surface segmented and visualized in L-T plane, are shown in blue. Ferrite and martensite appear transparent. Fig. 4.6(b) shows the as-received material after punching. The fracture and sheared zone surfaces and the geometrical defect

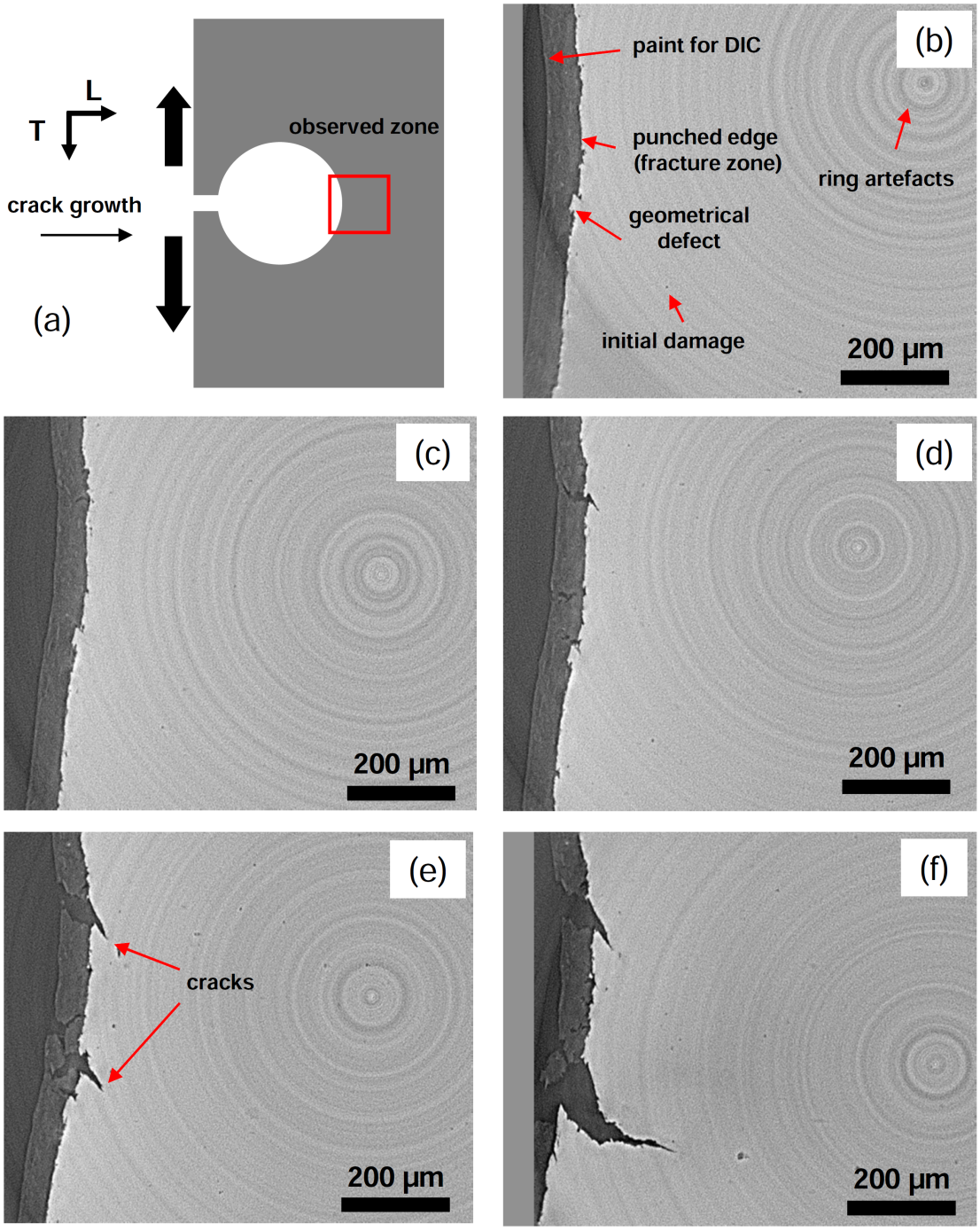

Figure 4.5 – 2D sections of laminography data taken at the fracture zone at $320\mu m$ from the edge surface of the sheet plane of reconstructed laminography data showing damage evolution from a punched edge at different CMODs (a) schematic drawing illustrating specimen geometry, ROI location and loading and crack growth directions (b) material at delivery state; (c) CMOD=$3mm$; (d) CMOD=$4mm$; (e) CMOD=$4.5mm$; (f) CMOD=$5mm$.

located in the fracture-to-sheared transition zone can be seen in fig. 4.6(b). The 3D section in fig. 4.6(d) shows the two cracks observed in the 2D section (4.5(d) corresponding to CMOD=$3mm$) formed in the fracture zone surface especially the one initiated close to the geometrical defect. A third crack which was not observed in the 2D sections presented in fig. 4.5 can be seen in 4.6(d) at the fracture-to-sheared transition zone inclined at $45°$ compared to the loading direction. We also observe the initiation of other cracks in the fracture zone surface and in the fracture-to-sheared transition zone (fig. 4.6(d) taken at CMOD=$4mm$). All the cracks are oriented at $45°$ with respect to the loading direction. Fig. 4.6(e) taken at CMOD=$4.5mm$

shows the crack growth and coalescence with the sheared zone surface via narrow coalescence sheets. The void growth near the edge surface is higher than in the bulk material (fig. 4.6(e)). In fig. 4.6(f), the final crack that crosses the specimen thickness and leads to the edge fracture is formed by the growth of the crack initially initiated close to the geometrical defect that acted as a stress concentration and the coalescence with the internal voids formed ahead of the crack. However, the mechanisms of crack growth remain the same for all the formed cracks.

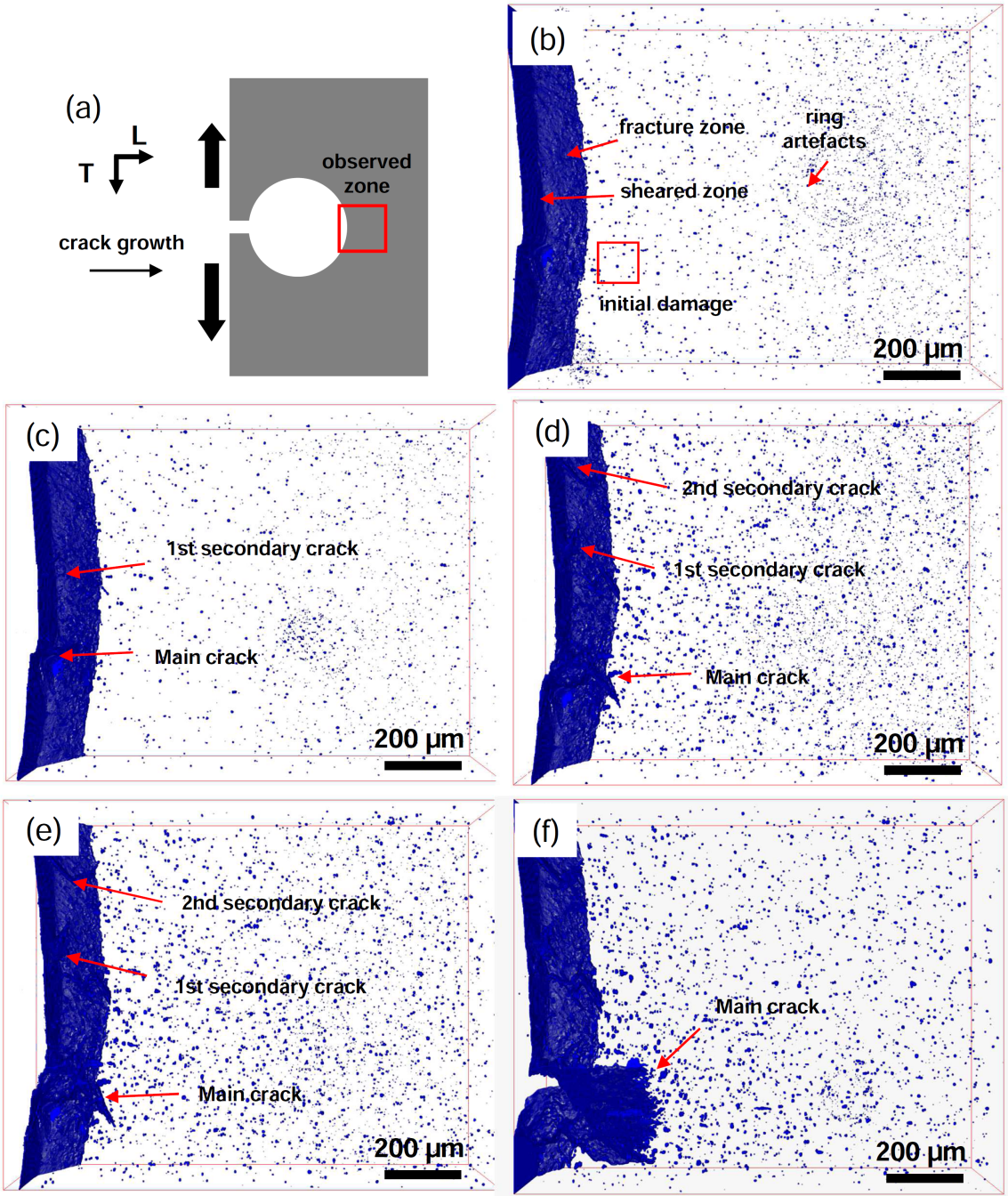

Figure 4.6 – 3D volumes of the reconstructed laminography data showing a region of $1240\times930\times310\mu m^3$ in the L-T plane at mid-thickness of the damage evolution from a punched edge at different CMODs. Voids, specimen surface and the crack are shown in blue. The steel matrix is made transparent (a) schematic drawing illustrating specimen geometry at the punched hole, observed area location and loading and crack growth directions; (b) material at delivery state; (c) CMOD = $3mm$; (d) CMOD=$4mm$; (e) CMOD=$4.5mm$; (f) CMOD=$5mm$.

The 3D volumes given in fig. 4.7 are the same as those observed in fig. 4.6 but seen from the side of the sheet. These 3D observations of a $330\times390\times210\mu m^3$ zone extracted at mid-thickness of the specimen show

the fracture and sheared zones with a view along the loading direction. Fig. 4.7(b) shows the voids nucleated close to the edge surface which are aligned along the martensite islands microstructural alignment (flow lines) during the punching process. The roughness of the fracture zone surface can also be seen (fig. 4.7(b)). The 3D volume at CMOD=2mm (fig. 4.7(c)) shows the growth of the pre-existing voids and the nucleation of new ones. A "needle shape" void formed close to the geometrical defect grows perpendicular to the sheared zone surface. The coalescence of the needle void formed close to the geometrical defect with the sheared zone surface occurred via a narrow coalescence sheet, and formed a crack at 45° with respect to the loading direction (fig. 4.7(d)). To the best of our knowledge, these observations of ductile crack propagation from a punched edge and coalescence with internal voids in the material bulk have never been observed before with such a high level of details and in situ. The 3D volume given in fig. 4.7(e) at CMOD=4mm shows the growth and the coalescence of voids following the flow lines corresponding to the martensite island alignment. Fig. 4.7(f) shows that the coalescence of the formed crack with the void clusters occurred at the crack tip.

4.4.2 The machined edge

The fig. 4.8 shows the 2D sections taken at mid-thickness of reconstructed laminography raw data (before filtering and binarization) for a machined edge specimen. We observe that these experiments do not present strong characteristic laminography artifacts. This is due to the fact that these acquisitions were performed later and with much better signal-to-noise ratio than those shown earlier for the punched edge. The fracture process revealed by these observations for the EDM machined edge is very different from the punched edge described above. The 2D sections in fig. 4.8(c) and (d) taken at CMOD= 3mm and 5.5mm respectively show that the damage nucleation and growth seem to be homogeneous. However, in the fig. 4.8(e), we observe a high damage amount leading to the formation of a cluster of aligned voids away from the edge surface which leads to the final crack shown in 4.8(f).

Fig. 4.9 shows the 3D volumes (1240×310×310μm^3) extracted at mid-thickness of post processed laminography data of damage evolution during the EDM machined edge loading. The 3D volume given in fig. 4.9(b) shows the machined edge in as-received state. The voids seem to be homogeneously distributed in the bulk material unlike the punched edge which presents an increased damage close to the edge surface. The damage growth seems to be homogeneous in the 3D volume given in fig. 4.9(c) which corresponds to CMOD=3mm. Fig. 4.9(d) at CMOD= 6.25mm shows the nucleation and growth of a new void population. The damage growth was higher in the bulk material away from the edge surface which is explained by the increased level of stress triaxiality in the bulk material (fig. 4.9(e) corresponding to CMOD=7.25mm). The crack leading to the final fracture occurred away from the edge surface (fig. 4.9(f) at CMOD=7.75mm). It was the result of the coalescence of voids nucleating and growing at least 1000μm away from the edge surface. We note that at the state presented in fig. 4.9(f), the crack close to the edge is still closed.

Fig. 4.10 shows the 2D minimal sections of the reconstructed laminography data shown in fig. 4.9 taken in the L-S plane. The initial specimen thickness was 0.8mm. At CMOD=5.5mm (fig. 4.10(b)), the deformation was homogeneously distributed in the specimen thickness. Necking was measured at the location of minimum thickness. In fig. 4.10(b), homogeneous necking of about 14% in the specimen thickness was observed. The increased stress triaxiality level occurred in the bulk material away from the edge surface was favored by the necking which was of about 40% and 27% at the edge (fig. 4.9(c) when CMOD is 7.25 mm). This is consistent with the higher damage growth in the bulk material observed in fig. 4.9(e).

For the punched edge, similar 2D sections have been examined and at crack initiation no necking was found ahead of the edge.

4.4.3 Quantitative analysis of damage evolution

Using the in-house code based on Python freeware, X-ray synchrotron laminography data were quantitatively analyzed. Fig. 4.11 shows the void volume fraction evolution, $< max_T(VVF) >_S$, in the L direction from the edge surface. For the punched edge the evolutions plotted correspond to the initial state, CMOD=2mm, CMOD=3mm, CMOD=4mm and CMOD=4.5mm. At the initial state of the punched edge, the $< max_T(VVF) >_S$ was of about 0.2% in the region situated at 200μm close to the edge surface and of 0.1% away from it, this is consistent with the litterature value [Dalloz et al., 2009] in terms of distance.

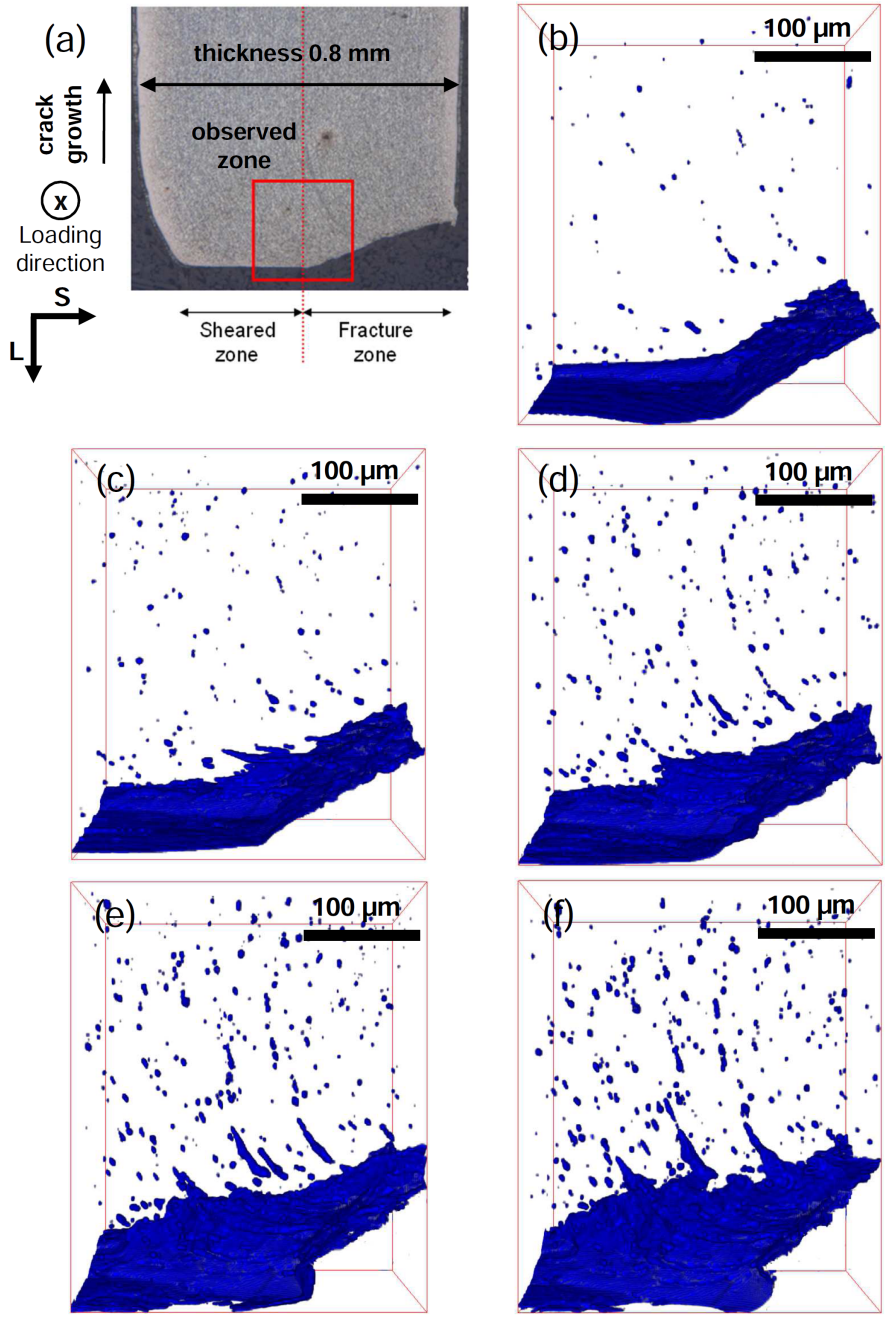

Figure 4.7 – 3D volumes of the reconstructed laminography data showing a region of $330\times400\times200\mu m^3$ in the L-S plane at mid-thickness of the damage evolution from a punched edge at different CMODs. Voids, specimen surface and the crack are shown in blue. The steel matrix is made transparent (a) schematic view illustrating specimen geometry, observed area location and loading and crack growth directions; (b) material at delivery state; (c) CMOD = $2mm$; (d) CMOD=$3mm$; (e) CMOD=$4mm$; (f) CMOD=$4.5mm$.

During notch opening, the $< max_T(VVF) >_S$ increases close to the edge surface. It reaches approximatively 0.35% at CMOD=$3mm$, 0.45% at CMOD=$4mm$ and 0.55% at CMOD=$4.5mm$. The maximum values shown for the CMOD=$4.5mm$ for the punched edge are measured close to the formed crack tip. This is in agreement with the results shown in (fig. 4.6), the void growth in the punched edge was higher close to the edge surface than in the bulk material.

The 3D sub-volumes of the machined edge analyzed correspond to the initial state, CMOD=$5.5mm$, CMOD=$6.25mm$ and CMOD=$7.25mm$. In the machined edge at the initial state after machining, the VVF measured was of about 0.1% across all the specimen thickness. As shown in fig. 4.9(b) the voids present in the DP600 bulk material are homogeneously distributed. At CMOD=5.5 and $6.25mm$, the $< max_T(VVF) >_S$ measured is

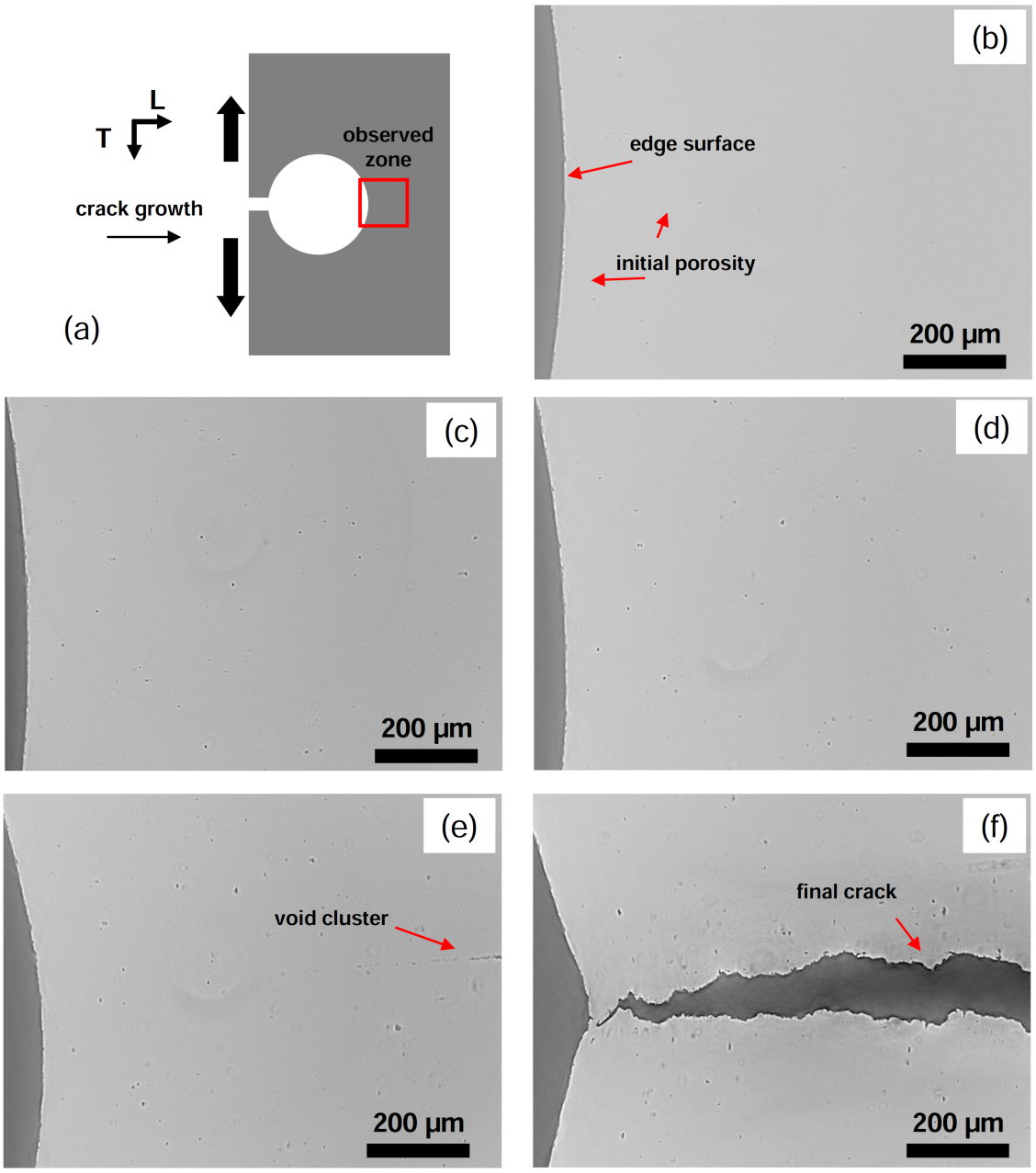

Figure 4.8 – 2D sections taken at mid-thickness of reconstructed laminography data showing damage evolution from a machined edge at differents CMODs (a) schematic drawing illustrating specimen geometry, ROI location and loading and crack growth directions (b) material at delivery state; (c) CMOD=3mm; (d) CMOD=6.25mm; (e) CMOD=7.25mm; (f) CMOD=7.75mm.

between 0.3 and 0.4%. The $< max_T(VVF) >_S$ measured in the machined edge at CMOD=7.25mm has reached more than 1% in the bulk material, however close to the edge surface the measured VVF was of about 0.35%. This was explained in 4.4.2 by the increased stress triaxiality generated away from the edge surface induced by necking in this area and thus the increased void density seen in fig. 4.9(e).

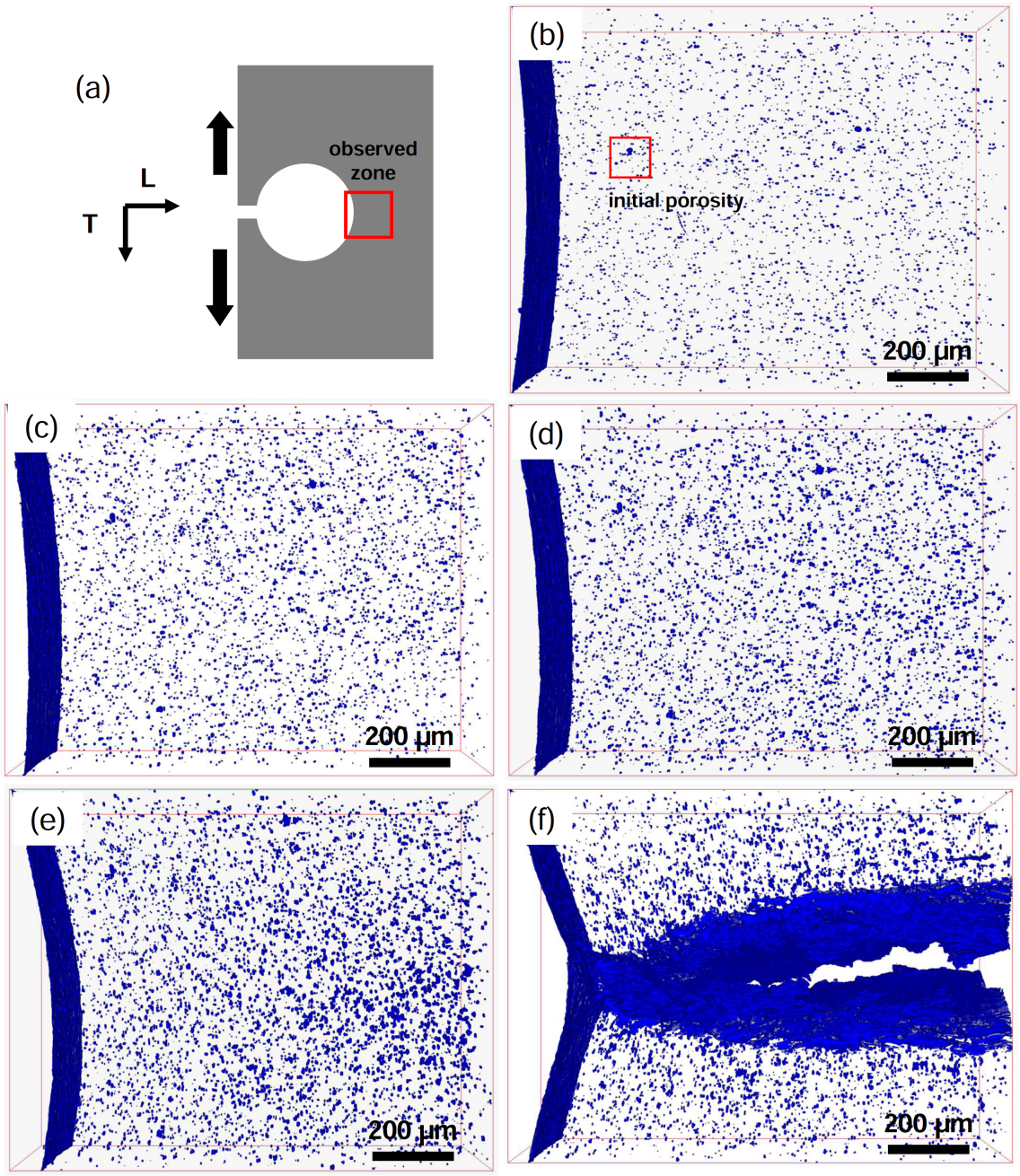

Figure 4.9 – 3D volumes of the reconstructed laminography data showing a region of 1240×930×310 μm^3 in the L-T plane at mid-thickness of the damage evolution from a machined edge at different CMODs. Voids, specimen surface and the crack are shown in blue. The steel matrix is made transparent (a) schematic drawing illustrating specimen geometry, observed area location and loading and crack growth directions; (b) material at delivery state; (c) CMOD = $3mm$; (d) CMOD=$6.25mm$; (e) CMOD=$7.25mm$; (f) CMOD=$7.75mm$ (final crack).

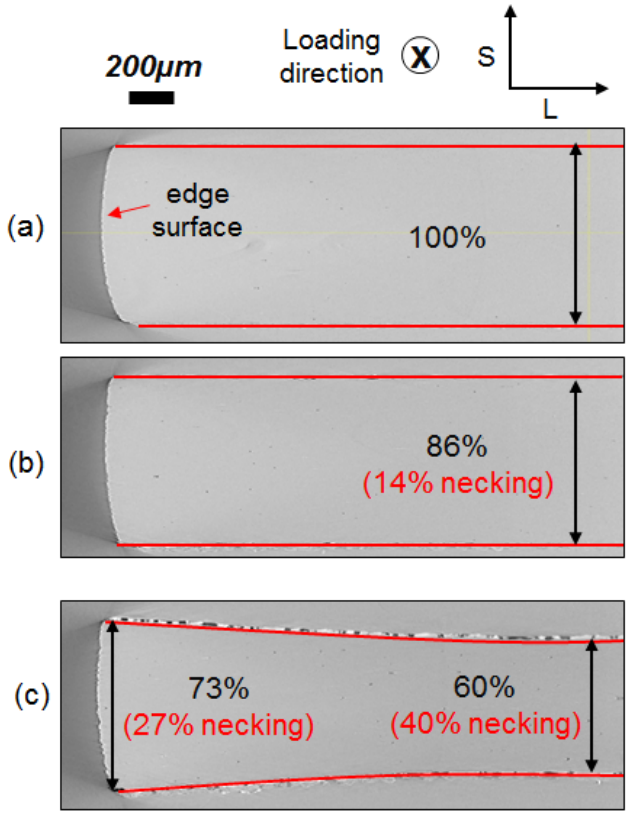

Figure 4.10 – 2D sections taken at the minimum L-S sections of reconstructed laminography data of damage evolution from a machined edge at differents CMODs: (a) material at delivery state; (b) CMOD=5.5mm; (c) CMOD=7.25mm. The specimen border was redrawn in red to improve clarity

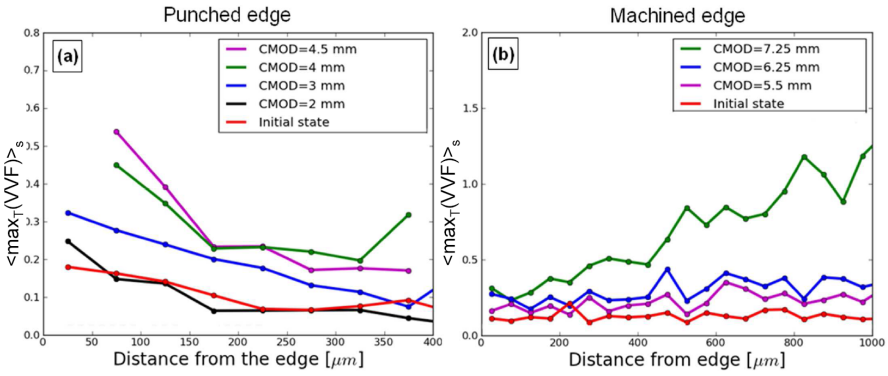

Figure 4.11 – Average of maximum void volume fraction values evolution in the studied DP steel at different CMODs: (a) punched edge. (b) machined edge

Part 2: Experimental investigation of edge fracture in FB steels using in situ 3D X-ray synchrotron laminography

4.5 Introduction

In this second part, damage mechanisms involved in edge fracture of a FB steel are studied. A punched edge produced with a clearance of 15% and a machined edge obtained by EDM (Electrical Discharge Machining) have been observed in 3D at initial state using X-ray laminography in order to quantify the effect of the cutting process on damage. In situ tensile tests were carried out to assess edge fracture via X-ray laminography technique. Digital image correlation has been performed using the images taken between loading steps in the region of interest where a spray paint speckle was applied on the specimen surface in order to determine the displacement field in the region of interest. The obtained X-ray laminography results have been compared to those obtained for the studied DP steel to understrand the impact of microstructures on the mechanical behavior at the edges. A quantification of damage evolution for the FB punched and machined edge during in situ laminography tests have been performed using the in-house python code discussed hereinbefore allowing to measure the average of maximum void volume fraction values. The in situ X-ray laminography observations presented in this part have been performed in ID15A beamline at ESRF Grenoble with a spatial resolution of $1.095\mu m$.

4.6 Punched edge profile

The FB punched edge hardening profile has been measured using the Vickers microindentation method with a load of $50g$. The hardening was calculated using the same formula introduced in part 1 of this chapter:

$$Hardening[\%] = \frac{HV_l - HV_\infty}{HV_\infty} \times 100 \tag{4.2}$$

Where HV_l is the microhardness measured at the distance l from the edge surface and HV_∞ is the base material microhardness. An increased hardness in the cutting-affected zone can be seen. The punching affected zone depth is approximately $500\mu m$. The obtained profile will be taken into account in further numerical analysis in order to study the pre-straining effect.

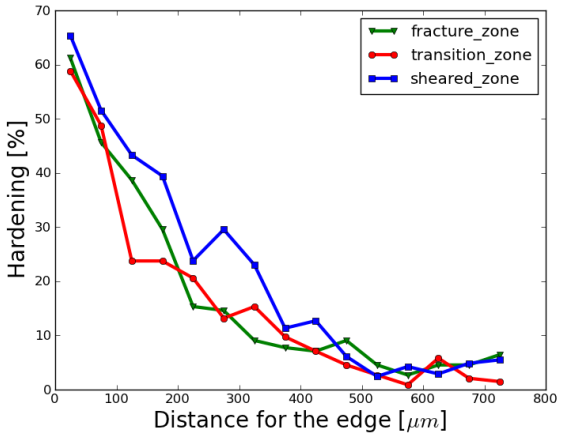

Figure 4.12 – The hardening profile along L direction on the investigated FB punched edge measured by Vickers microhardness technique in the fracture zone, sheared zone in the transition zone between both.

4.7 The punched edge

Using the two-screw loading device and the sample geometry described hereinbefore, in situ X-ray laminography observations have been carried out during mechanical testing of a hole with a radius of $5mm$ produced by punching with a clearance of 15%. An anti-buckling device was used to avoid the sample out-of-plane motion. For X-ray laminography observations, the rotation axis angle on the laminograph device was chosen to around 30° (=90° - θ). The acquisition of projection images was performed employing a filtred white beam centered around a $60keV$ X-ray energy with an isotropic voxel size of $(1.095\mu m)^3$.

4.7.1 2D sections of punched edge of the studied FB steel

2D sections at different loading steps taken in the fracture zone at $270\mu m$ from the sample surface are given in figure 4.13. These sections have been taken from filtered and binarized volumes using a 3D median filter with a radius of 2 voxels. The initial internal voids can be seen in black in the matrix. We notice that it is hard to distinguish particles from voids via X-ray laminography. At initial state, the edge surface exhibits a roughness in the fracture zone. Two microcracks initiate at the edge surface at CMOD=$3mm$ (see fig. 4.13(c)). In fig. 4.13(d), a microvoid is formed away from the edge surface at 700 μm. The microcrack is inclined at 45° compared to the loading direction. The formed microcrack grows and microvoids nucleate ahead of the crack tip (see fig. 4.13(e) and (f)). In fig. 4.13(g), we observe that the propagation direction of the formed crack is inclined at 45° compared to the loading direction and the void formed ahead of the edge surface grows following the loading direction.

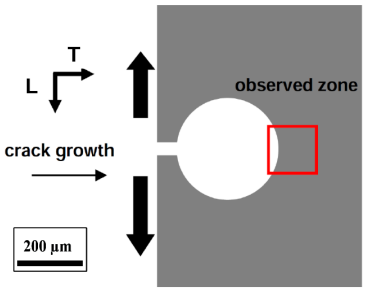

(a)

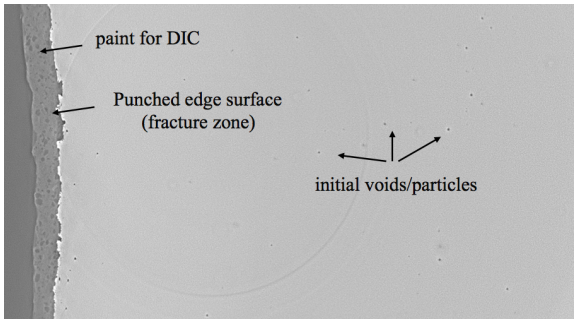

(b)

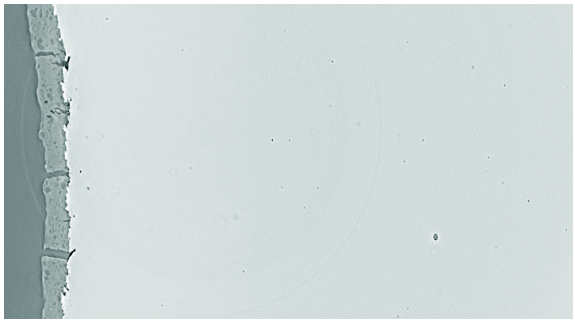

(c)

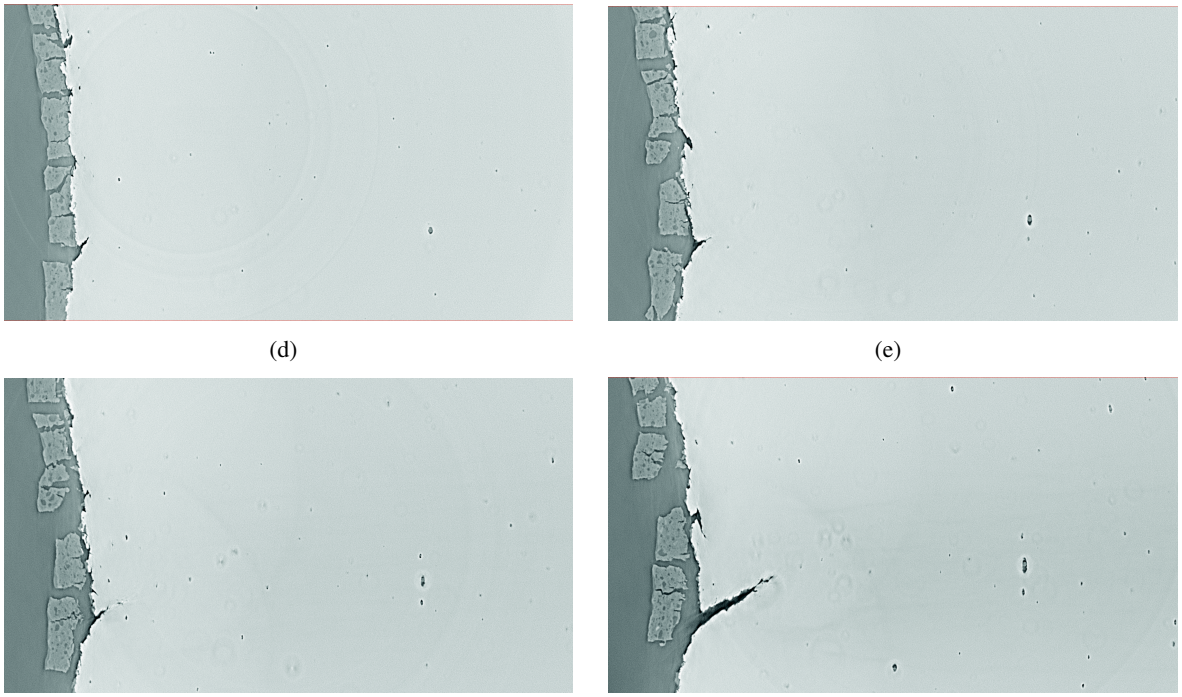

Figure 4.13 – 2D sections of laminography data taken at the fracture zone at 250 μm from the edge surface of the sheet plane of reconstructed laminography data showing damage evolution from a punched edge at different CMODs (a) schematic drawing illustrating specimen geometry, ROI location, loading and crack growth directions and the scale of shown sections; (b) material at delivery state; (c) CMOD=3mm; (d) CMOD=3.75mm; (e) CMOD=4mm; (f) CMOD=4.75; (g) CMOD=5mm

During mechanical testing of the studied DP punched edge, no necking has been observed. On the contrary, the FB punched edge presents a necking near the edge surface and ahead of it. Figure 4.14 gives 2 LS sections corresponding to CMOD=4.25mm taken at 100μm and 600μm ahead of the edge surface showing the necking that undergoes the punched edge during mechanical loading.

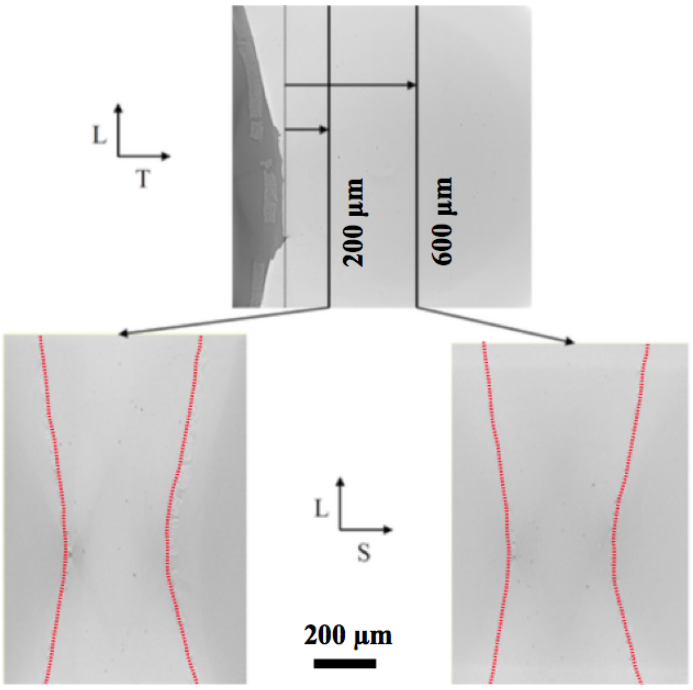

Figure 4.14 – 2D sections of reconstructed laminography data of punched edge taken at two different positions from the edge surface at CMOD=4.25mm (the specimen border was redrawn in red to improve clarity)

4.7.2 3D observations of punched edge of the investigated FB steel

In situ X-ray synchrotron laminography has made possible, for the first time, the visualization in three dimensions of the damage evolution from a FB punched edge during mechanical loading. Regions of $1240\times930\times310$ μm^3 taken at each loading step are shown in figure 4.15. The voids and the edge surface segmented and visualized in L-T plane, are shown on red. Bainite and ferrite appear transparent. The as-received material after punching is shown in fig. 4.15(b). During mechanical loading, the void distribution seems to be homogeneous near the edge surface and ahead of it (fig. 4.15(c) and (d)). At CMOD=4.25 corresponding to fig. 4.15(e), the void growth near the edge surface is slightly higher than the one observed ahead of the edge surface. In figure 4.15(f), a crack initiated on the edge surface and inclined at 45° to the loading direction can be observed. An increased void growth is also observed ahead of the crack tip at CMOD=5mm. The crack propagates and coalesces with the internal damage leading to the fracture of the tested specimen.

The 3D volumes given in figure 4.16 are the same as those in figure 4.15 but seen along the loading direction. These volumes of $540\times310\times310\mu m^3$ extracted at mid-thickness of the specimen show the fracture zone and the sheared zone with a view along the loading direction. Figure 4.16(b) shows the punched edge profile as delivery state after punching operation. Voids nucleated close to the edge surface and needle-shape voids initiated at the fracture zone surface can be seen. The needle-shape prolate voids are consistent with those found during testing of base materials. Figures 4.16(c) and (d) corresponding to CMOD=3mm and CMOD=4mm respectively show the growth of the needle-shape voids and pre-existing internal voids during mechanical loading. A crack inclined at at 45° to the loading direction is formed in the fracture-to-sheared transition zone (see fig. 4.16(e) and (f)). At CMOD=4.75 corresponding to figure 4.16(g), the crack formed coalesces with the internal voids and propagates to the sheet bulk inclined by 45° compared to the loading direction.

4.8 The FB600 machined edge

4.8.1 Qualitative 2D observations provided during in situ X-ray laminography testing

The figure 4.17 shows the 2D sections taken at mid-thickness of filtered reconstructed laminography data. We observe the presence of a laminography artifact which does not influence strongly the segmentation of the voids. The acquisitions were performed with much better signal-to-noise ratio than those shown earlier for the DP punched edge. The fracture mechanism observed for the studied FB machined edge with a radius of $5mm$ produced by EDM is similar to the DP machined edge discussed above but very different from the FB punched edge described hereinbefore. The sections given in figures 4.17(b), (c) and (d) corresponding to the initial state, CMOD=3mm and CMOD=4mm show that the edge surface does not present any microcrack. However, in the fig. 4.8(e), we observe a high damage amount leading to the formation of a cluster of aligned voids away from the edge surface which leads to the final crack of the specimen.

The 2D minimal sections of the reconstructed laminography data taken in the T-S plane are shown in figure 4.18. The initial specimen thickness was $0.8mm$. The deformation was homogeneously distributed in the specimen thickness at CMOD=2.5mm. At this loading step, homogeneous necking of about 26% in the specimen thickness was observed. At CMOD=4.75mm, the necking was about 50% in the bulk material and 40% at the egde. This is due to the increased level of the stess triaxiality occured in the bulk material away from the edge surface. The L-S sections taken at different positions from the edge surface given in figure 4.19 show the necking occured during mechanical loading of the FB600 machined edge at CMOD=4.75 mm.

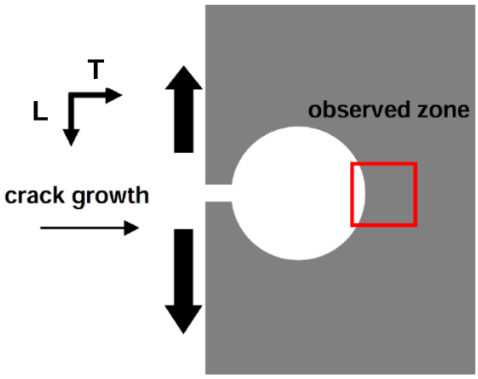

(a)

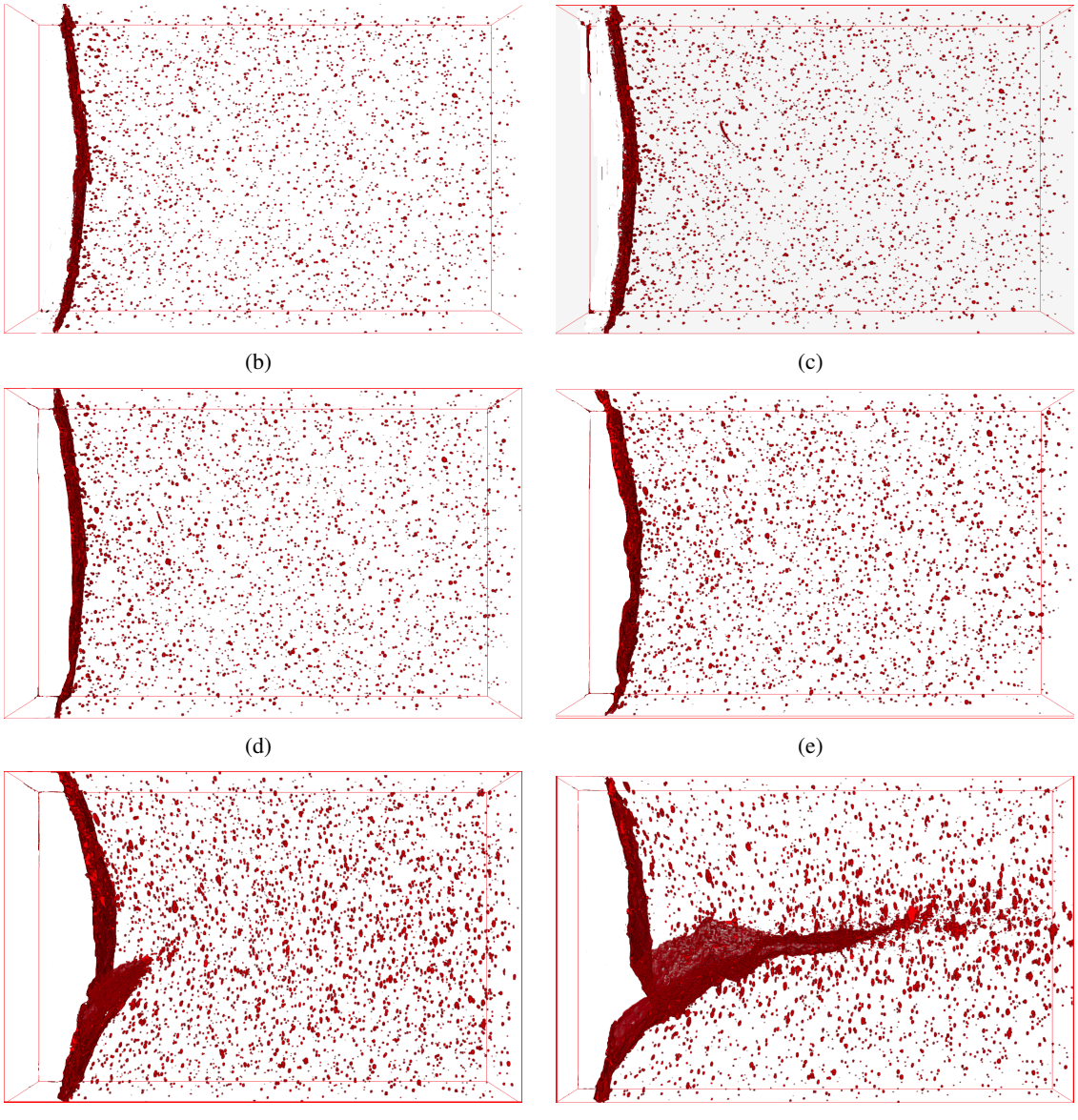

(b) (c)

(d) (e)

(f) (g)

Figure 4.15 – 3D volumes of the reconstructed laminography data showing a region of 1240×930×310 μm^3 in the T-L plane at mid-thickness of the damage evolution from a punched edge at different CMODs. (a) schematic drawing illustrating specimen geometry at the punched hole, observed area location and loading and crack growth directions; (b) material at delivery state; (c) CMOD = 2mm; (d) CMOD=3mm; (e) CMOD=4.5mm; (f) CMOD=5mm; (g) CMOD=5.5mm

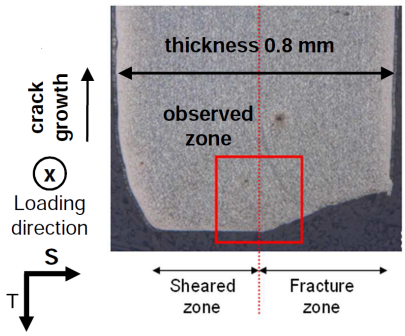

(a)

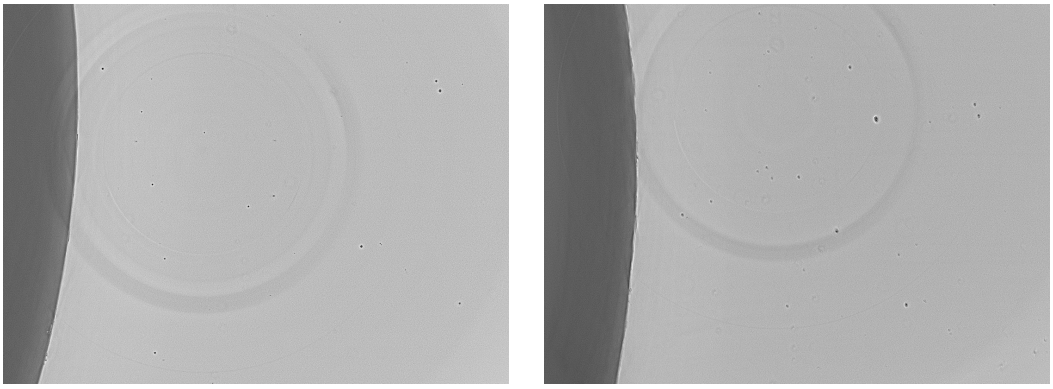

(b) (c)

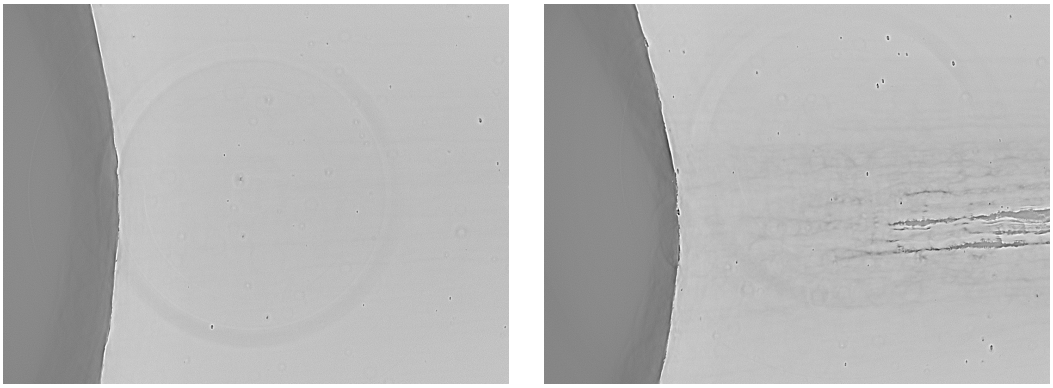

(d) (e)

Figure 4.17 – 2D sections taken at mid-thickness of reconstructed laminography data showing damage evolution from a machined edge at differents CMODs (a) schematic drawing illustrating specimen geometry, ROI location and loading and crack growth directions (b) material at delivery state; (c) CMOD=3mm; (d) CMOD=4.5mm; (e) CMOD=5mm

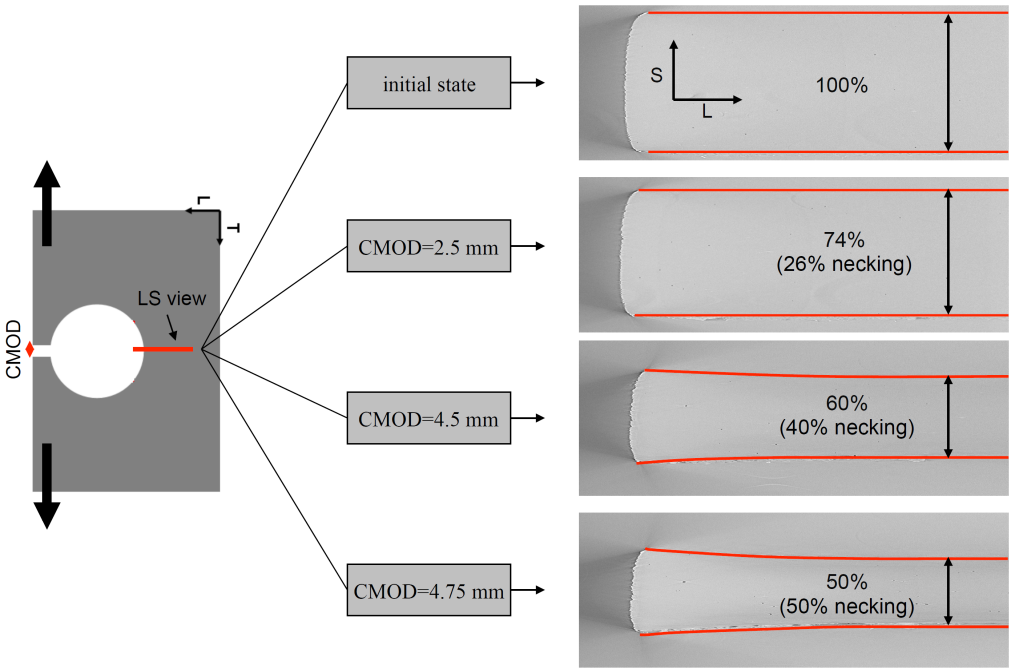

Figure 4.18 – 2D sections of reconstructed laminography data of machined edge taken at the minimal T-S sections at different CMODs (the specimen border was redrawn in red to improve clarity)

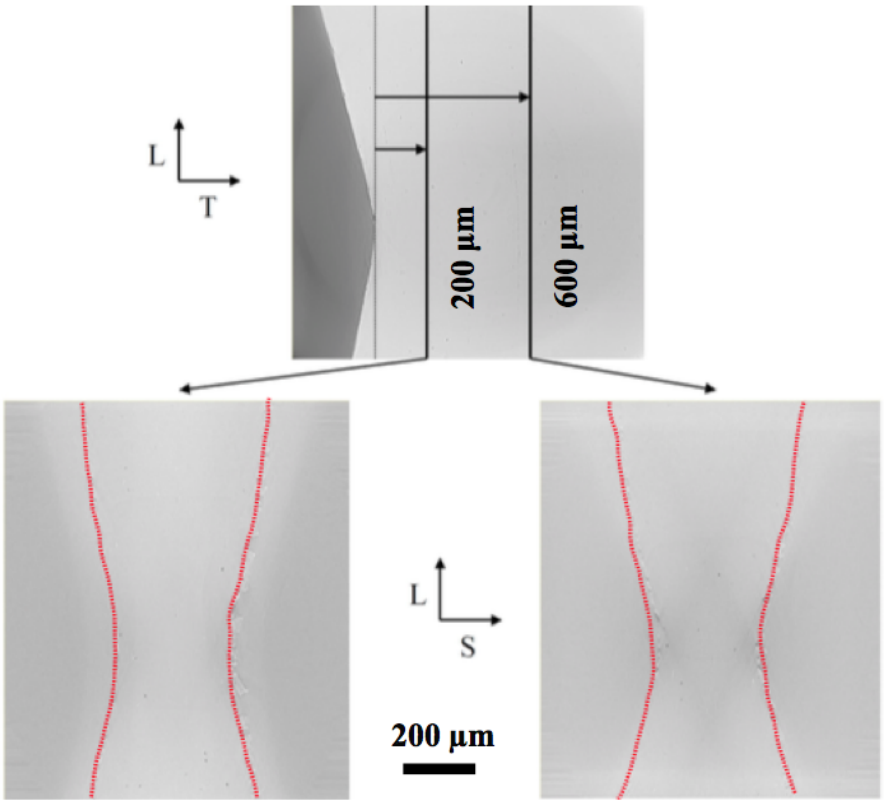

Figure 4.19 – 2D sections of reconstructed laminography data of machined edge taken at two different positions from the edge surface at CMOD=4.75mm (the specimen border was redrawn in red to improve clarity)

4.8.2 Qualitative 3D observations provided during in situ X-ray laminography testing

Figure 4.20 shows the 3D volumes (1240×930×310 μm^3) extracted at mid-thickness of post-processed X-ray laminography data acquired during the in situ mechanical testing of the studied EDM FB machined edge. The as-received state of the investigated machined edge is given in fig. 4.20(b). The voids seem to be

homogeneously distributed in the bulk material at the initial state (fig. 4.20(b)) and during the first steps of mechanical loading (fig. 4.20(c) and (d)). The growth of the pre-existing voids and the nucleation of new void population are observed at CMOD=4.5mm (fig. 4.20(e)). The damage growth was higher in the bulk material away from the edge surface which is explained by the increased stress triaxiality and plastic strain in the bulk material (see fig. 4.20(f)). The final crack of the specimen was initiated in the bulk material, which was the result of the coalescence of void nucleating and growing away from the machined edge surface, which is still closed close to the edge.

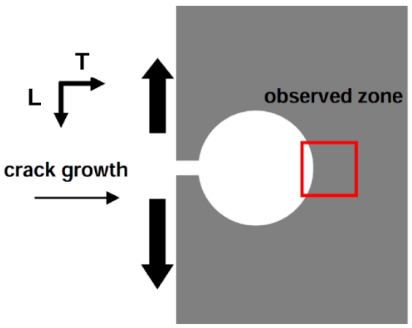

(a)

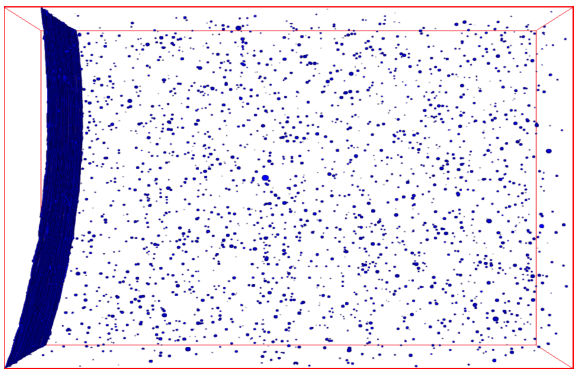

(b)

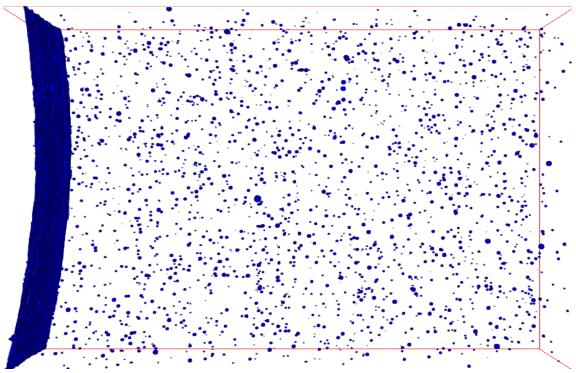

(c)

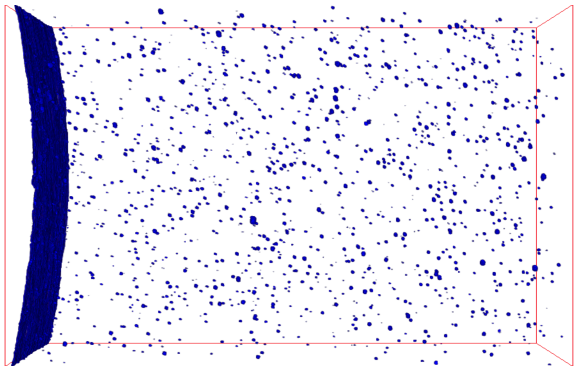

(d)

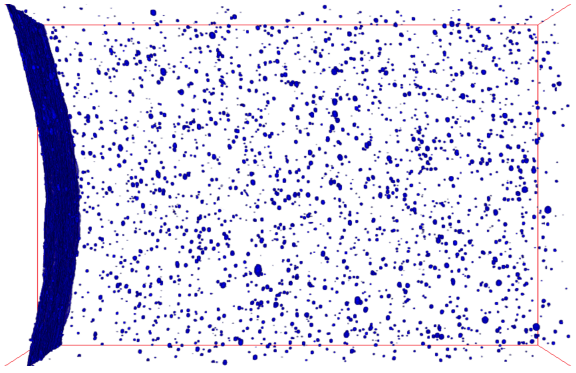

(e)

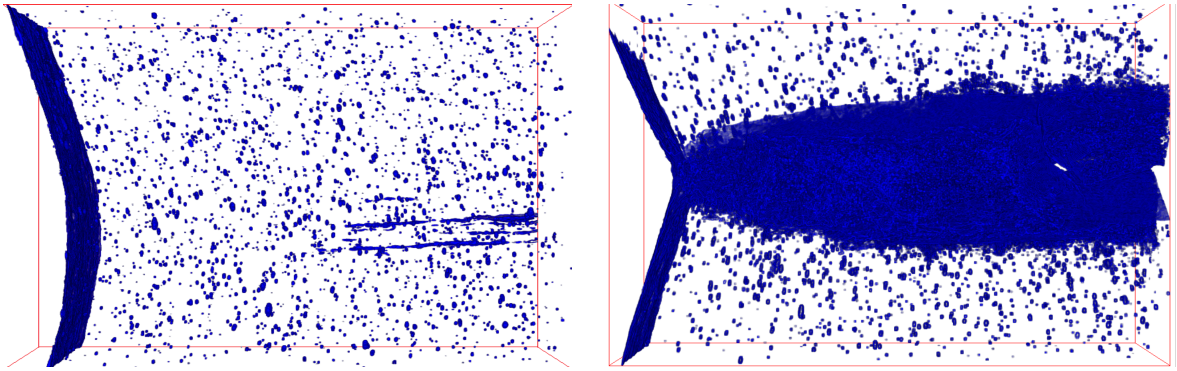

(f) (g)

Figure 4.20 – 3D volumes of the reconstructed laminography data showing a region of 1240×930×310 μm^3 in the T-L plane at mid-thickness of the damage evolution from a punched edge at different CMODs. (a) schematic drawing illustrating specimen geometry at the punched hole, observed area location and loading and crack growth directions; (b) material at delivery state; (c) CMOD = 3mm; (d) CMOD=3mm; (e) CMOD=4.5mm; (f) CMOD=5mm; (g) CMOD=5.5mm

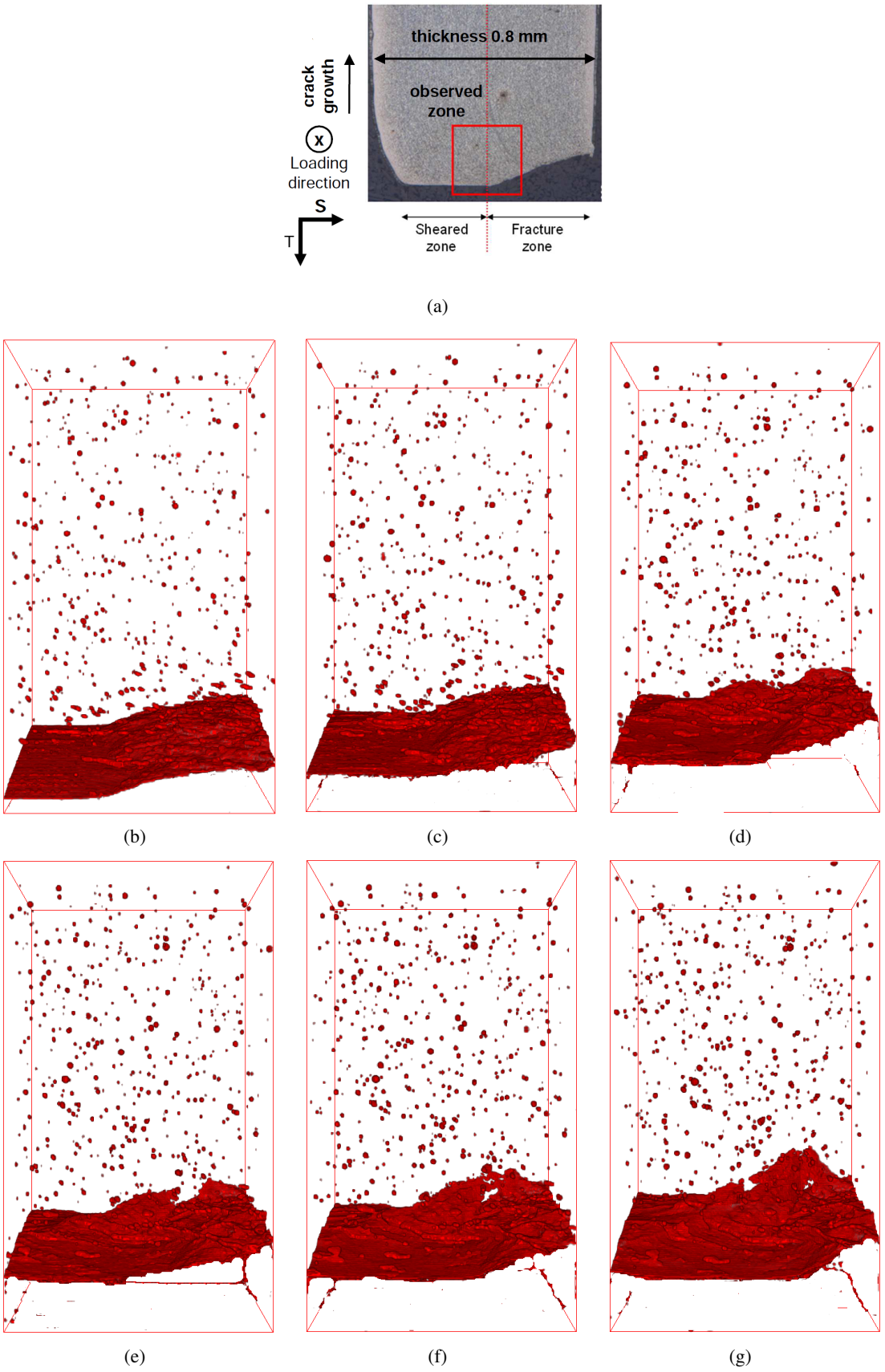

Figure 4.16 – 3D volumes of the reconstructed laminography data showing a region of $540 \times 310 \times 310 \mu m^3$ in the L-S plane at mid-thickness of the damage evolution from a punched edge at different CMODs. Voids, specimen surface and the crack are shown in red. The steel matrix is made transparent (a) schematic view illustrating specimen geometry, observed area location and loading and crack growth directions; (b) material at delivery state; (c) CMOD = $3mm$; (d) CMOD=$4mm$; (e) CMOD=$4.25mm$; (f) CMOD=$4.5mm$; (g) CMOD=$4.75mm$

Part 3: Quantification of in situ X-ray synchrotron laminography tests of DP and FB studied edges

4.9 Quantification of X-ray laminography observations

4.9.1 Digital image correlation

Surface digital image correlation (DIC) was performed using Correli^{Q4} software in order to measure the displacement fields in the region of interest. Between loading steps, images were taken in the region of interest where a spray paint speckle was applied on the specimen surface. The DIC was performed by updating the reference image and using an element size of 180×180 μm^2 and a ROI of 4×2 mm^2. The DIC results are used for comparison and as input data for FE simulation. Figure 4.21(b) shows the evolution of displacement of the point A (see fig. 4.21(a)) taken at the same position for the FB punched and machined edges with the CMOD values measured in the CMOD measurement location shown in fig. 4.3. We observe that the displacement of the point A for the punched edge and the machined edge evolve in the same way during mechanical loading. The fracture of the punched edge and of the machined edge occurred at CMOD=5 mm and at CMOD=5.75 mm, respectively.

For the DP steel, the DIC results of DP punched and machined edge are given in figure 4.21(c). A strong reduction of ductility (approximately 38%) is observed due to the presence of the punched edge. Indeed, the fracture of the machined edge occured at CMOD=7.25 mm, in contrast, a crack appears during mechanical loading of the DP punched edge at CMOD=4.5 mm.

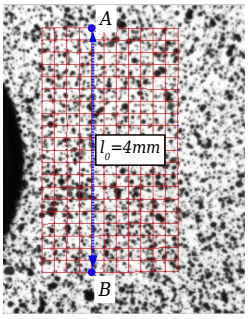

(a)

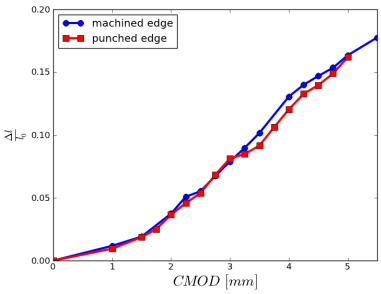

(b)

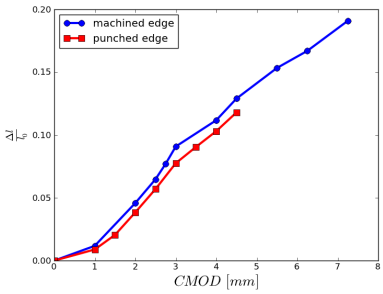

(c)

Figure 4.21 – (a) Schematic draw showing the ROI and the initial mesh used for digital image correlation and the location of displacement measurement. (b) The evolution of displacement of $\frac{\Delta l}{l_0}$ with CMOD for the punched and machined edges: (b) FB steel, (c) DP steel

4.9.2 Damage quantification

4.9.2.1 Initial state

To quantify the impact of punching process on the mechanical state of the studied punched edge the void number N and the void size R_{eq} were measured using a strategy to quantify damage in X-ray tomography data described in chapter 2. The quantification method consists in discretizing the X-ray laminography data of the punched edge at initial state into sub-volumes of $350\times50\times50$ μm^3 taken from the fracture zone and the sheared zone (see fig. 4.22).

The distributions of void number and mean void size from the edge surfaces are given in figure 4.22(b) and (c) for the FB punched edge and in figure 4.22(d) and (e) for the FB machined edge. For the two studied punched edges, we observe that close to the fracture zone the damage initiation is higher than in the bulk material away from the edge surface. However, the sheared zone does not exhibit a difference in void density close to the edge surface and ahead of it. The mean equivalent void radius distribution in the specimen thickness is homogeneous in the sheared zone and the fracture zone for the DP punched edge and the FB punched edge (see 4.22(c) and (e)). We conclude that punching process causes a pre-damage close to edge surface for the studied materials. For the two studied punched edges, at initial state, there are twice more micrometer-size voids close to the fracture zone than away from the edge for both materials.

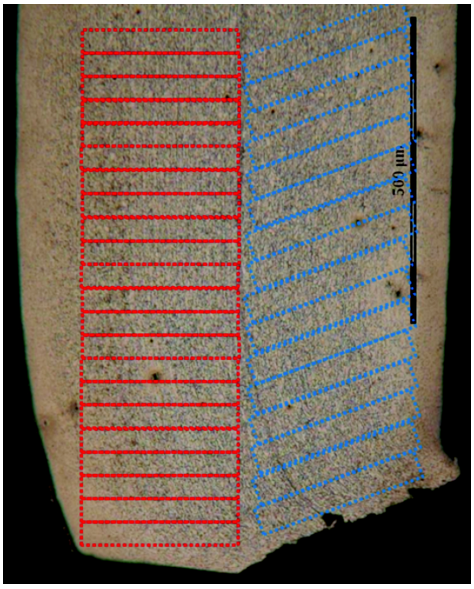

(a)

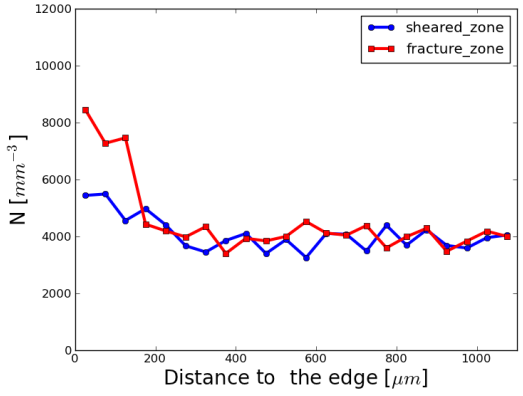

(b) FB steel

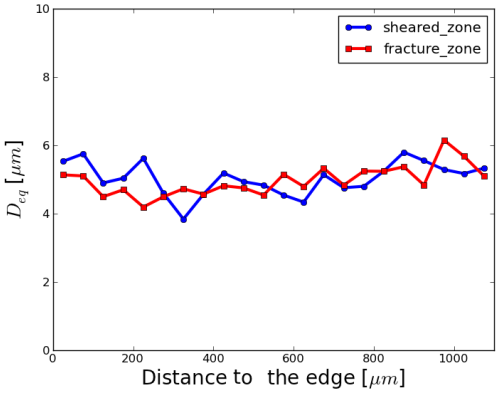

(c) FB steel

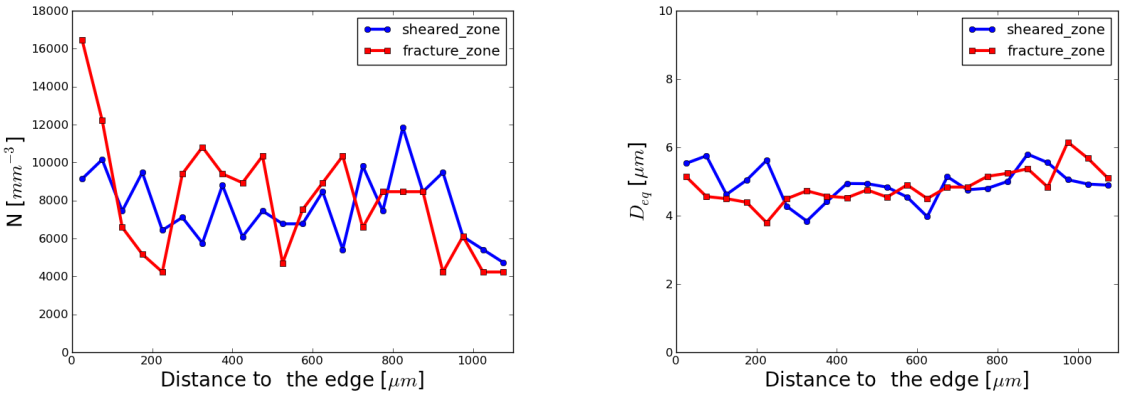

(d) DP steel

(e) DP steel

Figure 4.22 – Damage quantification in the studied punched edges for both materials: (a) schematic illustration of the discretization method used to quantify damage (voids) in the investigated punched edge; (b) and (d) distribution of void number from punched edge surface in sheared and fractured zones for the FB and DP steels, respectively; (c) and (e) evolution of void size in the sheared and fracture zones from the punched edges surface for the FB and DP steels, respectively

4.9.2.2 Quantitative analysis of damage evolution

Using the quantification method described in the first part of this chapter, the average of the maximum values of void volume fraction $< max_L(VVF) >_S$ was measured in X-ray laminography data for the studied punched and machined edge using sub-volumes of 1240×930×310 μm^3 and a ROI of 50×50×50 μm^3. For the punched edge, the plotted evolutions corresponded to the initial state, CMOD=4 mm and CMOD=4.75 mm. For the punched edge, the measured $< max_L(VVF) >_S$ at initial state was 0.35% at 50 μm close to the edge surface and about 0.15% away from it. During mechanical loading, the $< max_L(VVF) >_S$ increases close to the edge surface. At CMOD=4.75 mm, the $< max_L(VVF) >_S$ reaches approximately 0.74% close to the edge surface and about 0.4% in the bulk material. This is in agreement with the results shown in fig. 4.15. Void growth was observed close to the edge and in the bulk but it was higher close to the edge surface than in the bulk materials. The void growth observed in the bulk material away from the edge surface is explained by the substantial necking that the specimen undergoes during mechanical loading and which generates an increased level of the stress triaxiality.

The 3D analyzed sub-volumes of the machined edge correspond to the initial state, CMOD=4 mm and CMOD=5 mm. At the initial state, the measured $< max_L(VVF) >_S$ was of about 0.15% across all the specimen thickness. At CMOD=4 mm, the measured $< max_L(VVF) >_S$ remained similar from the edge surface to the material bulk in the analyzed sub-volume along the L-direction. However, at CMOD=5 mm $< max_L(VVF) >_S$ reaches approximately 0.8% in the bulk material in 900 μm away from the edge surface but close to the edge surface it was of about 0.4%.

4.10 Conclusions

The experimental study presented in this part aimed at characterizing the initial damage state and subsequent damage evolution during mechanical loading for DP and FB steels: 1) a *punched edge* and 2) a *machined and finely ground edge*. For the DP steel, A strong reduction of ductility of approximately 38% is observed on DIC results. This is due to the presence of punched edge.

3D imaging using synchrotron radiation computed laminography has allowed us to identify different defects that the DP punched edge contains at the initial state. These include: roughness in the fracture zone, needle-shape voids in the bulk from fracture zone and alignment of needle voids along the flow lines i.e. martensite alignments. The 3D in situ laminography observation carried out on a sample with a circular punched hole has allowed us to characterize, for the first time, the damage evolution from a cut-edge in situ and in 3D

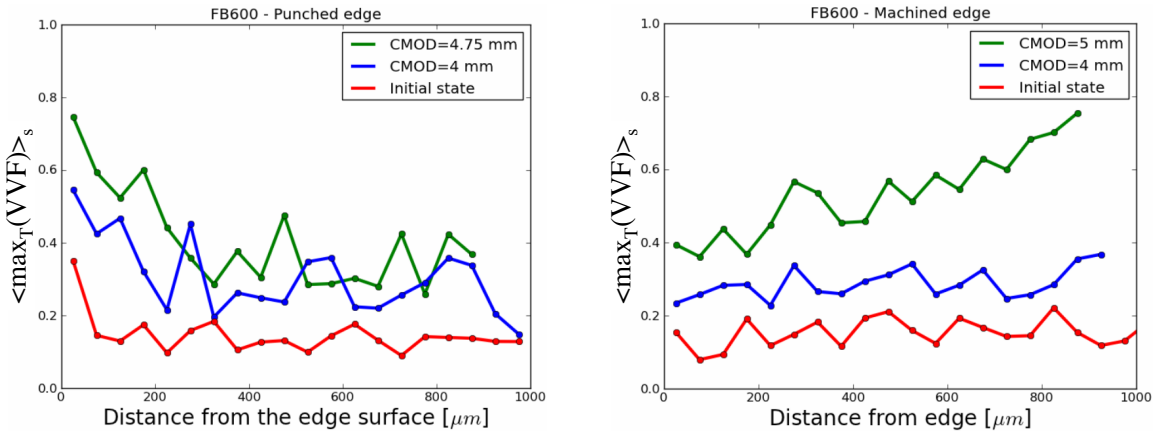

(a) (b)

Figure 4.23 – Average of maximum void volume fraction values evolution during in situ laminography testing of the studied FB steel at different CMODs: (a) punched edge. (b) machined edge

during mechanical loading. The novelty of high energy synchrotron laminography is that regions of interests in large flat steel specimens can be investigated. Due to this possibility, boundary conditions close to those encountered during metal sheet forming are applied here. The growth of needle voids was especially along flow lines from fracture zone surface but also in the bulk along the martensite alignments. The initial void growth direction corresponds thus to the S direction (thickness). We observe that the coalescence of needle voids from the fracture zone with the sheared zone occurs via narrow coalescence zones (void sheets). These cracks are inclined by 45° compared to the L-direction. Several cracks are formed, especially in the fracture zone, but the one located close to a geometrical defect grows faster.

In contrast, for the case of the DP machined edge, the damage does not start from the edge but in the material bulk that has undergone substantial necking during loading. The local necking appearing away from the edge is accompanied with an increased damage accumulation that leads to the final crack.

3D image analysis was performed to quantify the damage at initial state and its evolution during mechanical loading. A slightly increased level of void volume fraction was measured close to the punched edge surface (in the punching-affected zone). The damage starts in a very localized way from the fracture zone (needle-shape voids) because cutting strongly weakens the material locally.

For the FB steel grade, the following conclusions can be made:

- The fracture of the FB punched edge was observed at CMOD=5 mm and the FB machined edge fracture occurred at CMOD=5.75 mm.
- At delivery state, using X-ray laminography the impact of punching process was studied. Indeed, roughness of fracture zone and many needle-shape microcracks initiated at the fracture zone were observed.
- The studied punched edge exhibits an increased void density near the edge surface particularly in the fracture zone. However, the mean void size remains similar from the edge surface to the material bulk in the sub-volumes along the L-direction.
- During mechanical loading, using the quantification method discussed in the first part of this chapter, the maximum value of VVF, $< max_T(VVF) >_S$, which is relatively increased near the edge surface at initial state, seems to increase in a homogeneous way in the studied sub-volume along T direction. Substantial necking was observed at two positions for CMOD=5mm : 200 and 600 μm from the edge surface. The homogeneous increase of void size measured in the FB punched edge, unlike the case of DP punched edge, is mainly due to the substantial necking along the T direction during loading. These experimental findings are different from those obtained for the DP punched edge for which similar 2D sections have been examined. At crack initiation no necking was found ahead of the edge.

- For the FB machined edge, the maximum value of VVF $< max_T(VVF) >_S$ is homogeneous along the T direction in the studied sub-volume. In contrast, during loading this value $< max_T(VVF) >_S$ became higher away from the edge surface. This is due to the void coalescence that occurs in the bulk material which has undergone substantial necking. These experimental results obtained for the FB machined edge are consistent with those observed in the DP machined edge.
- Using X-ray laminography 2D sections, void nucleation was observed on some particles and an increased void growth was observed along the loading direction for the punched and machined edges.

Chapter 5

Numerical simulation of edge fracture in DP and FB steels

Contents

5.1 Résumé

Des calculs 3D par éléments finis couplés à la corrélation d'image ont été réalisés en utilisant les lois de comportement élasto-plastiques des matériaux étudiés. Ceux-ci ont montré que le profil de bord poinçonné ne permet pas de localiser la triaxialité de contrainte et la déformation plastique proche du bord. Ces paramètres mécaniques locaux ont été localisés loin de la surface des bords ce qui est cohérent avec le niveau d'endommagement important apparu dans cette région lors des essais de laminographie. Ces calculs ont servi pour valider les critères d'endommagement de germination et de croissance de cavités identifiés sur les matériaux de bases. Pour les deux matériaux étudiés, en introduisant le pré-écrouissage et le pré-endommagement induits par la découpe, la fraction volumique de cavités est maximale proche de la surface du bord poinçonné lors du chargement mécanique. Par contre, la fraction volumique de cavités est relativement plus importante, pour les deux matériaux, loin des bords usinés lors du chargement mécanique.
L'essai d'expansion de trou a été utilisé pour réaliser une étude paramétrique permettant de valider les critères de germination et de croissance de cavités développés en faisant varier l'épaisseur de la tôle et la pré-déformation. Pour les deux matériaux, une chute de ductilité, relative à la réduction de ratio d'expansion de trou (HER), est observée pour les bords poinçonnés. Pour l'acier FB, les résultats expérimentaux et numériques ont montré que le ratio d'expansion de trou, pour les quatre épaisseurs étudiées, augmente quand l'épaisseur de la tôle augmente. Il a été expérimentalement et numériquement montré que la pré-déformation n'a aucune influence sur la formabilité du bord usiné FB. Par contre, les calculs éléments finis ont mis en évidence la sensibilité de la nuance DP à la pré-déformation et au pré-endommagement. Les valeurs du HER prédites par le modèle proposé, basé sur une valeur critique de fraction volumique de cavités (f_c) de l'ordre de 0.2% pour les deux matériaux, sont inférieures aux valeurs expérimentales. Cette sous-estimation est dûe au caractère très local du modèle qui consiste à mesurer le HER lorsqu'un point d'intégration atteint la valeur critique f_c=0.2%.

In this part, a numerical study is carried out in order to interpret the mechanical behavior at the investigated cut-edges. Using elasto-plastic behavior of the studied materials, a numerical simulation of the mechanical test performed during synchrotron X-ray laminography observations is presented. This was performed to understand the effect of edge profile on the mechanical behavior at the edges. The plastic strain and the stress triaxiality evolution have been calculated in order to build a link between those local mechanical parameters and mechanical behavior at the studied edges. Hole expansion simulation has been performed using the void nucleation criterion, the void growth model and the void coalescence conditions identified on X-ray tomography data. Those identified criteria have been used as post-processing of elasto-plastic calculations of notch opening test and hole expansion test for the two investigated materials. A part of the 3D numerical study of the DP punched and machined edge presented in this chapter has been published in [Kahziz et al., 2015].

5.2 Introduction

The numerical investigation presented in this part performed using elasto-plastic constitutive equations with optimized parameters provided by ArcelorMittal Global R&D was carried out using Z-set software in order to interpret the mechanical behavior at edges for both materials and reproduce the experimental results obtained via in situ X-ray synchrotron laminography. 2D plane-stress finite element analysis was carried out on the whole specimen geometry in order to extract the displacement fields around the punched and the machined edge that will be used as boundary conditions for the optimized 3D elasto-plastic simulation. The determined displacement fields have been validated using 2D digital image correlation via Correli software on images taken on in situ laminography specimens surface after each loading step.

To validate the identified criteria based on Chu and Needleman approach and Rice and Tracey model modified by Huang modeling void nucleation and growth in the studied materials, respectively, the notch opening test (the in situ laminography test) and hole expansion test were used.

5.3 Constitutive equations of the studied materials

The invariant stress and strain rate measures $\underline{\sigma}$ and $\underline{\dot{\varepsilon}}$ are defined by transport of the Cauchy stress $\underline{\mathbf{T}}$ and strain rate $\underline{\mathbf{D}}$ into the corotational frame characterized by the rotation $\underline{\mathbf{Q}}(\underline{\mathbf{x}},\mathbf{t})$. This change of frame takes place at each material point:

$$\begin{cases} \underline{\sigma} = \underline{Q}\cdot\underline{T}\cdot\underline{Q}^T, \\ \underline{\dot{\varepsilon}} = \underline{Q}\cdot\underline{D}\cdot\underline{Q}^T, \\ \underline{Q}\ such\ as\ \dot{\underline{Q}}^T\cdot\underline{Q} = \underline{\Omega}\ \text{(corotational)}, \end{cases} \tag{5.1}$$

where $\underline{\Omega}$ is the skew-symmetric part of the gradient $\underline{\mathbf{L}}$ of the velocity field [Besson et al., 2010]. The strain rate tensor $\underline{\dot{\varepsilon}}$ is split into elastic and plastic contributions, the evolution of the latter being given by the plastic flow rule.

$$\underline{\dot{\varepsilon}} = \underline{\dot{\varepsilon}}_e + \underline{\dot{\varepsilon}}_p \tag{5.2}$$

$$\underline{\sigma} = \underline{\underline{E}}.\underline{\varepsilon}_e \tag{5.3}$$

$$f(\underline{\sigma}, p) = J_2(\underline{\sigma}) - R(p) \tag{5.4}$$

$$\dot{\underline{\varepsilon}}_p = \dot{p}\frac{\partial f}{\partial \underline{\sigma}} = \frac{3}{2}\frac{\underline{s}}{J_2(\underline{\sigma})} \tag{5.5}$$

where $J_2(\underline{\sigma})$ is the Von Mises invariant of the stress tensor, $\underline{\mathbf{s}}$ is the deviatoric part of the stress tensor $\underline{\sigma}$, $R(p)$ is the non-linear hardening law. A Non-linear (Armstrong-Frederick type) kinematic hardening was included in the model using two back-stresses [Chaboche, 2008].

$$\underline{X} = \underline{X}_1 + \underline{X}_2 \tag{5.6}$$

$$with\ \dot{\underline{X}}_1 = \frac{2}{3}C_1\dot{\underline{\varepsilon}}_p - \dot{p}D_1\underline{X}_1\ \ and\ \ \dot{\underline{X}}_2 = \frac{2}{3}C_2\dot{\underline{\varepsilon}}_p - \dot{p}D_2\underline{X}_2 \tag{5.7}$$

where C_1, D_1, C_2 and D_2 are materials parameters. An isotropic hardening function $R(p)$ was chosen.

$$R(p) = R_0 + Q(1 - \exp(-bp)) \tag{5.8}$$

Table 5.1 shows the optimised material parameters of the investigated DP600 laboratory steel that reproduce very well tensile and reverse shearing curves (fig. 5.1). Reverse shearing corresponds to in plane shearing where the shearing direction is inverted at a given strain [Rèche et al., 2012]. These material parameters are identified using unpublished tensile and reverse shearing tests performed at ArcelorMittal Global R&D for the material of our study.

Table 5.1 – Optimised material parameters for constitutive equations

	$R_0\ [MPa]$	$Q\ [MPa]$	b	D_1	$C_1\ [MPa]$	D_2	$C_2\ [MPa]$
DP steel	217	274	23.19	2.36	767	155	30000
FB steel	426	151	6.45	0.5	330	175	25480

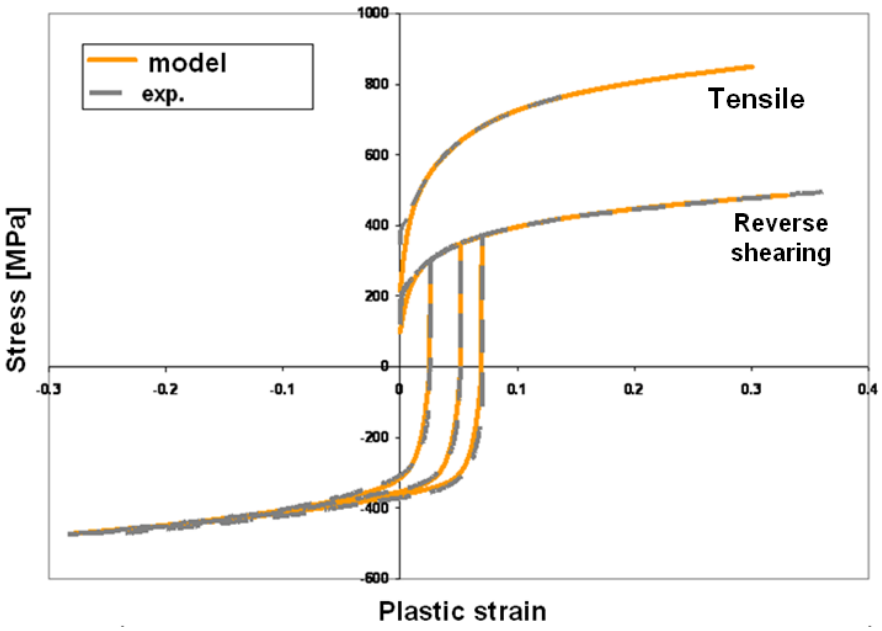

(a)

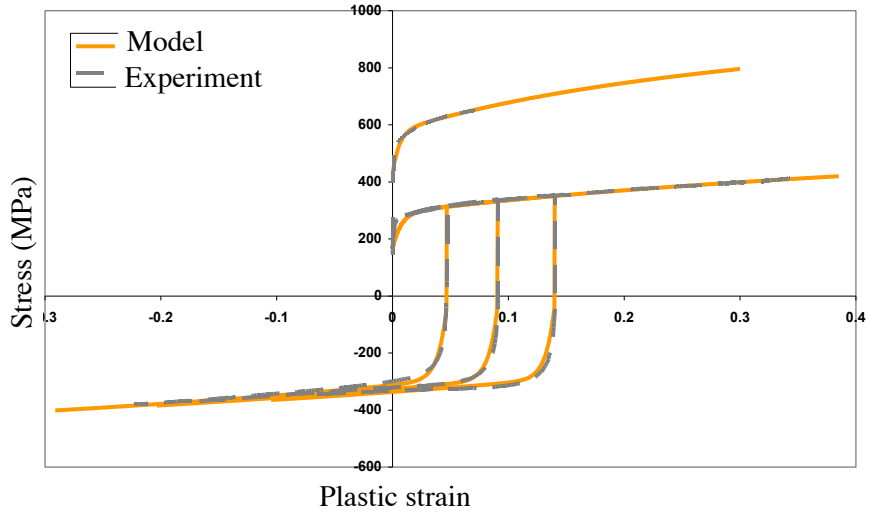

(b)

Figure 5.1 – True tensile stress-strain and reverse shearing curves of the investigated materials: (a) DP steel, (b) FB steel

5.4 Notch opening simulation (in situ laminography test)

To interpret further the present results in particular the crack initiation location for the punched and the machined edge for the studied materials, we carried out some finite element simulations which are presented in this section.

5.4.1 Digital image correlation and 2D FE analysis

Using the simple 2 screws loading device (see fig. 4.3(a) and also [Morgeneyer et al., 2013]), the displacements applied on the specimen ROI were not known. The ROI is quite small compared with the whole

specimen dimensions. A structural zoom analysis was then proposed to simulate a zone just a bit bigger than the ROI (see figures 5.2 and 5.3). A 2D plane-stress finite element analysis had been carried out using the Z-set software on the whole specimen geometry in order to extract the displacement fields around the punched and the machined edge that will be used as input data for the optimized 3D elasto-plastic simulations (fig. 5.2(c)). The displacements of the points A and B, corresponding to the upper corners of the ROI used for DIC (fig. 5.2(c)) were calculated and compared to the ones measured using DIC in order to validate the used approach.

Surface digital image correlation (DIC) was performed using Correli^{Q4} on the ROI images taken on the in situ laminography specimen surface in order to determine precisely the real displacements applied to the edges. Fig. 5.2(b) shows the displacement of the upper side of the correlation box measured at CMOD=2mm in the T-direction. The DIC allowed to conclude that the upper and bottom correlation box sides moved symmetrically in the T-direction with respect to the middle axis (dotted line black in fig. 5.2(a)). We observed that during plastic deformation, all the upper side nodes and the right side nodes remained aligned at different CMODs in the T-direction and L-direction respectively. The affine functions corresponding to these aligned displacement of the upper and the right side of the correlation box in the L and T directions were thus determined. The plot in fig. 5.2(b) gives the upper side nodes displacements (dots) on the punched edge ROI surface and the corresponding fitted function measured at CMOD= 1, 2, 3 and 4mm in the T-direction. There was a good agreement between the 2D plane-stress finite element simulation and the surface digital correlation (fig. 5.2(d)).

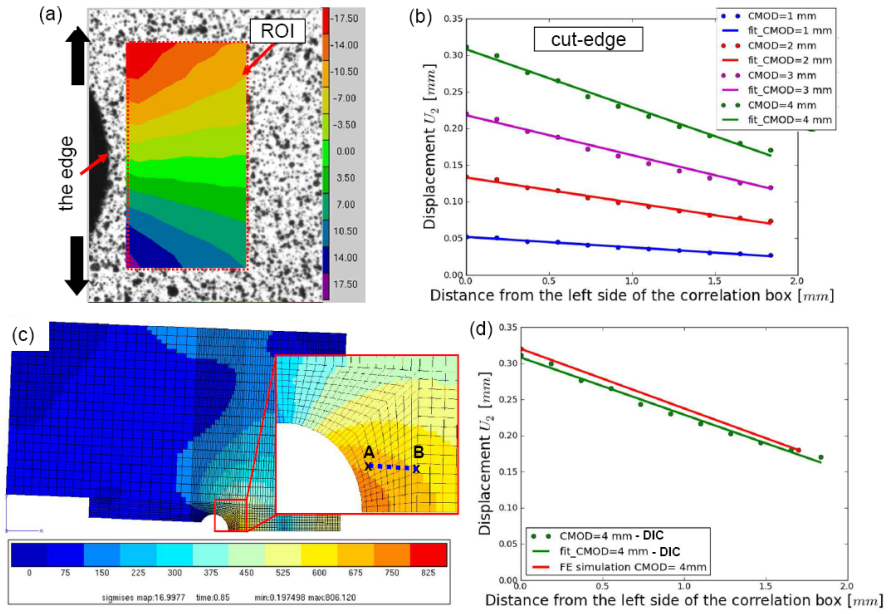

Figure 5.2 – (a) Displacement fields cartography of the punched edge at CMOD=2mm measured by DIC; (b) Displacement of the top side of the correlation box of the punched edge at different CMODs; (c) von Mises stress cartography calculated by 2D FE analysis on the laminography specimen; (d) the correlation box top side displacement along the T direction found by DIC and 2D FE analysis.

The constitutive law described in section5.3 was used to simulate the wedge opening in order to assess the difference between the punched edge and the machined edge behaviors. The boundary conditions applied for the 3D finite element analysis on the meshes showed in fig. 5.3 were obtained from the 2D simulation and they are:

- Left $U_L(y,t) = (A_1.y + B_1)t$
- Right $U_L(y,t) = (A_2.y)t$
- Top $U_T(x,t) = (A_3.x + B_3)t$
- Bottom $U_T = 0$ (symmetry)

Where A_1, A_2, A_3, B_1 and B_3 are constants identified using 2D FE simulation. The values of these constants are given in the table 5.2.

For the DP steel, diameters of the punched hole and the machined hole were 5 mm and 6 mm respectively. This leads to a difference in boundary conditions of the DP punched and machined edges calculated using 2D plane-stress FE simulation (see table 5.2). In contrast, the FB punched and machined holes diameter was 5 mm.

Table 5.2 – Boundary conditions constants for 3D finite element simulation.

	A1	B2	A2	A3	B3
DP punched edge	0.048	-0.12	0.022	-0.061	0.25
DP machined edge	0.042	-0.11	0.017	-0.058	0.26
FB punched and machined edges	0.048	-0.118	0.022	-0.058	0.25

5.4.2 3D finite element analysis

The 3D analysis was performed in order to understand the influence of the edge profile resulting from the punching process on the stress triaxiality distribution and study the behavior of punched and machined edges. The stress triaxiality ratio is defined as: $\tau = \frac{1}{3}\sigma_{kk}/\sigma_{eq}$, where σ_{kk} is the trace of the stress tensor and σ_{eq} the von Mises equivalent stress. In addition to the edge profile, the work hardening caused by the punching process in the region adjacent to the punched edge face was taken into account through the initial accumulated plastic strain $p_0 = p(t = 0)$. This allowed us to understand hardening of the cutting affected zone observed in 4.2(b) (400μm). The affected zone in the punched edge is shown in fig. 5.3(a). It consists of eight rows of elements of 50μm corresponding to the colored regions in fig. 5.3(a). The accumulated plastic strain values introducing the work hardening of the affected zone have been taken from the punched edge hardening profile seen in 4.2(b). It was introduced as follows:

- 1st row of elements (the punched edge surface) $p_0 = 48\%$
- 2nd row $p_0 = 42\%$ (∼50 μm from edge)
- 3rd row $p_0 = 36\%$ (∼100 μm from edge)
- 4th row $p_0 = 30\%$ (∼150 μm from edge)
- 5th row $p_0 = 24\%$ (∼200 μm from edge)
- 6th row $p_0 = 18\%$ (∼250 μm from edge)
- 7th row $p_0 = 12\%$ (∼300 μm from edge)
- 8th row $p_0 = 6\%$ (∼350 μm from edge)

5.4.2.1 DP steel

The stress triaxiality and the accumulated plastic strain were extracted from FE simulations in order to understand the link between these local mechanical parameters and the edges behavior. The fig. 5.4 shows the stress triaxiality level and the accumulated plastic strain calculated for the prestrained punched edge, the punched edge and the machined edge at CMOD= 4.5mm. An increased level of stress triaxiality and accumulated plastic strain was found in the material bulk for the punched and the machined edges.

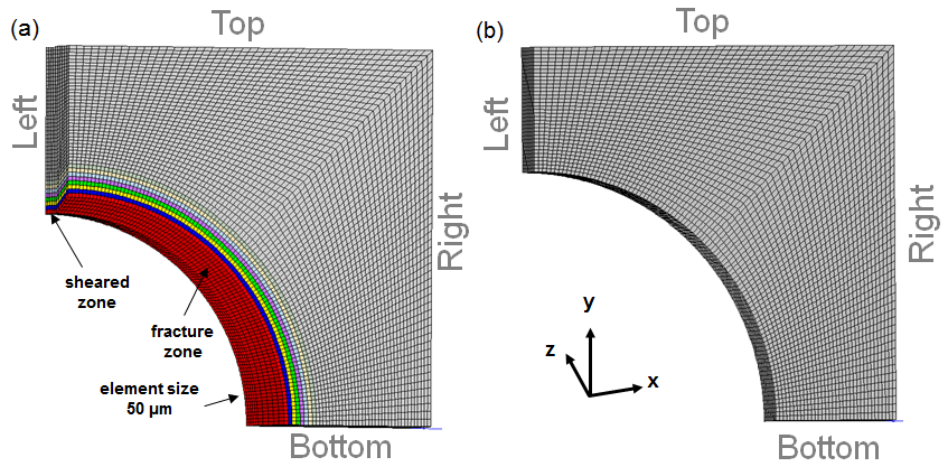

Figure 5.3 – Full thickness meshes of the investigated zone used for the 3D FE analysis: (a) 3D mesh of the punched edge taking into account the affected zone (with colors); (b) 3D mesh of the machined edge.

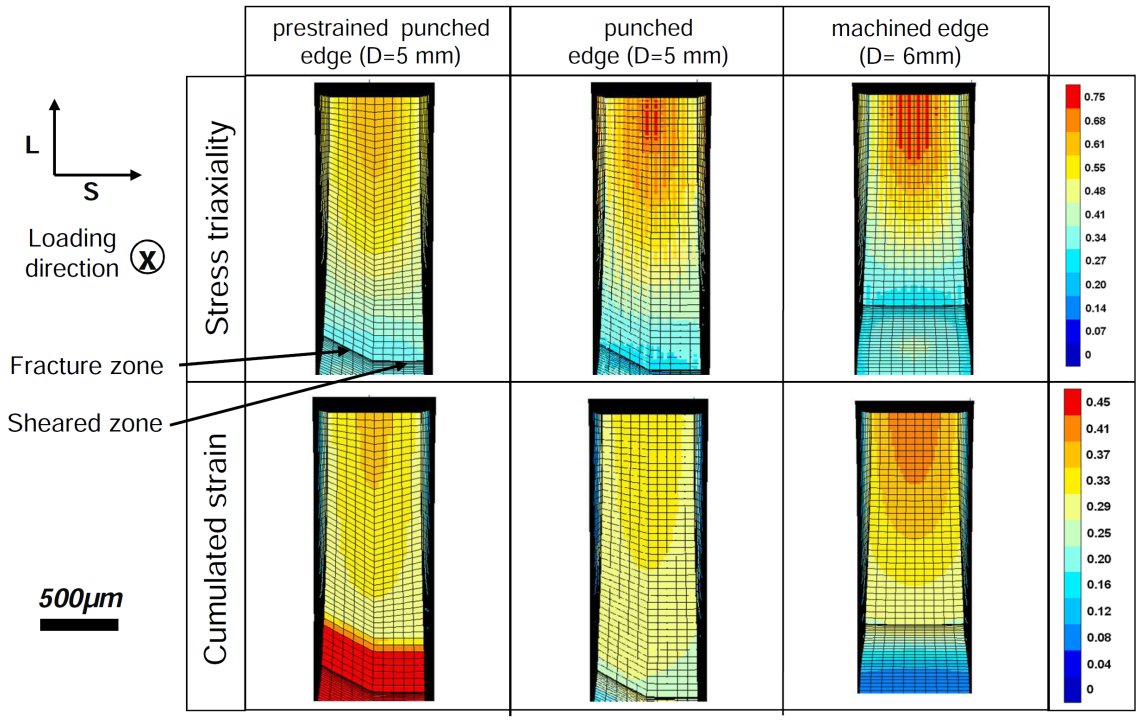

Figure 5.4 – Stress triaxiality and accumulated plastic strain in prestrained punched-edge, punched-edge and machined-edge calculated at CMOD=4.5mm.

The fig. 5.5 shows the evolution of the stress triaxiality and the accumulated plastic strain at mid-thickness. The accumulated plastic strain in the prestrained punched edge is higher close to the edge surface than away from it. This is due to the initial plastic strain introduced to take into account the hardening of the affected zone. Ahead of the edge, there is no difference between the behavior of the prestrained punched edge and the punched edge. The machined edge presents an increased level of stress triaxiality and accumulated plastic strain compared to the two other investigated edges.

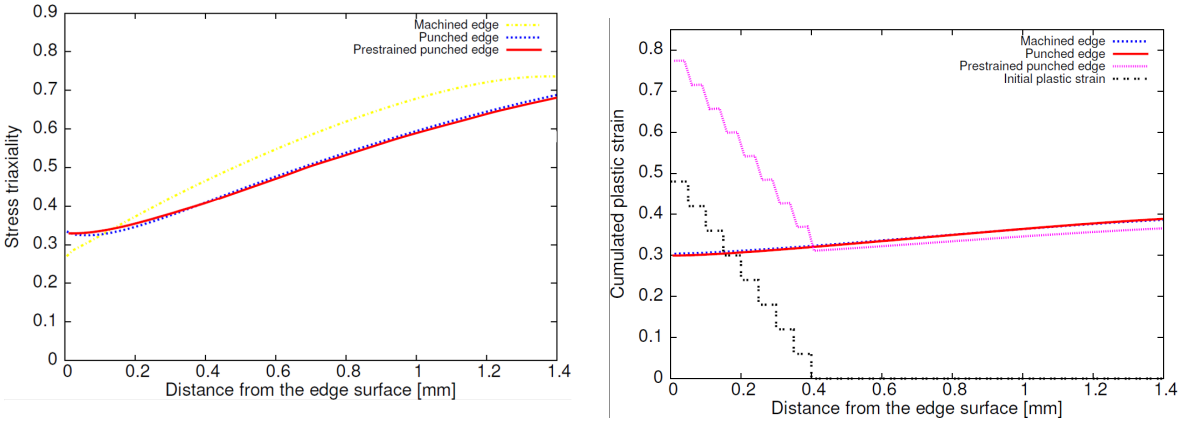

(a) (b)

Figure 5.5 – Evolution of stress triaxiality (a) and cumulated plastic strain (b) in prestrained punched-edge, punched-edge and machined-edge at CMOD=4.5mm at mid-thickness for the DP steel.

5.4.2.2 FB steel

The accumulated plastic strain and the stress triaxiality has been calculated using 3D meshes in order to interpret the mechanical behavior observed for the FB punched and machined edges. The pre-straining of the punched edge has been considered in FE simulations. For the three edge conditions studied for the FB steel, an increased level stress triaxiality was observed in the material bulk ahead of the edge surface. The punched edge without pre-strain and the machined edge show that the cumulated plastic strain is higher ahead of the edge surface. In contrast, the pre-straining of punched edge induced a higher level of accumulated plastic strain close the edge surface. The evolutions of the accumulated plastic strain and the stress triaxiality of the studied edge conditions are given in figure 5.6.

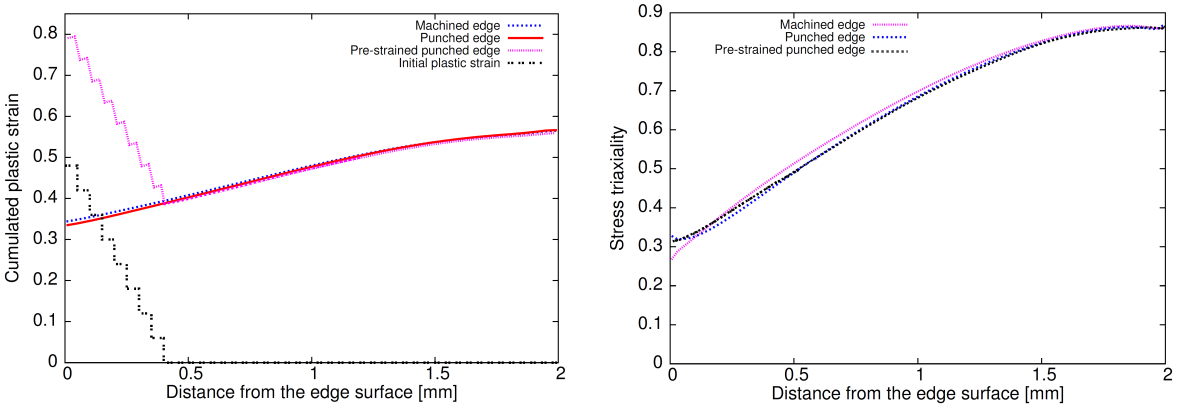

(a) (b)

Figure 5.6 – Evolution of the cumulated plastic strain (a) and the stress triaxiality (b) in prestrained punched-edge, punched-edge and machined-edge at CMOD=5mm at mid-thickness for the FB steel.

5.4.3 Damage prediction

Chu and Needleman criterion and Rice and Tracey model modified by Huang have been used to calculate the void density and the void equivalent diameter during the mechanical loading of the laminography specimen. Void density and void equivalent diameter were used to calculate the void volume fraction.

$$f = N.\frac{4\pi}{3}R_{eq}^3 \tag{5.9}$$

The pre-damage and the pre-strain of the punched edge induced by the cutting process measured using X-ray laminography data and Vickers microindentation method respectively have been considered in the next FE simulations of the in situ laminography test.

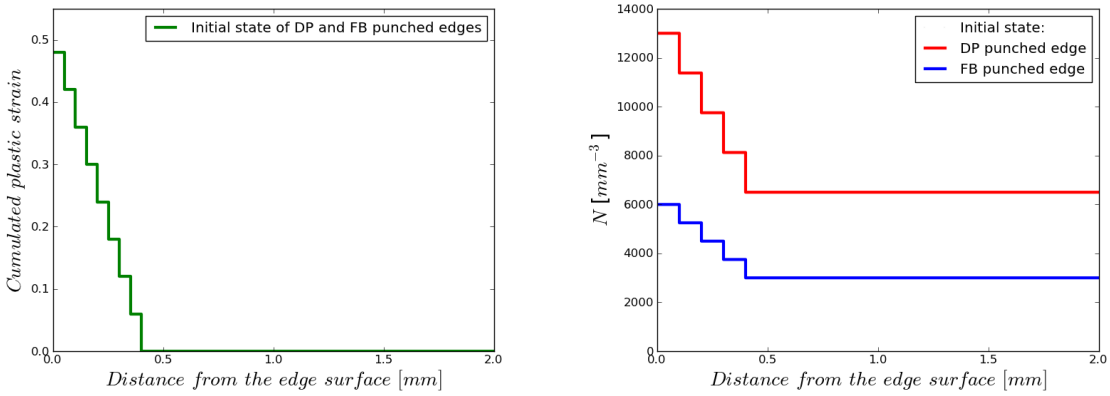

(a) (b)

Figure 5.7 – The initial parameters used to consider the pre-damage and the pre-strain of punched edges of the two investigated steels: (a) pre-strain measured by Vickers microindentation technique, (b) pre-damage measured using X-ray laminography technique

Figure 5.8 shows the evolution, for DP and FB steels, of void volume fraction at mid-thickness for the punched and the machined edges at CMOD=9mm. We observe that the void volume fraction is higher close to the edge surface for the DP and FB punched edges. This is due to the initial pre-damage and pre-strain introduced in FE simulations. However, for the DP and FB machined edge, the void volume fraction is slightly higher in the material bulk than close to the edge. This is consistent with the increased stress triaxiality and cumulated plastic strain levels ahead of the edge surface for both machined edges.

The experimental results provided using X-ray laminography show that a crack appears at CMOD=4.5mm and at CMOD=7.75mm in the DP punched and the DP machined edges. For the FB punched and machined edges, the fracture occurs at CMOD=5mm and CMOD=5.5mm respectively. The void volume fractions calculated at CMOD=9mm in these simulations are lower than the identified void volume fraction at coalescence f_c=0.002 for both base materials. This can be explained by the roughness of the fracture zone in the punched edges, the needle voids initiated in the punched edges surfaces at initial state, segregations bands which are not taken into account in these simulations. However, the main experimental trends are reproduced by the present model for both materials.

- The failure of the machined edge will occur after the failure of the punched edges.

- The failure of the punched edge will initiate at the edge while it will occur in the bulk for the machined one.

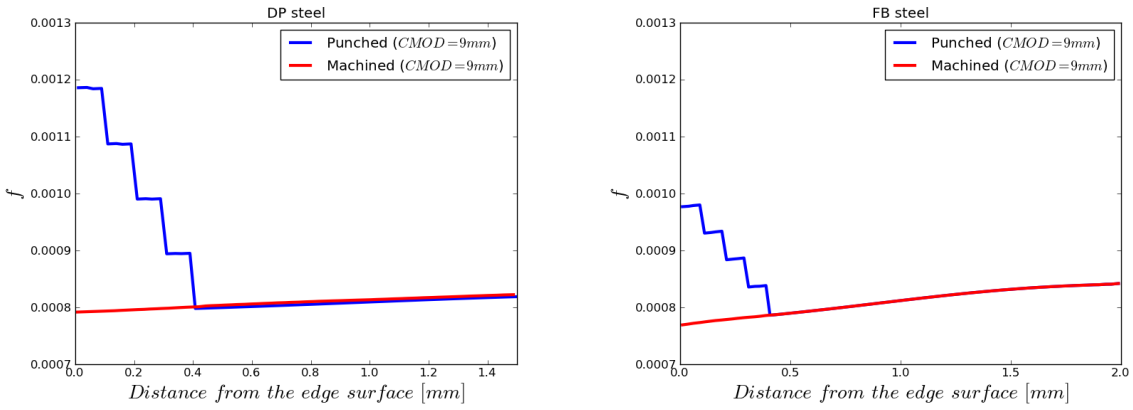

(a) (b)

Figure 5.8 – Evolution of void volume fraction in machined edge and prestrained punched-edge at CMOD=9mm at mid-thickness for: (a) DP steel, (b) FB steel.

5.5 Hole expansion test

The hole expansion test (HET) is often used by the forming community as an excellent tool to study the formability and edge fracture of automotive materials. Hole exansion tests have been carried out using a sample of 105×105 mm^2 with a 10mm diameter hole. These experiments were performed in ArcelorMittal Global R&D using a conical punch head. The studied punched holes have been produced with a clearance of 12%. A parametric study was carried out using four sheet thicknesses to investigate the stretchability of the studied FB steel. The effect of pre-straining on hole expansion ratio (HER) of the FB machined edge has been studied using cold-rolling process to induce the pre-strain. In order to avoid any effect of strip thickness on HER, the hot-rolled product was rectified prior to cold-rolling to get comparable cold-rolled thickness, whatever the cold-rolling ratio.

A numerical study of hole expansion has been performed for the DP and FB steels using four sheet thickness and two sample geometries with a 10mm diameter hole. Axisymmetric meshes have been used to carry out these FE simulations using Z-Set software. The void nucleation and void growth criteria developed hereinbefore were used as post-processing plugins to calculate the void density and the void equivalent diameter which were used to calculate the void volume fraction during hole expanding. The value of f_c was then used in finite element simulations to estimate HER.

The experimental and numerical hole expansion ratio presented in this section was measured using the relationship:

$$HER_{exp} = \frac{D_f - D_0}{D_0} \; x \; 100 \tag{5.10}$$

$$HER_{num} = \frac{D_c - D_0}{D_0} \; x \; 100 \tag{5.11}$$

Where D_0 is the initial hole diameter and D_f is the hole diameter when a through-thickness appears at the edge. D_c is the hole diameter when the void volume fraction reachs 0.002 ($f_c = 0.002$) in an integration point of the used mesh.

5.5.1 Samples geometry and meshes

The experiments of hole expansion on FB steel sheets have been performed using four sheet thicknesses for punched edge experiments and two pre-strain conditions used cold-rolled FB sheets to study the the effect of pre-straining. Table 5.3 shows the sheet thickness values used for experimental and finite element analysis of

hole expansion test. Experiments have been carried out on specimen with a 10mm hole diameter and finite element simulation was performed using specimens with a 5mm and a 10mm hole diameter. The thickness values and the pre-strain level used to study the effect of pre-strain on hole expansion ratio of a machined hole are given in table 5.4. Schematics of hole expansion test used for finite element analysis is shown in figure 5.9. For finite element simulations, the hole expansion tools (blades and punch) have been chosen to be purely elastic rigid.

Table 5.3 – Sheet thickness values used for experimental tests and FE simulations of hole expansion test (values in mm)

Experiments	0.8	1.2	2	2
FE analysis	0.8	1.6	2.4	3.2

Table 5.4 – Sheet thickness values and pre-strain levels used to investigate the effect of pre-strain (thickness values in mm) - ($D_0 = 10mm$)

Thickness	1.2	1.1	1.3
pre-strain (p_0)	0	0.1	0.5

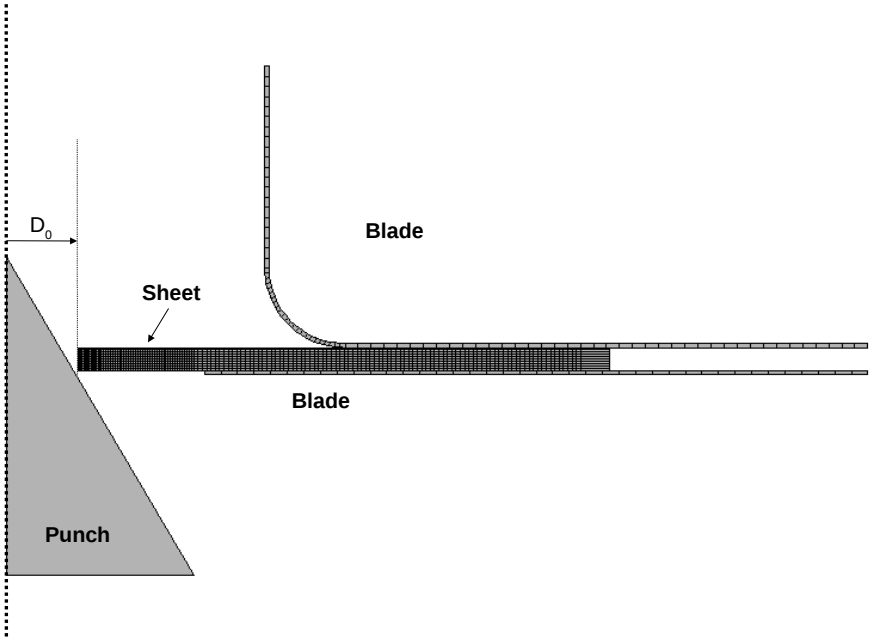

Figure 5.9 – Schematics of hole expansion specimen used in the FE simulations

5.5.2 Results

5.5.2.1 Effect of pre-strain

For the FB steel, the experimental results of machined hole expansion with two different pre-strain levels 0.1 and 0.5 are shown in figure 5.10. We observe that, up to ε=0.5, the hole expansion ratio on machined edge is found to be independent on the pre-strain levels. The results of finite element analysis confirm that there is

no difference between hole expansion ratios of the machined hole and the pre-strained machined hole for the studied hole diameter. HER given in 5.10 corresponds to the hole expansion ratio at coalescence found via finite element analysis. The hole expansion ratios experimentally measured are higher than those found using numerical simulations. This is due to the difference between the methods used to measure the HER. Indeed, the experimental HER are measued when a through-thickness crack is observed at the edge. In contrast, HER calculated using finite element simulations corresponds to HER when the void volume fraction reachs f_c=0.002 in at least one element in the edge.

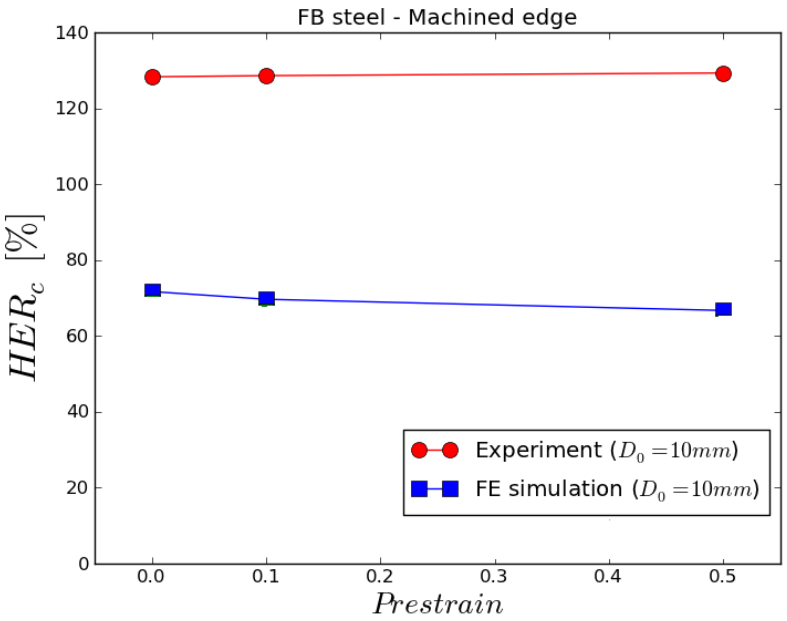

Figure 5.10 – Results of hole expansion test of FB steel sheets with machined hole and two pre-strain levels

5.5.2.2 Effect of sheet thickness

For the FB steel, hole expansion tests have been performed on specimens with a 10mm punched hole diameter with different sheet thickness. For the punched hole, the pre-damage and pre-strain induced by punching process are considered in these simulations using the profiles shown in figure 5.7. We observe that, up to 3.2mm sheet thickness, the hole expansion ratio increases with the sheet thickness (see figure 5.11).

Figure 5.12 shows the experimental and numerical results of hole expansion test of DP punched edge machined edge for different sheet thickness values. We observe that the numerical HERs for punched and machined edges is very lower than the numerical one for all the studied sheet thickness values. This is due to the method used to calculate the numerical HER (HER_{num}) corresponding to the measurement of HER when f=0.002 in an integration point of the sheet mesh which is a very local approach. Experimental HER of DP steel presented in figure 5.12 show that a reduction of ductility (HER) due to the punched edge can be observed. For the DP punched edge, the experimental results show that the HER is maximal for the 2 mm thick sheet and that HER decreases for higher sheet thickness values (3 and 5.5 mm).

We observe, for the FB steel, that the gap between HER of the machined edge and HER of the punched edge, i.e. reduction of ductility due to the presence of punched edge, remains approximately constant when the sheet thickness increases. However, for the studied DP steel, the reduction of ductility is higher for increased sheet thickness values. The reduction of ductility (in terms of HER) due to the presence of punched edge is higher for the DP steel.

The HER values calculated via finite element simulations are lower than those measured in the standard hole expansion test because they are locally calculated. For the punched edges, we can explain this by the roughness of the fracture zone, the needle voids initiated on edges surface after punching, segregations bands which are not taken into account in these finite element simulations. The same difference was observed for laminography specimens.

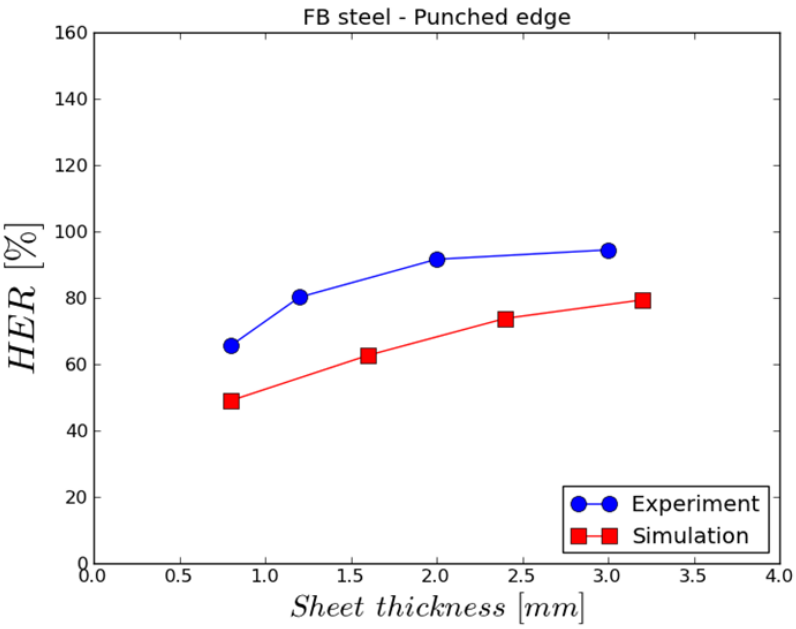

Figure 5.11 – Results of hole expansion test of FB steel sheets with punched holes

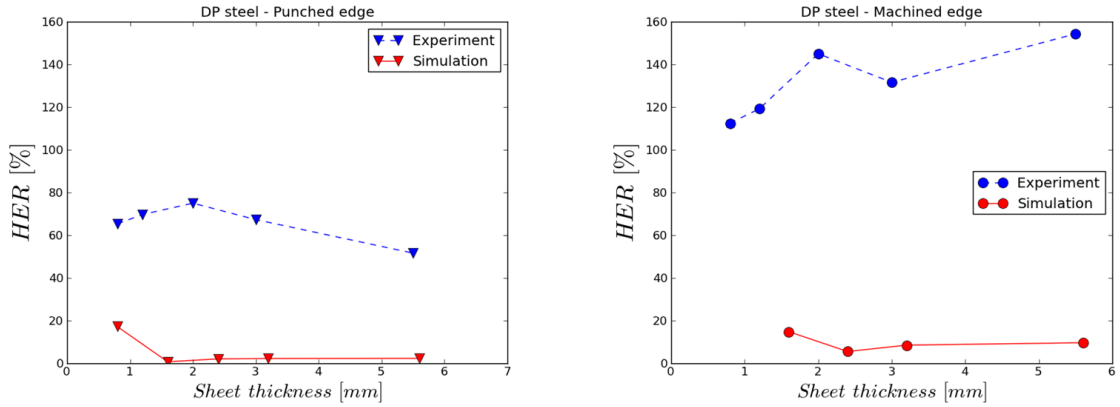

(a) (b)

Figure 5.12 – Experimental and numerical results of hole expansion test of DP steel: (a) punched edge, (b) machined edge

Figures 5.13 and 5.14 show some examples of the finite element simulation of hole expansion test of punched and machined edge with a 5mm hole diameter for both materials. We observe that the DP edges reach the void volume fraction at coalescence (f_c=0.002) early compared to the FB punched and machined edges. This can be explained by the increased amount of initial porosity (N_0=6500 mm^{-3}) in DP steel and the high number of possible nucleation sites in this steel grade compared to the FB steel where the initial void density is N_0=3000 mm^{-3}.

5.6 Discussion

Finite element simulation, using elasto-plastic constitutive laws, have been performed in order to interpret the mechanical behavior at the punched and the machined edges.

The FE analysis of the *in situ* laminography tests showed for both materials that the bulk has undergone an increased stress triaxiality and accumulated plastic strain for the punched and the machined edge. These results allowed us to explain the behavior of the machined edge observed using *in situ* X-ray laminography.

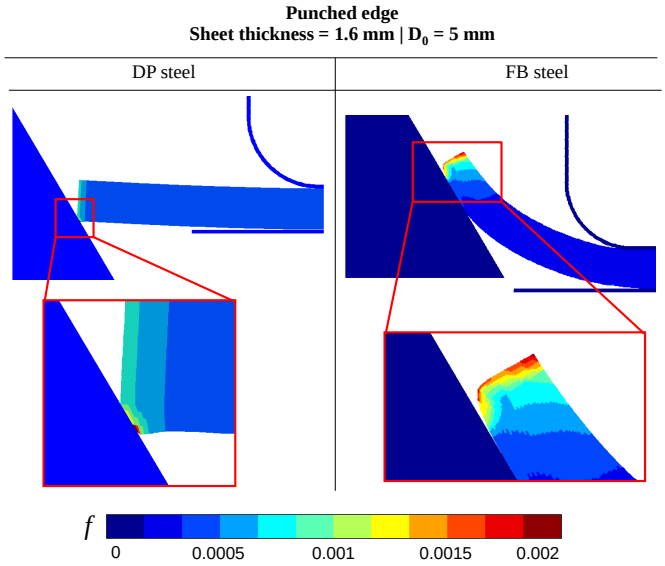

Figure 5.13 – Cartography of void volume fraction distribution in sheet thickness during hole expansion at HER = 4.2% for the DP punched edge and HER = 59% for the FB punched edge.

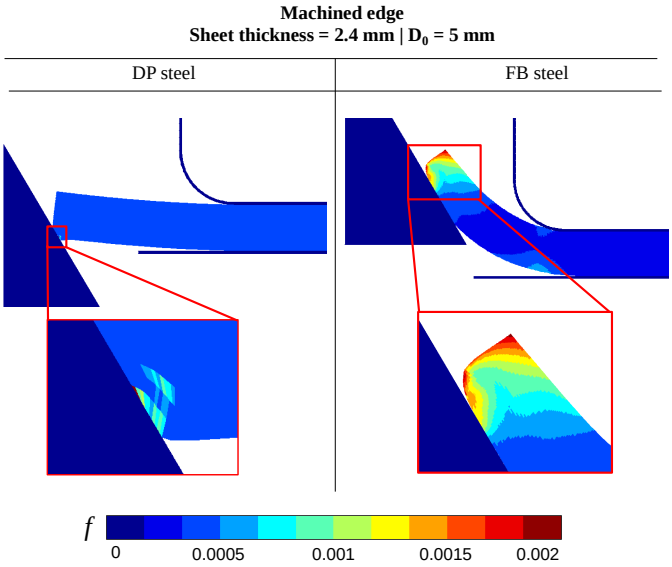

Figure 5.14 – Cartography of void volume fraction distribution in sheet thickness calculated via finite element simulation of hole expansion test at HER = 12.1% for the DP machined edge and HER = 84.7% for the FB machined edge.

Using FE mesh taking into account the punched edge profile does not localize the stress triaxiality and the accumulated plastic strain close to the edge surface.

For both materials, using the fracture criterion, which is an uncoupled and local criterion, developed in this study based on experimental measurements provided by X-ray tomography, the main experimental trends have been reproduced. We observe a reduction of ductility (in terms of CMOD) that is due to the presence of punched edge. Indeed, the failure of the machined edges will occur after the failure of the punched ones. The failure of the punched edges will initiate on the edges surface, in contrast, for the machined edges, the failure will occur ahead of the edges surface.

Hole expansion test using different sheet thickness values have been carried out to validate the developed fracture criterion for the investigated materials. Numerical simulation of hole expansion test showed that for the DP steel, the presence of punched edge causes a reduction of HER of about 70%.

It was found that the HER of FB machined edge is independent on the pre-strain level. The experimental and numerical results of hole expansion test show that, for the FB punched edge, the HER increases with the

sheet thickness. However, the hole expansion experiments performed for the DP steel using different sheet thickness values (0.8; 1.2 2;3 and 5.5 mm) show that the HER presents a maximum for the 2 mm thick sheet and that it decreases for the higher sheet thickness values (3 and 5.5 mm). In contrast, for the numerically investigated sheet thickness values (0.8; 1.6; 2.4 and 3.2 mm), the HER of the DP punched and machined edges increases with the sheet thickness.

It is shown that the developed fracture criterion in this study, which has been first validated on *in situ* tensile test in SEM, allowed us to reproduce and interpret the mechanical behavior of the punched and the machined edge for both materials. This uncoupled fracture critrion, based on microstructural parameters provided using *in situ* X-ray tomography, has been used for post-processing of elasto-plastic calculations. To improve the HER prediction, this criterion could be used, for example, when f=0.002 in all the element in the ROI. A second way which could improve the quantitative prediction of punched and machined edge failure for laminography test and hole expansion test, is the use of fully-coupled simulations based for example a GTN model.

5.7 Conclusions

2D digital image correlation and 3D finite element simulations were perfomed to interpret the edge behavior in terms of mechanical fields. Using elasto-plastic constitutive laws of the studied materials, it was found for the punched edges of both materials that:

- Meshing the edge profile geometry does not allow to move the maximum of the stress triaxiality and plastic strain in the edge region.
- The behavior of the machined edge observed experimentally can be reproduced in the simulation. The maximum of the stress triaxiality and the plastic strain are localised in the simulation far ahead of the edge which is consistent with the increased level of void growth in the machined edge observed during in situ X-ray laminography experiment.
- Numerically accounting for the pre-straining introduced in the cutting-affected zone does not localize maximum of triaxiality in the edge region either.

Using the quantitative data of X-ray tomography/laminography giving the evolution of initial void density (N_0) and void size (R_0) from the punched and machined edges surface, void nuclation and void growth criteria has been validated on *in situ* laminography test and hole expansion test. It was found that:

- For laminography test, the void volume fraction at CMOD=9mm in DP and FB punched edges is increased close to the edge surface than ahead of it. This is consistent with the increased level of strain and of pre-damage in this punching-affected zone.
- For machined edges, the void volume fraction is slightly higher in bulk material. This can be explained by the increased stress triaxiality and plastic strain that undergoes the bulk material.
- It is expected that the punched edges break before the machined ones since for a given CMOD, the maximal void volume fraction is higher close to the punched edge surface.
- Experimental and finite element analyis results of hole expansion test show that hole expansion ratio increases with the sheet thickness for the FB steel whatever the edge condition. However, for the DP steel, the experiments show that the maximal HER is reached for a 2 mm thick sheet.
- A reduction of ductility of FB steel (HER reduction of about 38%) due to the presence of punched edge was observed in hole expansion simulations. In contrast, the pre-strain has no influence on HER for this material.
- Finite element simulations of hole expansion test performed for the DP steel show that the presence of punched edge causes a reduction hole expansion ratio.

- The experiments and the finite element analysis show that the pre-strain of the FB machined edge has no influence on hole expansion ratio for three studied sheet thicknesses. In contrast, the numerical simulation on DP steel show that the hole expansion ratio is dependent on pre-strain level. This is can be explained by the increased number of voids at initial state and the higher number of possible nucleation sites in this grade compared to the FB steel.

General conclusions and proposals for future work

Résumé

Dans le contexte environnemental actuel, les aciers avancés sont de plus en plus utilisés dans l'industrie automobile, afin de réduire la consommation de carburants et ainsi l'émission de CO_2, grâce à leur résistance mécanique. Parmi ces aciers THR, les nuances DP (ferrite-martensite) et FB (ferrite-bainite) offrent un bon compromis entre résistance mécanique et formabilité. En revanche des cas de déchirure s'initiant sur un bord découpé, lors des opérations de mise en forme d'un acier DP, ont été détectés. Cela a fini par incriminer ces bords découpés par cette chute de ductilité qui limite l'utilisation de ces aciers dans les structures automobiles.

L'objectif de ce travail est de comprendre le comportement de l'endommagement et la cinématique de germination et croissance de cavités des deux matériaux de base DP et FB avant d'étudier le comportement des bords découpés dont l'analyse est complexe à cause du chevauchement de phénomènes mécaniques. L'investigation des mécanismes d'endommagement des matériaux de base et des bords découpés a été réalisée via des techniques d'imagerie 3D et de la simulation numérique par éléments finis. Les deux aciers étudiés, DP (14% martensite) et FB (50% bainite), présentent une résistance à la traction d'environ 600 MPa avec un écrouissage et gradient de dureté entre les phases plus élevés pour l'acier DP.

Afin de révéler le lien entre la microstructure et les mécanismes d'endommagement, des essais de traction en MEB in situ ont été réalisés. La rugosité de la surface de l'éprouvette induite par la plasticité rend la visualisation de cavités qui pourraient être formées par décohésion des interfaces ferrite-martensite plus difficile à détecter. Ces essais ont montré que :

- Pour l'acier DP, une germination de cavités sur des particules a été observée.
- L'endommagement de l'acier FB a lieu majoritairement sur les particules de la seconde phase.

Les essais de tomogaphie in situ ont été réalisés afin de caractériser l'évolution de l'endommagement en trois dimensions à une échelle micrométrique dans le volume du matériaux où l'état de la triaxialité de contrainte et la déformation plastique sont plus élevées qu'à la surface.

- Acier DP :
  - L'endommagement est allongé suivant la direction L (direction de laminage) quelle que soit la direction de chargement
  - Une cavité sous forme d'aiguille apparait dans la zone centrale de l'éprouvette, lors du chargement suivant la direction T, qui correspondrait à une bande de ségrégation
  -
- Acier FB :
  - Lors du chargement suivant la direction L, la coalescence de cavités très allongées suivant la direction du chargement a lieu dans une zone perpendiculaire à la direction de traction.
  - Dans le cas du chargement suivant la direction T, l'acier FB présente une forte tolérance à l'endommagement.

La caractérisation MEB des sections des éprouvettes testées en tomographie a montré, pour l'acier DP, que l'endommagement est dû à la décohésion aux interfaces martensite-ferrite, par contre, pour l'acier FB des cavités, qui s'amorcent sur les carbures, de taille inférieure à 1 μm, qui ne sont pas détectables en microtomographie, ont été observées proche de la surface de l'éprouvette.

La quantification des données de tomographie a montré que l'acier DP contient deux fois plus de cavités initiales que l'acier FB et que la densité de cavités augmente clairement lors du chargement mécanique. La

fonction de Chu et Needleman [Chu and Needleman, 1980] a été utilisée pour prédire la cinétique de germination de cavités pour les deux matériaux ayant un nombre maximal de sites de germination très différents. Pour la modélisation de la croissance de cavités le modèle de Huang [Huang, 1991] étant une modification du modèle de Rice et Tracey [Rice and Tracey, 1969] a été optimisé.

Les essais de laminographie ont permis de caractériser la rupture de bords découpés (bord poinçonné et bord usiné) en appliquant des conditions aux limites proches à celles de la mise en forme des aciers. La chute de ductilité mesurée par la réduction d'ouverture d'entaille est entre 30 et 40% pour l'acier DP et 5 et 10% pour l'acier FB. La caractérisation de l'état initial par laminographie a montré que les bords poinçonnés présentent une rugosité au niveau de la zone rompue et un micro-endommagement sous forme d'aiguille que s'initie sur la surface des bords poinçonnés. Pour l'acier DP, lors du chargement mécanique, ce micro-endommagement suit les lignes d'écoulement et coalesce avec la zone cisaillée. Aucune striction n'a été observée sur le bord poinçonné DP au moment de l'initiation de fissure. Par contre, pour le bord usiné, l'endommagement est plus important loin de la surface du bord ($\sim$800 μm) où le matériau subit une striction importante. Pour l'acier FB, une striction a été observée lors du chargement du bord poinçonné. La rupture de ce dernier s'initie sur la surface sur bord, par contre, dans le cas du bord usiné la rupture s'est initiée loin du bord. Les données de laminographie ont montré que les deux matériaux présentent à l'état initial plus de cavités dans la zone affectée par la découpe que dans le volume. Pour les bords poinçonnés DP et FB, l'endommagement reste plus important proche de la surface des bord lors du chargement mécanique. En revanche, l'endommagement croit plus vite loin de la surface des bords ce qui est cohérent avec la striction observée dans cette zone.

Des calculs 3D par éléments finis couplés à la corrélation d'image ont été réalisés en utilisant les lois de comportement élasto-plastiques des matériaux étudiés. Ceux-ci ont montré que le profil de bord poinçonné ne permet pas de localiser la triaxialité de contrainte et la déformation plastique proche du bord. Ces paramètres mécaniques locaux ont été localisés loin de la surface des bords ce qui est cohérent avec le niveau d'endommagement important apparu dans cette région lors des essais de laminographie. Ces calculs ont servi pour valider les critères d'endommagement de germination et de croissance de cavités identifiés sur les matériaux de bases. Pour les deux matériaux étudiés, en introduisant le pré-écrouissage et le pré-endommagement induits par la découpe, la fraction volumique de cavités est maximale proche de la surface du bord poinçonné lors du chargement mécanique. Par contre, la fraction volumique de cavités est relativement plus importante, pour les deux matériaux, loin des bords usinés lors du chargement mécanique.

L'essai d'expansion de trou a été utilisé pour réaliser une étude paramétrique permettant de valider les critères de germination et de croissance de cavités développés en faisant varier l'épaisseur de la tôle et la pré-déformation. Pour les deux matériaux, une chute de ductilité, relative à la réduction de ratio d'expansion de trou, est observée pour les bords poinçonnés. Pour l'acier FB, les résultats expérimentaux et numériques ont montré que le ratio d'expansion de trou, pour les quatre épaisseurs étudiées, augmente quand l'épaisseur de la tôle augmente. Il a été expérimentalement et numériquement montré que la pré-déformation n'a aucune influence sur la formabilité du bord usiné FB. Par contre, les calculs éléments finis ont mis en évidence la sensibilité de la nuance DP à la pré-déformation et au pré-endommagement.

Advanced High Strength Steel (AHSS) grades offering high strength are developed and proposed by steel-makers for automotive industry. For environmental and safety reasons, the use of AHSS expands increasingly in automotive industry in order to reduce vehicle weight and fuel consumption. Compared to conventional steel grades, these steels are known for their improved formability and crash worthiness. Among these AHSS grades, dual phase (DP) and ferrite-bainite (FB) steels with their composite microstructure consisting of ferritic ductile matrix containing respectively a hard martensitic or bainitic second phase in the form of islands present a good compromise between strength and resistance to damage. The use of automotive parts made of DP steels is often seen reduced due to the presence of cut-edges. Indeed in automotive industry, most used cutting processes are shearing and punching because of their speed, simplicity and low cost. Using these forming operations the mechanical performance of formed automotive parts can be affected. Cases of failure in DP steels which initiate on blanked edges were detected. This may lead to a drop in vehicle performance.

This study aimed at better understanding the damage behavior and the void nucleation and growth kinetics of the two base materials, DP and FB steels, before assessing edge fracture that is even more complex due to pre-damage and pre-strain using recent 3D imaging techniques and finite element analysis. The approach used during this PhD project was based on coupling experimental and numerical analysis. DP steel consisting in a ferrite-martensite composite microstructure and exhibiting an increased sensitivity to cut edges and a FB steel less sensitive to cut edges have been investigated in this study. Both materials exhibit an ultimate tensile strength of approximately 600 MPa with higher phase hardeness gradient and higher work hardening for the DP steel. The martensite fraction in DP steel and bainite fraction in FB steel are approximately 14% and 50% respectively.

Main results

To assess ductile damage mechanisms in DP and FB base materials, in situ X-ray synchrotron tomography experiments have been carried out at ESRF high energy beamline ID15 at micrometer resolution. Using this technique the damage evolution has been assessed in three dimensions in the bulk material, where stress triaxiality and plastic strain are known to be higher than at the surface in qualitative and quantitative way. In situ tensile testing of both base materials using nearly smooth specimens in T and L directions leaded to the following results:

- DP steel
  - During testing in L direction, voids are elongated in the loading direction following the alignment of martensite islands.
  - For T testing, voids are elongated normal to the loading direction, due to early local coalescence. In particular at the specimen centre, needle shaped prolate voids with length of several hundreds of micrometers are seen. These could be linked to central segregation band.
  - Void nucleation occurs until the failure of the observed specimen. This is due to the high number of possible nucleation sites.
- FB steel
  - For L testing, highly elongated voids in loading direction are seen. Final coalescence of these voids occurs through narrow region oriented normal to the loading direction.
  - During loading in T direction, a very long needle-shape void nucleated normal to the loading direction along the L direction (about 400 μm) that may be linked to a segregation band.

Because of the limitations of X-ray synchrotron imaging to reveal the microstructural components of the studied steels, i.e. ferrite, bainite and martensite, in-situ tensile tests were performed in a scanning electron microscope in order to establish a link between the microstructure and the mechanisms of void nucleation. It was found that:

- For the DP steel, damage nucleated on particles has been observed and damage on ferrite-martensite interfaces may be present, however, it is hard to observe it due to the increased surface roughness caused by plasticity.
- For FB steel, damage mainly arises from second phase particles.

SEM observations at cross sections and fracture surfaces of tomography specimens after polishing and 0.2% etching have been carried out in order to identify damage nucleation sites in the investigated materials. These observations leaded to the following results:

- For DP steel, voids of different sizes are seen below the fracture surface. Some of them are close to ferrite and martensite interfaces and smaller than the resolution limit in microtomography.
- For FB steel, voids with sizes below 1µm are found close to the fracture surface in link with carbide interfaces.

The fracture surface of DP steel during L loading is mainly covered by small dimples with a typical diameter of 2 μm. For the T loading of DP steel, the central segregation zone is clearly seen on the fracture surface. For the L loading of FB steel, the fracture surface exhibits two dimple populations. one population of large voids that originated from micrometer particles. These are the voids also seen in tomography that elongated in loading direction. The second population of small voids has diameters in the order of 1 μm, i.e. below tomography resolution limit. These small voids led to coalescence of the large voids of anisotropic shape.

Damage has been quantified via 3D image analysis in terms of evolution of the void density, the equivalent void diameter and the evolution of the largest cavities. It is found that the DP material contains twice more micrometre-size initial voids than the FB material. It is hard to distinguish particles from voids so that for the FB material most of the found void may actually be particles. While the number of voids in the DP steel increases constantly, which is consistent with the high number of possible nucleation sites at ferrite-martensite interfaces, the number of nucleating voids in the FB steels decreases after some deformation indicating reduced nucleation compared to DP steel. A Chu and Needleman nucleation function is successfully fitted on both nucleation kinetics, with very different numbers for the maximum amount of possible nucleation sites. Using a correction of the void growth model of Rice and Tracey taking into account the stress triaxiality in the pre-exponential term proposed by Huang where the stress triaxiality is calculated via Bridgman approach, the growth of the largest cavities was successfully fitted.

In situ X-ray laminography experiments have been carried out at ESRF high energy beamline ID19 at micrometer resolution to assess in three dimensions and for the first time edge fracture in the investigated DP and FB steel keeping the mechanical boundary conditions of engineering relevance close to metal forming conditions, using two edge conditions: punched edge and machined edge produced via EDM process. These experiments leaded to the following results:

- DP steel
  - A strong reduction of ductility measured by Crack Mouth Opening Displacement (CMOD) of approximately 30% - 40% is observed on DIC results. This is due to the presence of punched edge
  - At initial state, the DP punched edge contains several defects. These include: roughness in the fracture zone, needle-shape voids in the bulk from fracture zone and alignment of needle voids along the flow lines i.e. martensite alignments.
  - The growth of needle voids was especially along flow lines from fracture zone surface but also in the bulk along the martensite alignments.
  - The coalescence of needle voids from the fracture zone with the sheared zone occurs via narrow coalescence zones (void sheets).
  - In terms of quantification, using the methodology discussed in chapter 4, it was found that DP punched edge exhibits twice more initial voids close to edge surface that ahead of it.

  - The hardening caused by the punching process was measured by the Vickers microindentation method using a load of 50g. It is approximately 50% close to the edge surface.
  - For the DP machined edge, the damage does not start from the edge but in the material bulk that has undergone substantial necking during loading. The local necking appearing away from the edge is accompanied with an increased damage accumulation that leads to the final crack.

- FB steel

  - A reduction of ductility measured by CMOD of approximately 5% - 15% is observed on DIC results. This lower reduction compared to DP steel is due to the high damage tolerance that the studied FB steel exhibits.
  - During loading of FB punched edge, needle voids grew and coalesce with the internal damage and necking has been observed close to the edge surface.
  - For the FB machined edge, failure occurs via necking of a zone about 800 µm away from the FB machined edge surface and subsequent failure via classical ductile fracture mechanisms.
  - The FB punched edge contains twice more initial voids close to edge surface than away from it.

Finite element simulations and digital image correlation were perfomed to interpret the edge behavior in terms of mechanical fields. Using elasto-plastic constitutive laws of the studied materials, it was found for the investigated materials that:

- Edge profile geometry does not allow to localise the maximum of the stress triaxiality and plastic strain in the edge region.
- The behavior of the machined edge observed experimentally can be reproduced in the simulation. The maximum of the stress triaxiality and the accumulated plastic strain are localised in the FE simulation ahead of the edge which is consistent with the increased level of void growth in the machined edge observed during in situ X-ray laminography experiment.

Using the quantitative data of X-ray tomography/laminography giving the evolution of initial void density (N_0) and void size (R_0) from the punched and machined edges surface, the fracture criterion has been validated using FE simulations of *in situ* laminography test and hole expansion test. It was found that:

- For *in situ* laminography test, the void volume fraction at CMOD=9mm in DP and FB punched edges is increased close to the edge surface than ahead of it. This is consistent with the increased level of strain and of pre-damage in this punching-affected zone.
- For machined edges, the void volume fraction is slightly higher in bulk material. This can be explained by the increased stress triaxiality and plastic strain that undergoes the bulk material.
- It is expected that the punched edges break before the machined ones since for a given CMOD, the maximal void volume fraction is higher close to the punched edge surface.
- Experimental and finite element analyis results of hole expansion test show that hole expansion ratio increases with the sheet thickness for the FB steel whatever the edge condition. However, for the DP steel, the experiments show that the maximal HER is reached for a 2 mm thick sheet.
- A reduction of ductility of FB steel (HER reduction of about 38%) due to the presence of punched edge was observed in hole expansion simulations. In contrast, the pre-strain has no influence on HER for this material.
- Finite element simulations of hole expansion test performed for the DP steel show that the presence of punched edge causes a reduction hole expansion ratio.

- The experiments and the finite element analysis show that the pre-strain of the FB machined edge has no influence on hole expansion ratio for three studied sheet thicknesses. In contrast, the numerical simulation on DP steel show that the hole expansion ratio is dependent on pre-strain level. This is can be explained by the increased number of voids at initial state and the higher number of possible nucleation sites in this grade compared to the FB steel.

Proposals for future work

For complementary investigations, some results obtained in this work can be used. Some proposals are given:

- The experimental results provided in this study could be used as input in finite element codes predicting the ductile damage mechanisms.
- The X-ray tomography results found for the investigated DP and FB steels in this study could be used in order to establish the link between the local event of coalescence and the macroscopic coalescence.
- The Chu and Needleman nucleation function and Rice and Tracey law with Huang's modification model can be validated on the experimental data obtained via in situ X-ray laminography assessment of crack propagation in a DP steel using a CT-like specimen (see figure 5.15).

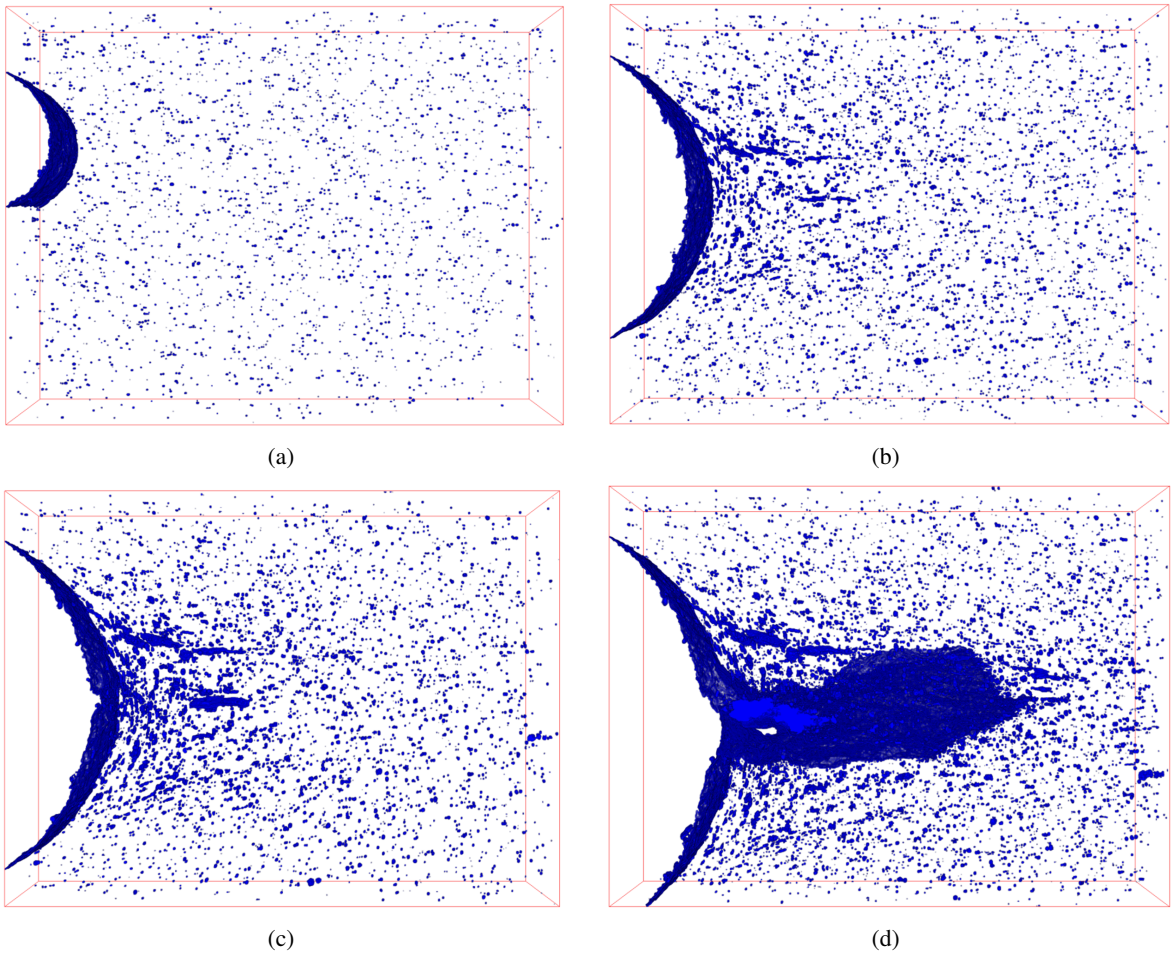

Figure 5.15 – A 300 μm thick volume provided using X-ray synchrotron laminography observations of the DP CT-like sample. Notch surface and rendered voids are shown in blue. The sample surface is made half-transparent. (a) initial state, (b) CMOD= 2.75 mm, (c) CMOD= 3.5 mm, (d) CMOD= 3.75 mm

To go further in the understanding of the damage mechanisms and the mechanical behavior of cut edges and their impact on steel sheets formability:

- Perform in situ experiments using higher resolution would be of use as damage processes are on smaller scales
- Differentiate between particles and voids would be useful but is currently hard.
- Use X-ray holotomography technique to better understand the impact of cutting processes on microstructures at initial state. This 3D imaging technique allows one to visualize in three dimensions the damage in link with the microstructure.
- Perform modeling of the rough surface on punched edges and accounting for void shape in a coupled model (GTN like with modification for shape). It would be interesting if this could be studied and included in a physically based multiscale approach to study the nucleation at interfaces on the nano to micro-scale
- Study the damage mechanisms involved during cutting a FB steel sheets. Figure 5.16 shows the formation of needle-shape voids during shearing test.

In terms of potential improvement of materials, design of a FB microstructure without inclusions and segregation line should lead to improved mechanical strength et decrease the sensitivity to cut edges. One way to verify the hypothesis of the influece of the segregation line is to reduce the sheet thickness in a nonsymmetric way.

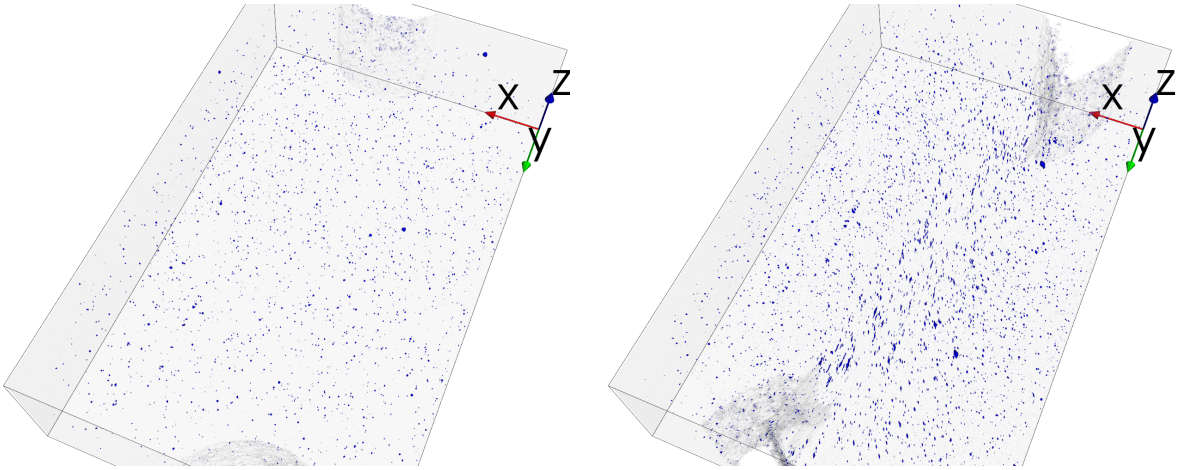

(a) (b)

Figure 5.16 – A 400 μm thick volume provided using X-ray synchrotron laminography observations of the studied FB steel during shearing test. The distance between notches is about 1 mm. Rendered voids are shown in blue. The material is made half-transparent. (a) initial state, (b) after deformation (Courtesy: Y. Cheng)

- For DP steels, it would be interesting to understand the micromechanisms that occur at the ferrite-martensite interfaces using a multiscale modeling.
- To improve the failure prediction in the simulations of in situ laminography test and hole expansion test, void nucleation and growth criteria suggested in this study could be further developped to enhance the failure prediction for the DP steel. Fully-coupled models (for example GTN model) could also be used.

Bibliography

[Abramoff et al., 2004] Abramoff, M. D., Magelhaes, P. J., and Ram, S. J. (2004). Image processing with imagej. *Biophotonics international*, 11(7):36–42.

[Adamczyk and Michal, 1986] Adamczyk, R. and Michal, G. (1986). Sheared edge extension of high-strength cold-rolled steels. *Journal of Applied Metalworking*, 4(2):157–163.

[AHSS Guidelines, 2009] AHSS Guidelines (2009). *Advanced High Strength Steels (AHSS) Application Guidelines, version 4.1*. WorldAutoSteel.

[Al-Abbasi and Nemes, 2003] Al-Abbasi, F. and Nemes, J. (2003). Micromechanical modeling of dual phase steels. *International Journal of Mechanical Sciences*, 45(9):1449–1465.

[Allain et al., 2012] Allain, S., Bouaziz, O., and Takahashi, M. (2012). Toward a new interpretation of the mechanical behaviour of as-quenched low alloyed martensitic steels. *ISIJ international*, 52(4):717–722.

[Argon et al., 1975] Argon, A., Im, J., and Safoglu, R. (1975). Cavity formation from inclusions in ductile fracture. *Metallurgical Transactions*, 6(4):825–837.

[Arlazarov et al., 2013] Arlazarov, A., Bouaziz, O., Hazotte, A., Gouné, M., and Allain, S. (2013). Characterization and modeling of manganese effect on strength and strain hardening of martensitic carbon steels. *ISIJ International*, 53(6):1076–1080.

[Avramovic-Cingara et al., 2009a] Avramovic-Cingara, G., Ososkov, Y., Jain, M., and Wilkinson, D. (2009a). Effect of martensite distribution on damage behaviour in dp600 dual phase steels. *Materials Science and Engineering*, 516:7–16.

[Avramovic-Cingara et al., 2009b] Avramovic-Cingara, G., Saleh, C., Jain, M., and Wilkinson, D. (2009b). Void nucleation and growth in dual-phase steel 600 during uniaxial tensile testing. *Metallurgical and Materials Transactions*, 40(13):3117–3127.

[Azuma et al., 2012] Azuma, M., Goutianos, S., Hansen, N., Winther, G., and Huang, X. (2012). Effect of hardness of martensite and ferrite on void formation in dual phase steel. *Materials Science and Technology*, 28(9-10):1092–1100.

[Bacha, 2006] Bacha, A. (2006). *Découpe des tôles en alliages d'aluminium : analyse physique et mécanique*. PhD thesis, École Nationale Supérieure des Mines de Saint-Etienne.

[Balendra and Travis, 1970] Balendra, R. and Travis, F. (1970). Static and dynamic blanking of steel of varying hardness. *International Journal of Machine Tool Design and Research*, 10(2):249–271.

[Bao and Wierzbicki, 2004] Bao, Y. and Wierzbicki, T. (2004). On fracture locus in the equivalent strain and stress triaxiality space. *International Journal of Mechanical Sciences*, 46(1):81–98.

[Ben-Bettaieb et al., 2011] Ben-Bettaieb, M., Lemoine, X., Bouaziz, O., Habraken, A. M., and DuchÃªne, L. (2011). Numerical modeling of damage evolution of dp steels on the basis of x-ray tomography measurements. *Mechanics of Materials*, 43(3):139–156.

[Benzerga, 2000] Benzerga, A. (2000). *Rupture ductile des toles anisotropes*. PhD thesis, École Nationale Supérieure des Mines de Paris.

[Benzerga, 2002] Benzerga, A. (2002). Micromechanics of coalescence in ductile fracture. *Journal of the Mechanics and Physics of Solids*, 50(6):1331–1362.

[Benzerga et al., 2004] Benzerga, A., Besson, J., and Pineau, A. (2004). Anisotropic ductile fracture: Part ii: theory. *Acta Materialia*, 52(15):4639–4650.

[Beremin, 1981] Beremin, F. (1981). Cavity formation from inclusions in ductile fracture of a508 steel. *Metallurgical Transactions A*, 12(5):723–731.

[Besson, 2010] Besson, J. (2010). Continuum models of ductile fracture: A review. *International Journal of Damage Mechanics*, 19(1):3–52.

[Besson et al., 2010] Besson, J., Cailletaud, G., J.-L., C., and S., F. (2010). *Non Linear Mechanics of Materials*. Springer.

[Bhadeshia and Honeycombe, 2006] Bhadeshia, H. and Honeycombe, R. (2006). *Steels: microstructure and properties, 3rd Edition*. Butterworth-Heinemann.

[Bouaziz et al., 2010] Bouaziz, O., Douchamps, S., Durrenberger, L., and Bui-Van, A. (2010). The double bending test: a promising new way for an optimal characterization of cut-edges ductility. In *International Deep-Drawing Research Group*, pages 164 – 169, London.

[Breitling et al., 1997] Breitling, J., Chernauskas, V., Taupin, E., and Altan, T. (1997). Precision shearing of billets—special equipment and process simulation. *Journal of Materials Processing Technology*, 71(1):119–125.

[Brown and Clarke, 1975] Brown, L. and Clarke, D. (1975). Work hardening due to internal stresses in composite materials. *Acta metallurgica*, 23(7):821–830.

[Brown and Embury, 1973] Brown, M. and Embury, D. (1973). A model of ductile fracture in two-phase materials. In *The 3rd international conference on strength of metals and alloys*, pages 164 – 169, London.

[Buffiere et al., 2010] Buffiere, J.-Y., Maire, E., Adrien, J., Masse, J.-P., and Boller, E. (2010). In situ experiments with x ray tomography: an attractive tool for experimental mechanics. *Experimental Mechanics*, 50(3):289–305.

[Bull et al., 2013] Bull, D., Helfen, L., Sinclair, I., Spearing, S., and Baumbach, T. (2013). A synthesis of multi-scale 3d x-ray tomographic inspection techniques for assessing carbon fibre composite impact damage. *Composites Science and Technology*, 75:55–61.

[Chaboche, 2008] Chaboche, J. (2008). A review of some plasticity and viscoplasticity constitutive theories. *International Journal of Plasticity*, 24(10):1642–1693.

[Chen et al., 2004] Chen, Z., Tang, C., and Lee, T. (2004). An investigation of tearing failure in fine-blanking process using coupled thermo-mechanical method. *International Journal of Machine Tools and Manufacture*, 44:155–165.

[Cho et al., 1999a] Cho, Y.-R., Chung, J.-H., Ku, H.-H., and Kim, I.-B. (1999a). Effect of controlled cooling on the formability of ts 590 mpa grade hot-rolled high strength steels. *Metals and Materials*, 5(6):571–578.

[Cho et al., 1999b] Cho, Y.-R., Chung, J.-H., Ku, H.-H., and Kim, I.-B. (1999b). Effect of controlled cooling on the formability of ts 590 mpa grade hot-rolled high strength steels. *Metals and Materials*, 5(6):571–578.

[Chu and Needleman, 1980] Chu, C. and Needleman, A. (1980). Void nucleation effects in biaxially stretched sheets. *Journal of Engineering Materials and Technology*, 102(3):249–256.

[Dalloz, 2007] Dalloz, A. (2007). *Étude de l'endommagement par la découpe des aciers dual phase pour application automobile*. PhD thesis, École Nationale Supérieure des Mines de Paris.

[Dalloz et al., 2009] Dalloz, A., Besson, J., Gourgues-Lorenzon, A.-F., Sturel, T., and Pineau, A. (2009). Effect of shear cutting on ductility of a dual phase steel. *Engineering Fracture Mechanics*, 76(10):1411–1424.

[Davies, 1978] Davies, R. (1978). Influence of martensite composition and content on the properties of dual phase steels. *Metallurgical and Materials Transactions A*, 9:671–679.

[Douissard et al., 2012] Douissard, P. A., Cecilia, A., Rochet, X., Chapel, X., Martin, T., van de Kamp, T., Helfen, L., Baumbach, T., Luquot, L., Xiao, X., Meinhardt, J., and Rack, A. (2012). A versatile indirect detector design for hard x-ray microimaging. *Journal of Instrumentation*, 7(09):P09016.

[Fang et al., 2002] Fang, G., Zeng, P., and Lou, L. (2002). Finite element simulation of the effect of clearance on the forming quality in the blanking process. *Journal of Materials Processing Technology*, 122(2):249–254.

[Fang et al., 2003a] Fang, X., Fan, Z., Ralph, B., Evans, P., and Underhill, R. (2003a). Effects of tempering temperature on tensile and hole expansion properties of a c–mn steel. *Journal of Materials Processing Technology*, 132(1–3):215 – 218.

[Fang et al., 2003b] Fang, X., Fan, Z., Ralph, B., Evans, P., and Underhill, R. (2003b). The relationships between tensile properties and hole expansion property of c-mn steels. *Journal of Materials Science*, 38(18):3877–3882.

[Fansi et al., 2013] Fansi, J., Balan, T., Lemoine, X., Maire, E., Landron, C., Bouaziz, O., Bettaieb, M. B., and Habraken, A. M. (2013). Numerical investigation and experimental validation of physically based advanced {GTN} model for {DP} steels. *Materials Science and Engineering: A*, 569:1–12.

[French and Weinrich, 1975] French, I. and Weinrich, P. (1975). The effects of hydrostatic pressure on the mechanism of tensile fracture of aluminum. *Metallurgical Transactions A*, 6(6):1165–1169.

[Gammage et al., 2005] Gammage, J. J., Wilkinson *, D. S., Embury, J. D., and Maire, E. (2005). Damage studies in heterogeneous aluminium alloys using x-ray tomography. *Philosophical Magazine*, 85(26-27):3191–3206.

[Geni and Kikuchi, 1999] Geni, M. and Kikuchi, M. (1999). Void configuration under constrained deformation in ductile matrix materials. *Computational Materials Science*, 16:391–403.

[Goijaerts et al., 2001] Goijaerts, A., Govaert, L., and Baaijens, F. (2001). Evaluation of ductile fracture models for different metals in blanking. *Journal of Materials Processing Technology*, 110(3):312–323.

[Goijaerts et al., 1999] Goijaerts, A., Govaert, L., and F.P.T., B. (1999). Prediction of ductile fracture in metal blanking. *Journal of Manufacturing Science and Engineering*, 122(3):476–483.

[Goijaerts et al., 2000] Goijaerts, A., Stegeman, Y., Govaert, L., Brokken, D., Brekelmans, W., and Baaijens, F. (2000). Can a new experimental and numerical study improve metal blanking? *Journal of Materials Processing Technology*, 103(1):44–50.

[Grange et al., 1977] Grange, R., Hribal, C., and Porter, L. (1977). Hardness of tempered martensite in carbon and low-alloy steels. *Metallurgical and Materials Transactions A*, 8(11):1775–1785.

[Gurson, 1975] Gurson, A. (1975). *Continuum Theory of Ductile Rupture by Void Nucleation and Growth: Yield criteria and flow rules for porous ductile media*. Technical report (Brown University. Division of Engineering). Division of Engineering, Brown University.

[Hambli, 2001] Hambli, R. (2001). Comparison between lemaitre and gurson damage models in crack growth simulation during blanking process. *International Journal of Mechanical Sciences*, 43(12):2769–2790.

[Hambli, 2002] Hambli, R. (2002). Prediction of burr height formation in blanking processes using neural network. *International Journal of Mechanical Sciences*, 44(10):2089–2102.

[Han and Margolin, 1989] Han, S.-K. and Margolin, H. (1989). Void formation, void growth and tensile fracture of plain carbon steel and a dual-phase steel. *Materials Science and Engineering: A*, 112:133–141.

[Hansen and Pradhan, 1981] Hansen, S. and Pradhan, R. (1981). Structure–property relationships and continuous yielding behavior in dual-phase steels. *Fundamentals of Dual-Phase Steels*, pages 113–144.

[Hasegawa et al., 2004] Hasegawa, K., KAWAMURA, K., URABE, T., and HOSOYA, Y. (2004). Effects of microstructure on stretch-flange-formability of 980 mpa grade cold-rolled ultra high strength steel sheets. *ISIJ International*, 44 (3):603–609.

[Helfen et al., 2005] Helfen, L., Baumbach, T., Mikulik, P., Kiel, D., Pernot, P., Cloetens, P., and Baruchel, J. (2005). High-resolution three-dimensional imaging of flat objects by synchrotron-radiation computed laminography. *Applied Physics Letters*, 86(7):071915–071915–3.

[Helfen et al., 2012] Helfen, L., Morgeneyer, T. F., Xu, F., Mavrogordato, M. N., Sinclair, I., Schillinger, B., and Baumbach, T. (2012). Synchrotron and neutron laminography for three-dimensional imaging of devices and flat material specimens. *International Journal of Materials Research*, 2012(2):170–173.

[Helfen et al., 2011] Helfen, L., Myagotin, A., Mikulík, P., Pernot, P., Voropaev, A., Elyyan, M., Di Michiel, M., Baruchel, J., and Baumbach, T. (2011). On the implementation of computed laminography using synchrotron radiation. *Review of Scientific Instruments*, 82(6):–.

[Helfen et al., 2007] Helfen, L., Myagotin, A., Rack, A., Pernot, P., Mikulík, P., Di Michiel, M., and Baumbach, T. (2007). Synchrotron-radiation computed laminography for high-resolution three-dimensional imaging of flat devices. *Physica Status solidi A*, 204:2760–2765.

[Hell, 2011] Hell, J. (2011). *Aciers bainitiques sans carbure : Caractérisations microstructurales multi-échelles et in situ de la transformation austénite – bainite et relations entre microstructure et comportement mécanique.* PhD thesis, Université Paul VErlaine de Metz.

[Henke et al., 1993] Henke, B. L., Gullikson, E. M., and Davis, J. C. (1993). X-ray interactions: photoabsorption, scattering, transmission, and reflection at e= 50-30,000 ev, z= 1-92. *Atomic data and nuclear data tables*, 54(2):181–342.

[Hild, 2002] Hild, F. (2002). A software for displacement field measurements by digital image correlation. *LMT Cachan, report 252.*

[Hilditch and Hodgson, 2005] Hilditch, T. and Hodgson, P. (2005). Development of the sheared edge in the trimming of steel and light metal sheet: Part 1, experimental observations. *Journal of Materials Processing Technology*, 169(2):184–191.

[Huang, 1991] Huang, Y. (1991). Accurate dilatation rates for spherical voids in triaxial stress fields. *Journal of Applied Mechanics*, 58(4):1084–1086.

[Hyun et al., 2002] Hyun, D., Oak, S., Kang, S., and Moon, Y. (2002). Estimation of hole flangeability for high strength steel plates. *Journal of Materials Processing Technology*, 130–131:9 – 13. {AFDM} 2002 S.I.

[Ismail, 20O7] Ismail, A. B. (20O7). *Modélisation de la découpe des tôles ferromagnétiques*. PhD thesis, Université Technologique de Campiègne.

[Jacques et al., 2007] Jacques, P., Furnémont, Q., Lani, F., Pardoen, T., and Delannay, F. (2007). Multiscale mechanics of trip-assisted multiphase steels: I. characterization and mechanical testing. *Acta Materialia*, 55(11):3681–3693.

[Jha et al., 2012] Jha, G., Das, S., Lodh, A., and Haldar, A. (2012). Development of hot rolled steel sheet with 600 mpa uts for automotive wheel application. *Materials Science and Engineering: A*, 552:457–463.

[Johnson and Slater, 1967] Johnson, W. and Slater, R. (1967). A survey of the slow and fast blanking of metals at ambient and high temperatures. In *Proceedings of the International Conference on Manufacturing Technology*, pages 825 – 851.

[Kadkhodapour et al., 2011] Kadkhodapour, J., Butz, A., and Rad, S. Z. (2011). Mechanisms of void formation during tensile testing in a commercial, dual-phase steel. *Acta Materialia*, 59(7):2575–2588.

[Kahziz et al., 2015] Kahziz, M., Morgeneyer, T., Mazière, M., Helfen, L., Bouaziz, O., and Maire, E. (2015). In situ 3d synchrotron laminography assessment of edge fracture in dual-phase steels: quantitative and numerical analysis. *Accepted for publication in Experimental Mechanics*.

[Kim et al., 2010] Kim, J. H., Lee, M., Kim, D., Matlock, D., and Wagoner, R. (2010). Hole-expansion formability of dual-phase steels using representative volume element approach with boundary-smoothing technique. *Materials Science and Engineering: A*, 527(27–28):7353–7363.

[Koplik and Needleman, 1988] Koplik, J. and Needleman, A. (1988). Void growth and coalescence in porous plastic solids. *International Journal of Solids and Structures*, 24(8):835–853.

[Krauss, 1999] Krauss, G. (1999). Martensite in steel: strength and structure. *Materials science and engineering: A*, 273:40–57.

[Krauss, 2001] Krauss, G. (2001). Deformation and fracture in martensitic carbon steels tempered at low temperatures. *Metallurgical and Materials transactions A*, 32(4):861–877.

[Lafrance, 1999] Lafrance, M. (1999). Propriéés d'emploi des tôles fortes en acier. *Revue de Métallurgie*.

[Lambert-Perlade, 2000] Lambert-Perlade, A. (2000). *Rupture par clivage de microstructures d'aciers bainitiques obtenues en conditions de soudage*. PhD thesis, École Nationale Supérieure des Mines de Paris.

[Landron, 2011] Landron, C. (2011). *Ductile damage characterization in Dual-Phase steels using X-ray tomography*. PhD thesis, Institut National des Sciences Appliquées de Lyon.

[Landron et al., 2010] Landron, C., Bouaziz, O., Maire, E., and Adrien, J. (2010). Characterization and modeling of void nucleation by interface decohesion in dual phase steels. *Scripta Materialia*, 63(10):973–976.

[Landron et al., 2013] Landron, C., Bouaziz, O., Maire, E., Adrien, J., et al. (2013). Experimental investigation of void coalescence in a dual phase steel using x-ray tomography. *Acta Materialia*, 61(18):6821–6829.

[Landron et al., 2011a] Landron, C., Maire, E., Adrien, J., Bouaziz, O., Michiel, M. D., Cloetens, P., and Suhonen, H. (2011a). Resolution effect on the study of ductile damage using synchrotron x-ray tomography. *Nuclear Instruments and Methods in Physics Research Section B: Beam Interactions with Materials and Atoms*, (0):–.

[Landron et al., 2012a] Landron, C., Maire, E., Adrien, J., Suhonen, H., Cloetens, P., and Bouaziz, O. (2012a). Non-destructive 3-d reconstruction of the martensitic phase in a dual-phase steel using synchrotron holotomography. *Scripta Materialia*, 66(12):1077–1080.

[Landron et al., 2012b] Landron, C., Maire, E., Adrien, J., Suhonen, H., Cloetens, P., Bouaziz, O., et al. (2012b). Non destructive 3d reconstruction of the martensitic phase in a dual-phase steel using synchrotron holotomography. *Scripta Materialia*, (0):–.

[Landron et al., 2011b] Landron, C., Maire, E., Bouaziz, O., Adrien, J., Lecarme, L., and Bareggi, A. (2011b). Validation of void growth models using x-ray microtomography characterization of damage in dual phase steels. *Acta Materialia*, 59(20):7564–7573.

[Lara et al., 2013] Lara, A., Picas, I., and Casellas, D. (2013). Effect of the cutting process on the fatigue behaviour of press hardened and high strength dual phase steels. *Journal of Materials Processing Technology*, 213:1908–1919.

[Le Jolu et al., 2014] Le Jolu, T., Morgeneyer, T. F., Denquin, A., Sennour, M., Laurent, A., Besson, J., and Gourgues-Lorenzon, A.-F. (2014). Microstructural characterization of internal welding defects and their effect on the plastic behavior of FSW joints of AA2198 Al-Cu-Li alloy. *Metallurgical and Materials Transactions A*, 45:5531–5544.

[Lee et al., 1995] Lee, T., Chan, L., and Wu, B. (1995). Straining behaviour in blanking process - fine blanking vs conventional blanking. *Journal of Materials Processing Technology*, 48:105–111.

[Levy et al., 2013] Levy, B., Gibbs, M., and Tyne, C. (2013). Failure during sheared edge stretching of dual-phase steels. *Metallurgical and Materials Transactions A*, 44(8):3635–3648.

[Levy and Van Tyne, 2011] Levy, B. and Van Tyne, C. (2011). Review of the shearing process for sheet steels and its effect on sheared-edge stretching. *Journal of Materials Engineering and Performance*, pages 1–9.

[Levy and Van Tyne, 2012] Levy, B. and Van Tyne, C. (2012). Effect of a strain-hardening rate at uniform elongation on sheared edge stretching. *Journal of Materials Engineering and Performance*, pages 1–8.

[Maillard, 1991] Maillard, A. (1991). *Etude expérimentale et théorique du découpage*. PhD thesis, Université Technologique de Compiègne.

[Maire et al., 2005] Maire, E., Bordreuil, C., Babout, L., and Boyer, J.-C. (2005). Damage initiation and growth in metals. comparison between modelling and tomography experiments. *Journal of the Mechanics and Physics of Solids*, 53(11):2411–2434.

[Maire et al., 2008] Maire, E., Bouaziz, O., Michiel, M. D., and Verdu, C. (2008). Initiation and growth of damage in a dual-phase steel observed by x-ray microtomography. *Acta Materialia*, 56(18):4954–4964.

[Maire et al., 2011] Maire, E., Zhou, S., Adrien, J., and Dimichiel, M. (2011). Damage quantification in aluminium alloys using in situ tensile tests in x-ray tomography. *Engineering Fracture Mechanics*, 78(15):2679–2690.

[Mazinani and Poole, 2007] Mazinani, M. and Poole, W. (2007). Effect of martensite plasticity on the deformation behavior of a low-carbon dual-phase steel. *Metallurgical and Materials Transactions A*, 38(2):328–339.

[McClintock, 1968] McClintock, F. A. (1968). A criterion for ductile fracture by the growth of holes. *Journal of Applied Mechanics*, 35(2):363–371.

[Misra et al., 2001] Misra, R., Thompson, S., Hylton, T., and Boucek, A. (2001). Microstructures of hot-rolled high-strength steels with significant differences in edge formability. *Metallurgical and Materials Transactions A*, 32(13):745–760.

[Morgeneyer et al., 2009] Morgeneyer, T., Besson, J., Proudhon, H., Starink, M., and Sinclair, I. (2009). Experimental and numerical analysis of toughness anisotropy in {AA2139} al-alloy sheet. *Acta Materialia*, 57(13):3902–3915.

[Morgeneyer et al., 2013] Morgeneyer, T., Helfen, L., Mubarak, H., and Hild, F. (2013). 3d digital volume correlation of synchrotron radiation laminography images of ductile crack initiation: An initial feasibility study. *Experimental Mechanics*, 53(4):543–556.

[Morgeneyer et al., 2011] Morgeneyer, T., Helfen, L., Sinclair, I., Proudhon, H., Xu, F., and Baumbach, T. (2011). Ductile crack initiation and propagation assessed via in situ synchrotron radiation-computed laminography. *Scripta Materialia*, 65(11):1010–1013.

[Mori, 2012] Mori, K. (2012). Smart hot stamping of ultra-high strength steel parts. *Transactions of Nonferrous Metals Society of China*, 22, Supplement 2(0):s496–s503.

[Mori et al., 2013] Mori, K., Abe, Y., Kidoma, Y., and Kadarno, P. (2013). Slight clearance punching of ultra-high strength steel sheets using punch having small round edge. *International Journal of Machine Tools and Manufacture*, 65(0):41–46.

[Mori et al., 2008] Mori, K., Saito, S., and Maki, S. (2008). Warm and hot punching of ultra high strength steel sheet. *{CIRP} Annals - Manufacturing Technology*, 57(1):321–324.

[Myagotin et al., 2013] Myagotin, A., Voropaev, A., Helfen, L., Hanschke, D., and Baumbach, T. (2013). Efficient volume reconstruction for parallel-beam computed laminography by filtered backprojection on multi-core clusters. *IEEE Transactions on Image Processing*, 22(12):5348–5361.

[Nakada et al., 2014] Nakada, N., Mizutani, K., Tsuchiyama, T., and Takaki, S. (2014). Difference in transformation behavior between ferrite and austenite formations in medium manganese steel. *Acta Materialia*, 65:251–258.

[P., 1964] P., B. (1964). Bstudies in large plastic flow and fracture with special emphasis on the effects of hydrostatic pressure. *Harvard University Press, Cambridge, MA*.

[Papasidero, 2014] Papasidero, J. (2014). *Etude expérimentale et numérique de la rupture ductile sous chargement multiaxial*. PhD thesis, École Polytechnique, France.

[Pardoen and Delannay, 1998] Pardoen, T. and Delannay, F. (1998). Assessment of void growth models from porosity measurements in cold-drawn copper bars. *Metallurgical and Materials Transactions A*, 29(7):1895–1909.

[Pardoen and Hutchinson, 2000] Pardoen, T. and Hutchinson, J. (2000). An extended model for void growth and coalescence. *Journal of the Mechanics and Physics of Solids*, 48(12):2467–2512.

[Pardoen and Pineau, 2007] Pardoen, T. and Pineau, A. (2007). Failure mechanisms of metals. In *Comprehensive Structural Integrity Encyclopedia*. Elsevier.

[Park and Thompson, 1988] Park, I.-G. and Thompson, A. W. (1988). Ductile fracture in spheroidized 1520 steel. *Acta Metallurgica*, 36(7):1653–1664.

[Paul, 2013] Paul, S. K. (2013). Effect of martensite volume fraction on stress triaxiality and deformation behavior of dual phase steel. *Materials & Design*, (0):–.

[Paul et al., 2014] Paul, S. K., Mukherjee, M., Kundu, S., and Chandra, S. (2014). Prediction of hole expansion ratio for automotive grade steels. *Computational Materials Science*, 89:189 – 197.

[Pyttel et al., 2000] Pyttel, T., John, R., and Hoogen, M. (2000). A finite element based model for the description of aluminium sheet blanking. *International Journal of Machine Tools and Manufacture*, 40(14):1993–2002.

[Ramazani et al., 2013] Ramazani, A., Schwedt, A., Aretz, A., Prahl, U., and Bleck, W. (2013). Characterization and modelling of failure initiation in dpsteel. *Computational Materials Science*, 75:35–44.

[Ramos et al., 1979] Ramos, L. F., Matlock, D. K., and Krauss, G. (1979). On the deformation behavior of dual-phase steels. *Metallurgical and Materials Transactions A*, 10(2):259–261.

[Rèche et al., 2012] Rèche, D., Besson, J., Sturel, T., Lemoine, X., and Gourgues-Lorenzon, A. (2012). Analysis of the air-bending test using finite-element simulation: Application to steel sheets. *International Journal of Mechanical Sciences*, 57(1):43–53.

[Rice and Tracey, 1969] Rice, J. and Tracey, D. (1969). On the ductile enlargement of voids in triaxial stress fields. *Journal of the Mechanics and Physics of Solids*, 17(3):201–217.

[Roumina et al., 2013] Roumina, R., Embury, J., Bouaziz, O., and Zurob, H. (2013). Mechanical behavior of a compositionally graded 300m steel. *Materials Science and Engineering: A*, 578:140–149.

[Saeidi et al., 2014] Saeidi, N., Ashrafizadeh, F., Niroumand, B., Forouzan, M., and Barlat, F. (2014). Damage mechanism and modeling of void nucleation process in a ferrite–martensite dual phase steel. *Engineering Fracture Mechanics*, 127:97–103.

[Sakaki et al., 1983] Sakaki, T., Sugimoto, K., and Fukuzato, T. (1983). Role of internal stress for continuous yielding of dual-phase steels. *Acta Metallurgica*, 31(10):1737–1746.

[Sartkulvanich et al., 2010] Sartkulvanich, P., Kroenauer, B., Golle, R., Konieczny, A., and Altan, T. (2010). Finite element analysis of the effect of blanked edge quality upon stretch flanging of ahss. *CIRP Annals - Manufacturing Technology*, 59(1):279–282.

[Shaimi and Moulin, 2004] Shaimi, A. and Moulin, A. (2004). Advanced high strength steels products. *Internal Report, ArcelorMittal Global R&D Maizières-l'es-Metz*.

[Shen et al., 2013] Shen, Y., Morgeneyer, T. F., Garnier, J., Allais, L., Helfen, L., and CrÃ©pin, J. (2013). Three-dimensional quantitative in situ study of crack initiation and propagation in {AA6061} aluminum alloy sheets via synchrotron laminography and finite-element simulations. *Acta Materialia*, 61(7):2571–2582.

[Shim et al., 2004] Shim, K., Lee, S., Kang, B., and Hwang, S. (2004). Investigation on blanking of thin sheet metal using the ductile fracture criterion and its experimental verification. *Journal of Materials Processing Technology*, 155–156(0):1935–1942.

[So et al., 2012] So, H., FaAmann, D., Hoffmann, H., Golle, R., and Schaper, M. (2012). An investigation of the blanking process of the quenchable boron alloyed steel 22mnb5 before and after hot stamping process. *Journal of Materials Processing Technology*, 212(2):437–449.

[So et al., 2009] So, H., Hoffmann, H., and Golle, R. (2009). Blanking of press hardened ultra high strength steel. In *Proceedings of 2nd International Conference on Hot Sheet Metal Forming of High-performance Steel*, pages 137 – 145, Luleo, Sweden.

[Speich et al., 1981] Speich, G., Demarest, V., and Miller, R. (1981). Formation of austenite during intercritical annealing of dual-phase steels. *Metallurgical Transactions A*, 12(8):1419–1428.

[Steinbrunner et al., 1988] Steinbrunner, D. L., Matlock, D., and Krauss, G. (1988). Void formation during tensile testing of dual phase steels. *Metallurgical Transactions A*, 19(3):579–589.

[Steven and Haynes, 1956] Steven, W. and Haynes, A. (1956). The temperature of formation of martensite and bainite in low-alloy steel. *Journal of the Iron and Steel Institute*.

[Sudo and Iwai,] Sudo, M. and Iwai, T. Deformation behavior and mechanical rroperties of ferrite - bainite - martensite (triphase) steel. *Journal of the Iron and Steel Institute of Japan*.

[Szewczyk and Gurland, 1982] Szewczyk, A. and Gurland, J. (1982). A study of the deformation and fracture of a dual-phase steel. *Metallurgical Transactions A*, 13(10):1821–1826.

[Taupin et al., 1996] Taupin, E., Breitling, J., tsu Wu, W., and Altan, T. (1996). Material fracture and burr formation in blanking results of {FEM} simulations and comparison with experiments. *Journal of Materials Processing Technology*, 59(1–2):68–78.

[Taylor et al., 2014] Taylor, M., Choi, K., Sun, X., Matlock, D., Packard, C., Xu, L., and Barlat, F. (2014). Correlations between nanoindentation hardness and macroscopic mechanical properties in {DP980} steels. *Materials Science and Engineering: A*, pages –.

[Thomas, 2012] Thomas, D. J. (2012). Effect of mechanical cut-edges on the fatigue and formability performance of advanced high-strength steels. *Journal of Failure Analysis and Prevention*, 12(5):518–531.

[Thomason, 1990] Thomason, P. (1990). *Ductile Fracture of Metals*. Pergamon Press.

[Thompson, 1987] Thompson, A. W. (1987). Modeling of local strains in ductile fracture. *Metallurgical Transactions A*, 18(11):1877–1886.

[Toda et al., 2011] Toda, H., Maire, E., Yamauchi, S., Tsuruta, H., Hiramatsu, T., and Kobayashi, M. (2011). In situ observation of ductile fracture using x-ray tomography technique. *Acta Materialia*, 59(5):1995–2008.

[Tong et al., 2005] Tong, W., Tao, H., Jiang, X., Zhang, N., Marya, M., Hector, L., and Gayden, X. (2005). Deformation and fracture of miniature tensile bars with resistance-spot-weld microstructures. *Metallurgical and Materials Tractions A - Physical Mettalurgy and Materials Science*, 36A(10):2651–2669.

[Tvergaard and Needleman, 1984] Tvergaard, V. and Needleman, A. (1984). Analysis of the cup-cone fracture in a round tensile bar. *Acta Metallurgica*, 32(1):157 – 169.

[Ueda et al., 2014] Ueda, T., Helfen, L., and Morgeneyer, T. (2014). In-situ laminography study of three-dimensional individual void shape evolution at crack initiation and comparison with gtn-type simulations. *Accepted for publication in Acta Materialia*.

[Wang et al., 2015] Wang, K., Greve, L., and Wierzbicki, T. (2015). Fe simulation of edge fracture considering pre-damage from blanking process. *International Journal of Solids and Structures*, pages –.

[Wang et al., 2014] Wang, K., Luo, M., and Wierzbicki, T. (2014). Experiments and modeling of edge fracture for an ahss sheet. *International Journal of Fracture*, 187(2):245–268.

[Weck, 20O7] Weck, A. (20O7). *The role of coalescence on ductile fracture.* PhD thesis, McMaster University, Canada.

[Weck and Wilkinson, 2008] Weck, A. and Wilkinson, D. (2008). Experimental investigation of void coalescence in metallic sheets containing laser drilled holes. *Acta Materialia*, 56(8):1774–1784.

[Wierzbicki and Bao, 2004] Wierzbicki, T. and Bao, Y. (2004). Bridgman revisited: On the history effect on ductile fracture. *Massachusetts Institute of Technology, Cambridge, MA*.

[Wu et al., 2012] Wu, X., Bahmanpour, H., and Schmid, K. (2012). Characterization of mechanically sheared edges of dual phase steels. *Journal of Materials Processing Technology*, 212(6):1209–1224.

[Xu et al., 2010] Xu, F., Helfen, L., Moffat, A. J., Johnson, G., Sinclair, I., and Baumbach, T. (2010). Synchrotron radiation computed laminography for polymer composite failure studies. *Journal of Synchrotron Radiation*, 17(2):222–226.

[Yerra et al., 2013] Yerra, S., Martin, G., Véron, M., Bréchet, Y., Mithieux, J., Delannay, L., and Pardoen, T. (2013). Ductile fracture initiated by interface nucleation in two-phase elastoplastic systems. *Engineering Fracture Mechanics*, 112:77–100.

Étude expérimentale et numérique des mécanismes d'endommagement ductile et rupture des bords découpés des aciers avancés pour l'automobile

La performance mécanique des pièces de structures automobiles fabriquées à partir de tôles d'acier à très haute résistance (THR) est souvent réduite à cause des bords découpés. Ce phénomène a été étudié pour deux nuances d'aciers ferrite-bainite (FB600) et ferrite-martensite (DP600). Les micromécanismes d'endommagement ont été caractérisés en utilisant la tomographie in situ et MEB in situ. Pour l'acier DP, la germination de cavités a eu lieu sur les inclusions et aux interfaces ferrite-martensite. De plus, des cavités sous forme d'aiguille ont été observées dans la zone centrale correspondant à la ligne de ségrégation. Les mêmes mécanismes de germination ont été observés dans le cas de l'acier FB en plus de la germination aux interfaces des carbures. L'analyse d'image a montré que l'acier DP présente une densité initiale de cavités et une densité de cavités germées plus élevées que celles de l'acier FB. Des bords poinçonnés et usinés des nuances DP et FB ont été caractérisés par laminographie in situ lors d'un chargement mécanique. Pour les bords poinçonnés, la zone rompue est rugueuse et un micro-endommagement sous forme d'aiguille initié sur la surface et dans le volume suit les lignes d'écoulement. Lors du chargement mécanique, les cavités sous forme d'aiguilles croissent à partir de la zone rompue et coalescent avec la zone cisaillée. En revanche, pour les bords usinés, l'endommagement s'initie loin de la surface de bords ($\sim$ 800 μm). Une analyse des données 3D a été réalisée pour quantifier l'état initial de l'endommagement et son évolution. L'acier FB a été plus résistant aux bords découpés que l'acier DP. Des simulations 3D par éléments finis ont que seuls ces paramètres ne modifient pas localement les champs mécaniques. Finalement, des simulations axisymétriques par éléments finis de l'essai d'expansion de trou ont été réalisées pour différentes épaisseurs de tôle en utilisant les critères d'endommagement identifiés.

Mots clés : aciers DP et FB, endommagement ductile, rupture de bords, tomographie/laminographie à rayons X, simulation numérique

Experimental and numerical investigation of ductile damage mechanisms and edge fracture in advanced automotive steels

Abstract:
The mechanical properties of automotive structures made of advanced high strength steels (AHSS) is often seen reduced by the presence of cut edges. Damage micromechanisms for these two base materials were assessed using synchrotron tomography and SEM. It was revealed for the DP steel that damage nucleated from particles and ferrite-martensite interfaces. In addition, needle shaped voids, that are consistent with the presence of segregation lines, were seen. For the FB steel, the same observations hold true except that the decohesion on interfaces sets in at higher strains. Quantitative image analysis also showed that the initial number of voids and the number of nucleating voids was higher for DP steel than for FB steel which was also seen to be more damage tolerant. Punched and machined edges made of DP600 and FB600 steel were mechanically loaded during in situ laminography testing. It was found that the fracture zone of the punched edge was rough and that needle-shape voids initiated at the surface and in the bulk followed material flow lines. During mechanical in situ testing the needle voids grew from the fracture zone surface and coalesced with the sheared zone. In contrast, for the machined edge the damage started away from the edge ($\sim$ 800 μm) where substantial necking has occurred. 3D image analysis was performed to quantify the initial damage and its evolution. The FB600 was more resistant to cut edges than the DP600 steel. 3D elasto-plastic FE calculations were carried out to investigate mechanical fields, potentially affected by the edge profile and pre-hardening profile. These parameters were not found to substantially modify the mechanical fields. Finally, axisymmetric 2D simulations for hole expansion were carried out for different sheet thicknesses using a post-processed damage evaluation calibrated on in-situ tomography data.
Keywords: DP and FB steels, ductile damage, edge fracture, X-ray tomography/laminography, finite element simulation

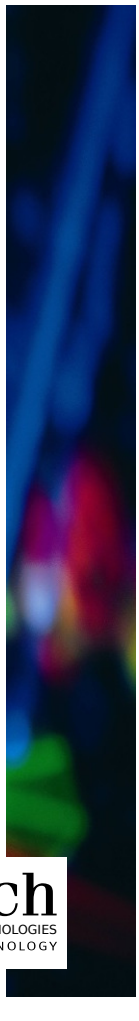

MINES ParisTech

ParisTech
INSTITUT DES SCIENCES ET TECHNOLOGIES
PARIS INSTITUTE OF TECHNOLOGY